Antarctic Alteration of Meteorites

Thesis

ANTARCTIC ALTERATION OF METEORITES

Thesis submitted for the degree of Doctor of Philosophy

Department of Physical Sciences

The Open University

By

Elisabeth Dawn Steer, MGeol.

21st March 2016

ABSTRACT

The discovery of large accumulations of meteorites in Antarctica is comparably recent, with annual collection expeditions beginning in 1974. Since then, over 50,000 meteorites have been recovered from the icefields of Antarctica. Many of those meteorites have had long residence times of up to 2 Ma mostly encased in ice; during which many of the meteorites have undergone considerable alteration. Understanding the paths of alteration allows reconstruction of original features, but additionally it gives a unique opportunity to examine a natural laboratory of cold, water-restricted alteration environments similar to those on Mars today and in its history.

To fully understand the weathering of meteorites in these environments, six L6 chondrites in a variety of weathering states have been examined and characterised petrologically, chemically, and magnetically. Chemical analyses undertaken are major and trace elements measured in bulk and in spatially resolved analysis and bulk oxygen isotopes.

Petrology has proven to control the weathering patterns and alteration state of the meteorite. A chemical weathering index has been developed to characterise the state of weathering using bulk chemical data, which also links with the petrological findings. This is especially evident in micro features created by shock, which promote rapid mineral breakdown and acidification of alteration fluids, which, fundamentally changes the nature and speed of the alteration. Shock generated features have created increased vulnerability to weathering and so areas that have undergone significant shock on Mars are more vulnerable to weathering and breakdown. However, the heterogeneity that is inherent to alteration environments of low water to rock ratios results in short transport distances for elements, resulting in little bulk chemical change with significant mineralogical alteration.

ACKNOWLEDGMENTS

There is no way I could ever manage to thank everyone who has helped me in some way over the last few years, as there have been so many, but I would like to thank as many as I can below in no particular order. I hope I haven't forgotten anyone, but it's been a long haul and there are many people to thank.

Firstly I want to thank my supervisors Susanne, Monica and Ian without whom I would not have been able to do my PhD. I want to thank Susanne in particular for all the days, nights and weekends she has put in gradually moulding me into a functioning researcher. I really couldn't have done it without the constant support and encouragement.

I couldn't have done my analytics without the technical help and advice from Sam Hammond, who put up with me bothering her a lot. Also thanks to Andy Tindle, Jenny Gibson, Richard Greenwood, Jérôme Gattacceca, the team from CEREGE, Diane Johnson and John Watson. Conversations with many people helped shape my thesis; in particular discussion with Richard Greenwood and Jérôme Gattacceca has been invaluable. I thank Sarah Sherlock and Rhian Jones for being my viva examiners and Axel Hagermann for organising and chairing the viva.

Thanks to my family, for always reminding me that there was a life outside of my thesis and always being incredulous at me working over holidays.

My friends have provided me with a lot of emotional support over the years and have listened to an awful lot of moaning, so thanks to James Mortimer, Dan Dawson, Mohit Melwani-Daswani, Ed Allanwood, Erika Kaufmann, Jean-David Bodénan, Jess Barnes, Feargus Abernethy, Alice Griffiths, the DPS houseband, Wolverton Town band, Tom Barratt, Roy Adkin, Joe Rushton and everyone in the PhD student office.

Finally I have to thank Mark, without whom I would've undoubtable been a blubbering wreck and never would have finished.

Table of Contents

LIST OF FIGURES

CHAPTER 1

CHAPTER 2

CHAPTER 3

CHAPTER 4

CHAPTER 5

CHAPTER 6

LIST OF TABLES

CHAPTER 1

CHAPTER 2

CHAPTER 3

CHAPTER 4

CHAPTER 5

CHAPTER 1 – INTRODUCTION

Of the 50,000 meteorites which make up the world's collection, over 30,000 have been recovered from Antarctica (Meteoritical Bulletin – accessed 01/15). They are a crucial resource for planetary scientists, expanding sample collections of other solar system bodies, allowing the detailed chemical and geological studies of these bodies which is not afforded by space (rover and orbiter) missions. They also provide a valuable cache of information about alteration processes unique to low temperature, water-restricted environments. This thesis is a study of a group of meteorites, their terrestrial weathering products and the processes they have experienced on Earth. The objective is to understand more completely the alteration process that occurs under cold desert conditions so that the findings can be extrapolated to rocks on the cold desert surface of Mars.

1.1. DISCOVERY AND ACCUMULATION METHOD OF METEORITES IN ANTARCTICA

The discovery of large accumulations of meteorites in Antarctica is a recent development. The earliest meteorite known to have been recovered from Antarctica was an L5 ordinary chondrite (named Adelie Land) found by Douglas Mawson's field party in 1912 (Mawson, 1915; Grady, 2000) which was brought back and studied by a geologist in the party (Bayly and Stillwell, 1923). In 1961, a pallasite meteorite (named Thiel Mountains) was discovered at Thiel Mountains (Fig.1.1) and was described as having been found on hard blue ice that was constantly polished by high speed windblown particles (Ford and Tabor, 1971). The meteorite was associated with moraine material, thus the authors assumed the meteorite had been transported in the glacier with the terrestrial rocks. This was accompanied by the important observation that wind is a critical component of erosion in Antarctica.

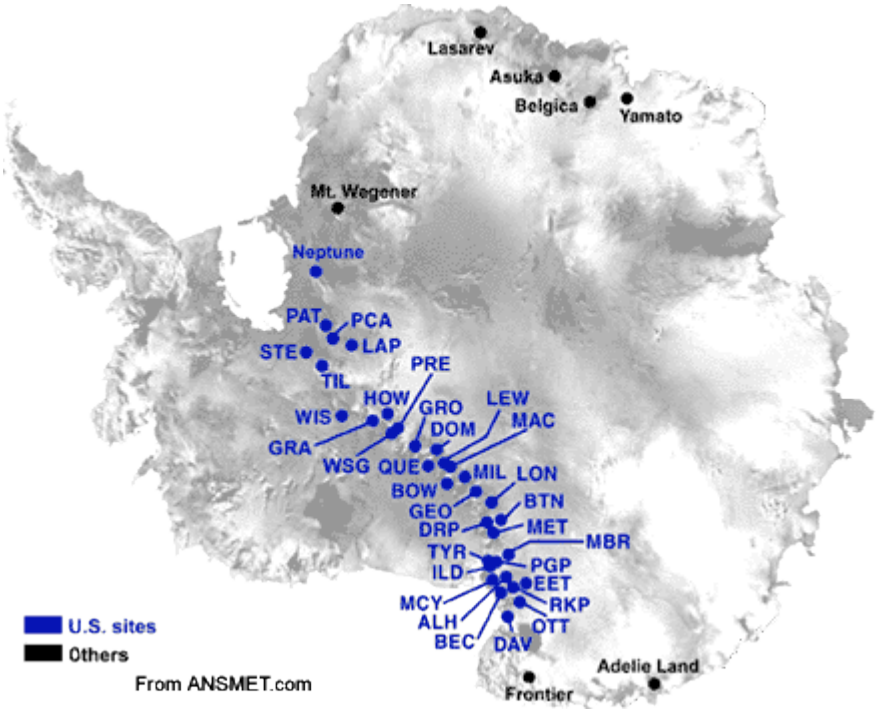

Code	Site Name	Code	Site Name	Code	Site Name	Code	Site Name	Code	Site Name
ALH	Allan Hills	**DEW**	Mt. DeWitt	**ILD**	Inland Forts	**MIL**	Miller Range	**RKP**	Reckling Peak
BEC	Beckett Nunatak	**DOM**	Dominion Range	**KLE**	Klein Ice Field	**ODE**	Odell Glacier	**SAN**	Sandford Cliffs
BOW	Bowden Neve	**DRP**	Derrick Peak	**LAP**	LaPaz Ice Field	**OTT**	Outpost Nunatak	**SCO**	Scott Glacier
BTN	Bates Nunataks	**EET**	Elephant Moraine	**LAR**	Larkman Nunatak	**PAT**	Patuxent Range	**STE**	Stewart Hills
BUC	Buckley Island	**FIN**	Finger Ridge	**LEW**	Lewis Cliff	**PCA**	Pecora Escarpment	**SZA**	Szabo Bluff
CMS	Cumulus Hills	**GDR**	Gardner Ridge	**LON**	Lonewolf Nunataks	**PGP**	Purgatory Peak	**TEN**	Tentacle Ridge
CRA	Mt. Cranfield	**GEO**	Geologists Range	**MAC**	MacAlpine Hills	**PRA**	Mt. Pratt	**TIL**	Thiel Mountains
CRE	Mt. Crean	**GRA**	Graves Nunataks	**MBR**	Mount Baldr	**PRE**	Mt. Prestrud	**TYR**	Taylor Glacier
DAV	David Glacier	**GRO**	Grosvenor Mountains	**MCY**	MacKay Glacier	**QUE**	Queen Alexandra Range	**WIS**	Wisconsin Range
DNG	D'Angelo Bluff	**HOW**	Mt. Howe	**MET**	Meteorite Hills	**RBT**	Roberts Massif	**WSG**	Mt. Wisting

Figure. 1.1. Map published on the ANSMET (Antarctic Search for Meteorites) website (http://caslabs.case.edu/ansmet/) showing the locations of all icefields from which meteorites have been collected to date. Samples for this study are from Queen Alexandra Range (QUE) and Allan Hills (ALH). Two of the first sites from which meteorites were collected are the Theil Mountains (TIL) and the Yamato Mountains. The full list of acronyms used is given in the table above.

In 1969, the 10th Japanese Antarctic Research Expedition (JARE) embarked on a campaign of glacial movement study in the Yamato Mountains (Fig. 1.1). These host many blue ice fields similar to that described at the Thiel Mountains by Ford and Tabor (1971). During a survey of one such icefield a JARE party discovered nine meteorites, which were returned to a geologist on the Science Council of Japan (Harvey, 2003). The resulting study of these nine meteorites revealed that the nine meteorites represented five different petrological groups, consisting of E, H, L chondrites, a carbonaceous chondrite and a diogenite. The small statistical likelihood of coincidental occurrences of different meteorite types in such a small area was noted, suggesting that there was a concentration mechanism behind it (Yoshida et al., 1971). Yoshida et al. (1971) noted moraine fields in the area and suggested that their existence was a product of the movement of the icefields, predicting that many more meteorites were likely to be present on the icefields. From this discovery, the 14th JARE expedition was encouraged to look for meteorites and consequently in 1973 found 12 more in the same patch of blue ice. On this basis, the 15th JARE expedition was sent with the single aim of finding meteorites and found 663 specimens. In 1975, an American counter-part, the Antarctic Search for Meteorites (ANSMET), was established by William Cassidy. ANSMET conducted joint expeditions with the Japanese teams for the next three seasons. Both programmes are still operational and are responsible for the collection of over 30,000 meteorites (Meteoritical bulletin – accessed 01/15).

This large scale collection is only possible because of the concentration of meteorites in the blue ice fields, which itself is due to a combination of the glacial movements first observed by Yoshida et al. (1971) and the mechanism of high speed wind abrasion observed by Ford and Tabor (1971). The next section describes how, after landing on Earth, the meteorites undergo several processes that concentrate them before and after they reach the concentration place (Fig 1.2.; Cassidy et al., 1992).

1.2. THE BLUE ICEFIELDS

The direct infall rate of meteorites in Antarctica is around 6/km^2/Ma (Cassidy, 1983). Some meteorites land directly on ablation surfaces, whilst others fall on the accumulation zones of glaciers, and become buried by the infalling precipitation that drives glacier movement (Cassidy, 1983; Cassidy et al., 1992). In accumulation zones, the weight of infalling snow compresses the ice and forces it to move outwards, upon which the glacier either moves towards the sea, melting and depositing its contents, or pushes against a geographical barrier such as a mountain belt (Cassidy et al., 1992; Harvey, 2003). The barrier has to be sufficiently extensive that the ice cannot be diverted around it; the ice is then forced upwards and ablated by the fierce katabatic (downhill flowing) winds that were first observed by Ford and Tabor (1971) to create the blue icefields, leaving behind all entrained material (Fig. 1.2). In Antarctica, the main meteorite traps are formed at the base of the Transantarctic Mountain Belt and the Yamato mountains.

The ablation of ice at blue icefields has been estimated to average at 5-6 cm/year (Cassidy, 1992), thus the accumulation of a large group of meteorites takes a long time. Older, more stable fields, such as Allan Hills, have been more fruitful for meteorite recovery. Ablation at mountain ranges exhumes deep ice from the bottom of the glacier, which is often sediment-laden and creates moraines. Moraines are mainly terrestrial material, additions from bedrock that have been picked up by the glacier during its movement. Moraines also contain disproportionate amounts of liquid water: moraines have a low albedo that creates effective warm patches in the icefields (Bintanja and Broeke, 1995). The deep ice shows a characteristic blue colour (due to a lack of air bubbles) that is visible from satellite photography (Harvey, 2003). Fig. 1.1 shows icefields from which meteorites have been collected successfully.

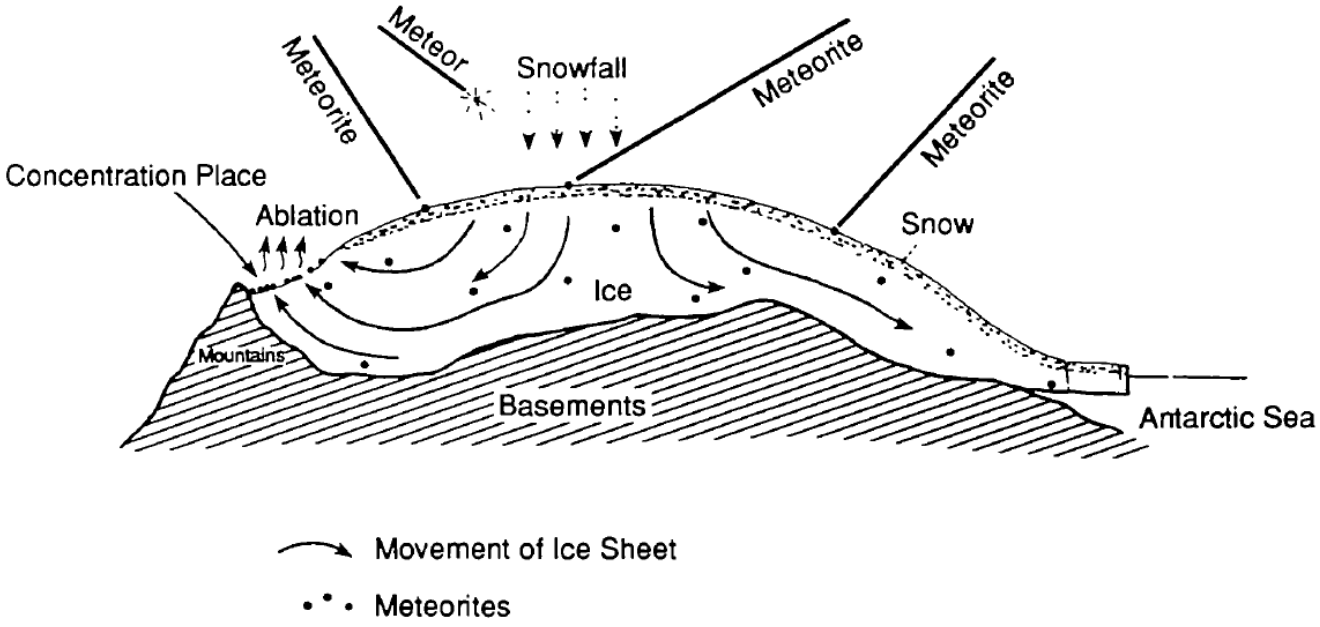

Figure.1.2. From Cassidy et al. (1992). This diagram describes the journey of meteorites in Antarctica from infall to the ablation plane. Note that most are transported out onto and lost at sea.

The extent of the blue icefields is determined by mass balance of the ice, which is easily affected by small scale environmental changes such as changes in precipitation and temperature (Binjanja and Broeke, 1995). Small changes in temperature can affect the katabatic winds necessary to create the negative mass balance that produces blue icefields, and so the blue icefields are of variable stability and the meteorite accumulations are likely to be periodically formed, and covered, on a 1000 year timescale (Binjanja and Broeke, 1995; Benoit and Sears, 1999). The blue icefields have a lower albedo compared to surrounding snow so their subsurface temperature can be up to 6 ^{o}C higher than the surrounding snow (Boggild et al., 1995). Once the blue icefields are formed, they perpetuate their existence, as their low albedo actively prevents snow settling on them (Bintanja and Broeke, 1995). Subsurface melting can also be created by bands of dark volcanic ash that occur in many icefields, e.g. at Allan Hills (Boggild et al., 1995).

As meteorite accumulations take a long time to form, the destruction of meteorites through weathering processes must also take a long time, otherwise they would not exist. Chemical erosion and destruction of the meteorites is slowed down, because of the low humidity, temperature and water availability (Jull, 2001). Slower chemical weathering means that the meteorites on the accumulation surfaces have longer terrestrial residence ages compared with meteorites found in more temperate climates. Antarctic meteorites have a maximum terrestrial residence age of 3 Ma (Welten et al., 2008) compared to a maximum age of 250,000 yrs for hot desert finds (Jull, 2001). The relative speed of weathering between hot and cold deserts has been estimated by Bland (2001) to be 2-3 orders of magnitudes slower in cold deserts. Thermoluminescence measurements suggest that Antarctic meteorites spend most of their terrestrial residence time travelling in the glacier, frozen in the ice in conditions where they are unlikely to be altering (Benoit and Sears, 1999).

1.3 TIMING OF WEATHERING PROCESSES

Weathering occurs at four different intervals of the meteorites' journey: 1) after landing but before burial in the glacier, upon which weathering is assumed to cease, 2) resumption during the initial exhumation, around 1 m below the ablation surface, 3) during residence on the ablation surface, 4) in the laboratory/museum ambient conditions after collection.

1) Weathering begins when the meteorite first lands on a surface of the glacier. Little is known about this stage since it has not been directly observed, but it is assumed to be similar to the final stage of weathering when the meteorite is exhumed from the glacier (Mittlefehldt and Lindstrom, 1990). Between the first two weathering events there is a period of cryostasis, where the meteorite is buried and transported in a glacier. This stage is assumed to have no effect on the meteorite's mineralogy (Harvey, 2003). The duration of burial entirely depends on the speed and extent of the glacier and its movement. This weathering hiatus prevents any easy correlation

between terrestrial residence age and the extent of weathering (Bland, 1998; Jull, 2001; Harvey, 2003).

2) Meteorites recovered from encasing ice have been observed to be extensively weathered, demonstrating that weathering occurs before the meteorites reach the ablation surface (Harvey and Score, 1991). Weathering can occur up to a metre depth beneath the surface of a glacier as the meteorite is slowly exhumed. At 1 m depth, water can exist as thin films of liquid (Benoit and Sears, 1999). This observation has led to the zone of weathering being redefined, as it was previously thought to occur mainly on the surface of the icefields. The lower albedo of meteorites and dark ash bands that frequently occur in the icefields leads to the presence of pools and films of water existing around meteorites at depths of up to 1 m, allowing formation of secondary minerals and redistribution of elements within the meteorite (Noll et al., 2003; Boggild et al., 1995). The speed of exhumation is dependent on climatic conditions and the speed of glacial movement, and so subsurface weathering can persist for an unknown length of time before the meteorite reaches the surface of the glacier.

3) Similar warming of meteorites occurs on the ablation surface: During an expedition to the ablation surface of the Elephant Moraine icefield, L. Schultz (Schultz 1986) placed a heat sensor inside a piece of Allende meteorite and observed it for several days. The centre of the meteorite frequently heated to 5 ^{o}C even with air temperatures of -10 ^{o}C. Wind chill appeared to play an important part, but the albedo of the meteorite allowed the presence of liquid water within it, accelerating the weathering. Similar temperature experiments on terrestrial dolerites were carried out by André et al. (2004), the results of which showed that the rock temperatures were frequently found to be 20 ^{o}C higher than the surrounding air.

The climate-driven thermal changes also result in mechanical stresses between mineral boundaries or different mineral types, as the extent of expansion and

contraction of minerals from heating and cooling varies between minerals. This can lead to failure along the mineral boundaries and disintegration (André et al., 2004). Mechanical weathering in Antarctica is of vast significance, since it creates intramineral fractures for fluids and gases to exploit, and it also exposes fresh reactive mineral surfaces to weathering processes. Once intramineral and transmineral fractures have been mechanically opened, water is drawn in by capillary action and once in the pore spaces, it survives for a much extended period of time: liquid water has been calculated by Gooding (1986) to exist in thin (>15 molecular layers thick) films down to a temperature of 263-264 K.

Meteorite size also makes a significant difference to weathering speed. Small meteorites recovered from Antarctica are statistically more likely to be highly weathered than large meteorites (Benoit and Sears, 1999). Benoit and Sears (1999) found that meteorite fragments in Allan Hills >150 g can take up to 300,000 years to fully weather, but fragments <150 g may only take 40,000 years to reach the highest degree of weathering. This is because a higher surface/volume ratio is exposed to the weathering environment.

As Antarctic meteorites are found so frequently with evaporite minerals on their exterior surfaces, their presence has gained its own weathering designation (see Section 1.4.1.; Velbel 1988). Surface exposure time correlates poorly with weathering state, in part because of the pulsatory nature of the weathering processes that are related to climatic changes (e.g., fluctuations in temperature, weather; Benoit and Sears, 1999). A final process that can occur after exhumation and before collection is wind transport of small (< 100 g) meteorites. These can be trapped in crevasses and re-buried, then exhumed again (Krahenbuhl and Langenaur, 1994).

4) Although laboratory or museum weathering is poorly documented (Lee and Bland, 2004; Jull et al., 1988), it is a colloquially well-known process. Laboratory weathering was clearly shown by Losiak and Velbel (2011), who found that year of collection was correlated with prevalence of evaporite deposits. Meteorites collected in 2003 were stored in a freezer which malfunctioned, and the rapid appearance of evaporites was observed. The brief excursion of temperature had a clear effect on the samples and demonstrated the detrimental effect of accidents during curation (Losiak and Velbel, 2011).

1.4 Mineralogical Changes

1.4.1 Weathering Scales

The current weathering index used for hand specimens collected by ANSMET (Antarctic Search for Meteorites) is based on percentages of rust covering the meteorite. These categories span from A-C with increasing amounts of weathering; 'A' being minor rustiness with some haloes around metal grains and minor stains along fractures, and 'C' being severe rustiness with almost all metal particles stained. An additional 'e' was added to this classification scheme to account for evaporite deposits. In 1993, a scale was proposed by Wlotzka (1993) for a weathering scale classification based on thin section examination with a scale of W0 – W6 based on microscopic observations of rust progression (Table 1.1, Fig. 1.3). It was originally produced to improve on the ANSMET A-C based weathering scale, but has been applied to all meteorite finds. However, this weathering scale is not one listed on the Meteoritical Bulletin, which still uses the ANSMET scale.

Previously, Mössbauer spectroscopy has been used to attempt to classify weathering more quantitatively, using the oxidation state of iron as a proxy for weathering (Burns et al., 1995). Ordinary chondrites are presumed to contain little ferric iron (iron as Fe^{3+}) before

they fall to Earth (unless in rare pre-terrestrial smectites). The extent of oxidation to ferric iron can be measured, where is assumed to be associated with terrestrial alteration products. Although correlation between weathering grade and amount of oxidised Fe has been confirmed, an attempt to link this to terrestrial age was unsuccessful, probably because of the unknown time spent by a sample resident within a glacier (Burns et al., 1995).

A common weathering index used by most geologists describing non-meteoritic samples is the Chemical Index of Alteration (CIA). This index largely concerns the breakdown of feldspar and volcanic glass as it ratios the (relatively) immobile Al_2O_3 to other major components of feldspar. It is given by molecular proportions ascertained from bulk measurements using the formula:

$$\mathrm{CIA} = \left(\frac{\mathrm{Al_2O_3}}{\mathrm{Al_2O_3 + Na_2O + K_2O + CaO}}\right) \mathrm{x100}$$

(Nesbitt and Young, 1982).

No comparable chemical index exists for meteorites, and the CIA has not been applied to the field of meteoritics before, most likely because it does not encompass the breakdown of ferromagnesian minerals.

Table 1.1. Weathering grades as defined in Wlotzka (1993)

Weathering Grade	Definition
W0	No visible oxidation of metals and should be similar to falls, although some falls can be W1
W1	Minor haloes of alteromorph around metals and troilite with minor veins
W2	Between 20-60% oxidised metal
W3	Heavily oxidised metals and troilite with 60-95% being replaced
W4	Complete oxidation of metals and troilite, no alteration of silicates
W5	Beginnings of silicate alteration along fractures
W6	Massive replacement of silicates by clay minerals and oxides

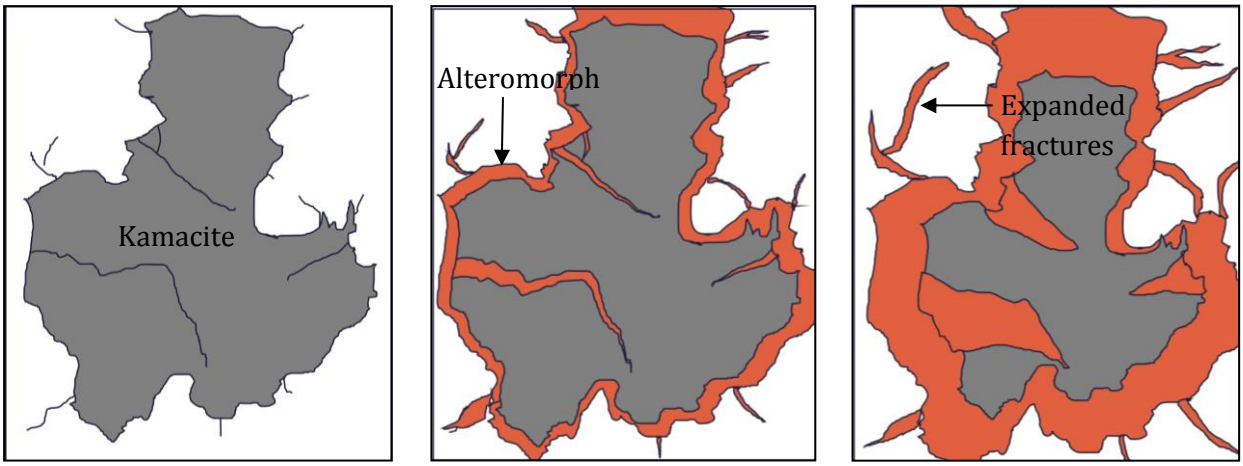

Fig. 1.3. Progression of oxidation during the alteration of a kamacite grain, representing various weathering grades of the Wlotzka (1993) weathering scheme. 1) W0 grade. An unaltered grain with some fractures cross cutting and surrounding. 2) W1 grade. Alteromorphs form a halo around the grain, fractures are exploited and widened. 3) W3 grade. The original kamacite grain is mostly altered with a halo wider than the original grain and the surrounding fractures having been widened, lengthened and filled with veins.

1.4.2 WEATHERING OF FE-NI METALS AND SULPHIDES

The most prevalent form of Antarctic alteration is the presence of "rust" comprised of hydrous Fe oxides. The rust in meteorites is a result of the alteration of kamacite (Fe with up to 7.5 wt. % Ni), taenite and tetrataenite (Fe with greater than 20 wt. % Ni) and troilite (FeS) (Gooding, 1982), producing Fe-oxides and oxyhydroxides (Lee and Bland, 2003). The four most visible types of weathering in meteorites are detailed by Gooding (1982) as: 1) Rinds and veins in the fusion crust, 2) veins and pockets filling areas other than the fusion crust, 3) rinds or mantles on kamacite, taenite and troilite, 4) myrmekitic oxide fillings within kamacite and taenite particles (Fig. 1.3).

The sequence of Antarctic weathering is correlated with changes in value of the Gibbs free-energy of the minerals calculated from the decompositions reactions (Gooding, 1982) which show the preferential alteration of kamacite and taenite over olivine (Gooding, 1982). In ordinary chondrites, the phases most susceptible to weathering are kamacite and taenite. A homogeneous kamacite or taenite grain weathers centripetally, forming haloes of alteration minerals around the parent grains (Wlotzka, 1993; Lee and Bland, 2003). The alteration products are often layered and are created from the oxidation of the native Fe and Ni. The alteration halo progressively thickens at an inconsistent rate, with initial weathering proceeding much more quickly before subsequent weathering progresses more slowly (Lee and Bland, 2003). The inconsistent weathering rate is because the initial halo coats and protects the parent metal grain and since the alteration products have low porosity, they then restrict fluid access to the mineral surfaces. Veins radiate from the area that is undergoing alteration (Fig. 1.3) and the extent of this in some Antarctic meteorites demonstrates the extent to which fluids play an important role in weathering (Velbel et al., 1991).

The Fe-oxides and oxyhydroxides found as Antarctic weathering products are mainly goethite (α - FeO(OH)) and hematite (Fe_2O_3), but also found are: lepidocrocite (γ -

$Fe^{3+}O(OH)$), akaganeite (β-$Fe^{3+}O(OH,Cl)$), maghemite ($Fe^{3+}{}_2O_3$) and magnetite ($Fe^{2+}Fe^{3+}{}_2O_4$) (Gooding, 1981; Gooding; 1986; Bland et al., 2006).

The Fe-oxides and oxyhydroxides produced by the oxidation of kamacite and taenite vary in composition depending on the nickel content of the parent mineral. The products of kamacite alteration usually retain the same Fe/Ni ratio as the parent mineral, whereas the products of taenite alteration will lead to an alteration product that contains a higher Fe/Ni ratio than the parent mineral. This indicates that some Ni is removed from the site of taenite alteration and either is transported elsewhere in the meteorite or removed entirely from the system (Lee and Bland, 2003). The difference in Fe and Ni mobility is most likely due to the limited ability of the alteration products to incorporate Ni in their structure. The remaining nickel remains in its divalent state and is removed from the system (White et al., 1967).

Within single samples of ordinary chondrites, the original porosity is highly variable, ranging between 5-25% (Flynn et al., 1999). A rapid decrease of porosity is seen as the first 20% of Fe metal is oxidised, and then stabilises (Bland, 2003; Bland, 2006). Lee and Bland (2003) calculated the volume change resulting from alteration of kamacite and taenite to Fe-oxides and oxyhydroxides. They found that common Fe-oxides and oxyhydroxides in the meteorites have a larger volume than their parent minerals. Thus, as weathering increases so does the net volume of the meteorite solids causing the porosity to decrease (Fig. 1.3). The extent of the reduction in porosity varies depending on how the volume of the alteration product compares to the original parent grain.

Troilite (FeS) alters at a much slower rate than native metal when exposed to the same weathering environment, and at a much reduced speed in cold deserts in comparison to hot deserts (Lee and Bland, 2003), but it is known to alter to similar products as kamacite and taenite, forming Fe-oxides and oxyhydroxides (Lee and Bland, 2003). Oxide formation

from troilite also requires sulphur to be removed from the meteorite, as the amount of sulphur in the alteration products is usually below 2 wt. %. Alteration of troilite also produces a smaller volume of alteromorphs compared to kamacite and taenite (Lee and Bland, 2003).

Major alteration products of metallic iron are Cl rich akaganéite (β - $Fe^{3+}O(OH,Cl)$) and goethite (α - $Fe^{3+}O(OH)$) (Burns et al., 1995; Lee and Bland, 2003). Akaganéite contains on average 5 wt.% Cl and forms veins and films between mineral boundaries at the interfaces between uncorroded iron and oxides (Buchwald, 1990). Addition of Cl to the fluid causes a decrease in pH, which further facilitates the corrosion of metals. A low water volume enhances the effects of chlorine, as there is no removal mechanism for the corrosive Cl (Buchwald, 1990). Chlorine chemistry and its effect is discussed further in Section 1.6.

1.4.3 SILICATE WEATHERING

In Antarctic meteorites, all ferromagnesian silicates are known to alter to some degree (Bland et al., 2006). This is evidenced by the occurrence of minor amounts of Si and Mg in non-silicate alteration products and based on Mössbauer spectroscopy. Burns et al. (1995) observed that pyroxenes and olivines in Antarctic meteorites appeared to weather at the same speed. This is highly unusual because in higher temperature environments, in both terrestrial and martian conditions, it is well documented that olivine dissolves preferentially over pyroxene (Loughnan, 1969; Changela and Bridges 2010). A potential reason for the disparity in silicate alteration speeds is because of the topotactic nature of the olivine alteration, where the alteration product inherits the crystal lattice structure of the olivine, making it more resistant to further weathering (Bland, 2000; Bland et al., 2006).

In a comparison study between hot and cold desert weathering of meteorites, Lee and Bland (2003) studied alteration products in chondrites and came to the conclusion that silicates in Antarctic conditions are more susceptible to weathering with respect to metal

and sulphides, than in hot deserts. In general, silicate weathering leads to the formation of "iddingsite" which is usually used as a general term for a mixture of smectite clays and Fe oxide particles (e.g. Smith et al., 1987). Reference to "sialic rust" is also relatively common in the study of weathering meteorites, and describes alteration products largely formed from the dissolution and re-precipitation of elements from olivine and pyroxene (Gooding, 1986; Lee and Bland, 2003).

The dissolution of olivine usually begins by the formation of conical etch pits (Fig. 1.4.) that then can merge into amorphous pitted regions (Velbel 2009). The pits open up proximal to fractures, and active weathering surfaces, and can form in isolation or as part of en-echelon structures (Velbel 2009). The en-echelon arrangements of pits form along crystallographic weaknesses in the olivine that are usually devoid of alteration products, suggesting that the material has been transported within the sample or out of it entirely. Smectites formed from pyroxene create denticulated margins underneath the deposits, and then they drape over the denticular margins (Fig. 1.5.; Velbel and Barker, 2008). This contrasts with pre-terrestrial aqueous alteration products (such as hydrothermal deposits) which have smooth interfaces with olivine.

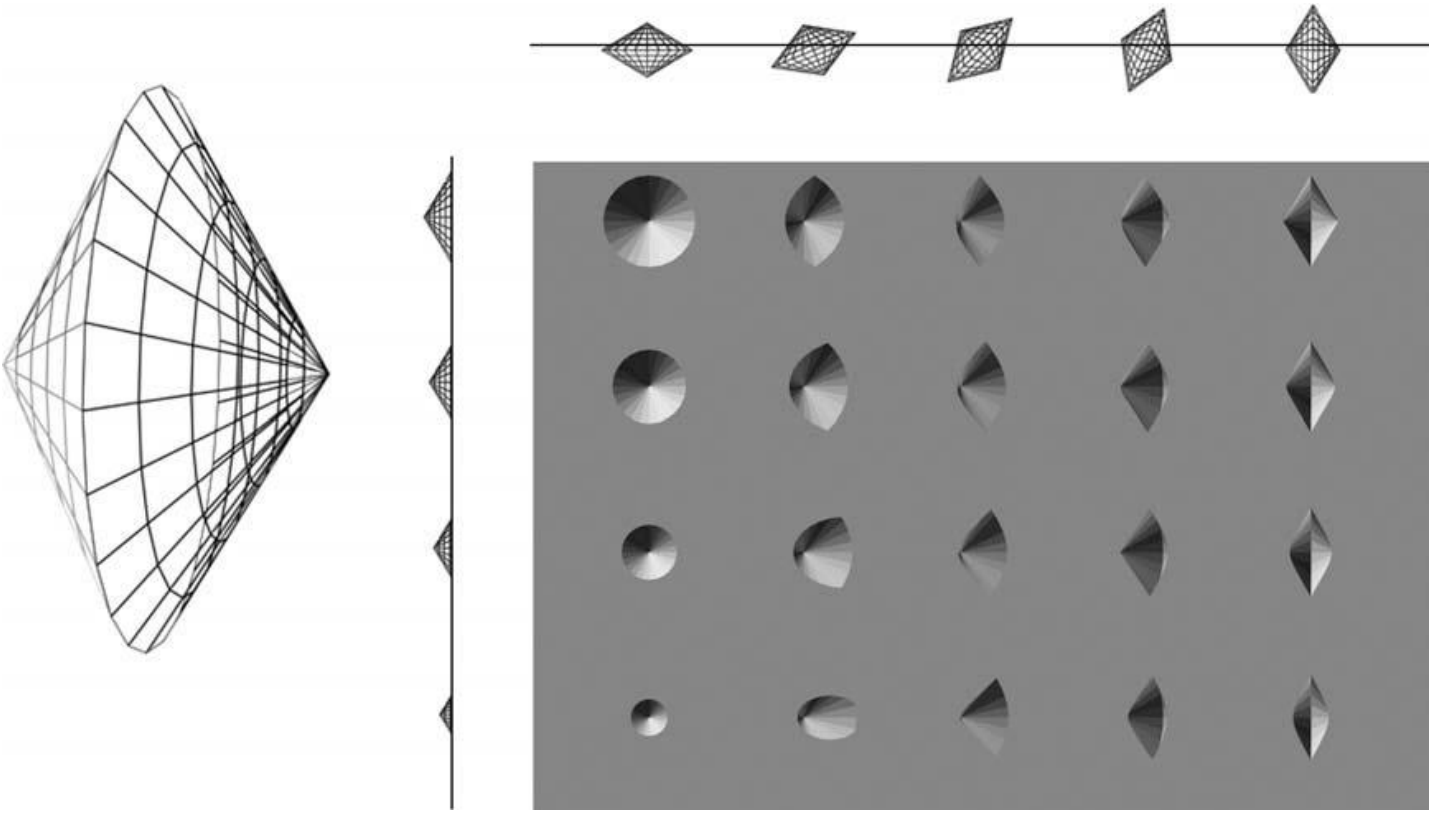

Figure. 1.4. Taken from Velbel (2009). Diagram demonstrates the basic etch-pit shape that forms in olivine crystals. The image on the left is the basic shape, and on the right demonstrates the shapes often seen in natural systems where the etch-pit is rotated at different angles.

Smectites are common alteration products and are usually formed through the hydration of pyroxenes and olivine (Velbel and Barker 2008) and so requires the presence of liquid water. The production of clays in veins and on the active weathering surfaces of silicates has the potential to limit the porosity and permeability of the meteorites leading to a limitation of weathering (Bland 2006). However, formation of smectites also speeds up the weathering process to some extent as they are porous and volumetrically larger, causing mechanical stress within the rock (Velbel and Barker 2008). Mechanical stress from drying-wetting cycles that naturally occur in weathering environments results in changes to smectite volume and shape, which can then dislocate them from the active weathering surface, creating open fractures that allow access to the fresh mineral surface (Velbel and Barker 2008).

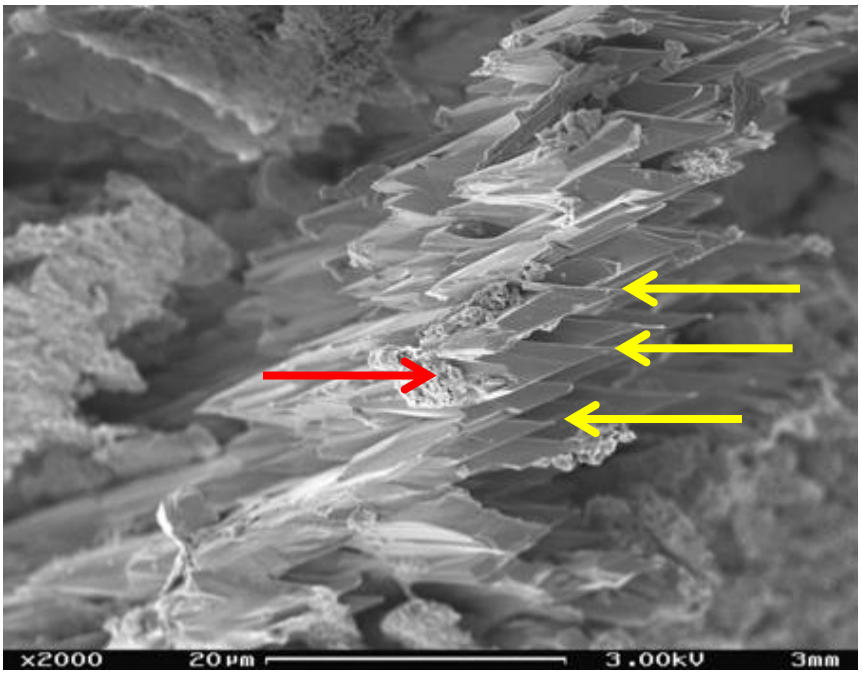

Fig. 1.5. Denticulated margins of a weathering pyroxene with smectite covering. Taken from Velbel and Barker (2008). Yellow arrows indicate denticulated margin, red arrow indicates smectite covering.

1.4.4 EVAPORITES

The third group of alteration products formed in Antarctic meteorites is evaporites. These occur in around 5 % of all Antarctic meteorites, either on external surfaces (fusion crust) or in fractures (Meteoritical Bulletin – accessed 01/15). The efflorescence consists primarily of the Mg-carbonate nesquehonite ($MgCO_3 \cdot 3H_2O$), with lesser amounts of starkeyite ($MgSO_4 \cdot 4H_2O$), hydromagnesite ($Mg_5(CO_3)_4(OH)_2 \cdot 4H_2O$), gypsum ($CaSO_4 \cdot 2H_2O$), jarosite ($KFe^{3+}{}_3(SO_4)_2(OH)_6$) and epsomite ($MgSO_4 \cdot 7H_2O$) (Yabuki et al., 1976; Marvin, 1980; Gooding, 1982; Velbel et al., 1991). The Mg-carbonates found in Antarctic meteorites preferentially form on achondrites and equilibrated ordinary chondrites, whereas sulphates form primarily on carbonaceous chondrites and unequilibrated ordinary chondrites. This relationship between types of meteorite and species of evaporites hints at the evaporites being a product that is internally derived from the breakdown of the meteorite, rather than from external addition (Losiak and Velbel 2011).

Further evidence for evaporites being derived from an internal source has been found in a statistical study by Losiak and Velbel (2011) of all meteorites recovered by ANSMET before 2011. Results show that carbonaceous chondrites have the most occurrences of evaporite alteration products (with over 50 % of CK carbonaceous chondrites showing evaporite deposits), but with L group ordinary chondrites display evaporite products in fewer than 5 % of finds. There is also a noticeable correlation between petrological type in ordinary chondrites, whereby more evaporites occur in type 3 than type 6. Higher abundances of evaporites are on lower petrological types and are thought to be formed preferentially because of the greater abundance of amorphous and poorly crystalline material which is more readily weathered thus enabling the constituents to be released and become available for the formation of the evaporite assemblage (Velbel, 1988; Losiak and Velbel, 2011).

The presence of evaporites and weathering class do not correlate well, and the occurrence of rust and evaporitic deposits appears almost unrelated. However, there is a clear geographical dependency in the occurence of evaporite products, with some icefields producing far more evaporite-encrusted meteorites than others. The most productive evaporite formation field is Lewis Cliff, which is also geographically adjacent to one of the least productive fields (Losiak and Velbel, 2011). The percentage of evaporite occurrence is not related to distance from the sea, so the probability of sea spray as a main contributor has been discounted (Losiak and Velbel, 2011).

Many meteorites that host evaporites have a surficial enrichment of rubidium and iodine, with interiors depleted in Rb, Co, Ca and I (Velbel et al., 1991). The combination of the geochemical differences of evaporite-bearing meteorites and the petrological preferences suggest that the main source of Mg carbonates is from the breakdown of olivine: Mg is released and combines with atmospheric CO_2 (Velbel et al., 1991; Losiak and Velbel,

2011). This was deduced theoretically based on thermodynamic considerations and bulk measured geochemistry, not measured directly.

1.4.5 Antarctic Varnish

Antarctic varnish is a detrital deposit that forms on all rocks of Antarctica including meteorites (Giorgetto et al., 2007; Hallis, 2011; Dorn et al., 2013). It accumulates preferentially on rough surfaces and affects minerals that are in contact with it by making them more susceptible to weathering (Dorn et al., 2013). A discrete contact between Antarctic varnish and the underlying rock as seen in high magnification BSE imaging (Fig 1.6.; Krinsley et al., 1995; Dorn, 2009) demonstrates that the varnish is a product added to the rocks, and not derived from the underlying surface. The consistency of composition across different rock types also suggests the accretionary formation mechanism first suggested by Humboldt (1812, cited in Dorn et al., 2013). Observations of chemical independence from the underlying minerals and a sharp contact support the accumulation mechanism, because a product derived from the rocks themselves would have a continuous interface with the underlying rock, and it would result in an alteromorph that reflects chemical differences across different rocks.

Rock varnishes typically consists of amorphous material, clay minerals and Mn/Fe oxides (Giorgetti and Baroni, 2007), but vary considerably with geographical location. Antarctic varnish is often accompanied by fractures that are parallel to the surface of the rock and the varnish. The varnish can reach 100 μm thickness and drapes the surface, infilling cavities and surface irregularities and thinning over other parts. It can consist of many layers or lenses that are inconsistent and of variable compositions. The layers can also be separated by fractures that most probably formed after deposition, by dehydration and resulting volume reduction. Giogetti and Baroni (2007) reported that single layers appear to be homogeneous in composition and have high Si contents with minor Fe, S, Al, K and P. The Si-rich layers in contact with the rock surface are amorphous and can also contain sulphate

grains that are thought to be airborne particles or derived from sea spray (Giogetti and Baroni, 2007). Some of the sulphate crystals appear to have formed from the surrounding matrix and so may have been formed from re-mobilised oxidised sulphates. The sulphate layers appear to have formed close together and so the addition of sulphate particles may be related to episodic events such as volcanic outbursts or enhanced sea spray transportation (Giorgetti and Baroni, 2007). The Antarctic varnish is thought to provide the rock with some measure of protection from weathering and has also been found to host bacteria (Krinsley and Rusk, 2000; Dorn et al., 2013). Bacteria is key in enhancing Mn contents of the varnish and frequently leaves bacterial casts embedded in it. Therefore, desert varnish has been suggested as a potential astrobiological cache on other planets (Krinsley and Rusk, 2000; Dorn et al., 2013).

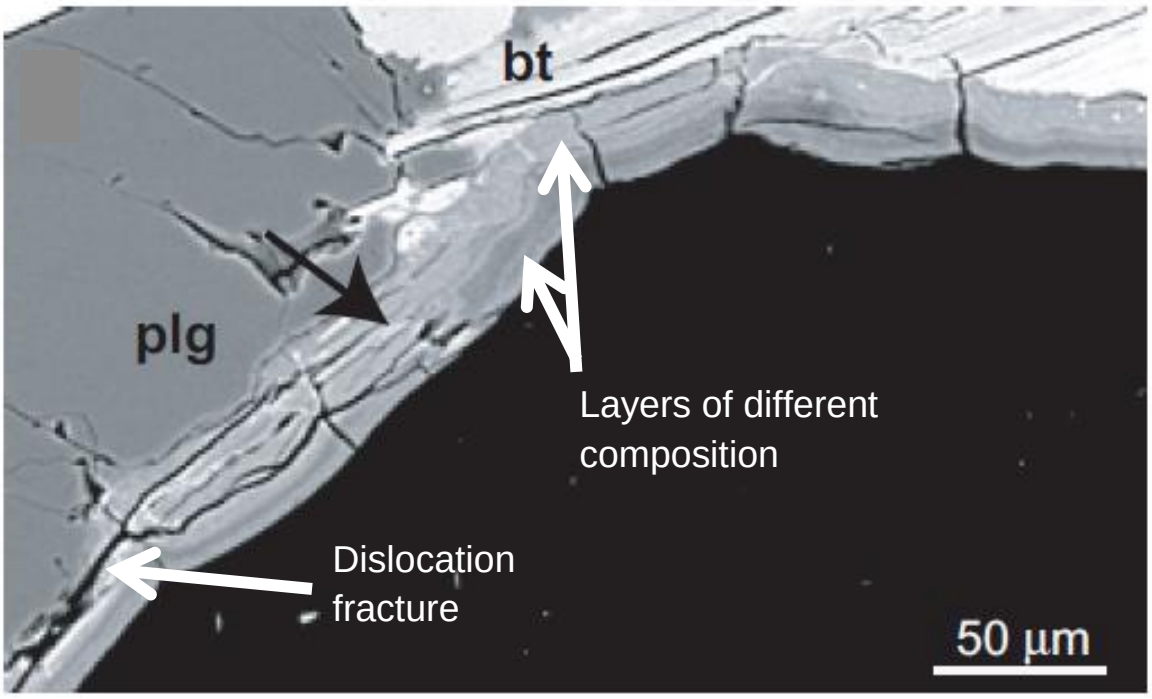

Fig. 1.6. An example of Antarctic varnish on an erratic diorite boulder in Antarctica taken from Giorgetti and Baroni (2007). The BSE images show the multi-layered product of variable composition and width draping the underlying surface. Plg – plagioclase, bt - biotite.

1.5. MAGNETIC PROPERTIES OF ALTERED METEORITES

Mineral alteration leads to the destruction of the original magnetic properties of meteorites (Rochette et al., 2003; Weiss et al., 2010; Uehara et al., 2012). The main magnetic minerals in L chondrites are tetrataenite, taenite and kamacite with some contributions from troilite which, as discussed in Section 1.3.2, are the first minerals to alter in the Antarctic environment. The change in magnetic properties of the meteorites is two-fold: the original magnetic minerals are removed, expunging extra-terrestrial magnetic properties, and are then replaced by minerals that themselves can be highly magnetic. Uehara et al. (2012) demonstrated that meteorites from the Atacama desert that were above weathering grade W3 (on the Wlotzka (1993) scale) have a terrestrial chemical remnant magnetization (CRM) that dominates, and masks, the original remnant magnetism. The weathering of kamacite and tetrataenite has been followed by replacement with magnetite and maghemite (a common product in hot deserts; Bland et al., 1996; Al-Kathiri et al., 2005) that has inherited terrestrial magnetic properties. Meteorites of W0-W1 have similar properties to falls as they have encountered minimal weathering and so are not thought to have experienced any significant alteration of magnetic properties, and magnetic susceptibility decreases as oxidation of metals proceeds (Rochette et al., 2003).

1.6. TRACE ELEMENT CHANGES IN WEATHERED ANTARCTIC METEORITES

The redistribution of trace elements in Antarctic meteorites is well documented and differs from hot desert alteration (Crozaz et al., 2003; Lee and Bland, 2006; Mittlefehld and Lindstrom, 1991). It is especially detrimental to the study of meteorites since many of the affected trace elements are used in dating systems (such as Rb-Sr and Pb-U) and others are used as diagnostic tools for parent body determination (Greenwood et al., 2012).

In hot deserts meteorites show a pronounced LREE enrichment with Sr, Ba and U contaminations, which is less pronounced in cold desert meteorites (Crozaz et al., 2003). The LREE enrichment arises mostly in olivine and low Ca pyroxene grains from

interaction with terrestrial fluids, and has a strong terrestrial crustal LREE isotope signature (Crozaz et al., 2003).

Changes in trace elements during hot desert terrestrial weathering usually involve sample interaction with an enriched fluid (e.g. Crozaz 2003), but can also arise from differential oxidation states of elements in weathered minerals. Martian meteorites that have undergone significant terrestrial weathering in Antarctica are noted for light REE enrichment in olivines and pyroxenes and negative Ce anomalies (Hsu et al., 2004). Because olivine and pyroxene contain low amounts of REE indigenously, the slight addition of LREE severely affects the element abundance pattern (Floss and Crozaz, 1991; Hsu et al., 2004). This addition is thought to be derived partly from the breakdown of phosphates and partly from enriched fluids (Floss and Crozaz, 1991).

Large positive Ce anomalies have been found in Antarctic meteorites in the bulk rock and in mineral separates, most pronounced in eucrites, but also found in diogenites and in Martian shergottites (Masuda et al., 1979; Lundberg et al., 1990; Crozaz et al., 2003). The Ce, along with other REEs are contained in the phosphates. When they are dissolved there is a general mobilisation of REEs and the Ce is separated as it easily oxidises to Ce^{4+}. The latter is relatively insoluble compared to trivalent REEs. A REE anomaly is thought to be most prevalent in eucrites because of the higher bulk concentration of REE in the meteorite group compared to others and, therefore, change is more easily detectable (Crozaz et al., 2003).

Minerals that exhibit Ce anomalies tend to be fractured and have more available mineral surfaces. The cracks and crystal defects caused by shock are major conduits for REE bearing fluids, causing them to be more likely a recipient of REE precipitation compared to the surrounding crystals (Crozaz et al., 2003). The most pronounced effect is observed in pyroxenes because of their low initial REE concentration and high tendency to fracture (Masuda et al., 1979; Lundberg et al., 1990; Crozaz et al., 2003). A correlation between Ce

anomalies and adsorbed water was discovered by Kagi and Takahashi (1998) using micro infrared spectroscopy. The amount of water adsorbed by a mineral was directly related to the Ce anomalies, with olivine and pyroxene adsorbing over twice as much water as plagioclase. This disparity of water adsorbtion creates the difference in Ce anomalies between the minerals. Differences in the lunar meteorite population resulted from the density of microfractures in the meteorites (Kagi and Takahashi, 1998).

High Se concentrations are also detected in some Antarctic meteorites; especially Antarctic eucrites. which show an order of magnitude higher Se content than non-Antarctic eucrites (Palme et al., 1983; Mittlefehldt and Lindstrom, 1990). The enrichment in Se is most pronounced on the exterior of the meteorite, although it is prevalent throughout (Mittlefehldt and Lindstrom, 1990). There is a possible association with a K anomaly, but data are too sparse for certainty (Mittlefehldt and Lindstrom, 1990). The addition of Se in Antarctica has been attributed to volcanic input via volcanic dust exhumed from ash bands in the icefields (Koeberl and Cassidy, 1991). A possible enrichment of Cs and Rb is seen on the exterior parts of some meteorites also, with some Ag, Cd and Sb enrichments persisting to depths of roughly a centimetre (Biswas et al., 1980).

As well as the addition of trace elements by terrestrial weathering, depletion in several elements is also detected when the host mineral is disaggregated and the constituent elements are removed from the system. Dennison and Lipschutz (1987) report significant depletions of Ag, Au, Bi, Cd, Co, Cs, Ga, In, Sb, Se, Te, Tl, U, Zn in rim samples of H chondrites compared to interiors, and hypothesise that this is from leaching on the ice sheet surface.

1.7. Halogen Additions

Halogen inventories in Antarctic meteorites show identified irregularities in that they do not correlate with external parameters (Dreibus et al., 1986; Heumann and Gall, 1987;

Langenauer and Krähenbühl, 1993; Shinonagu et al., 1994). Iodine is the only halogen to have a consistent enrichment across all meteorites collected from Antarctica, regardless of geographic location, which is not observed in non-Antarctic specimens (Dreibus et al., 1986; Heumann and Gall, 1987). Fluorine, bromine and chlorine contents are only enhanced in the more coastal icefields, and are therefore inferred as contributions from sea spray (Heumann et al., 1990; Langenauer and Krähenbühl, 1993). In addition to sea-spray, the sublimation of ice is likely to concentrate halogens on the surface (Buchwald and Clarke, 1989).

On specimen scale, the observed halogen contaminations decrease inward from the surface of the meteorite, but to varying extents. Iodine enrichment is most prominent at the surface of the meteorites and extends relatively deep into the meteorite (between 11-25 mm; Heumann et al., 1987; Ebihara et al., 1990; Heumann et al., 1990; Langenauer and Krähenbühl, 1993). Fluorine is mostly adsorbed onto the surface of the meteorite, and has the steepest contamination/concentration gradient of the halogens, extending, on average, only to the first 2.5 mm of samples (Langenauer and Krähenbühl, 1993). Over half of the fluorine content is found in the first 50 μm of the meteorite (Noll et al., 2003). Chlorine has the highest concentration just beneath the surface of the meteorites, likely due to the effects of leaching by water at the surface (Langenauer and Krähenbühl, 1993) and can extend down to 40 mm. Bromine contamination is low, making enrichment measurements difficult, but a surface enhancement is discernible with a maximum depth of contamination of less than 20 mm (Langenauer and Krähenbühl, 1993).

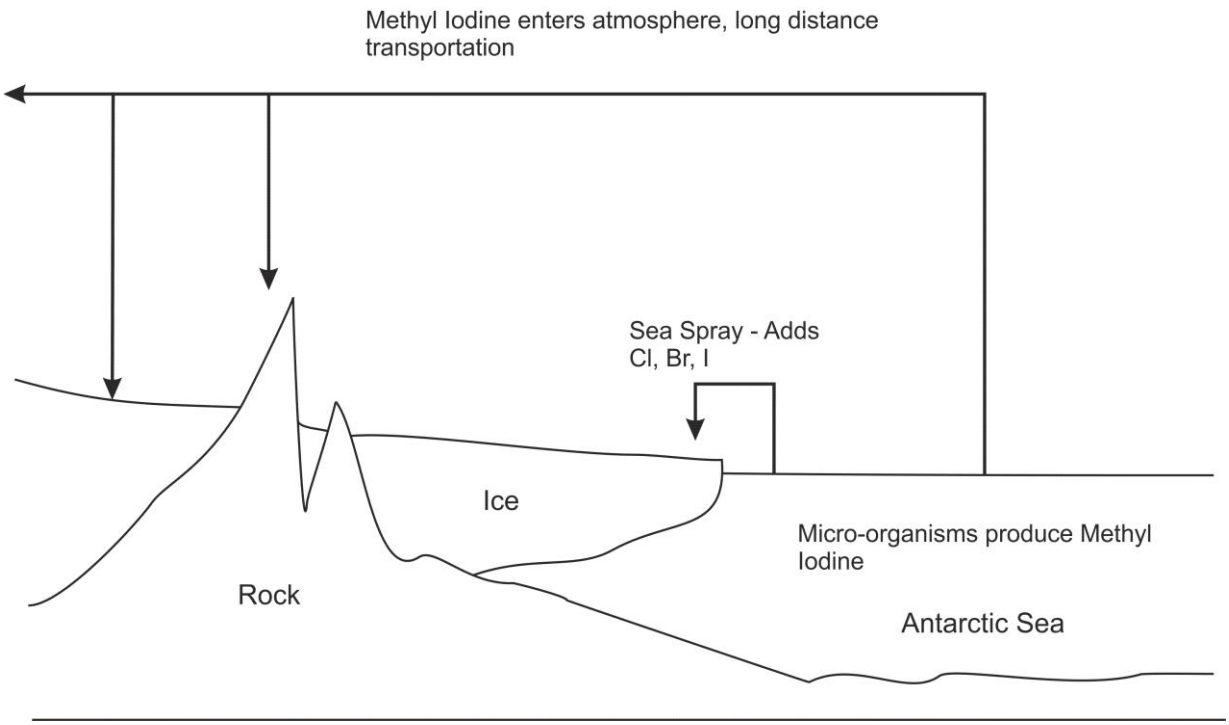

Fig. 1.7. Redrawn from Heumann et al. (1987). The figure describes the addition of halogens to Antarctica through sea spray derived and biologically produced components.

Iodine addition is a feature common to all meteorites recovered from Antarctica regardless of recovery site, thus the prevalence of the iodine over-abundance is indicative of the contaminant being introduced through atmospheric processes, rather than sea-spray, or other geographically limited processes (Heumann et al., 1990). The iodine enrichment across Antarctica is caused by the addition of methyl iodine (CH_3I) to the atmosphere by micro-organisms in the sea (Fig. 1.7.). Methyl iodine has a residence time of between 2-10 days in the atmosphere (Heumann and Gall, 1987; Hewitt and Jackson, 2008). The source of the methyl iodine was found through measurements of Antarctic atmosphere and seawater that had the same concentrations, demonstrating that the sea was the source of biogenically produced CH_3I (Heumann et al., 1990). With a residence time of 2-10 days, depending on atmospheric conditions (Hewitt and Jackson, 2008), methyl iodine can spread across the continent and is then preferentially absorbed by severely rusted meteorites increasing iodine enrichment (Langenauer and Krähenbühl, 1993).

This finding supported observations by Dreibus et al. (1986), who noted that the enrichment in iodine did not occur in the ice underneath the collected samples, but had been found to occur in deposits in Victoria Land and so is ubiquitous across Antarctica. Heumann et al. (1990) reported that the iodine abundance also extended to evaporite deposits on the surface layers of meteorites, and that the largest enrichments of iodine were found in chips directly beneath evaporite patches. Moreover, iodine enrichment is independent of other halogens. Iron meteorites have higher iodine abundances in corroded surfaces than stony meteorites, and so their corrosion products are assumed to absorb iodine preferentially from the environment.

The addition of fluorine, chlorine and other volatiles in many icefields is even more variable due to the potential addition of volatiles from Mt. Erebus (Buchwald and Clarke, 1989; Langenauer and Krähenbühl, 1993; Noll et al., 2003), which is known to degas unusually large amounts of HF and HCl (Zreda-Gostynska et al., 1997). The Cl input, however, is still most likely to be from sea spray, but increased by the Cl/F weight ratios of Erebus' emissions and meteorites found in Antarctica (Noll et al., 2003). The addition of potential volcanic additions is summarised in Fig. 1.8.

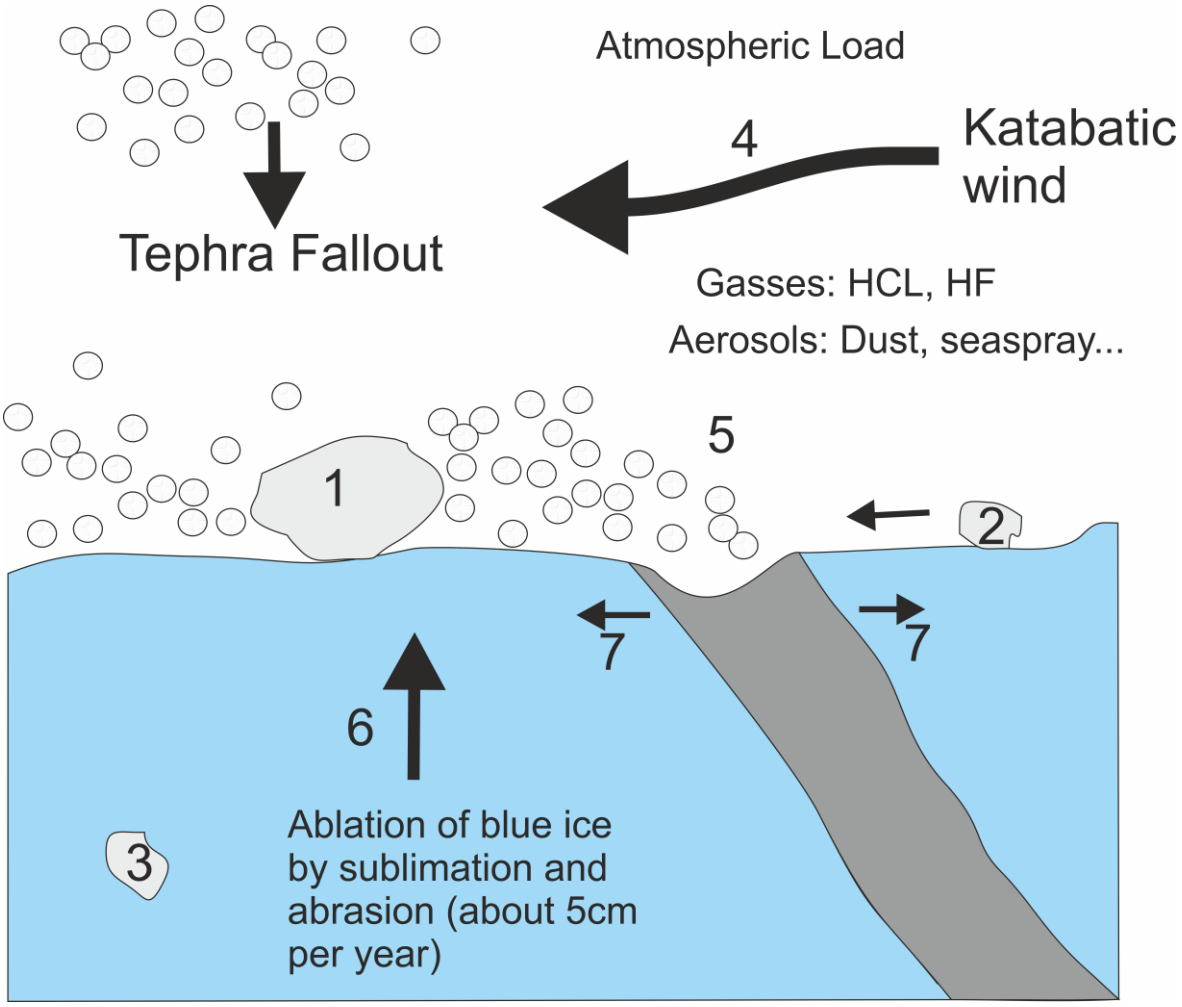

Figure. 1.8. – Summary of additions from volcanic activity. The addition of F, amongst other volcanic volatiles can come directly from volcanic aerosols in the atmosphere or from proximal deposits of volcanic ash. 1) A large meteorite is stranded on the surface of the ice and is too large for wind movement. Tephra fallout, gases and aerosols interact with it. 2) Smaller meteorites can be transported by the wind and be stranded in troughs. 3) A meteorite trapped in the ice slowly being exhumed. 4) Strong katabatic winds transport sea spray and aerosols. 5) Troughs form from higher albedo ash bands acting as a heat source. 6) Ice is constantly ablated, bringing debris to the surface. 7) Tephra bands expand and move depending on the angle and depth which may change with exhumation. Redrawn after Noll et al., (2003).

The addition of F via wind dispersal of volcanic plumes could presumably be seen in measurements from the windward and leeward sides of a single large meteorite, but the volcanic contamination does not stop at gaseous contributions. The addition of halogens through wind dispersion could mean that a small sample of a meteorite will not be representative of the whole sample, since the specimen might be derived, e.g., from the windward rather than the leeward side of the main specimen. Fluorine enrichment, when investigated with spatial resolution, is highly irregular (Noll et al., 2003).

F contamination could also be induced by the interaction of water with ash bands that are prevalent in the Antarctic blue ice (Noll et al., 2003). Ash bands are also exhumed through ablation of icefields, so katabatic winds contain a steady quantity of tephra and debris. In addition, the tephra bands have an increased albedo compared to the surrounding ice and store heat, creating troughs in the ice which can then collect windblown meteorites (Noll et al., 2003). Tephra from ash bands contain over 100 times more F than H chondrites measured in the same study (Noll et al., 2003). However, it is difficult to attribute F contents of meteorites to specific sources since Erebus is on the coast and so volcanic signatures will be mixed with marine sources.

F is highly unlikely to be released from a meteorite through weathering processes because of its low mobility in Antarctic conditions (Langenauer and Krähenbühl, 1992), and so it is an excellent tracer for contamination because concentrations of F are proportional to the exposure time on the ice (Langenauer and Krähenbühl, 1992).

1.8. OXYGEN

Oxygen has three stable isotopes: ^{16}O, ^{17}O and ^{18}O. Mass dependent fractionation of the isotopes allows relationships between meteorites to be determined, including recognition of common parent bodies (Clayton et al., 1976) and pairing of meteorites (Clayton et al., 1991). It is important that terrestrial alteration processes are well characterised and understood, to prevent erroneous parent body identifications. With the removal and replacement of many indigenous minerals as described in Section 1.4.3**,** the indigenous oxygen isotope ratios are disturbed and eventually tend to the composition of the terrestrial environment.

A study of the effects of Antarctic terrestrial contamination on oxygen isotopes was done by Tyra et al. (2007) using CM chondrites from Elephant Moraine where more weathered samples were creating shifts to lower $\delta^{18}O$ and higher $\Delta^{17}O$ through the deposition of terrestrial carbonates. Greenwood and Franchi (2004) examined the effect of weathering on CO chondrites and determined a similar effect, with the opposite effect in warm climate weathering (higher $\delta^{18}O$, lower $\Delta^{17}O$; Fig. 1.9.)

An evolution of altering fluid could potentially be seen if there were a very low water/rock (w/r) ratio and the reactions occurring between the rock and the fluid exceed the supply of

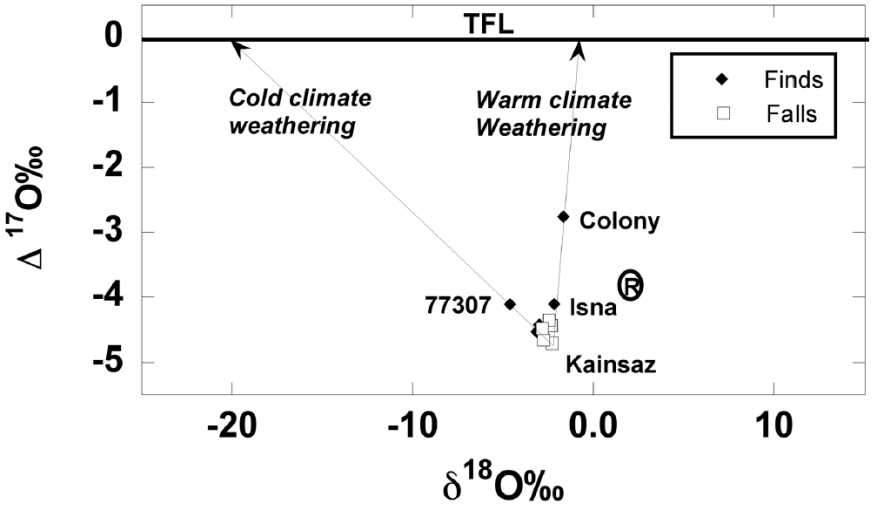

Fig. 1.9. Oxygen isotope progression in CO chondrites with weathering, adapted from Greenwood and Franchi 2004.

water to the system. Thus in low w/r ratio areas such as Antarctica, the altering fluids may acquire a non-zero $\Delta^{17}O$ (Tyra et al., 2007).

An overall increase of $\Delta^{17}O$ with weathering was observed by Greenwood and Franchi (2004). The changes in oxygen isotopic composition in weathered CO chondrites could be created by: removal of original phases with negative $\Delta^{17}O$ values, the altering fluid having high $\Delta^{17}O$ or formation of alteration products with higher $\Delta^{17}O$ (Fig. 1.9) (Greenwood and Franchi, 2004).

Studies of changes in oxygen isotopic composition caused by terrestrial weathering of Antarctic chondrites were undertaken by Bland et al. (2000). They described a two-stage alteration process, with the first stage having negligent effect on oxygen isotopic composition. The second stage occurs after over 25 % of the ferric iron in the meteorite (ascertained from Mössbauer analysis) has been converted to Fe^{3+} (Bland et al., 2000; Bland, 2006). At the second stage there is a significant (4-5 %) shift in $\delta^{18}O$ (Bland et al., 2000). Bland et al. (2000) attribute the initial lack of isotopic alteration to a topotactic replacement of primary silicates with clay minerals which hence inherit the original oxygen structure from the silicates.

The three studies described above are on three different groups of meteorite: CM (Tyra et al., 2007), CO (Greenwood and Franchi, 2004) and L chondrites (Bland et al., 2000). An important difference between these groups is the metal content, which, as a major draw of atmospheric oxygen, affects the alteration of oxygen isotopes significantly. In the L chondrite study (Bland et al., 2000) the shift in oxygen isotopes was attributed largely to the oxidation of Fe-Ni metals, and so the shifts are significantly increased in the more metal rich meteorites compared to the carbonaceous chondrites but the direction of the shift, towards the TFL, remains the same.

1.9. ANTARCTICA AS A MARTIAN ANALOGUE

The Dry Valleys of Antarctica are often used as a Martian analogue as the lack of moisture and the low temperature in the Dry Valleys makes it the most similar terrestrial environment to the current mid-latitudes of Mars (Wentworth et al., 2005; Chevrier et al., 2006; Velbel and Losiak 2010; Salvator et al., 2013). Both the Dry Valleys and the Martian surface have soil created from slow sublimation and migration of water-soluble ions, and so the alteration products that form are proven to be similar by comparison with Martian orbiter data and rover data (Wentworth et al., 2005). The relevance of the Antarctic Dry Valleys to Mars becomes evident when the following conditions are taken into consideration: the mean temperature of the Dry Valleys is -20 $^{\circ}$C, strong winds are prevalent, there is very low to no precipitation, freeze-thaw cycling is the strongest driver of mechanical weathering, salts are present and high solar radiation is incident on the surface (Gibson et al., 1983).

However, there is a significant difference between Mars and the Dry Valleys which controls the weathering patterns of all rocks – the quantity of oxygen in the atmosphere. The presence of oxygen in terrestrial weathering environments makes the products and processes fundamentally different to those on Mars. To mitigate these problems, weathering of meteorites can be studied. L6 meteorites contain significant amounts of Fe-Ni metal which is well documented to be highly susceptible to weathering and easily oxidised, thus locking much of the oxygen in alteration products, which results in reducing alteration fluids – making them more similar to those on Mars than in rocks without native Fe.

Another reason to use chondrites as martian analogues is the acidic environment that can be formed inside from the breakdown of sulphide minerals. In using a chondrite as a martian analogue, the weathering processes of ferromagnesian minerals in reducing, acidic conditions can be studied.

Martian rocks and soils have long been acknowledged to have evolved from basalts by processes that are different to terrestrial basalt weathering (McSween et al., 1999; McSween and Keil, 2000). Many Mars rovers have found evidence for the importance of acidic weathering to the alteration of primary basalts (Banin et al.,1997; Squyers et al., 2004). The fine-grained soil that covers much of Mars is homogenous over large areas and measurements by the Viking and Pathfinder landers found it to have a high sulphur content (6 - 8 wt. % S as SO_2). Sulphur concentrations measured at the MER landing site in Gusev crater regularly reach those levels, but have been found as high as 32 wt. % in the target 'disturbed Paso roble soil' (Gellert et al., 2006). The MSL Curiosity rover found 5.45 ± 0.1 wt. % SO_3 in the Rocknest sand drift (Blake et al., 2013); demonstrating the similarity of the Martian soil at very different landing sites (Blake et al., 2013). This similarity also extends to other elements, with iron (FeO^+, Fe_2O_3) much higher than in terrestrial samples, ranging from 16.3 ± 1.1 wt.-% at Gusev to 18.8 ± 1.2 and 19.19 ± 1.2 wt. % at Meridiani and Gale, respectively (Blake et al., 2013). The source of the large amounts of SO_2 in the soil is thought to be from volcanic addition (e.g., Clark and Baird 1979; Settle 1997; Tosca et al., 2004) and has been labelled the "acid fog" model (Banin et al., 1997; Settle 1979). Volcanically derived volatiles are thought to interact with the basaltic crust either by adsorption into fluids or through interaction with aerosols (Tosca et al., 2004; Zolotov and Mironenko, 2007). The result of the interaction of acid or acidic solution with the basaltic host rock is the production of amorphous ferric iron oxides and silica.

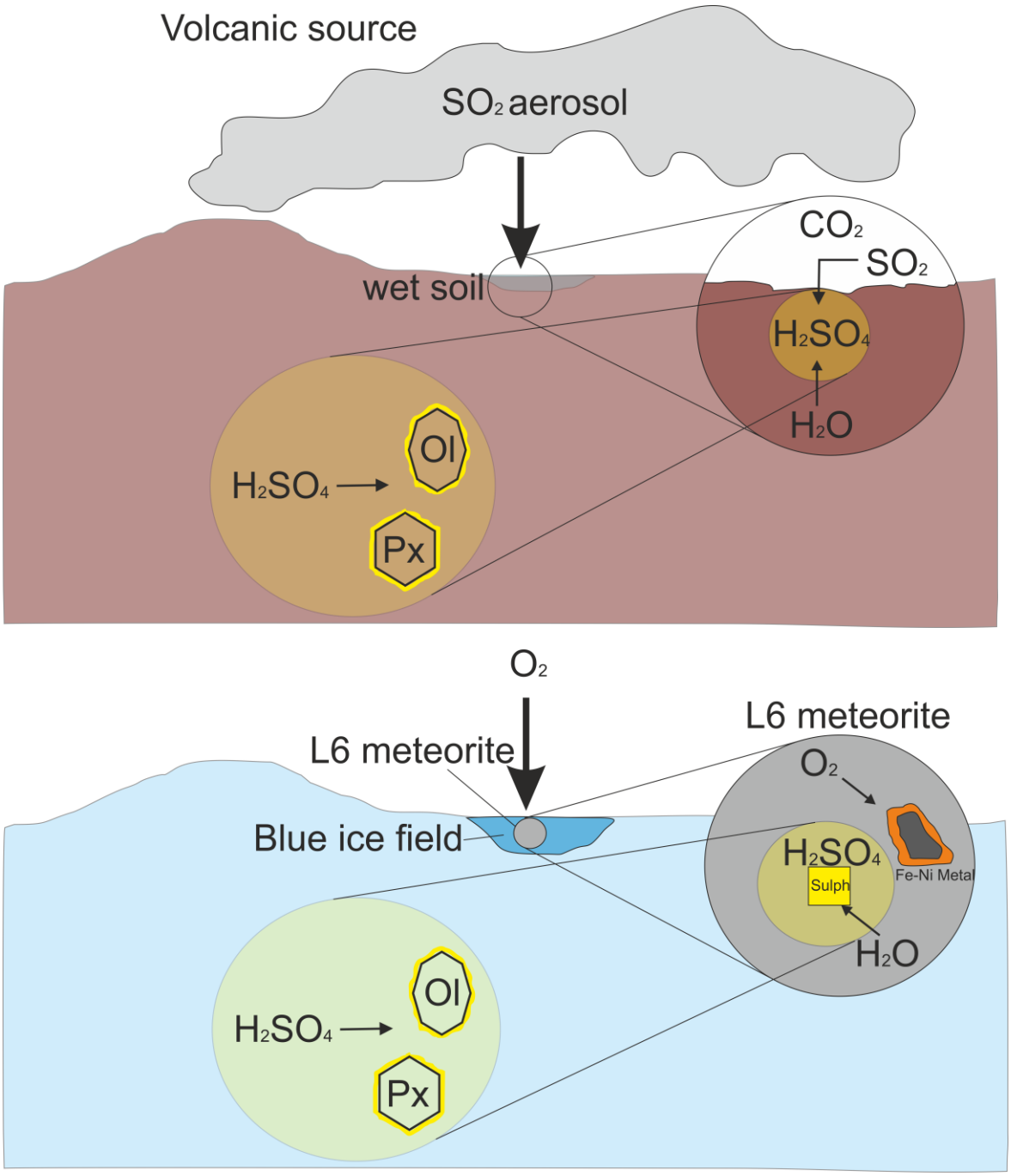

Fig. 1.10. Comparison diagram of martian acid fog model compared to weathering in an L6 chondrite. In both cases there is a reducing environment and sulphuric acid is present, interacting with silicate minerals. In the martian acid fog model there is an absorption of sulphur dioxide from volcanic emissions with water in soil, which creates sulphuric acid. This weathers ferromagnesiam minerals. In the Antarctic comparison – an L6 chondrite is interacting with thin films of liquid water. Much of the oxygen incorporated into the weathering system is trapped in Fe-oxides which form in haloes around Fe-Ni metal particles. In this case, the sulphuric acid is produced through weathering of sulphide minerals. This sulphuric acid then interacts with the ferromagnesiam minerals.

The fluid that interacts with the basaltic crust is of low pH and is likely to have a low water/rock ratio (Banin et al., 1997). This is known to decrease the rate of weathering in basalt (Jones and Brearley 2006) and so various experimental weathering studies have been performed in an attempt to recreate the conditions on the martian surface (Banin et al., 1979; Tosca et al., 2004; Golden et al., 2006). Notably all these experiments lack trace element data to assess the movement of trace elements in acidic conditions from common ferromagnesian minerals. This analogue study provides this information on the trace elements and also considers the spatial extent of acid movements from a point source. The latter can also be used as an analogue for travelling distances of acid deposited on a fresh basaltic surface into the subsurface (Fig. 1.10.).

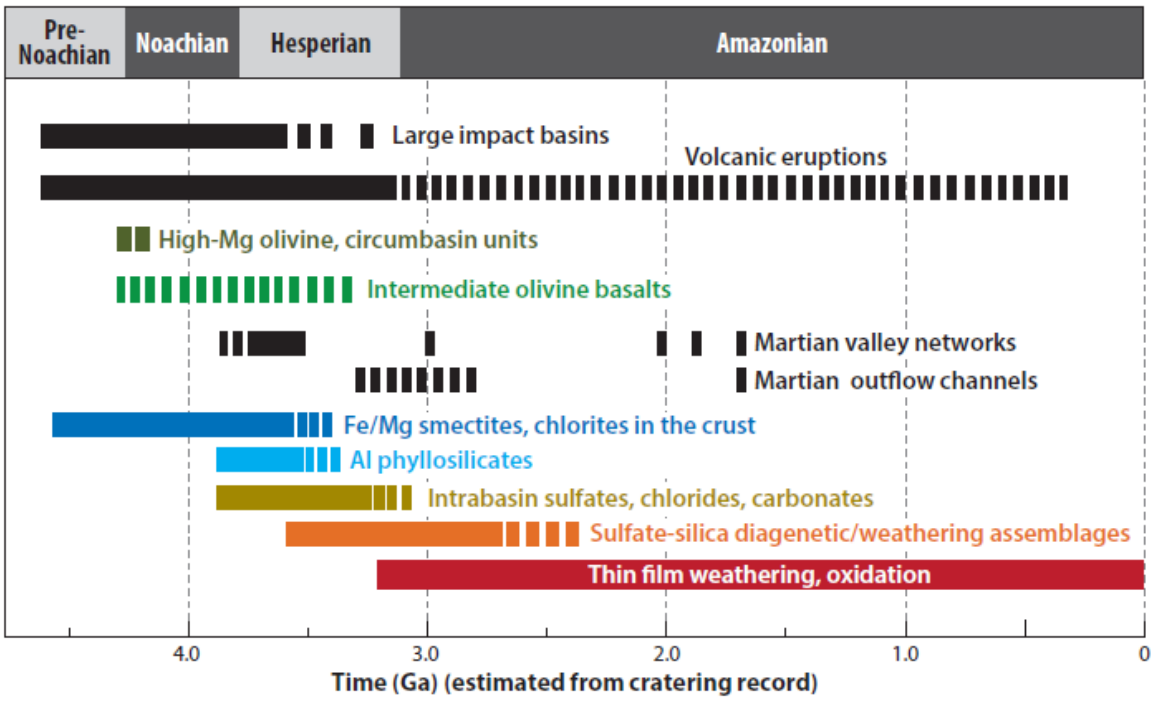

Fig. 1.11. Taken from Ehlmann and Edwards (2014), this figure describes the evolution and duration of alteration environments on Mars from 4.6 Ga to present day.

Weathering on the icefields of Antarctica is different in that even though precipitation is low, there is still there considerably more liquid water present in the icefields than Mars. However, the low temperature and limited availability of water makes the conditions in Antarctica similar to some models of ancient Mars (Levy et al., 2009; Niles and Michalski 2009). The evolution of weathering environments is summed up in Fig.1.11.

On Mars, environmental conditions similar to those observed in the Antarctic Dry Valleys produce nanophase hematite, goethite, ferrihydrite and smectites in the surface layers, as seen by the MER and Curiosity rovers (Chevrier et al., 2006 and references within).

The weathering patterns seen in silicates in the Antarctic soil are very similar to these found in Martian meteorites, with preferential weathering along planes of weakness in silicates – rimmed by dissolution. Dendrites are formed in pyroxenes, and are thought to occur under frozen conditions (Wentworth et al., 2005; Velbel and Losiak 2011).

1.10. Alteration Minerals on Mars

Alteration products requiring the presence of liquid water have been found in situ on Mars by rovers and landers. The catalogue of alteration minerals found by Opportunity, Curiosity, Spirit and Phoenix is extensive and is summed up in Table 1.2. Meteorites found on Earth that have originated from Mars also show a similarly extensive range of secondary minerals (Table 1.2.). Minerals found in the studied meteorites that are also on this list are of special interest.

The Opportunity rover has found a diverse spectrum of chemical alteration features in Gusev crater. These consist most recently of high Mn oxides, high in Ni occurring on the outer rims of basalt "Pinnacle Island" (Arvidson et al., 2015) and Ca sulphate veins but over a dozen alteration minerals have been found and most fall into the categories of Fe-oxyhydroxides, smectites, sulphates and salts. All of these require some fluid interaction to form, of varying pH and some are assumed to require large standing bodies of water (i.e.

Fe-smectites – Grotzinger et al., 2005; Ehlmann and Edwards, 2014). The exception to these minerals is the opaline silica observed by the opportunity rover, which is thought to originate from high temperature hot spring environments (Ruff et al., 2011).

Table 1.2. Summary of alteration minerals found in situ on Mars and the formation environments inferred.

Mission	Alteration Minerals Found	Likely formation environment
Phoenix Lander	1) Ca carbonate [1] 2) Perchlorate [2]	1) Restricted water content (low w/r ratio). Films of water interacting with CO_2 atmosphere [1] 2) Thin films of water from periglacial activity [3]
Opportunity Rover	1) Jarosite [4] 2) Hematite concretions [6] 3) Gypsum [8] 4) Fe 3^+ rich smectite [5]	1) Acidic, low temperature [5] 2) Physical weathering concretions, diagenetic precipitation and dissolution of secondary minerals [7] 3) <60 °C, Neutral pH [8] 2-4) Episodic playa lake [9]
Spirit Rover	1) Magnetite [10] 2) Hematite [12] 3) Goethite [11] 4) Ca/ Mg/Fe sulphates [12] 5) Aluminosilicates [11] 6) Halite [11] 7) Opaline Silica [13]	1- 6) Acidic solutions reacting with primary phases (especially olivine to make Mg/Fe carbonates). Temperature unspecified. [11] 6) Highly oxidized, low pH [11] 7) Hydrothermal system after acid sulphate leaching of basaltic precursor [13, 14]
Curiosity Rover	1) Saponites [15] 2) Phyllosilicates 3) Gypsum veins [15] 4) Magnetite [17] 5) Akaganeite [15] 6) Nontronite [18] 7) Hematite [15] 8) Anhydrite [15] 9) Bassanite [15] 10) Gypsum [15]	1) Authigenic [15] 2) Diagenetic [15] 3) Authigenic [16] 4) Authigenic or detrital concentration [15] 5) Breakdown of pyrrhotite with fluid water <100 °C [15] 6) Uncertain - Detrital or authigenic [18] 7) Potentially alteration of akaganeite [15] 8) Circum-neutral pH [15] 9) 5 km depth – Dehydration of gypsum [15] 10) Hydrous environment, mobolised sulphate rich layers [19]

[1] Boyton et al., 2009 [2] Hecht et al., 2009 [3] Cull et al., 2010 [4] Klingelhöfer et al., 2004 [5] Arvidson et al., 2015 [6] Arvidson et al., 2006 [7] McLennan et al., 2005 [8] Squires et al., 2012 [9] Grotzinger et al., 2005 [10] Bertelsen et al., 2004 [11] Ming et al., 2006 [12] Christensen et al., 2004 [13] Squyres et al., 2008 [14] Ruff et al., 2011[15] Vaniman et al., 2014 [16] Grotzinger et al., 2014 [17] Bish et al., 2013 [18] Poulet et al., 2005 [19] Nachon et al., 2014.

1.11. SAMPLE SELECTION

Meteorites from Antarctica were desired specifically because: 1) The weathering was on a long timescale not reproducible by laboratory experiments, 2) The liquid water interacting with the meteorites exists in small thin films and weathering is episodic, much like conditions experienced on current day Mars, 3) A range of meteorites of the same class can provide a spectrum of weathering states of the same starting material, where as a basaltic outcrop would not, 4) The presence of metal will help reduce altering fluid as it will quickly oxidise, thus locking some of the oxygen up in alteration products.

Samples were selected to span a number of physical properties that are known to directly influence weathering patterns. Several parameters were considered:

- Based on the work of Losiak and Velbel (2011) (described in Section 1.3.4.), meteorites from two icefields were selected to test any influence of the icefield (e.g. temperature fluctuations, liquid water presence, ice composition).
- Meteorite size plays a significant role in the speed of weathering because higher surface area/volume ratios aid weathering processes (Benoit and Sears 1999), thus meteorites of similar, large masses were desirable (500 g – 1 kg).
- A breadth of ANSMET designated weathering classes (described in section 1.3.1.) were selected in order to observe the different stages of weathering. In addition, a number of samples that allowed duplicates of the same weathering grade were sought so that all of the weathering classes could be covered and samples of the same weathering class could be compared to assess the variability within a single weathering class. The number of samples was limited by the analytics planned, and the assessment of time available led us to choose six samples.
- Similarly, a range of fracture grades were chosen to assess the importance of fractures in weathering systems.
- As native iron and nickel are known to weather readily, minimal metal contents were selected so that silicate weathering would not be swamped.

When all of these factors were taken into consideration and sample availability assessed, six L6 chondrites were chosen as L6 represented the only class which could fill all of the above considerations. These are: ALH 78130, ALH 84056, ALH 84058, ALH 85017, QUE 94214, QUE 99022 (Table 2.1.). For each meteorite, one sample from the rim and one from the interior was studied and throughout the study the designations R and I are used to distinguish "Rim" and "Interior" samples. Thin and thick sections from the rim and interior of each meteorite were provided by the Smithsonian Institution (Washington DC), along with chips of at least 1g for destructive studies. The chips were stored and prepared for study in a class 1000 clean room (< 1000 particles per cm^3 of air).

1.12. RESEARCH JUSTIFICATION AND OBJECTIVES

The process of alteration for many meteorites is long and proceeds through many stages. During the residence in Antarctica, the meteorites undergo many different processes which in turn affect each other, e.g. the breakdown of silicates to clays creating expansional fractures that allow greater fluid access to previously inaccessible areas. This research project is exploring the different features and signatures of weathering in cold deserts and testing the reliance on each other and on environmental factors. From a systematic study of petrographic features and chemical tracers removed/added by weathering minerals, a more comprehensive description of cold desert weathering can be made. The major objectives of this study are:

- To gain an understanding of the petrology during the progression of weathering in cold desert, low water/rock environments.
    - This will be achieved by characterising the mineralogy of six L6 chondrites of varying weathering states – spanning the weathering classes experienced in Antarctica (W0-W3, A-C ANSMET) and examining the alteration products and documenting the habit of formation.

- To understand the migration of major and minor elements from weathering minerals on a spatially resolved scale so quantifiable transport distances of different elements can be linked to alteration processes.
    - This is expected to result in a better understanding of the extent of spatially resolved element movement relative to bulk measured samples, and how much alteration of samples will translate to bulk changes, which are the most commonly used measurement.
    - To do this, EMPA and LA-ICP-MS will be used to analyse major and minor elements in meteorites of differing weathering states.
- To test the relationship between bulk and spatially collected data.
    - For this, bulk measurements of major and minor elements will be collected by ICP-MS and ICP-OES.
- Find links between petrological and elemental data, so that easily identifiable features can be linked to elemental changes.
- Relate the petrological links to rover sites on Mars so that the elemental data can be extrapolated to real areas of interest on Mars.

CHAPTER 2 – METHODS

2.1. SAMPLES AND PREPARATION

Six L6 chodrites (Tab. 2.1) were obtained from the NASA Curation facility, selecting large specimen from two icefields. There were three sub-samples each: a thin section, a thick section and bulk material. Fig. 2.1. details the experimental plan for the study: Thin sections were used for optical studies (detailed in section 2.2), SEM investigation (section 2.3.) and EMPA analysis (section 2.4.). Thick sections were used for LA-ICP-MS analysis (section 2.5.).

Table. 2.1. – Samples used in this study. All samples are from large specimen of L6 chondrites and were obtained from the NASA Curation facility.

Name	Weathering Grade*	Fracture Grade*	Terrestrial Residence ages (ka)	Whole recovered mass (g)*	Allocated Mass for this study (g)	Remaining Mass (g)
ALH 84056	Be	A/B	NA	2140.3	R: 0.975 I: 1.1	R: 0.26 I: 0.20
ALH 84058	B	A	NA	2002.5	R: 3.0 I: 1.3	R: 0.43 I: 0.28
ALH 85017	A	A	50-60[1]	2361.4	R: 0.94 I: 1.2	R: 0.31 I: 0.29
ALH 78130	B/C	B	33 ± 3.8[2]	2733.0	R: 2.58 I: 1.3	R: 0.31 I: 0.27
QUE 99022	C	B/C	NA	548.9	R: 1.63 I: 1.3	R: 0.30 I: 0.28
QUE 94214	B/C	A	NA	772.8	R: 1.78 I: 1.2	R: 0.26 I: 0.22

* Meteoritical Bulletin – accessed 08/2012
1 - Sears et al., 2011
2 - Cresswell et al., 1993

Name	Thin section number	Thick section number
ALH 84056	Rim - ALH 84056 14 Interior - ALH 84056 17	Rim - ALH 84056 15 Interior - ALH 84056 16
ALH 84058	Rim - ALH 84058 5 Interior - ALH 84058 8	Rim - ALH 84058 7 Interior - ALH 84058 6
ALH 85017	Rim - ALH 85017 8 Interior - ALH 85017 33	Rim - ALH 85017 9 Interior - ALH 85017 34
ALH 78130	Rim - ALH 78130 11 Interior - ALH 78130 15	Rim - ALH 78130 12 Interior - ALH 78130 15
QUE 99022	Rim - QUE 99022 11 Interior - QUE 99022 9	Rim - QUE 99022 12 Interior - QUE 99022 10
QUE 94214	Rim - QUE 94214 10 Interior - QUE 94214 8	Rim - QUE 94214 11 Interior - QUE 94214 9

Magnetic measurements were non-destructive and were carried out on the whole allocated sample mass before chips were taken for destructive ICP-MS and oxygen analysis (section 2.7.). Chips of 0.05 g mass were broken from the allocated mass for oxygen isotope analysis using an agate mortar and pestle (section 2.8.). A second piece between 0.4-1.9 g of each meteorite was powdered in an agate mortar for ICP-MS and ICP-OES analysis (section 2.6.). The reservoirs of powder used for ICP-MS studies were as large as reasonably possible to mitigate heterogeneity effects from the samples.

To assess how results from these bulk samples compared to observations from smaller micro-environments, two meteorites were chosen for more detailed ICP-MS and ICP-OES analysis. ALH 84058 was taken due to the large size of available sample and QUE 94214 was selected based on previous petrological studies, suggesting that it has a unique weathering pattern (described in Section 3.1.). Details of the subsamples are in Table 2.2.

The thin and thick sections of the samples were coated with 20 nm of carbon once optical studies were complete, to provide a conductive surface for SEM and EMPA work.

Table. 2.2. Subsamples taken for ICP-MS and ICP-OES studies from two meteorites

Meteorite	Subsample designation	Meteorite	Subsample designation
QUE 94214	GR – General rim sample with fusion crust removed	**ALH 84058**	GR – General rim sample
	UFC – Directly underneath the fusion crust with the fusion crust removed		GI – General interior sample
	FC – Pure fusion crust		FC – Pure fusion crust
	MC – Clean area with no visible rust from interior		MA – Most altered material in rim
	MA – Most visibly altered material in meteorite from interior		MC – Most clean sample from the rim
	INTM – Intermediate sample between MA & MC from interior		INTM – Intermediate sample between MA & MC from rim

2.1.1. SAMPLE PREPARATION FOR SOLUTION ICP-MS AND ICP-OES

The crushing method for the ICP solution work was adapted from Hallis (2010) and was as follows:

Glass vials to contain the powder were initially cleaned in the following steps:

1. Filled and coated in Decon 90 to remove grease
2. Filled and coated with Isopropanol to remove Decon 90 and particles
3. Thoroughly rinsed with de-ionised water
4. Dried in a 450 ^{o}C oven overnight

Pestle and mortars were cleaned initially and in-between every sample. Four mortar and pestles were used in rotation to speed the process and to maximise equipment drying time. The cleaning procedure is listed below:

1. Initially cleaned with acetone and a synthetic wipe (packaged in a clean environment), removing visible residue of previous crushing
2. Five minutes grinding with quartz sand and de-ionised water

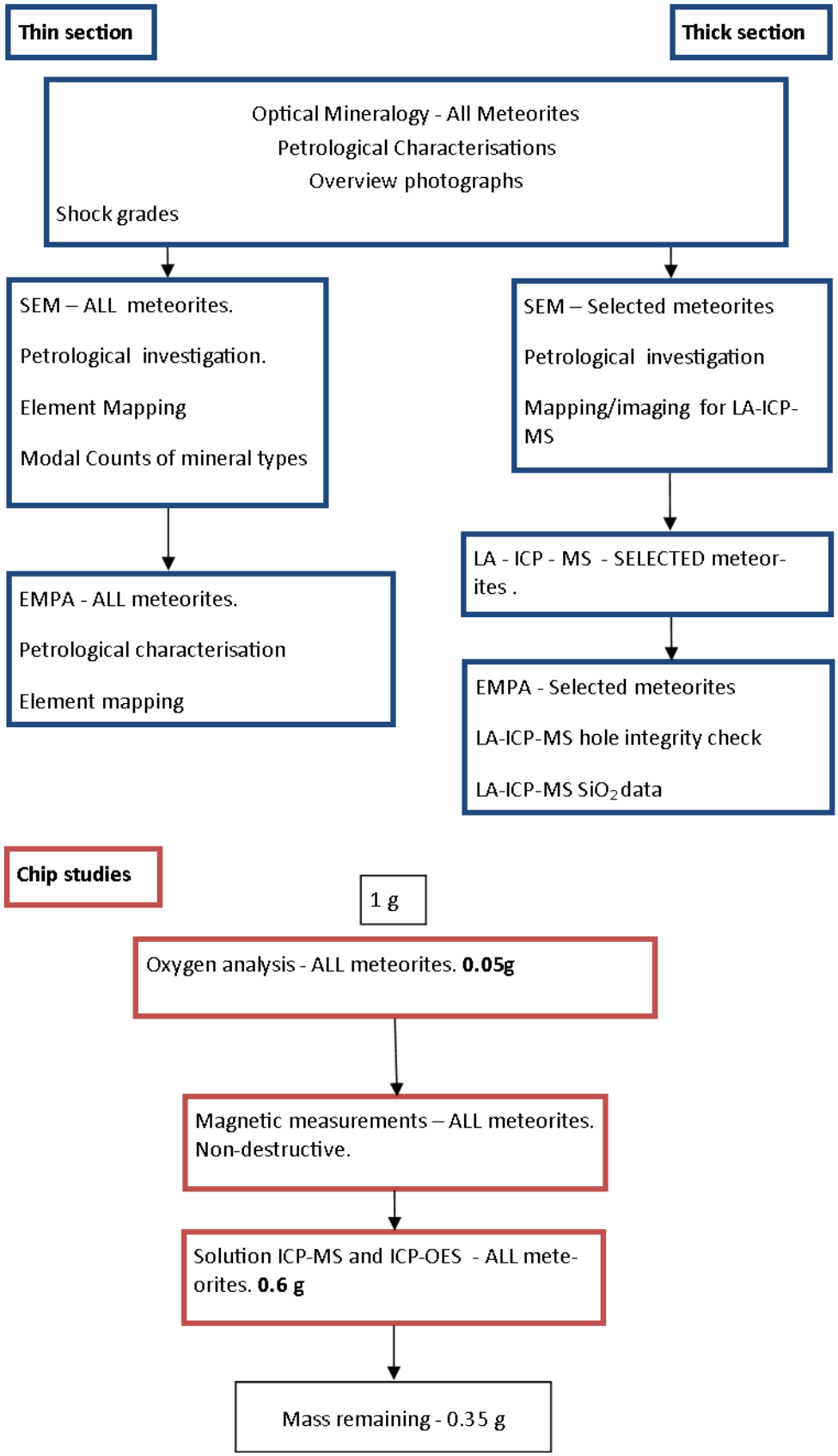

Fig. 2.1. Diagram showing the methods used in the study and the target associated average masses used in approximate chronological order. Blue – thin or thick section, red – chip.

3. Removal of sand by dowsing with de-ionised water
4. Cleaned with acetone
5. Cleaned with an approximately 70/30 mix of isopropanol and de-ionised water
6. Baked in an oven for upwards of 30 minutes at 450 ^{o}C
7. Removed and left to cool for 20 minutes before use

All crushing followed the procedure:

1. Aluminium foil covered surfaces with a double layer underneath mortar and pestle
2. Sample transferred to mortar and pestle, when necessary, split
3. At least 0.2 g of each sample conserved for future study
4. Remnants then placed in mortar and pestle with the underlying piece of foil used to construct a wall around it to deflect any chips thrown out by the powdering process
5. Sample crushed until powder resembled talc
6. Powder transferred to prepared vial using a small piece of foil folded into a "V" shape
7. Any chip that jumped out onto foil, or any powder that escaped, was put back in the

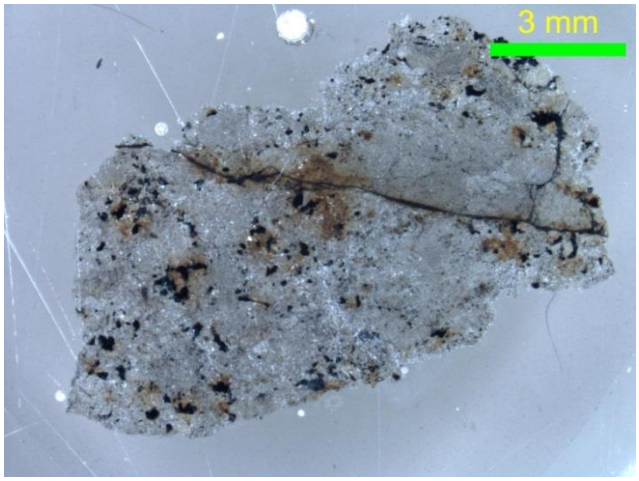

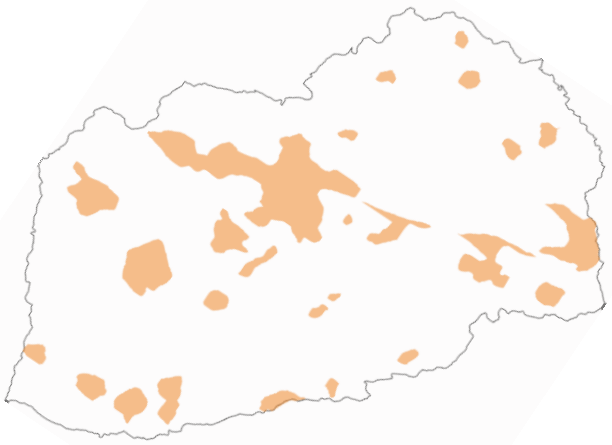

Fig. 2.2. Binocular photograph of ALH 84056 I thin section and the line drawing of the section indicating areas of rust coverage.

mortar with cleaned tweezers, or funnelling of foil

8. Full vial was weighed to ascertain if any mass was lost during the crushing process

2.2. Optical Microscopy

Optical microscopy was undertaken on thin sections to determine the general mineralogy. It allowed petrological descriptions of the samples before carrying out more detailed petrology using the scanning electron microscope (SEM). Optical microscopy focussed on three key points: (i) determining how extensively rusted each sample was - a measurement of the percentage area covered by visible rust was made from images taken using a binocular microscope (Fig. 2.2); (ii) determining the presence of melt veins and other shock-produced features, to establish the shock grade of the meteorite based on Stöffler (1991) and, (iii) to examine opaque phases.

In addition to the petrologic investigations, images of the whole samples were taken using the petrologic microscope to identify potential areas of interest to investigate at higher magnification and as navigation aids for observation by SEM.

2.3. Scanning Electron Microscopy (SEM) and Energy Dispersive X-ray Spectroscopy

Scanning electron microscopy (SEM) was used to examine samples at higher magnification than optical studies, to map the mineralogy (for navigation during EMPA and LA-ICP-MS analysis) and to create large image montages (Fig 2.3). SEM images were also used to carry out modal counts.

2.3.1. Instrumentation

For this study, an FEI Quanta 200 3D in the Department of Physical Sciences at The Open University was used. It is equipped with an Oxford Instruments X-Max 80 mm^2 EDS detector and uses Oxford Instruments INCA software.

2.3.2. BACKGROUND

Electron dispersive X-ray spectroscopy (EDS) was used to obtain semi-quantitative compositions of minerals in thin sections of the samples. EDS detectors comprise of an X-ray detector, which detects the amount and energies of reflected X-rays, then converts them to voltage signals. The ED spectrometer contains a Li-doped silicon crystal detector cooled by liquid nitrogen to reduce noise and prevent damage to the detector.

An electron beam is focused on a sample surface and there are two types of sample interaction (illustrated in Fig 2.3.):

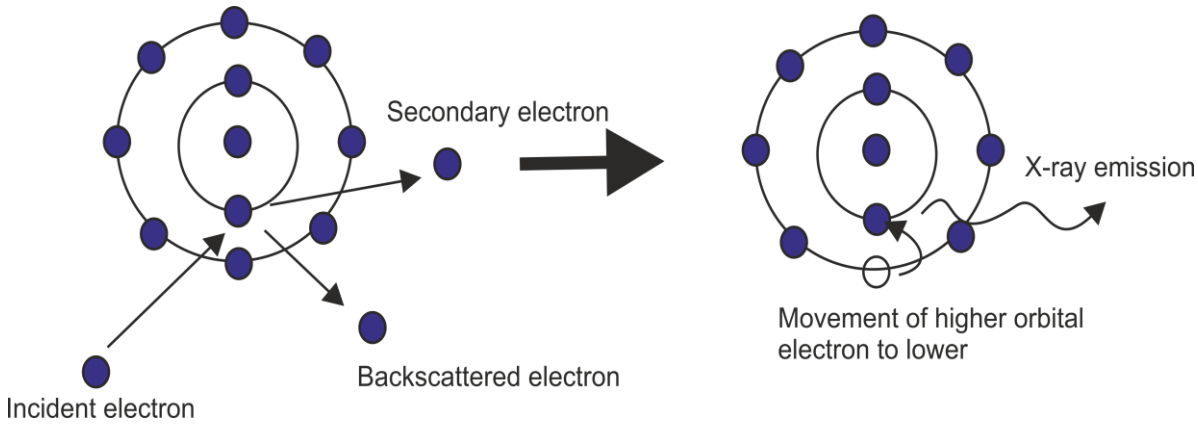

Fig. 2.3. Diagram showing the effect of electron beams on an atom. The incident electron collides with an electron in the inner shell of an atom and it is ejected as a secondary electron. The primary incident electron is backscattered. An electron from a higher orbital relaxes to the lower shell and an x-ray of unique energy to the atom is released (Goldstein et al., 2012).

1) The surface back scatters the electrons via elastic scattering. The reflected back-scattered electrons from the electron beam are counted by the back-scatter detector which translates the data into a BSE image. This is a greyscale image with the brightness reflecting the number of electrons that have been back-scattered. Bright areas represent a high level of back scattered electrons (and thus a low level of absorption) and dark areas indicate a lower level of reflectance (thus a high level of absorption). The level of absorption corresponds inversely with the atomic mass of

an element, resulting in more electrons reflected and a higher count rate on the back-scatter detector the higher the atomic mass. This allows for mineral discrimination based on the greyscale images, with silicate minerals being darker (as they contain the lighter elements) and Fe-Ni metals and sulphides being the brightest minerals (Fig. 2.4.). This feature has been utilised for modal counts.

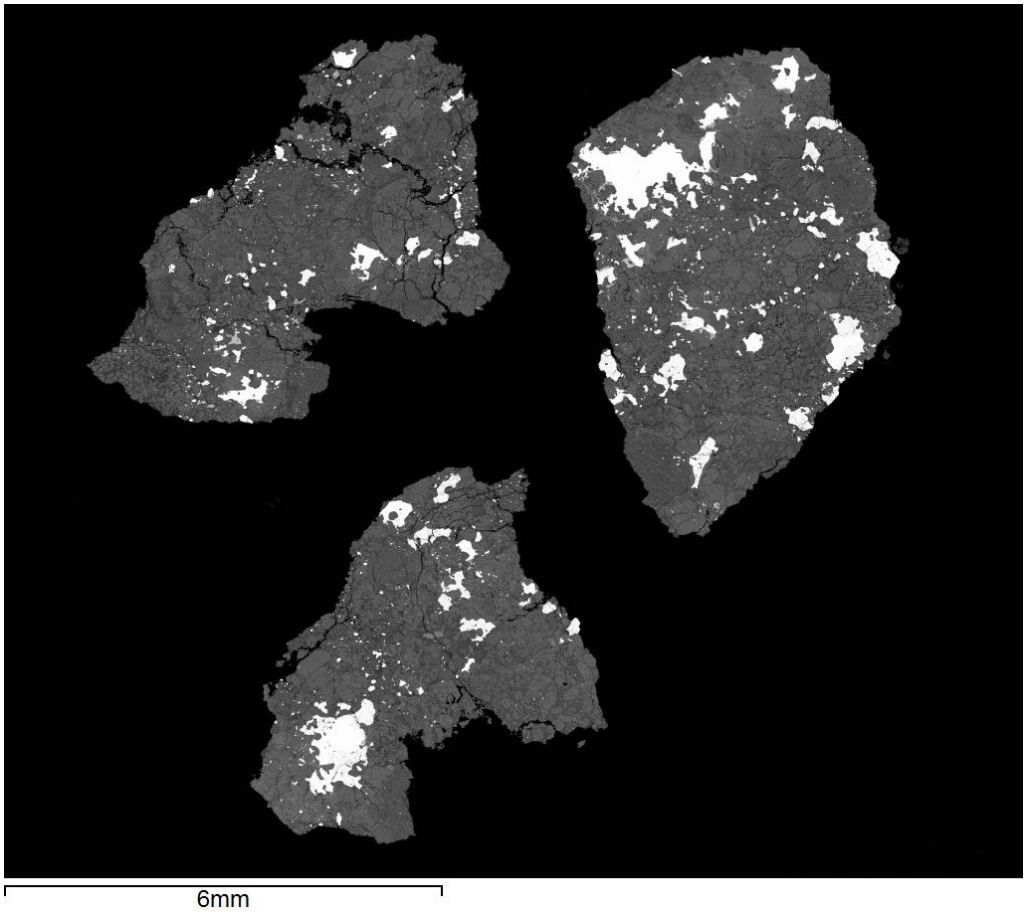

Fig. 2.4. BSE image of ALH 85017 I thin section. The BSE image is made of over 30 smaller images stitched together and allows navigation in instruments with small scale views such as the EMP and LA-ICP-MS. The greyscale corresponds to atomic mass, and so the bright white crystals have high atomic mass (they are kamacite, taenite and troilite crystals) and the darker crystals are silicates, chromite and phosphates with a lower average atomic number. The silicates can also be discriminated by differing greyscale.

2) The electron beam-surface interaction produces secondary electrons through inelastic scattering (in which energy is not conserved): the electron beam excites electrons in an atom from ground state to a higher state, causing electrons in the inner K orbital to be expelled (as secondary electrons, SE). This leaves an electron hole, which is filled by an electron (with higher energy) dropping down from an outer shell. The movement of electrons between shells results in production of X-rays with an energy characteristic of each element, as it reflects the unique binding energies of the electrons (Fig. 2.3.). The unique energy can then be detected by the EDS and thus allows the composition to be determined, with major elements being measured to ~0.1 wt. %. Secondary electrons released by inelastic interactions are identified by their low energy (< 50 eV) and detected by the SEM's secondary electron detector. Since these electrons originate from the surface of the sample, they provide topographic information which is translated into a SE image. This helps identify cavities and fractures in minerals (Fig 2.5.).

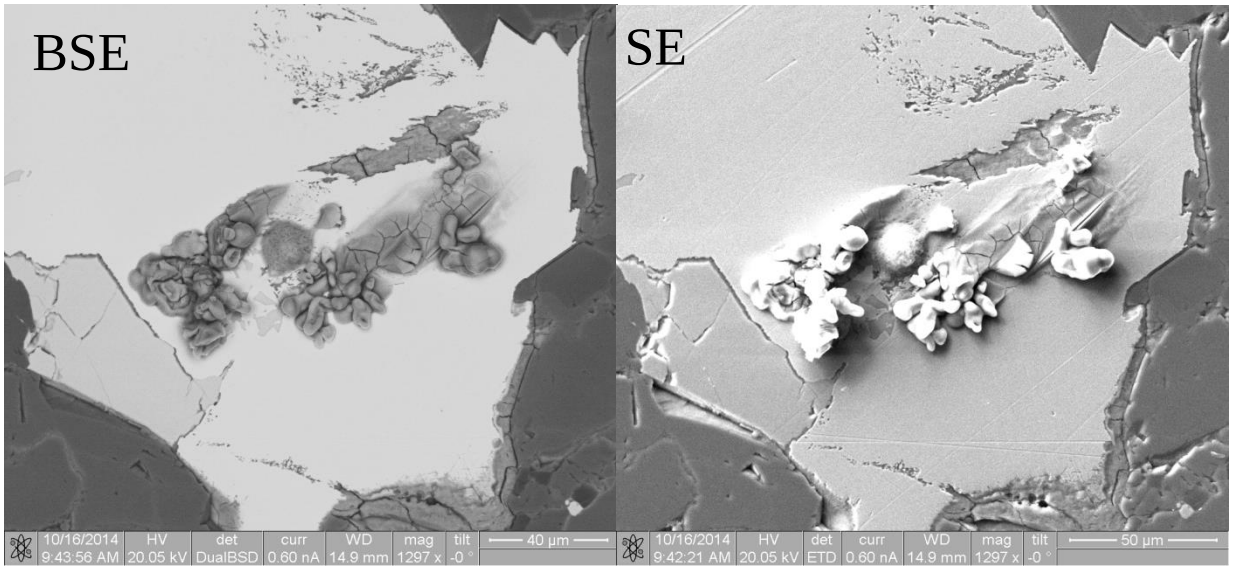

Fig. 2.5. BSE and SE image of the same locality in ALH 84058 I thick section. The topography is only visible in the SE image, whereas the BSE presents a flat, 2D image. This image shows the growth of Fe-oxyhydroxides on a kamacite grain.

2.3.3. ANALYTICAL METHOD, MAPPING AND MODAL COUNTS

The standard analytical set-up used was: 20.05 kV accelerating voltage, 0.6 nA beam current, 4-6 µm spot size at a working distance of 15 mm and magnification up to x 1500. Map magnification was typically x118, but varied with sample size (larger samples were mapped at lower magnification).

Using the INCA software, compositions were mapped compositionally and BSE images were generated (e.g. Fig. 2.4.). This is an automated process that generates single maps for each element that are then merged as false colour images in the image processing software – ImageJ. The resulting compositional maps are used to discriminate mineral phases. For most samples, only three elements were merged on each map, as discrimination became

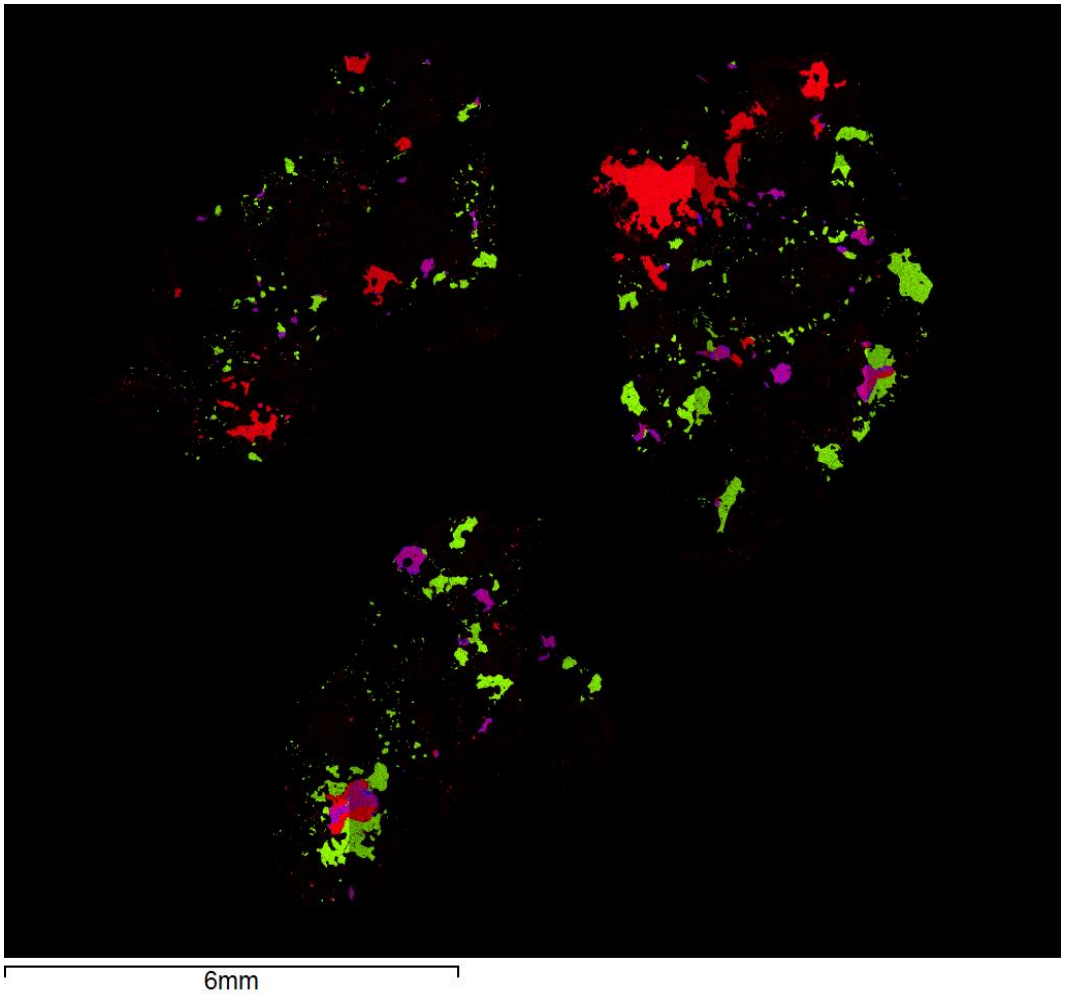

Fig. 2.6. False colour Fe, S, Ni composite map of ALH 85017 I. Fe—red, S—Green, Ni—Blue. From these three elements, three mineral species can be discriminated. The red crystals are kamacite (Fe), the purple are taenite (Fe-Ni) and the green are troilite (FeS).

difficult with the addition of more (Fig. 2.6.).

From a combination of the generated false colour images and BSE images, modal counts for each sample were performed using pixel counting in imageJ. Through manipulation of thresholds, different minerals were selected and measured based on colour discrimination. For silicate minerals and phosphates, this was done using BSE images. For metals and opaque minerals, the BSE image was not sufficient as kamacite, taenite and troilite all have similar levels of reflectance and could not be distinguished reliably from each other. Therefore, the false colour composites (of Fe, Ni and S) were used to determine modal counts of these minerals. For each sample, 7-15 images were utilised (as the sample size allowed) and then an average value taken. Fig. 2.7. illustrates a typical results of this method.

Six samples were measured on three separate occasions to confirm reproducibility and these were also compared to point counting results gained from manual point counting of BSE images. The variation between methods was in the order of 5%.

a)

b)

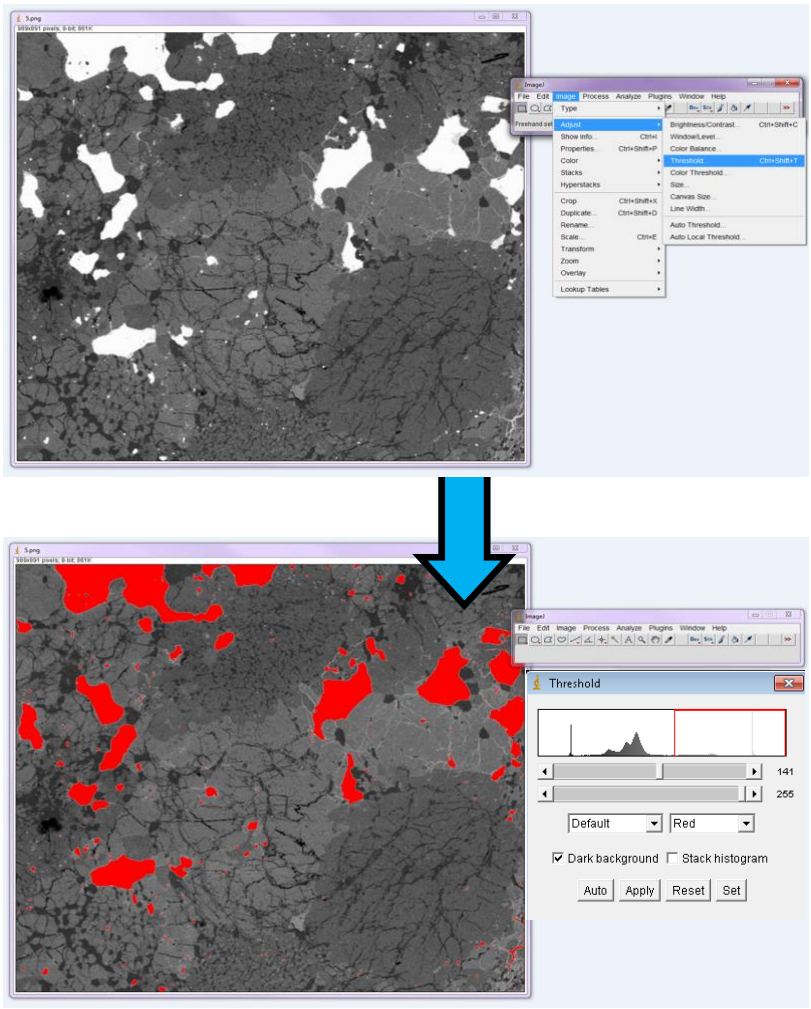

c)

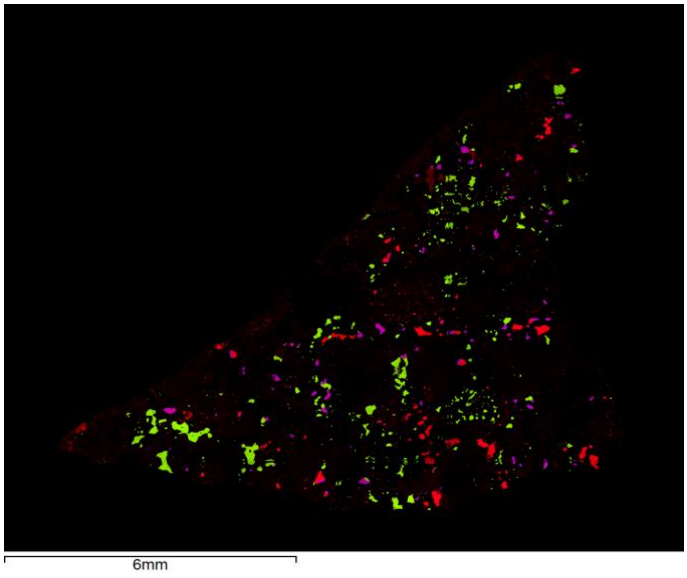

Fig. 2.7. Example of a modal count of a region of a thin section. a) BSE of ALH 84056 R thin section, FOV ~ 1mm. b) The thresholding tool in ImageJ is utilised to select areas of particular colour (in this case corresponding to kamacite) which are then measured in terms of pixel counts. These pixel counts are then ratioed together to get percentages. c) An example of a composite Fe, S and Ni map used for discrimination between metal grains and sulphides (ALH 78130 R). Red—Fe, green—S, blue—Ni.

BSE images were also used to assess the percentage of oxidation of kamacite, taenite and troilite. This was a measurement of the two dimensional area of minerals that had been transformed to an alteromorph so that a numerical measurement could be used to assess the level of weathering in different minerals. An example of how this measurement was performed can be seen in Fig. 2.8. Crystal sizes of 100 µm and above were used to avoid edge effects. For every sample, 12 – 32 measurements were made on different grains of each mineral. The number of measurements varied depending on the occurrence of the minerals, thus the dataset for taenite was consistently lower than kamacite and troilite as it

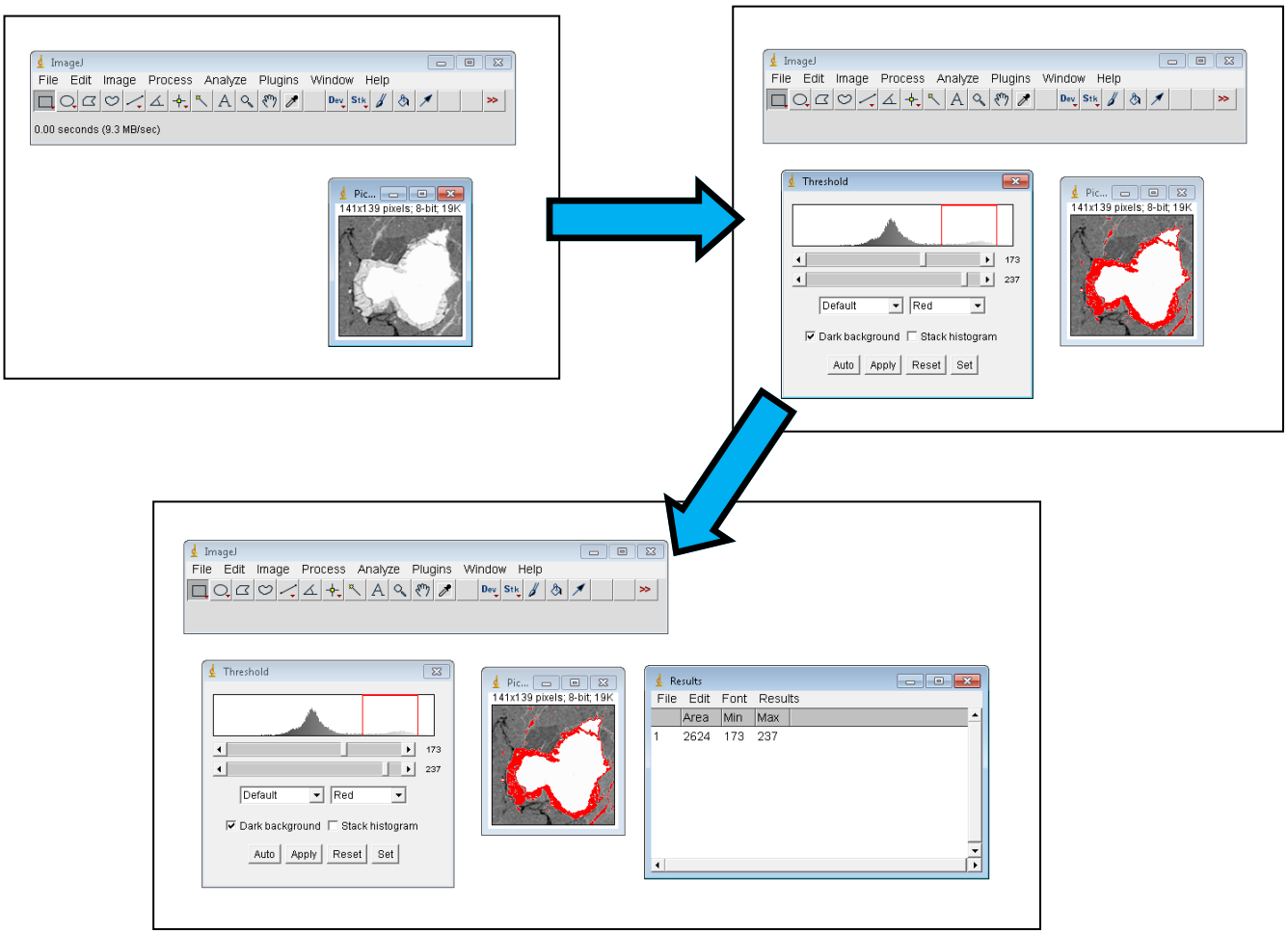

Fig. 2.8. Example of an oxidation measurement. The metal grains from BSE images are isolated to minimise measurements of Fe-oxyhydroxides not directly associated with the grain, then the alteromorphs are selected by colour discrimination. This is measured as a pixel count which is ratioed to the grain and alteromorph to get an oxidation percent.

was less abundant. Error bars were derived from repeat measurements.

As this is a 2D measurement as a 3D proxy, a hypothetical calculation is done below to show how the 2D area % oxidation may relate to the 3D volume. For this, a hypothetical spherical grain is used.

Three spherical grains of kamacite with radius 50 µm that have 10, 20, 50 % alteration are supposed.

100 µm grain, of which outer 10 µm is halo of alteration product (10%):

Total volume = 4.19×10^6 µm^3

90 µm grain volume = 3.05×10^6 µm^3

5 µm alteration product volume = 1.14×10^6 µm^3

Volume oxidised % = 27.1%

This has been calculated for a range of values displayed in table 2.3 and presented as a graph in Fig. 2.9.

Table 2.3. 2D percentage of areas altered and the resulting 3D volume % altered.

2D area altered %	% volume altered
0	0
10	27.1
20	48.8
30	65.7
40	78.4
50	87.5
60	93.6
70	97.3
80	99.2
90	99.9
100	100

A graph (Fig. 2.9.) has been drawn to show this relationship between 2D and 3D space in spheres.

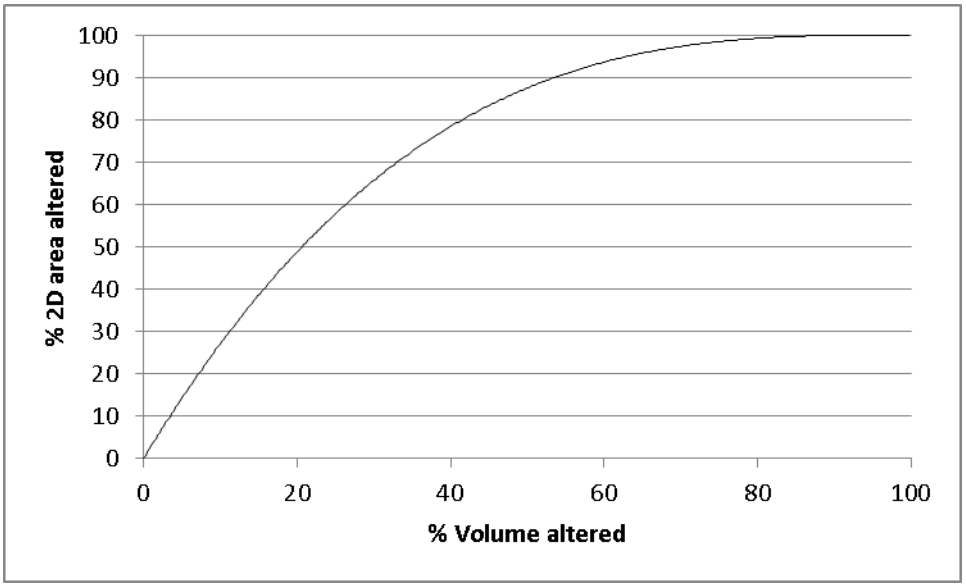

Fig. 2.9. A theoretical graph of 3D volume to 2D cross sectional % based on an assumption of spherical particles and even alteration.

This 3D volumetric estimate only works if the particles are spherical and have weathered equally across all the surfaces. As the 3D measurement is purely hypothetical based on spherical even weathering, the measurable 2D area is used and then 3D space can be discussed.

The area over which alteration products were deposited was also measured and named "vein coverage (%)". This was a measurement of the area where there were no open fractures, but infilled veins were present, and yielded a number that allowed the semi-quantification of the area of the sample that had definitely interacted with water, leading to the deposition of Fe-oxyhydroxides. The measurement was determined using BSE images and could be compared and contrasted with the rust (%) measurement that was obtained by binocular microscopy (Section 2.2).

2.4. ELECTRON MICROPROBE ANALYSIS (EMPA)

The electron microprobe was used to obtain more accurate chemical compositions of the minerals and to produce high resolution element maps. The EMP uses wavelength dispersive spectroscopy (WDS), which has a lower detection limit than EDS.

2.4.1. INSTRUMENTATION

A Cameca SX100 electron microprobe was used at The Open University. The Cameca SX100 has five spectrometers, with a selection of crystals in each, allowing five elements to be measured simultaneously.

2.4.2. BACKGROUND

The electron microprobe can operate in all modes as described for the SEM. Its imaging resolution is reduced compared to the SEM because it operates at a fixed working distance. In addition to the secondary and backscatter modes and the EDS (as detailed in section 2.4.2.), it has five wavelength dispersive spectrometers (WDS), which use the wavelength of the emitted X-rays. Characteristic X-ray wavelengths are identified and the background is subtracted at a higher resolution than in EDS spectra. Each spectrometer is turned to peak positions of separate elements, and so each spectrometer only analyses one element at a time. The X-rays emitted from the sample are diffracted by crystals in the spectrometers, which are of known lattice spacings, onto the detector. Quantitative analysis can be performed on any element above atomic weight 5.

The spectrometers are regularly calibrated against well characterised standards. WDS X-ray element maps show the spatial distribution of constituent elements and were used for this study at high magnification in small areas identified as areas of interest from the SEM work.

2.4.3. ANALYTICAL CONDITIONS

Operating conditions for all analysis were 20 kV accelerating voltage, 20 nA current, 10 µm spot size for primary minerals as a compromise between good analyses and BSE image quality, a defocussed 20 µm spot size was used for alteration products as they are beam sensitive, 1 µm spot size for maps. As only single elements can be measured in each spectrometer at once, maps were generated of either five or ten elements. The crystals in the EMP were: pentaerythritol and large pentaerythritol (PET, LPET), thallium acid phthalate and large thallium acid phthalate (TAP, LTAP), large lithium fluoride (LLIF).

2.5. SOLUTION ICP-MS AND ICP-OES

Solution ICP-MS and ICP-OES analysis was performed on all 12 samples (rims and interiors of 6 meteorites) in bulk powdered samples with some samples having subsets to test the heterogeneity of trace element distribution (table 2.2).

2.5.1. SOLUTION PREPARATION

All acids used in the digestion were TD grade (Teflon distilled) and the water used to dilute acids was purified through a millipore filtration system to a resistivity of >18.2 MΩ. Samples were digested in Teflon containers with most of the samples digested in 15 ml bottles and the subsamples detailed in Table 2.2 were digested in 7 ml bottles. Reference materials BHVO-2, BIR-1, AGV-1 and DNC-1 were also prepared at the same time using the same procedures along with a blank.

All samples were initially digested in HF acid for 24 hours and then dried down. HNO_3 was then added and left for 48 hours. In the first two hours of solution, the vials were put in a sonic bath twice for ten minutes to encourage dissolution. The samples were then left in a mixture of HNO_3 and HCl as some residue remained and they were left for 48 hours to allow complete dissolution. Once the samples had dried down, 3% HNO_3 and 97% H_2O was added resulting in a 1000x dilution of the powder weight into the final solution.

2.5.2. INSTRUMENTATION

Trace elements and major elements were both measured using ICP (inductively coupled plasma) methods. The trace-element concentrations were measured using an Agilient 7500a ICP-MS (Mass Spectrometer) at The Open University and the major elements were measured using an Teledyne-Leemans Prodigy high dispersion ICP-OES (Optical Emission Spectrometer). The ICP-OES was operated in axial view (Fig. 2.10.) using standards prepared using a certified stock solution of 100 ppm multi element standard (Fisher Scientific). Mean values were taken from three replicate analyses per sample. A standard was measured after every 5th measurement to assess drift of the ICP-OES; and in the ICP-MS, three standards were measured after every 5th measurement. These standard measurements were then used to drift correct.

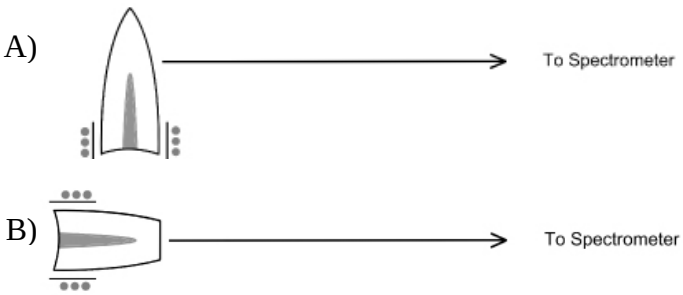

Fig. 2.10. Radial and axial views of the ICP-OES torch. A) Radial view or side on view of the torch is the traditional set-up but has poor sensitivity. B) Axial view or face on has a greater sensitivity but is more susceptible to interferences. Images taken from Teledyne Leeman Labs.

2.5.3. BACKGROUND

The ICP parts of both systems operate in the same way. A torch consisting of three quartz tubes is surrounded by a high powered radio frequency generator, which, when switched on, generates a strong electromagnetic field. The plasma is generated from argon which the torch ignites as a tesla unit creates a discharge through the gas. The argon gas is ionised and flows towards the radio frequency coil. A stable plasma is then created by the inelastic collisions between the charged argon particles and neutral particles. The nebulizer transforms the sample into a mist, which is added to the plasma, where it vaporizes. The sample collides with charged argon ions and electrons, which breaks the molecules down to charged ions. The ions lose and regain electrons repeatedly, emitting a characteristic wavelength for different elements.

In the ICP-OES system, transfer lenses focus the light onto a diffraction grating which splits the light into its component wavelengths. The component wavelengths fall on a photo detector which measures the intensity of the different wavelengths and correlates it to known standards. A basic schematic diagram of an ICP-OES is shown in Fig. 2.11.

In the ICP-MS system, the ions are extracted from the plasma through a series of cones and they are introduced into a mass spectrometer. Ions are then separated based on mass to charge ratios and a signal is transmitted to the detectors which is compared to known standard values and concentrations are determined.

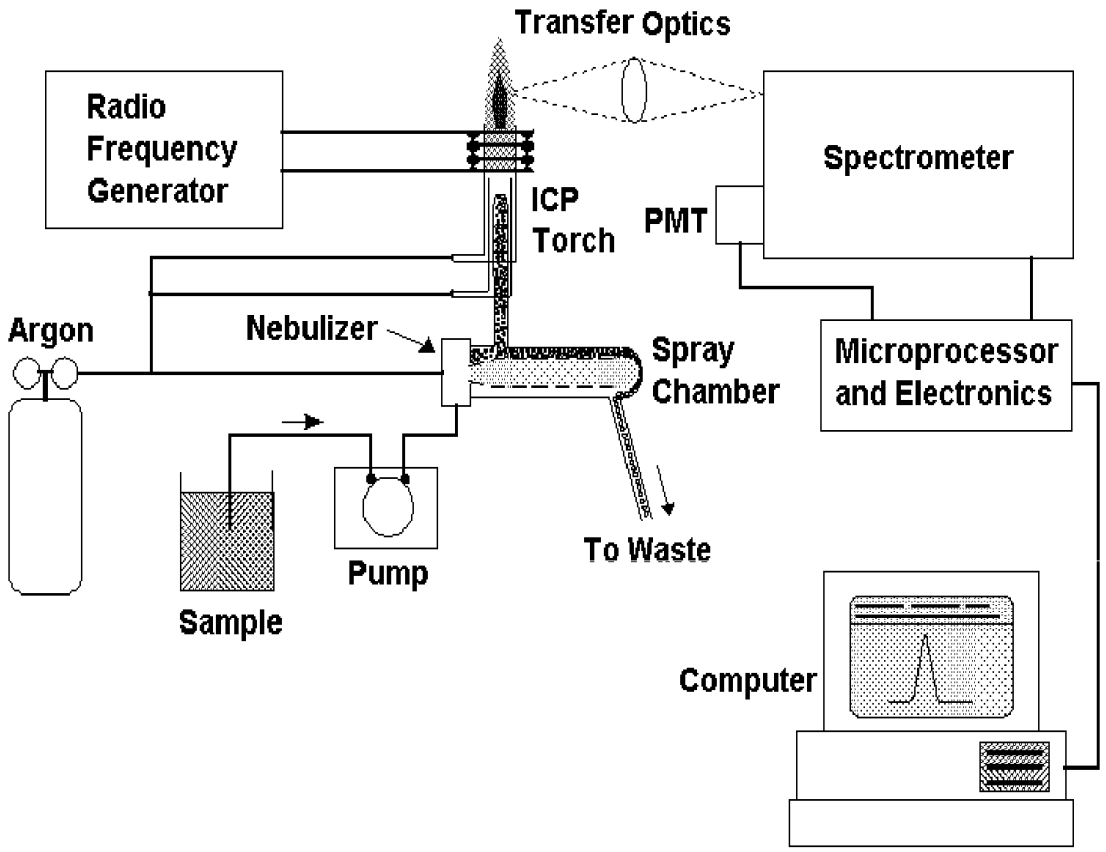

Fig. 2.11. Basic components of an ICP-OES, taken from http://analyticalprofessional.blogspot.co.uk/p/oil.html.

2.6. LA-ICP-MS

Laser ablation inductively coupled plasma mass spectrometry (LA-ICP-MS) was used to study trace elements with spatial resolution. Thick sections of the samples were used because their depth can be utilized to ablate larger volumes of sample without compromising spatial resolution, enabling an increased signal and reducing error. Minerals suitable for ablation were pre-identified from the BSE images and maps obtained by the SEM. Laser pits were examined by SEM after ablation, to verify the pit had not included surrounding minerals or underneath inclusions and to assess the sphericity and even sized structure.

2.6.1. INSTRUMENTATION

The instrument used was an Agilent 7500s ICP-MS with a New Wave 213 Nd:YA.G. deep UV (213 nm) laser system. The description of the ICP-MS is in Section 2.6.3. The pulsed laser ablates pits in the mineral surfaces in a He atmosphere and the ablated material is carried by He mixed with Ar before entering the plasma. Spot sizes used on the samples were 60 µm for silicates and 80 µm on sulphides and metals. This presented a problem in some samples, where mineral grains of sufficient size for the beam size were not present.

2.6.2. ANALYTICAL METHOD

Each analysis time totalled 240s. This included an initial 120s blank measurement, a 60s ablation time and a 60s washout time. For silicate analyses, a synthetic standard 50 ppm, NIST 612, was measured twice at the start of every analysis, and twice after every 8 analyses. For metal and sulphide analysis, three standards were used: the Filomena and Hoba meteorites and a NIST standard steel. These were measured at the start of every analysis and after every 8 sample analyses. Standard detection limits for lithophile trace elements are ~10 ppb. The wt. % of SiO_2 (determined by EMPA after analysis) was used as an internal standard for the silicates, as the wt. % of CaO (the usual internal standard) was below detection limit in many of the olivines in the samples studied. Care was taken to assure that laser pits were positioned away from cracks and fractures.

The data were reduced using Glitter software, which displays the signal of each measurement so that the user can set limits to the background and select the portion of signal. This was necessary to eliminate measurements of inclusions - many of the silicates had chromite inclusions. While inclusions below the surface are not visible on the surface of the thick section, they were clearly observable in the signal and could be removed by selecting the appropriate parts of the measurement. This also prevented the inclusion of

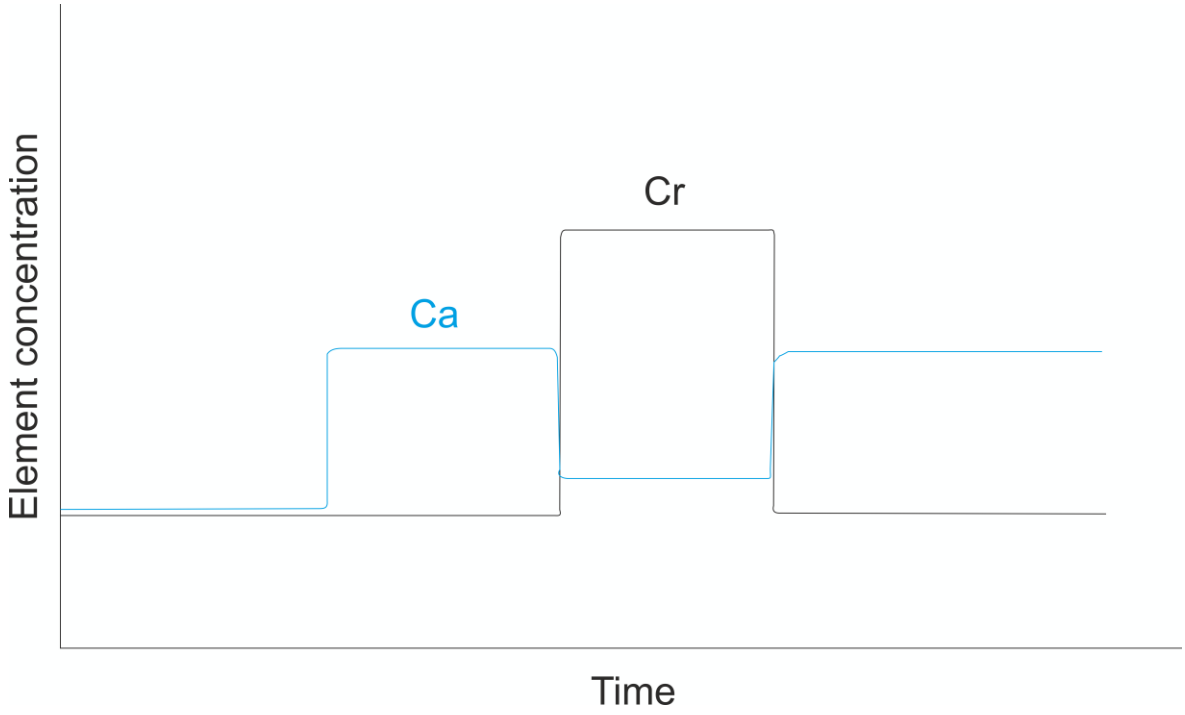

Fig. 2.12. Schematic representation of the output from LA-ICP-MS software – Glitter. As time progresses a Cr rich inclusion is ablated, evidenced from the sudden uptake of Cr and the drop in the Ca of the target crystal. In this case, the period of time before the Cr appeared was selected as the appropriate analysis.

data from points where a pit had reached the mineral underneath as a clear change in signal could be observed because different suites of trace elements appeared (Fig. 2.12).

2.7. Magnetic Measurements

Magnetic measurements were made to assess the level of changes in magnetic properties that could be related to petrological weathering.

2.7.1. Instrumentation

All measurements were undertaken at the Centre Européen de Recherche et d'Enseignement des Géosciences de l'Environnement (CEREGE). Hysteresis measurements were carried out using a Princeton Micromag Vibrating Samples Magnetometer, and susceptibility was measured with an Agico MKF susceptometer.

2.7.2. BACKGROUND

Susceptometers work by applying an alternating current to a coil, which magnetises the specimen, which in turn offsets the current. The offset is measured and is proportional to the susceptibility. The Agico MKF susceptometer rotates the sample and measurements are taken from three axes of the samples, providing a full susceptibility measurement that is not influenced by fabrics within the meteorite.

In a vibrating sample magnetometer (VSM), a sample is lowered between two pickup coils then vibrated at a known frequency and distance (from the coils). Each coil has a pole of an electromagnet attached which creates a magnetic field across the sample. The vibration of the sample physically moves the magnetic centre of the sample and so creates a change in the magnetic flux in the coils. This creates a voltage in the coils. The change in magnetic flux is proportional to the magnetic moment in the sample and so the moment can be deduced from the change in flux.

2.8. OXYGEN ISOTOPE MEASUREMENTS

Oxygen analysis analyses were used to ascertain if any changes in oxygen isotopic composition from alteration, would correlate with petrological features in the samples, and if the changes reflected the quantity of alteration products present.

2.8.1. INSTRUMENTATION

Oxygen isotope analysis was undertaken at The Open University using laser-assisted fluorination (using the protocols of Miller et al., 1999), and carried out by Dr. Richard Greenwood and Ms Jennifer Gibson. Between 2-3 mg of powder was required for each analysis, and replicate analyses of each meteorite were carried out. The powder was weighed into a small well, then melted by a focussed 10.6 μm radiation, 25 W CO_2

infrared laser in the presence of BrF_5. This drives off structural oxygen and replaces it with fluorine in the lattice structure. The oxygen from the lattice is expelled as a gas, which is then passed through two liquid nitrogen traps. This freezes out any excess BrF_5 and any other fluoride compounds that have been created during fluorination. The gas is then passed through a heated tube of KBr which converts any remaining F_2 to KF, releasing Br. The Br is then removed by an additional liquid nitrogen trap and purified oxygen is the only remaining gas. The oxygen is condensed onto a molecular sieve and then passed into a MAT 253 stable isotope ratio mass spectrometer for measurement of isotopic composition.

CHAPTER 3 – PETROGRAPHY

3.1 SAMPLE OVERVIEWS

All of the L6 chondrites studied have the same primary mineralogy: olivine, a low Ca pyroxene, plagioclase/maskelynite, troilite, kamacite, taenite and accessory phases of chlorapatite, merrillite, high-Ca pyroxene and chromite. The dominant mineral species is olivine (Table 3.1.). Alteration in the samples creates a number of habits and the nomenclature of total replacement is summarised in Fig. 3.1. Sample descriptions below are arranged from most to least weathered as described by the ANSMET weathering system.

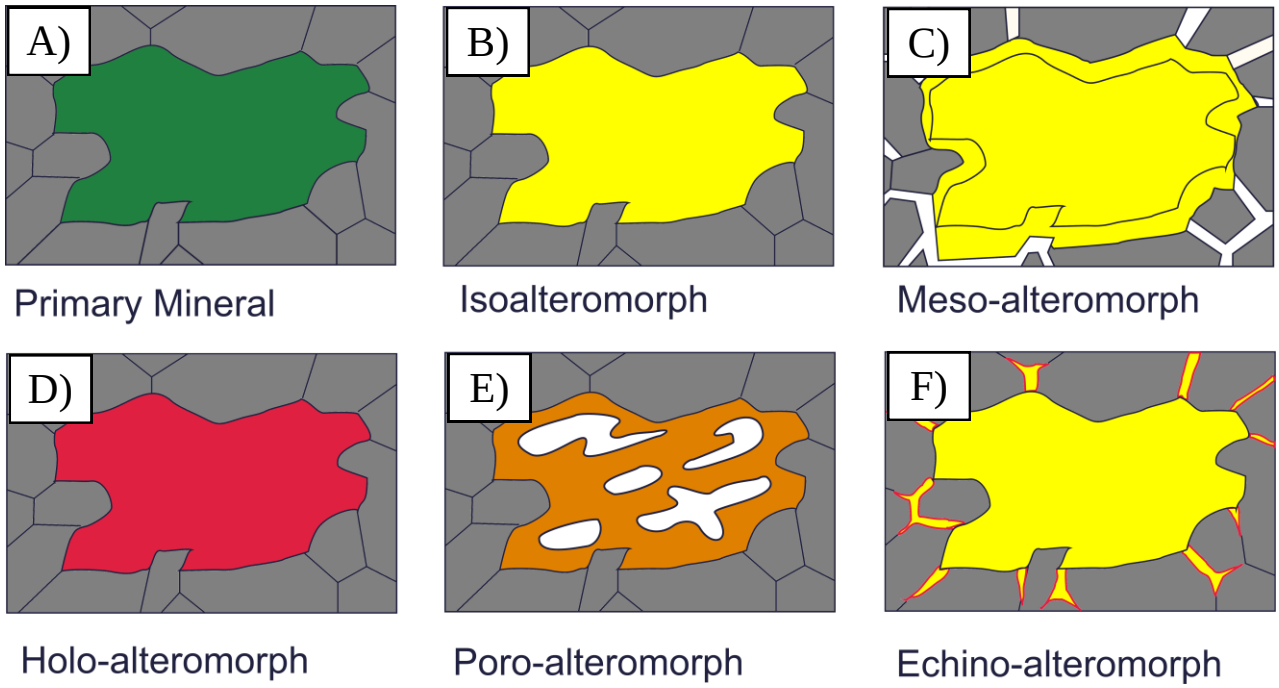

Fig. 3.1. Definitions of types of alteromorph found in the studied meteorites, adapted from Delvigne 1998. A) an un-altered primary mineral. B) Isoalteromorph—same shape and volume as the replaced parent grain. C) Meso-alteromorph—volumetrically larger than the parent grain and has thus caused mechanical stress and expansion. D) Holo-alteromorph—Same shape and size as the primary mineral but with an increased porosity. E) Poro-alteromorph—Same shape as the parent mineral with large pores open in the alteromorph. F) Echino-alteromorph—Alteration product is volumetrically larger than the parent, but has grown along adjacent fractures rather than forcing the rock apart.

Table 3.1. Modal percentages of mineral abundances in all samples with a typical error of 5% (relative). The method is discussed in section 2.4.3.

Sample		Olivine	Pyroxene	Feldspar	Troilite	Kamacite	Taenite	Chromite	Phosphates (cumulative)	Total
QUE 99022	R	46.2	29.7	11.2	8.5	2.1	1.7	0.4	0.2	100.0
	I	42.6	31.0	6.1	14.4	0.9	2.1	0.7	2.2	100.0
QUE 94214	R	39.0	27.0	20.8	6.5	4.2	1.1	0.6	0.8	100.0
	I	40.7	31.2	13.0	8.0	5.4	0.9	0.4	0.4	100.0
ALH 78130	R	43.1	31.7	16.2	3.6	3.4	0.6	0.7	0.7	100.0
	I	41.0	40.7	11.6	3.5	1.2	0.6	0.8	0.6	100.0
ALH 84056	R	41.5	33.2	16.6	4.2	1.7	0.6	1.6	0.6	100.0
	I	33.5	30.5	28.0	3.5	1.8	0.7	1.0	1.0	100.0
ALH 84058	R	35.1	37.5	16.6	5.3	1.5	1.7	1.0	1.3	100.0
	I	40.3	29.6	21.5	4.6	1.8	1.0	1.0	0.2	100.0
ALH 85017	R	46.4	26.4	21.2	2.7	1.4	0.9	0.7	0.3	100.0
	I	44.3	32.2	14.9	3.7	2.7	1.2	0.6	0.4	100.0

Table 3.2. Summary table of petrographic features in all meteorites in this study. R – Rim, I – Interior.

Sample	Weathering Grade [1]	Fracture Grade [1]	Wlotzka Weathering grade	Shock Grade	Porosity (%)	Rust Coverage (area %)	Altered Kamacite (%)	Altered Taenite (%)	Altered Sulphides (%)	Vein Coverage (%)
QUE 99022	C	B/C	W3	3	R: 1.5 I: 3.4	R: 100 I: 100	R: 68.96 I: 27.40	R: 60.81 I: 18.20	R: 19.51 I: 13.81	R: 80.0 I: 35.4
QUE 94214	B/C	A	W2	5	R: 2.0 I: 1.8	R: 80 I: 52	R: 14.60 I: 14.45	R: 12.88 I: 9.11	R: 5.93 I: 14.75	R: 9.7 I: 17.9
ALH 78130	B/C	B	W3	5	R: 1.2 I: 0.5	R: 66 I: 100	R: 32.04 I: 73.01	R: 14.03 I: 60.71	R: 13.73 I: 20.43	R: 17.5 I: 89.6
ALH 84056	Be	A/B	W1	5	R: 2.2 I: 1.3	R: 73 I: 13	R: 15.22 I: 9.56	R: 7.91 I: 3.26	R: 6.33 I: 5.53	R: 28.7 I: 5.0
ALH 84058	B	A	W1	4	R: 3.1 I: 3.0	R: 42 I: 33	R: 19.30 I: 17.09	R: 16.46 I: 13.75	R: 8.91 I: 6.96	R: 19.4 I: 11.0
ALH 85017	A	A	W1	4	R: 1.7 I: 3.4	R: 46 I: 38	R: 26.53 I: 17.28	R: 10.17 I: 8.66	R: 2.87 I: 3.58	R: 18.3 I: 14.2

[1] - taken from the Meteoritical Bulletin (07/15). [2] Wlotzka weathering scale, done myself for this study, based on Wlotzka (1993).

QUE 99022 (FIG. 3.2.)

QUE 99022 (Fig. 3.2.) is the most weathered meteorite studied with respect to the ANSMET weathering grade system (grade C). Despite being picked as an end member of the ANSMET weathering scale - when classified in this study, the meteorite was only a W3 on the Wlotzka weathering scale (Table 3.2.; for details about the Wlotzka weathering scale see Wlotzka, 1993). The sample studied is extensively rust stained with 100 % of the rim and interior stained orange. The sample contains 40 % coverage of opaque black impact melt veins (rim and interior) that appear opaque because of metal spherules within them. The sample is heavily fractured (Fig. 3.2) and the fusion crust in the rim sample has been completely removed by weathering. A large barred pyroxene chondrule remnant covers almost 10 % of the rim sample. Alteration products infill almost all of the fractures and pore spaces that occur around the melt veins, and much of the original kamacite has been altered to Fe-oxyhydroxides, yielding the second highest vein coverage of all the samples studied (Table 3.2; Fig 3.3.). An intensive zone of weathering occurs around the melt veins where the iron staining is darker.

QUE 94214 (FIG. 3.4.)

The ANSMET weathering grade places QUE 94214 (Fig. 3.4.) as one of the most weathered samples in the study with little fracturing. This is confirmed through observation of iron staining that occurs across 80% of the rim sample, and 52% of the interior sample. The rim is one of the most highly rusted of all the samples. It has fusion crust covering one side with veins clustered immediately underneath, however, much of the original fusion crust has been removed by weathering. The cluster of veins under the outer edges is filled with shock melt and alteromorphs (dissociated from their primary source). Iron staining occurs around weathered metal and sulphide grains and stains all silicate minerals, more so pyroxene and olivine than feldspars. Many small vesicles are in and just below the fusion crust. Melt veins were present in the chips of the samples, but

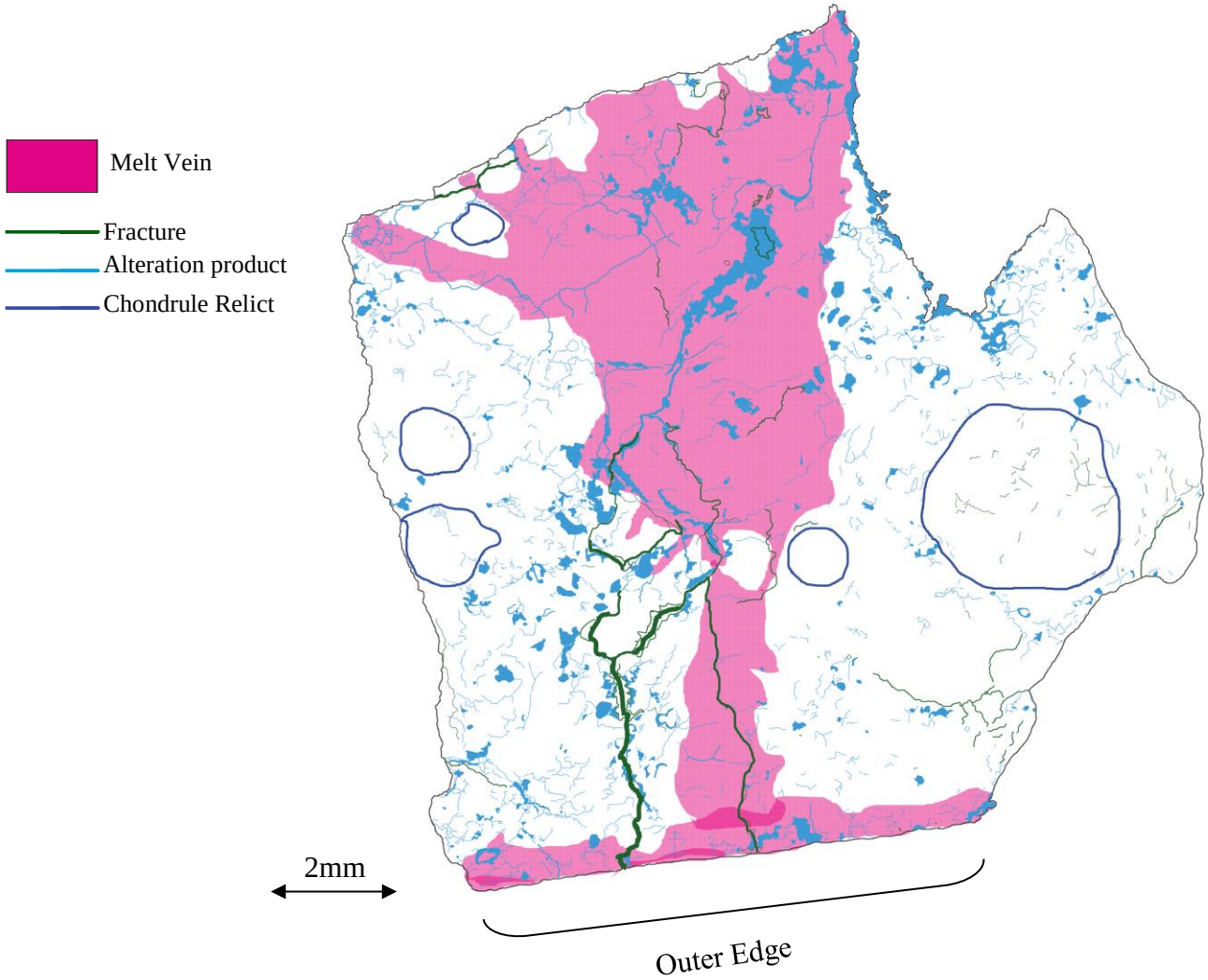

Fig. 3.2. Overview map of QUE 99022 rim thin section. Impact melt veins cover a large part of the sample. Large fractures from the outer edge travel through the melt veins. Rust prevails across the whole sample and so is not marked. A large barred chondrule covers a metal free patch on the right side.

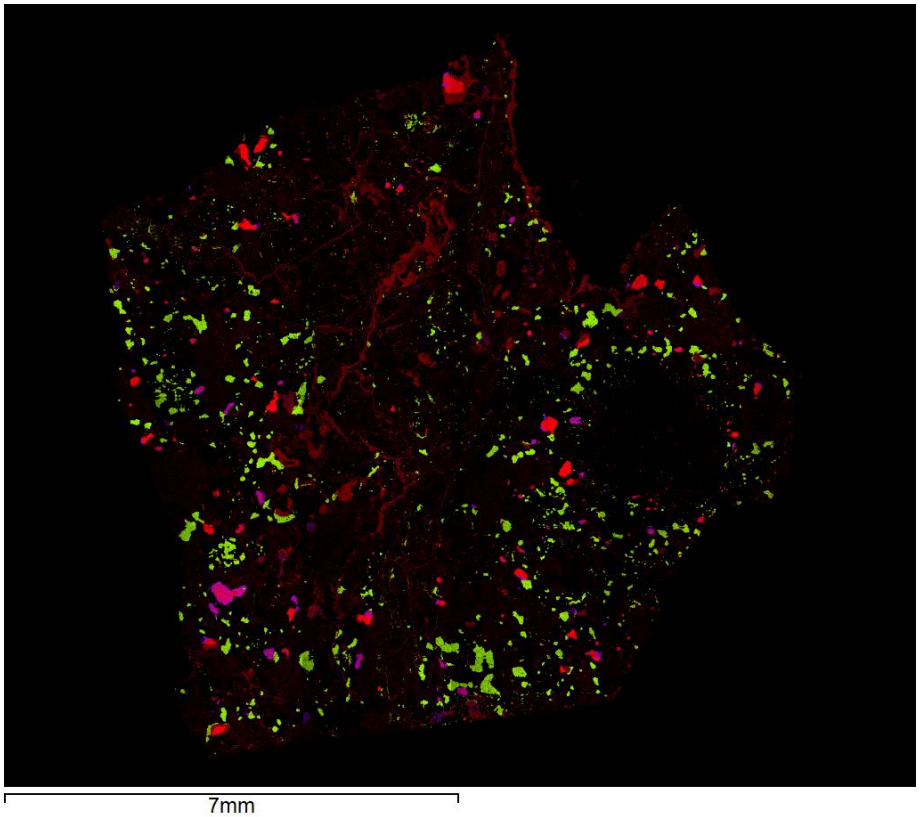

Fig. 3.3. Fe-S-Ni map of QUE 99022 rim thin section. Red—iron, green—sulphur, blue—nickel. The map shows the three opaque minerals in the sample, kamacite (bright red), taenite (purple) and troilite (green). The dull red areas are Fe-oxyhydroxides. There is an absence of kamacite, taenite and troilite around the melt vein due to them being melted into spherules then removed by weathering, evidenced by scraps of remnant parent material in some of the spherical grains of alteration product (section 3.2.5.).

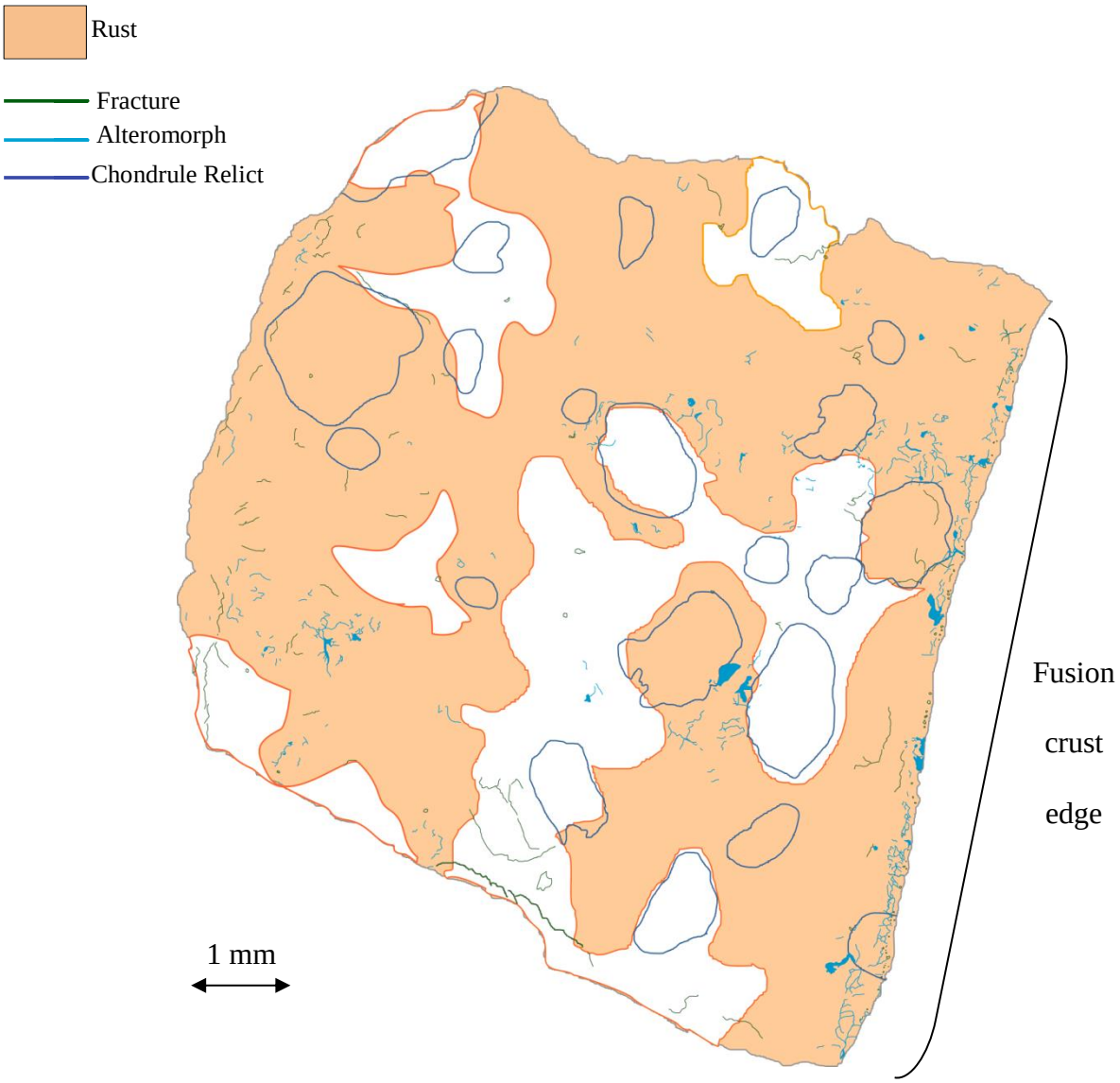

Fig. 3.4. Overview map of QUE 94214 rim section. Rust cover most of the sample, subsurface veins beneath the fusion crust are sulphide melt veins, those further in are alteromorphs. The rust diverts around silicate dominated chondrules.

not in the thin sections used for the petrography.

ALH 78130 (FIG. 3.5.)

Visible rust covers ~60% of the rim sample of ALH 78130 (Fig. 3.5.), following the fusion crust and some localised areas of rust around metals and sulphides. The ANSMET weathering designation is the same as QUE 94214 (B/C) and so it is one of the more weathered samples, but with a higher fracture grade than QUE 94214 (B). 70 % of the

fusion crust is accompanied by an optically dense black rim (~2 mm) of melt veins. The interior sample is 100 % covered in rust and is significantly more weathered than the rim. Melt veins cover a large part of the interior section whilst none are present in the rim section. Most of the Fe-Ni metals in the interior have been altered to Fe-oxyhydroxides. The alteration product vein coverage in the interior sample is the highest of any sample at 89 % coverage.

ALH 84056 (FIG. 3.6.)

The ANSMET weathering designation of ALH 84056 (Be; Fig. 3.6.) suggests that this is one of the lesser weathered meteorites and contains evaporites. Evaporites were not preserved in thin or thick section, and iron staining in the rim section is extensive at 73 %; however the interior has the lowest rust coverage of all the meteorites at 13 %. The vein coverage of the sample suggests that the rim is actually one of the more weathered samples, with 28 % vein coverage and the interior is the least weathered meteorite with only 5 % vein coverage. The interior of ALH 84056 has the lowest amount of alteration of the most weatherable phases (kamacite and taenite; Table 3.2) compared to the other meteorites. The amount of sulphide alteration is low, but not the lowest of all meteorites. The rim has a fairly high amount of kamacite alteration (15.2 %; Table 3.2) compared to the interior (9.58 %). Fusion crust is preserved along the full length of the rim sample. The internal sample is bisected by a melt vein and the section is dominated by a single large (6 mm width) cryptocrystalline chondrule which comprises a third of the section.

ALH 84058 (FIG. 3.7.)

The ANSMET designation of ALH 84058 (B) (Fig. 3.7.) gives it an intermediate weathering grade. The rim and interior have similar amounts of alteration with a small difference in rust coverage and amounts of altered metals and sulphides (see table 3.2). Rust covers 40 % of the rim and 35 % of the interior and vein coverage is in a middling range (19 % rim, 11 % interior). In the rim, the rust follows

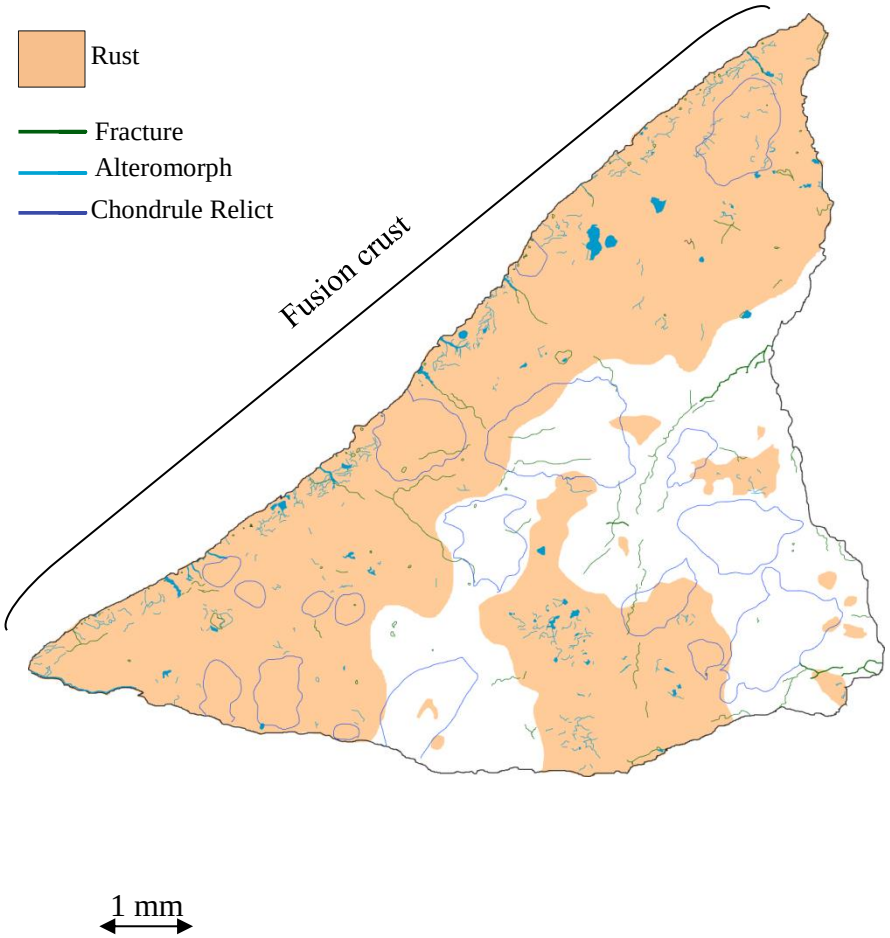

Fig. 3.5. Overview map of ALH 78130 rim section. Patches of rust are formed by clusters of alteration veins.

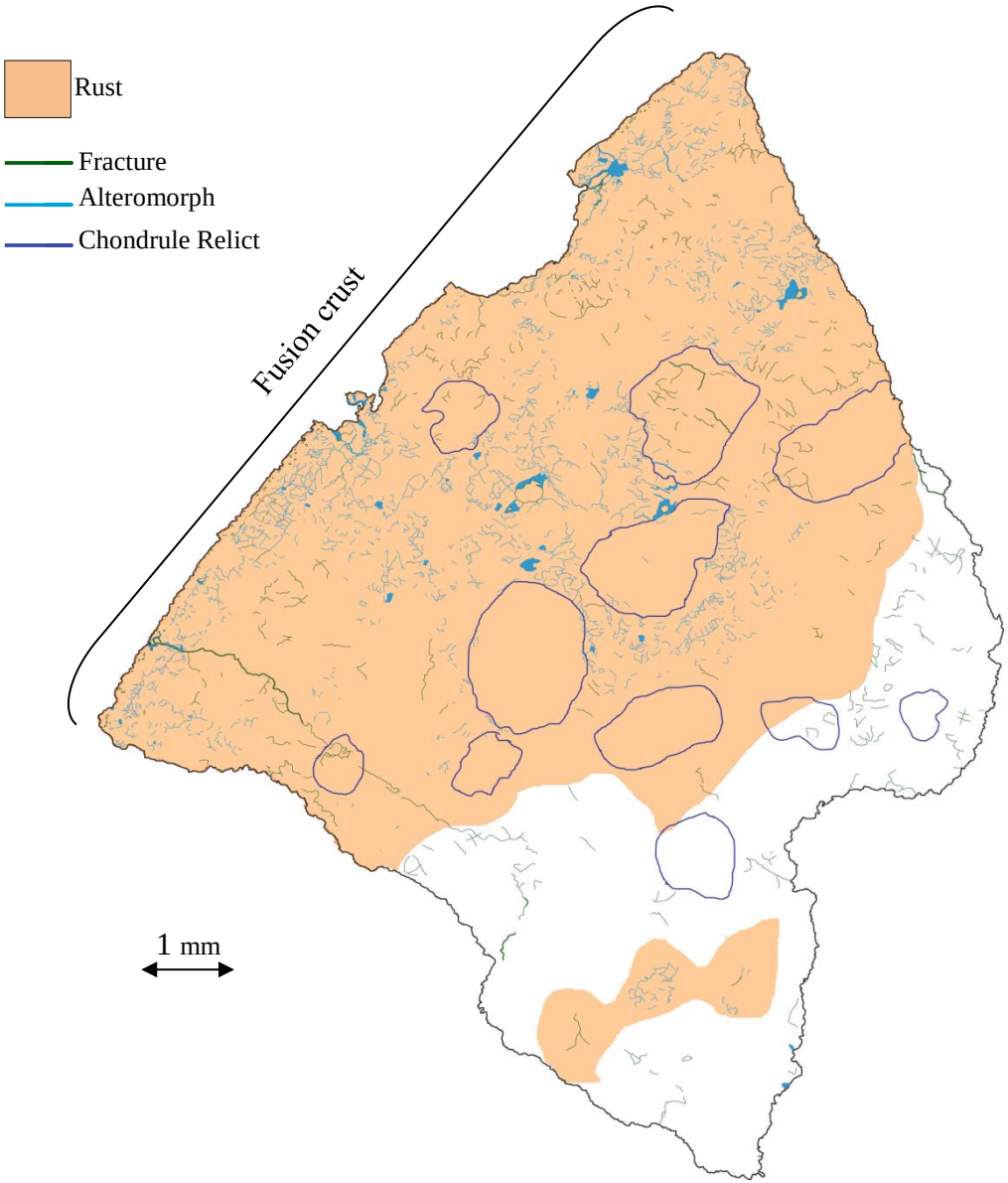

Fig. 3.6. Overview map of ALH 84056 rim. Clusters of veins almost always form outside the chondrule relicts.

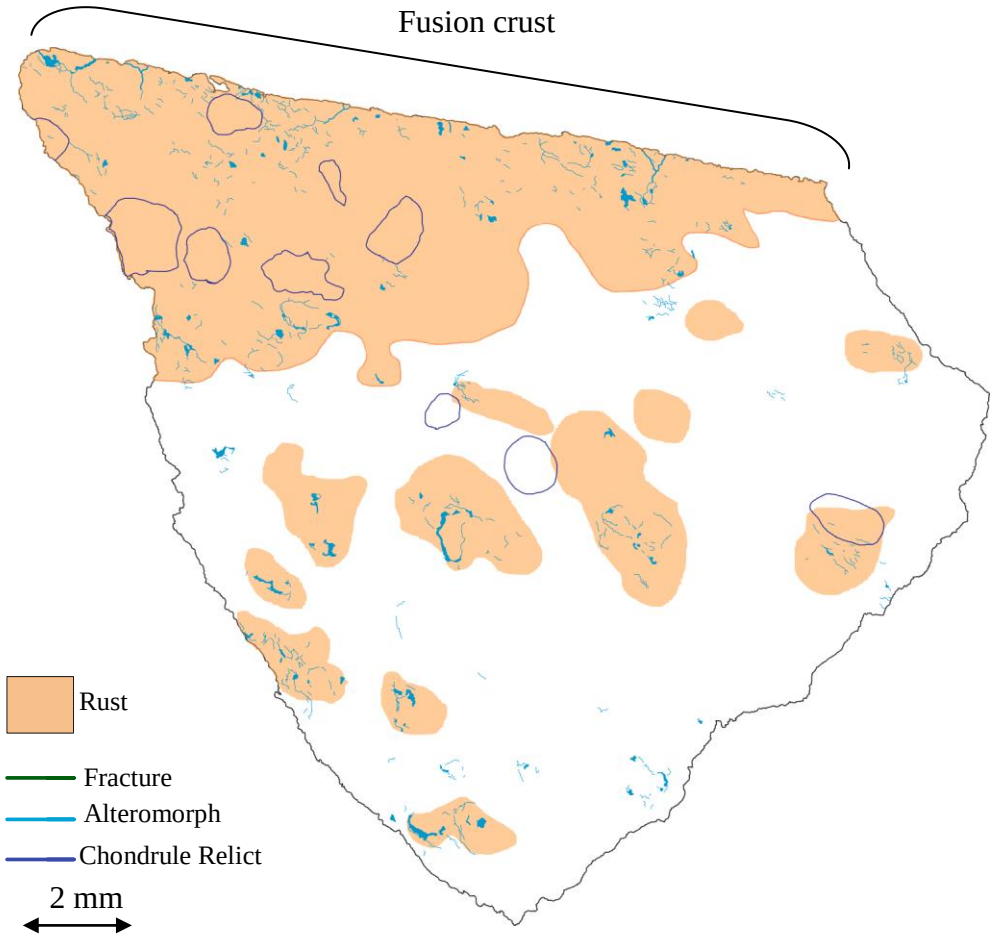

Fig. 3.7. Overview map of ALH 84058 thin section. Rust patches correlate with clusters of secondary veins.

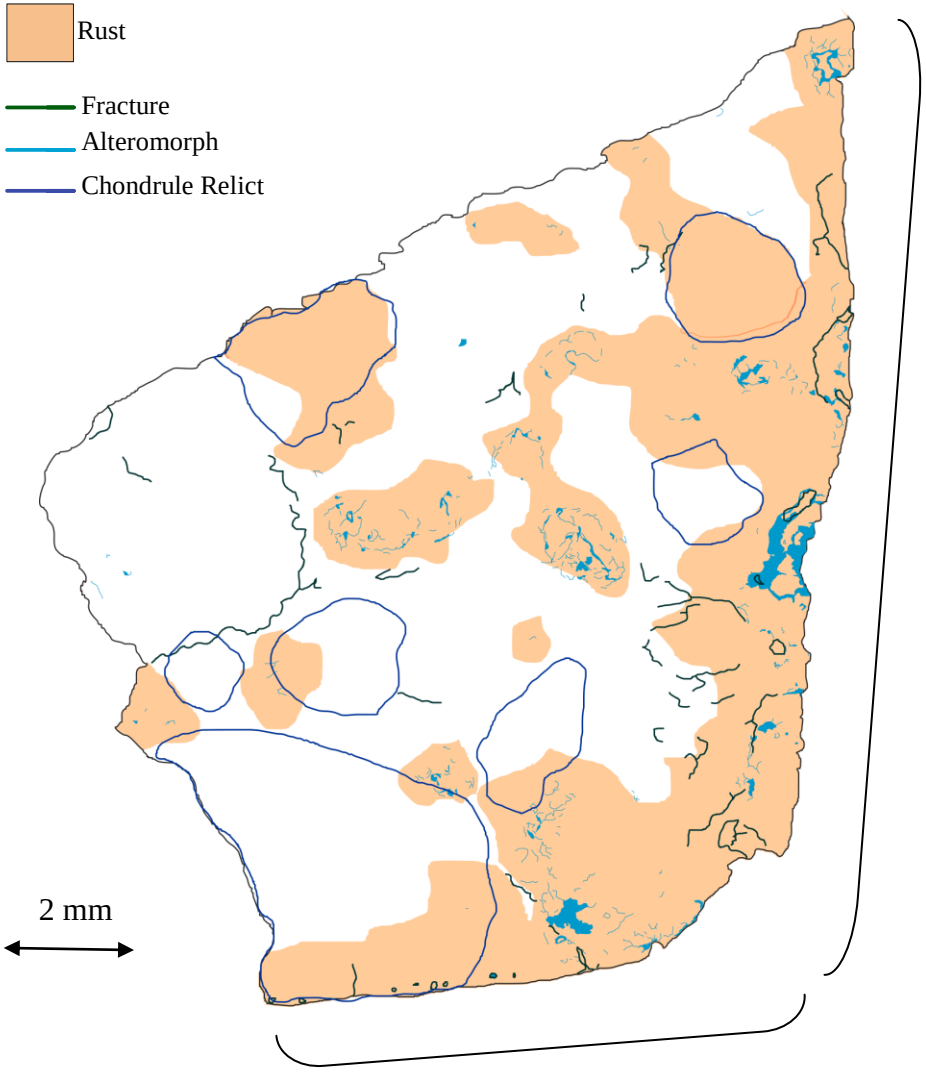

Fig. 3.8. Overview map of ALH 85017 rim thick section. Fusion crust covers a large part of the sample and some large patches of extensive alteration occur near the edge. A large silicate cryptocrystalline chondrule relict covers the bottom left side of the sample.

altering metal grains and fusion crust. No melt veins were observed in the samples. Fusion crust is present across the full length of exposed outer edge.

ALH 85017 (FIG. 3.8)

The ANSMET weathering designation of ALH 85017 (A) (Fig. 3.8.) puts it as the least weathered sample, but the vein coverage and rust coverage of both rim and interior are not the lowest values compared to the other meteorites investigated here and suggest that ALH 85017 is a moderately weathered meteorite. The rim section shows heavy oxidation of kamacite and moderate taenite alteration. Rust covers 46 % of the rim and 36 % of the interior. The thin section for ALH 85017 R was only used for EMPA analysis in suitable areas and not for petrological observations as the thin section was too thin and so lost much of the original textures. Because of this problem, only the thick section was utilised for petrological characterisation and so the alteration percentages of the rim section may be biased (see discussion in Section 3.8).

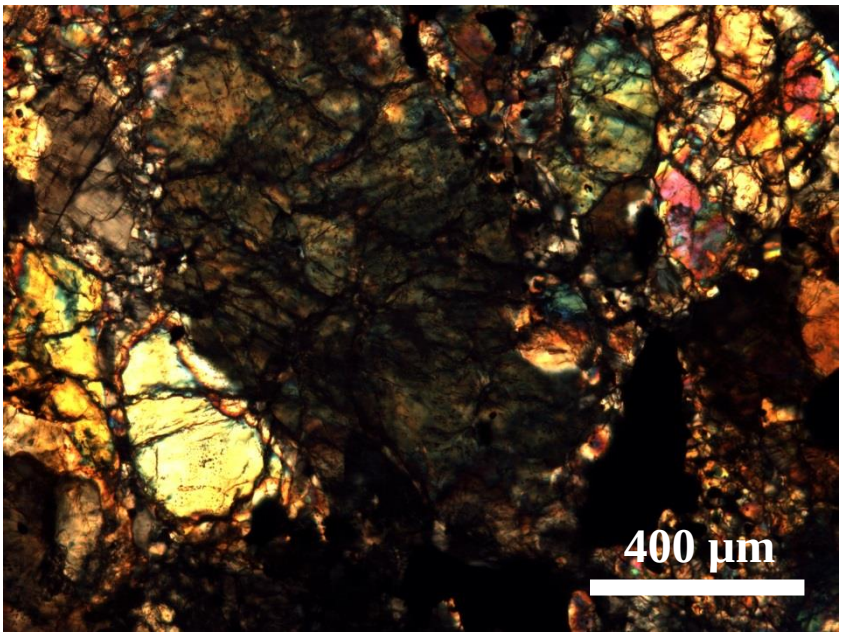

Fig. 3.9. Cross polarised light photograph of QUE 94214 R thin section displaying mosaic extinction of olivine.

3.2. MINERALOGY

3.2.1. OLIVINE: 33-47% ABUNDANCE

Habit and Occurrence:

In all samples, the olivine is mostly euhedral and occurs as small crystals (10 μm) up to large porphyroblasts (500 μm). Olivine is the silicate mineral that is most commonly stained with rust, and in transmitted light, rusted areas range from yellow to orange dependent on the proximity to altering metal grains and melt veins, with more intense staining proximal to both. All of the meteorites either exhibit mosaicised or undulose extinction of olivine, which defines their shock grade (Fig 3.9; Table 3.3; Section **3.7)**. No olivines show compositional zoning or textural evidence of disequilibrium with their surroundings (e.g., re-absorption of xenocrysts etc.).

Many olivine crystals contain inclusions of plagioclase < 30 μm and/or small metal and chromite grains < 20 μm which often follow planar structures. Small metal inclusions are most common in ALH 78130 and trace linear paths through the olivine crystals.

The fractures in olivine crystals come in three forms, i) intermineral fractures surrounding the crystal, ii) irregular large transmineral fractures cutting across many crystals and iii) regular planar fractures within single grains. All samples exhibit these fracture patterns. Some of the regular planar fractures near the outer edges of the meteorites are joined up and make a more irregular pattern.

Most olivine crystals contain regular planar fractures through planes of crystallographic weaknesses (Chen et al. 2006) and almost all have irregular transmineral fractures dross cutting the crystal, with larger olivine crystals having a greater density of fractures than the smaller crystals. They concentrate most of the fractures in the sample, reflecting the brittle nature of olivine. In QUE 94214, some olivine fragments occur in maskelynite, and have been rounded from peripheral melting.

There is a size dependency regarding the type of fracturing, with large olivines containing many transmineral and planar fractures and smaller (< 100 μm) olivines having intermineral fractures surrounding them.

Alteration Features:

Olivine alteration varies significantly between the different meteorites and the only sample in which olivine was not altered was the interior of ALH 84056. The most common type of alteration present in all other samples is dissolution along the margins of vein pathways. In QUE 99022, this is evidenced by sawtooth etching of olivine crystals. QUE 99022, one of the most altered samples, olivine has very few open fractures since most have been infilled with Fe-oxyhydroxides, with minor amounts of Si present. This minor addition of Si in the alteromorphs surrounding the olivine demonstrates that dissolution occurred. Around large veins, conical etching in the olivine is observed where small micro-cavities have formed (Fig. 3.10.). In the interior sample of ALH 78130, there is extensive dissolution of olivine around large veins where there are many embayments into olivine crystals (see Fig 3.11.). In the other four samples, only minor dissolution along vein edges is observed.

All samples also show some olivine dissolution adjacent to the fusion crust. In QUE 94214, it is also observed at the surface of the meteorite surrounding some of the larger veins. Silicates in the first 400 μm inwards from the surface of QUE 94214 are heavily weathered, there are pockets of clays and some olivine has been completely dissolved (with small fragments left behind), leaving cavities infilled with a mixture of undifferentiated silicates (Fig. 3.12.). Olivine alteration at the rim of ALH 78130 is minor and only visible at the edges of veins. ALH 84056 shows some slight dissolution of olivine within 200 μm of the fusion crust, ALH 84058 demonstrates a similar dissolution at the fusion crust, but also shows a preferential weathering in pockets of shock melted olivine, which have reformed to skeletal crystals.

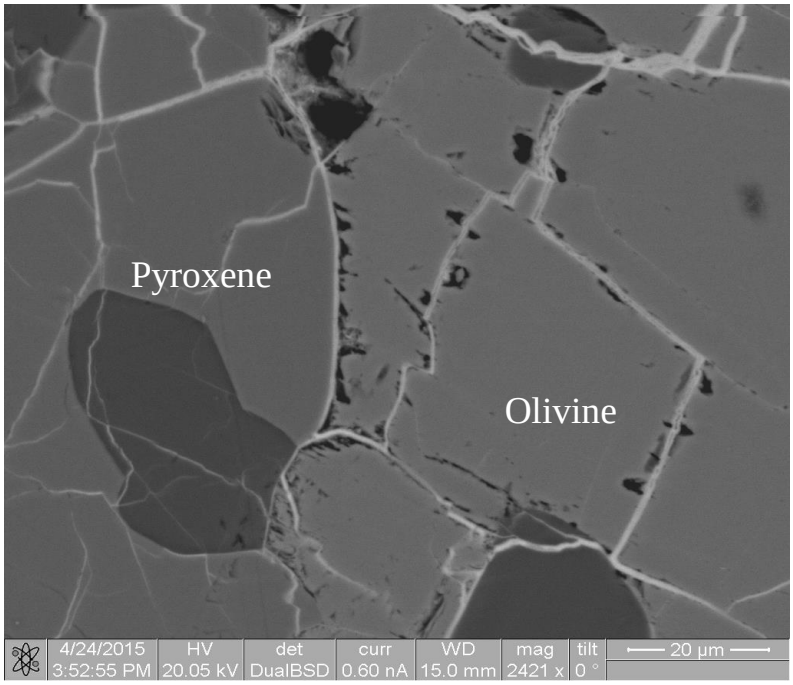

Fig. 3.10. QUE 99022 rim. BSE image of conical etch pits in olivine surrounding intermineral veins and transmineral veins. These pits are only present in olivine and not in adjacent pyroxene. The singular pits combine to make a sawtoothed edge.

Fig. 3.11. ALH 78130 interior. BSE image of a large vein with embayments in olivine at the margins. The alteration vein is due to deposits from solution and some detrital minerals from the surrounding walls that have been broken off. Small spherules < 0.5 µm of goethite/hematite have formed on the walls of the fracture. The alteration product itself is highly heterogeneous.

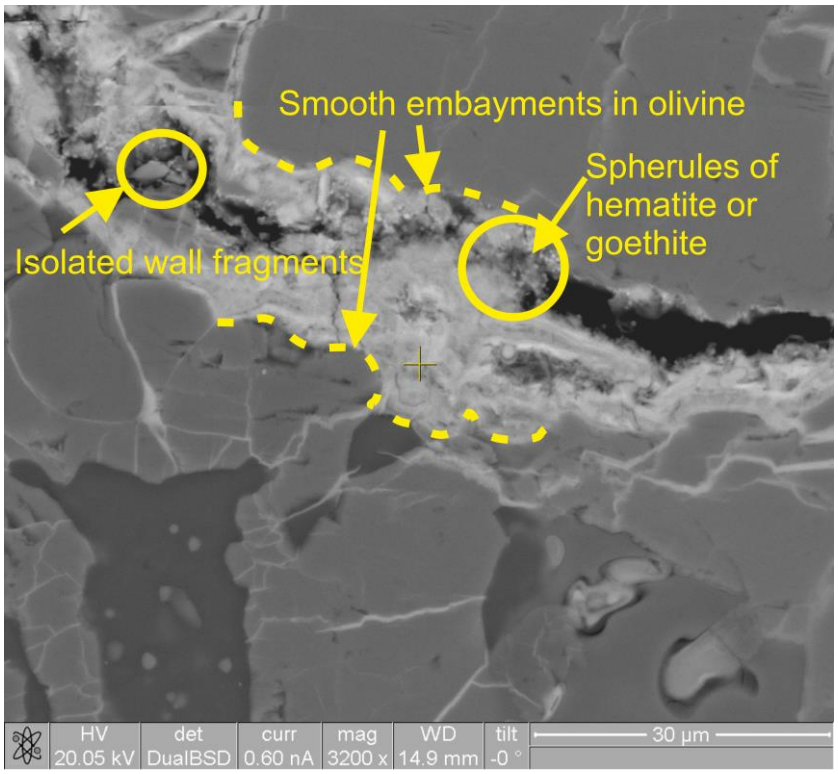

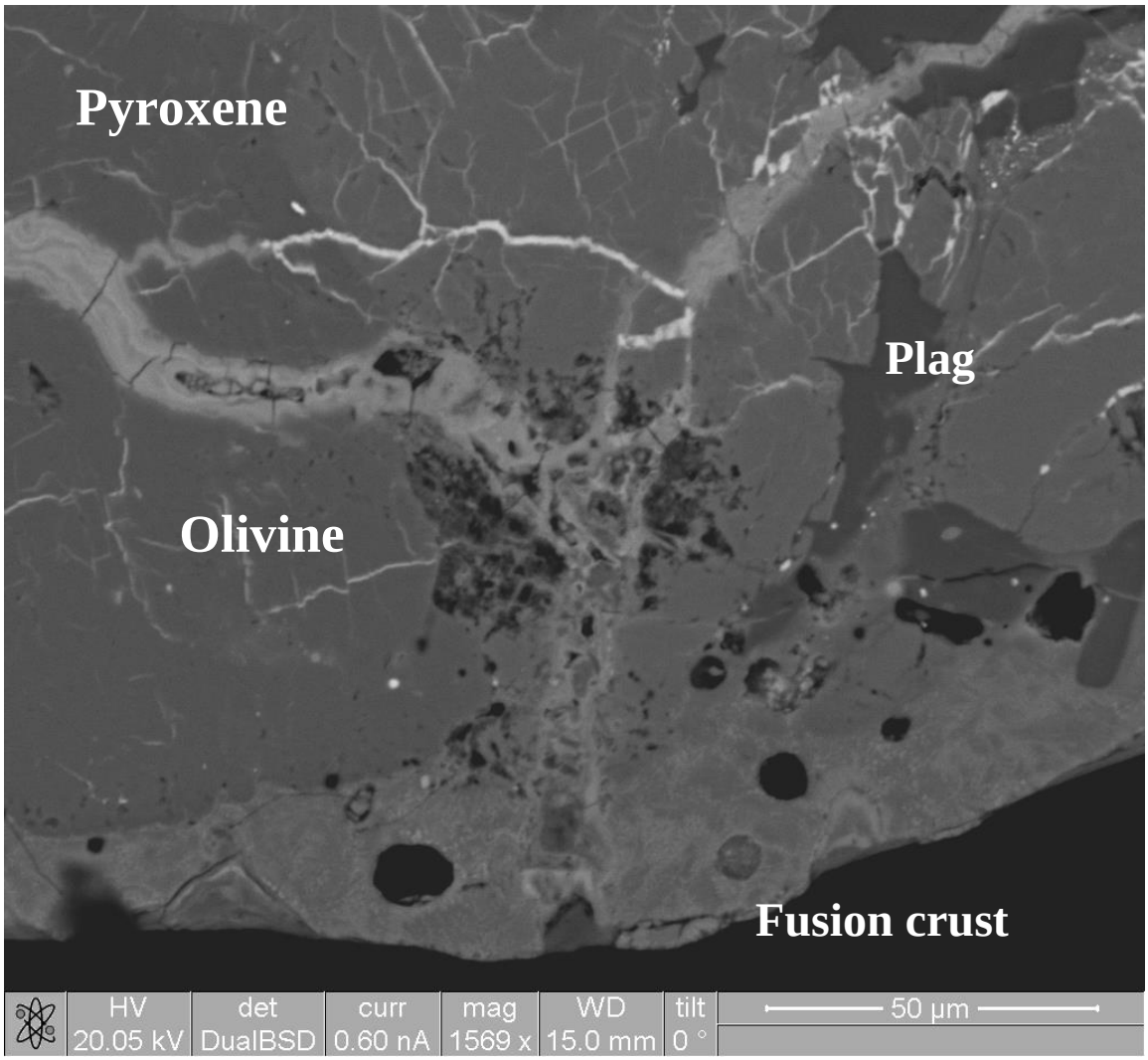

Fig. 3.12. BSE image of QUE 94214 rim. A large vein transects the fusion crust and surrounding the vein, the silicates are heavily pitted.

Olivine weathering at the rim of many meteorites is observed where there is direct contact with Antarctic varnish material (Fig 3.13.). This is especially apparent in ALH 84058 where pits have formed where there is olivine contacting with Antarctic varnish deposit (discussed further in Section 3.8). This type of weathering is observed in every meteorite that has Antarctic varnish (further discussion in **section 3.5.**).

A less common form of weathering occurs in the interior of QUE 94214 where the alteration of sulphides is driving the dissolution of olivine. Proximal to the altering sulphides, irregular-shaped pits are formed (Fig 3.14), without the conical form that is typical of olivine dissolution (Fig 1.4. in Section 1.4.3.).

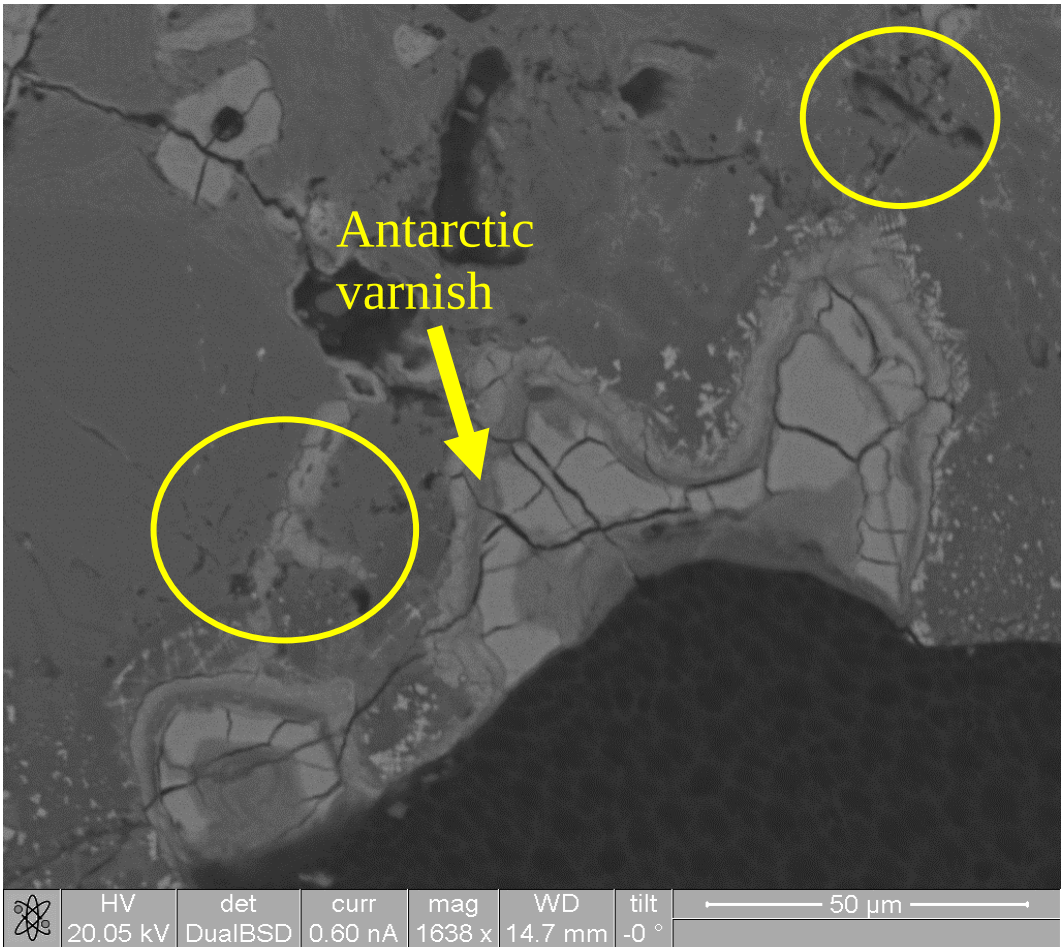

Fig. 3.13. ALH 84058 rim. BSE of Antarctic varnish, surrounded by pitting in olivine (circled).

Velbel and Barker 2008; Velbel and Losiak 2010). The individual pits coalesce into larger irregular pits of up to 10 µm across. The olivine surrounding the pits has a higher relative atomic weight compared to other surrounding olivines, as seen by colouration differences in BSE images. Size selection is apparent whereby larger crystals are more affected by pitting than smaller crystals.

A more minor case of sulphide driven olivine dissolution can be seen in ALH 78130 where etching is minor and consists of more regular conical pits in the interior sample of the meteorite, also in olivines proximal to sulphide grains. The importance of the proximity to weathering sulphides is compounded in the rim where the fusion crust network of sulphide veins has weathered and the surrounding olivine has been dissolved.

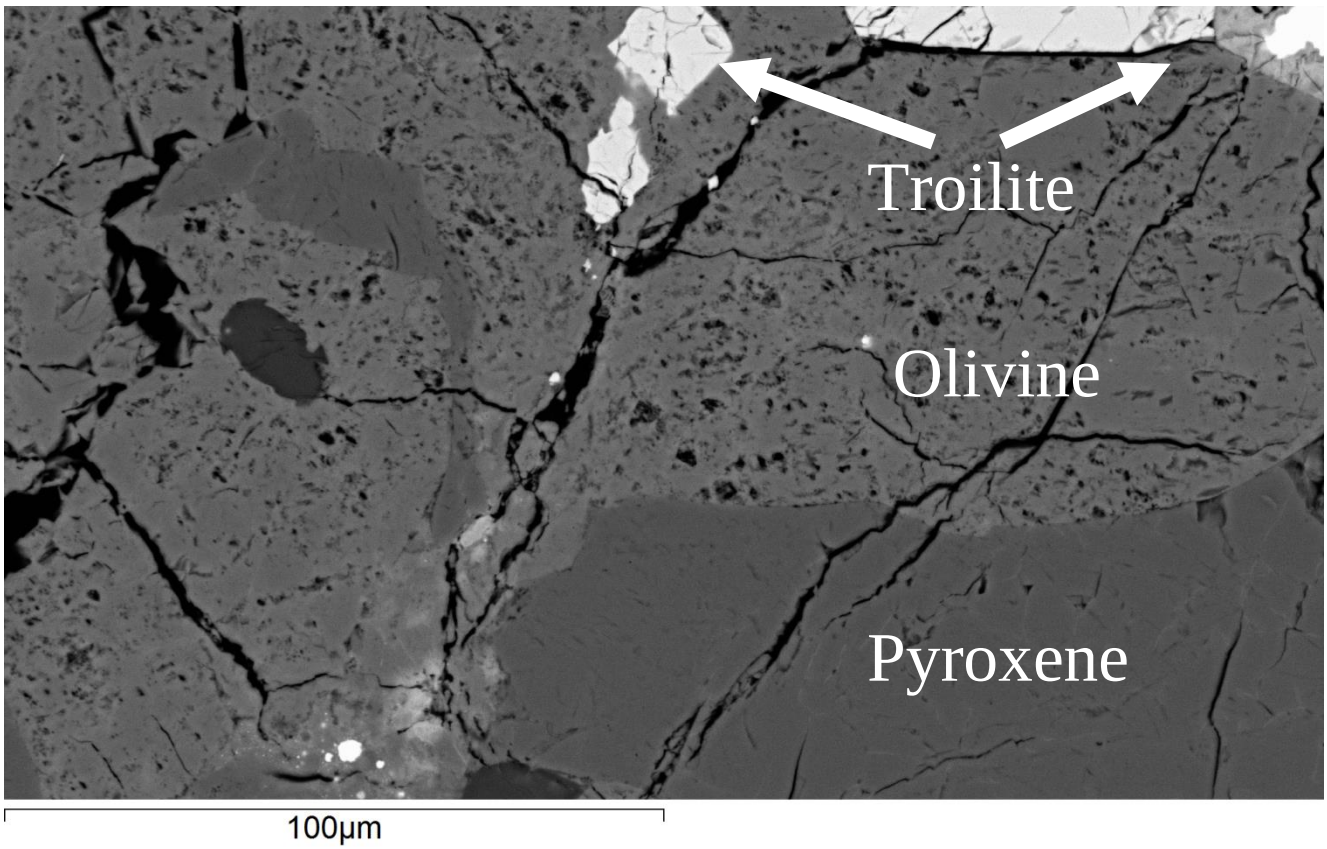

Fig. 3.14. QUE 94214 interior. BSE image of an olivine grain interfacing with a weathering troilite crystal which has extensive irregular dissolution pits.

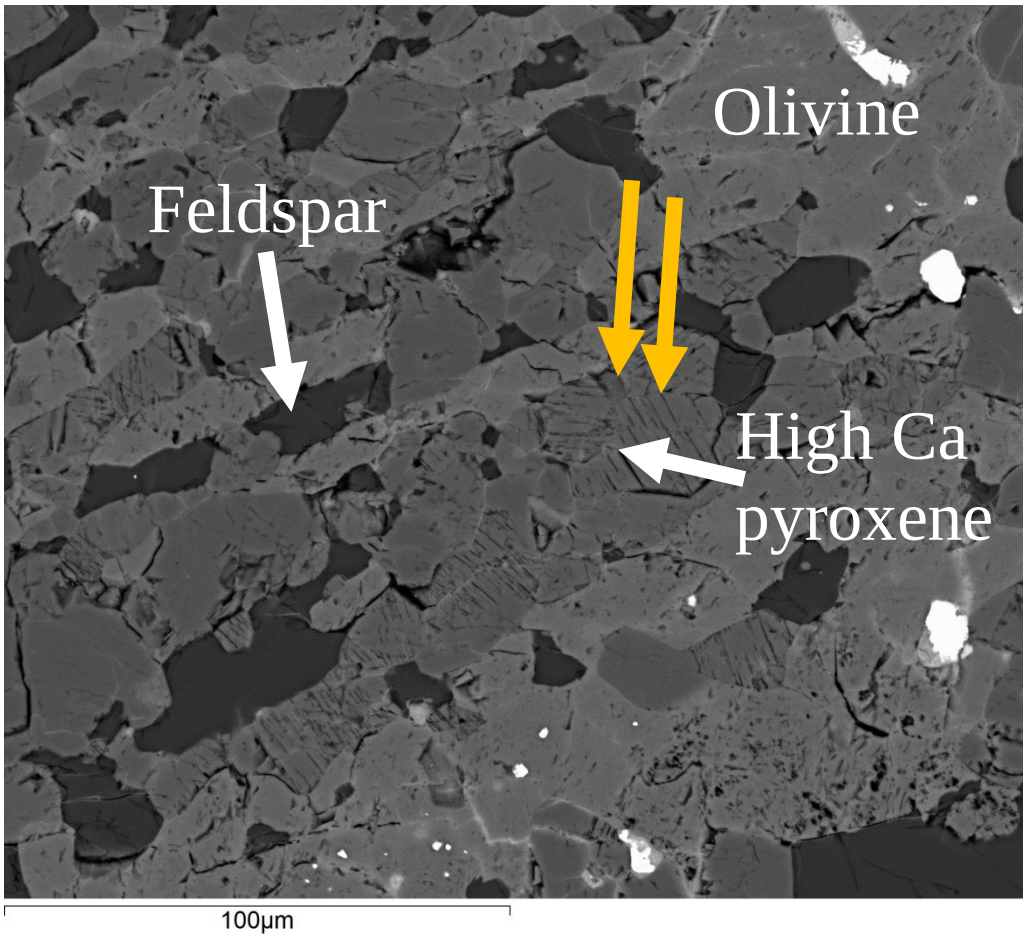

Fig. 3.15. QUE 94214 interior. BSE image of parallel pyroxene lamella etching near a weathered troilite. Yellow arrows point to the laminar etching in the pyroxene. White arrows are used to indicate mineral phases.

3.2.2. PYROXENE: 26-41 % ABUNDANCE

Habit and Occurrence:

All samples have a range of pyroxene crystal sizes from cryptocrystalline intergrowths with plagioclase, to larger porphyritic crystals, with the largest crystals being in ALH 84056 (1 mm). The other meteorites have pyroxenes of up to 500 μm in size. In all samples, all pyroxenes are subhedral. Intergrowths of cryptocrystalline pyroxene with plagioclase often occur as part of chondrule relicts and these patches frequently have intra-mineral fractures around the grains, but rarely exhibit trans-mineral fractures.

Large pyroxene grains host, proportionally, more inclusions than olivine crystals. The inclusions are mostly metal grains, chromite grains, phosphates and plagioclase, and usually follow lines of crystallographic weakness such as cleavage planes. Pyroxene crystals host fewer transmineral fractures than olivine crystals, the fractures in pyroxene crystals are less continuous than in olivine crystals and many fractures are not linearly extensive and do not connect with the outer edge of the crystals. The lower abundance of initial fractures results in fewer veins cross cutting pyroxene grains.

Alteration Features:

The dominant form of alteration in pyroxene crystals is minor dissolution at the margins of transmineral veins. Intermineral veins are, in general, narrower and appear less corrosive (e.g., Fig. 3.10). Meteorites, in which transmineral dissolution is the only form of pyroxene alteration, are: QUE 99022, ALH 84056 and ALH 85017. Alteration is almost completely absent from ALH 84056 with very few veins showing evidence of dissolution, and the veins are proximal to the metal grains.

In QUE 94214 there is clear stripping of material along cleavage planes in pyroxene adjacent to weathered sulphides, resulting in parallel weathered surfaces in each crystal (Fig. 3.15.). The pyroxene that is mostly affected is the smaller, high Ca diopside crystals

that are included in chondrule relicts. They have fewer veins through them than olivines, but small veinlets penetrate most of the crystals. Laminar stripping along cleavage planes rarely occurs in ALH 78130 and where it does it is adjacent to large transmineral veins.

Weathering for pyroxenes in contact with Antarctic varnish is apparent in ALH 84058 and ALH 84056 where there is minor pitting adjacent to deposits but this is far less extensive than for olivine. Pyroxene crystals at the rim of the meteorites are altered where melt veins of sulphide have been weathered (see Section 3.2.4.). This can be seen in ALH 84056 and ALH 84058.

Pyroxene appears to be less susceptible to weathering than olivine, as demonstrated where adjacent crystals on contact with the same veins exhibit a greater dissolution of olivine than of pyroxene (Fig 3.10.).

3.2.3. PLAGIOCLASE: 6-28 % ABUNDANCE

Habit and Occurrence:

Most plagioclase occurs as small interstitials crystals (around 10–20 μm), and less commonly in crystals of up to 200 μm, and are generally found in chondrule relicts, in fine grained intergrowths with pyroxene and olivine (Fig. 3.16. A).

In some samples plagioclase has been transformed to maskelynite: QUE 94214 (100 %), ALH 78130 (60 %), ALH 84056 (80 % in the rim, 40 % in the interior), QUE 99022, ALH 84058 and ALH 85017 (no maskelynite present). This was identified through optical microscopy. Where maskelynite occurs it is often surrounded by radial fractures surrounding the crystals (Fig. 3.16. B), especially in olivine than pyroxene and metal and sulphides containing few or no fractures.

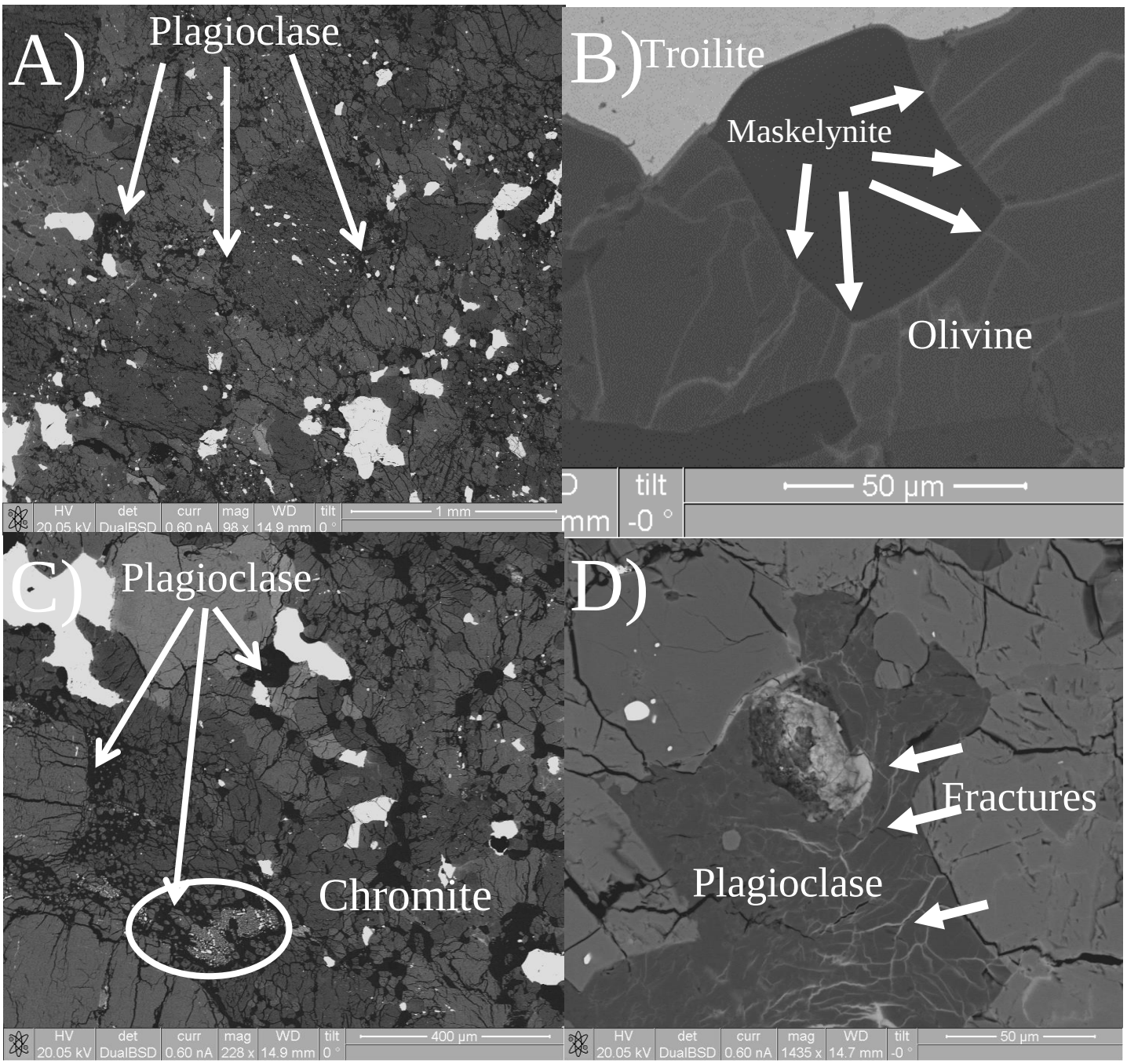

Fig. 3.16. BSE images of common features in plagioclase and maskelynite. A) ALH 84058 thin section with interstitial plagioclase. Plagioclase is the darkest phase in the sample, and several of the small crystals have been marked by arrows. Very few large grains of plagioclase exist, most are small (< 50 µm) crystals. B) QUE 94214 maskelynite crystal with radial fractures and an intra-mineral fracture surrounding it and none travelling through it. These fractures have been infilled by alteromorphs from the adjacent altering troilite. C) QUE 94214 maskelynite with many rounded inclusions and chromite. D) QUE 99022 plagioclase with many fractures throughout. Most have been infilled with alteromorph.

In QUE 94214 the patches of maskelynite often host rounded inclusions of other silicates (Fig. 3.16. C) and in some cases there are patches of chromite that form clusters of small (< 5 μm) subhedral and euhedral crystals known as chromite-plagioclase assemblages (Rubin 2003). These occur in all of the meteorites except ALH 84056, described in greater detail in the chromite Section **3.1.7**.

Fracture patterns across plagioclase and maskelynite are notably different. In plagioclase they are small transmineral fractures (< 2 μm) that are common, although rarely linearly extensive, with the fractures usually beginning and terminating in the interior of the crystal and not extending to the outer edges (Fig. 3.16. D). They form en-echelon patterns and so are assumed to be due to mechanical stresses. Fractures in maskelynite are rare and when they occur, they are large transmineral fractures, wider than 5 μm, and extend through adjacent crystals.

Alteration Features:

There is a clear distinction in alteration patterns in plagioclase and maskelynite. Because of the general absence of fractures in maskelynite, few veins penetrate the grains whereas there are many small veins in untransformed plagioclase with limited dissolution along vein edges. However, there is evidence for dissolution in surrounding alteromorphs evidenced by elevated Al signals determined by EDS analysis.

Both maskelynite and plagioclase are surrounded by intermineral veins where there are vein clusters. The radial fractures due to maskelynite formation are often infilled, however, as these fractures penetrate different minerals, they do not affect the alteration of the maskelynite. The resilience of maskelynite to alteration is demonstrated in grains of kamacite and taenite that have been totally altered in ALH 78130 and where inclusions of maskelynite remain in pockets of alteromorphs after the parent metal grain has completely weathered out.

3.2.4. TROILITE: 2.7-8.5 % ABUNDANCE

Habit and Occurrence:

Troilite occurs in all samples as very small crystals or between 2 µm - 800 µm in length. It has the most diverse range of textures of all the minerals present in the meteorites and is susceptible to restructuring by shock, and several shock-related textures appear in different meteorites (Fig 3.17). Troilite is more susceptible to localised melting than other opaques present (Bennett and McSween 1996) because it is more compressible than Fe-Ni metal, is a poor conductor of heat and has a comparatively low melting point. Seven Troilite textures are observed:

1) **No internal structures, homogenous**: This type of troilite surrounds chondrule relicts and occurs as large interstitial crystals that are all anhedral in shape and rarely occur in chondrule relicts (Fig. 3.17. A).
2) **Melt spherules**: In samples where melt veins are present (QUE 99022, ALH 78130, QUE 94214, ALH 84056) troilite melt spherules are a major constituent, never exceeding 5 µm in length (Fig. 3.17. B).
3) **Fusion crust substrate:** Veins of sulphide melt occur beneath the fusion crust of ALH 85017, ALH 78130, ALH 84056 and QUE 94214. It is not continuous along the fusion crust, but is localised to areas where sulphides were present near the fusion crust on entry to the Earth's atmosphere (Fig. 3.17. C).
4) **Swiss cheese texture (as described in Bennett and McSween 1996):** Localised melting can result in a bubbly texture on the margins of troilite grains and occurs in rare grains of ALH 84056 (Fig. 3.17. D). This is a texture that is so far only known to occur in troilite.

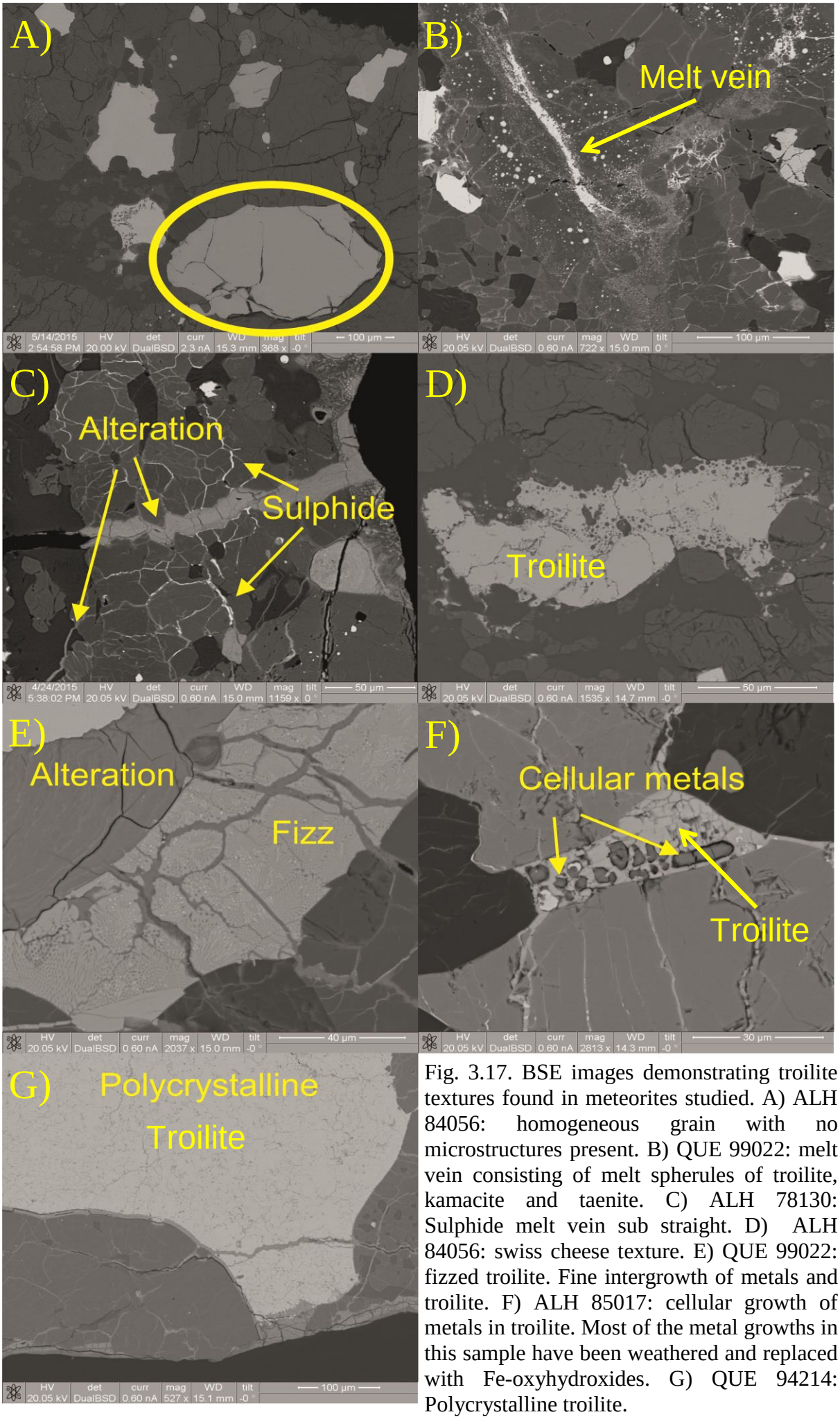

Fig. 3.17. BSE images demonstrating troilite textures found in meteorites studied. A) ALH 84056: homogeneous grain with no microstructures present. B) QUE 99022: melt vein consisting of melt spherules of troilite, kamacite and taenite. C) ALH 78130: Sulphide melt vein sub straight. D) ALH 84056: swiss cheese texture. E) QUE 99022: fizzed troilite. Fine intergrowth of metals and troilite. F) ALH 85017: cellular growth of metals in troilite. Most of the metal growths in this sample have been weathered and replaced with Fe-oxyhydroxides. G) QUE 94214: Polycrystalline troilite.

5) **Fizzed troilite:** Fizzed troilite occurs in QUE 99022, ALH 85017 and in some rare grains in ALH 84056. It is a mix of Fe-Ni metal and troilite and the Fe-Ni blebs occur as tiny (sub µm) inclusions in the main mass of troilite. This is a shock feature caused by temperature excursions between 100-600 °C (Bennett and McSween 1996) and commonly occurs at the contact between troilite and kamacite/taenite metal. Fizzed troilite fills well defined, discrete areas at points where sulphides and metal grains are in contact, with the exception of one area of QUE 99022 where the fizz mixture follows polygonal fractures in a troilite crystal (Fig. 3.17. E).
6) **Cellular growth:** In ALH 85017 there is a subtle variation on the fizz texture whereas a cellular growth of Fe-Ni metals is present, indicating a different cooling history. The cellular growth has cells of metal from 5-10 µm long and size of cell has been correlated with cooling rates by Scott (1982; Fig. 3.17. F).
7) **Polycrystalline troilite:** Polycrystalline troilite is observed in QUE 94214 and ALH 78130 covering large crystals (> 50 µm). This texture comprises of many irregular intersecting fractures and imperfections across the crystals with no regular angle of intersection between them. The troilite has been plastically deformed in several places, embaying into fractures in an echinoidal fashion. In ALH 78130 the polycrystalline texture is less well developed and less extensive than in QUE 94214, with fewer fractures and defects (Fig. 3.17. G).

Alteration features:

The varieties of texture create susceptibilities to weathering and weathering patterns, (Fig. 3.18) in the different types of troilite, and so are discussed in turn.

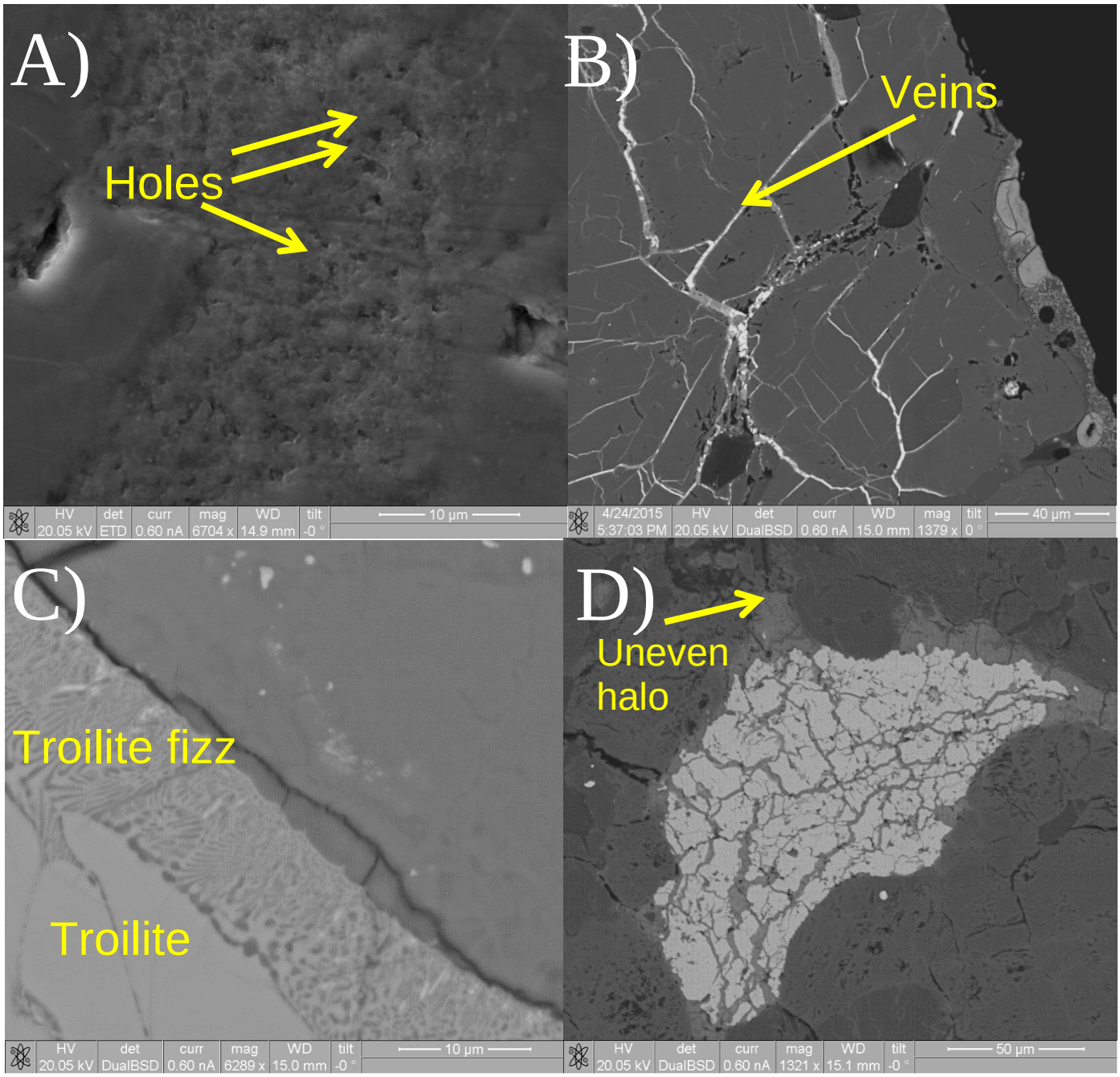

Fig. 3.18. Alteration patterns of troilite textures. A) ALH 78130 SEI image. Melt vein with few remaining troilite or metal grains. The removal of the opaque grains has resulted in a porous texture of silicates. B) ALH 78130 BSE image. Subsurface network of sulphide melt veins are altering to Fe-oxyhydroxides and silicate pitting surrounding the veins is evident. C) QUE 99022 BSE image. Troilite fizz where the metal has been preferentially weathered out leaving more surfaces of the troilite crystal to be altered along. D) QUE 94214 BSE image. Polycrystalline troilite grain that has been heavily altered. The troilite grain has veins cross cutting the whole grain and an uneven halo of alteration products. Silicate pitting is adjacent.

1) **No internal structures, homogenous:** Regular crystals of troilite with no shock modified textures, (e.g. ALH 84058, QUE 99022, ALH 84056), weather centripetally with haloes of Fe-oxyhydroxides surrounding the original sulphide grains. These alteromorphs contain little S. Alteration occurs along straight veins which penetrate the troilite and widen with the dissolution of the parent mineral. The dissolution is seen in the ragged edges of veins through the troilite.
2) **Melt spherules:** Melt spherules of troilite in the melt veins are present in QUE 99022, QUE 94214, ALH 78130 and ALH 84056 and are preferentially altered over larger crystals. The smaller spherules have a much increased surface area to volume ratio resulting in their quicker alteration, as there are more fresh surfaces for altering fluids to oxidise them. In ALH 78130 the melt veins contain no metal or sulphide grains (Fig. 3.18. A) and instead have empty spherule-shaped holes. These are assumed to have been grains that have been entirely weathered out with no subsequent deposition of alteromorph.
3) **Fusion crust substrate:** This is vulnerable to weathering because of its increased surface area compared to coherent grains of sulphide, and many have been replaced with veins of Fe-oxyhydroxides. Around these weathered veins are often pitted silicates (Fig. 3.18. B). In QUE 99022, there are no subsurface sulphide veins and instead there are alteration veins, suggesting that sulphide veins have been completely replaced.
4) **Swiss cheese texture:** This is not observed, probably because of the rare nature of this texture rather than it being more resistant to weathering.
5) **Fizzed troilite:** The areas of fizzed troilite have thicker alteration haloes than the homogenous crystals and the small metal inclusions can, in some places, be weathered out, leaving behind Fe-oxyhydroxides in the holes (Fig. 3.18. C). They are preferentially altered over homogenous crystals.

6) **Cellular growth:** This weathering pattern is the same as in fizzed troilite, with the cellular metal growths preferentially weathered out and leaving behind a porous troilite that has a larger surface area that is more vulnerable to oxidation and hydration.
7) **Polycrystalline troilite:** The fractures and imperfections that are in this type of troilite crystal have been widened and exploited by the subsequent incursion of fluids, resulting in ubiquitous veins of alteromorph. The troilite does not alter centripetally, but alters in an irregular pellicular fashion combined with an irregular digitate pattern, along the imperfections of the crystals (Fig 3.1; Fig. 3.18. D). The veins widen, as weathering persists, until the original troilite is completely replaced. A halo of weathering products is also formed, with a width similar to the veins that penetrate the crystals. The dissolution of troilite progresses along the veins that surround and penetrate it. In QUE 94214 alteration of troilite in the rim is proportionately less than in the interior section when compared to the other weathering minerals (Table 3.2).

3.2.5. KAMACITE: 0.9-5.4 % ABUNDANCE

Habit and Occurrence:

Kamacite occurs in four textures and is always closely associated with taenite, and thus some of the textures described below apply to both. On average kamacite crystals are larger than taenite crystals.

1) **Homogenous grains:** Homogenous grains of kamacite are present in all samples and are the dominant form in QUE 99022, QUE 94214 and ALH 85017, ranging in size from sub µm to 800 µm. Small crystals (<2 µm) are often included in cryptocrystalline chondrule relicts whilst larger crystals are usually interstitial.
2) **Plessite:** Pearlitic plessite intergrowths occur in ALH 84056 and ALH 84058 and are the dominant form of kamacite in these samples. Plessite structures are fine

grained intergrowths of kamacite and taenite, formed from the decomposition of taenite, which vary in crystal size (Fig. 3.19.; Bennett and McSween 1996).

3) **Hexagonal polycrystalline agglomerates:** This is an intergrowth in which tessellating hexagonal grains of taenite are surrounded by thin films of kamacite; here observed in ALH 78130, ALH 84056 and ALH 84058.

4) **Melt spherules:** Kamacite is part of the melt veins in ALH 78130 and ALH 84056 and occur in the same habit as troilite melt spheres. They are absent from the melt veins in the rim sample of QUE 99022.

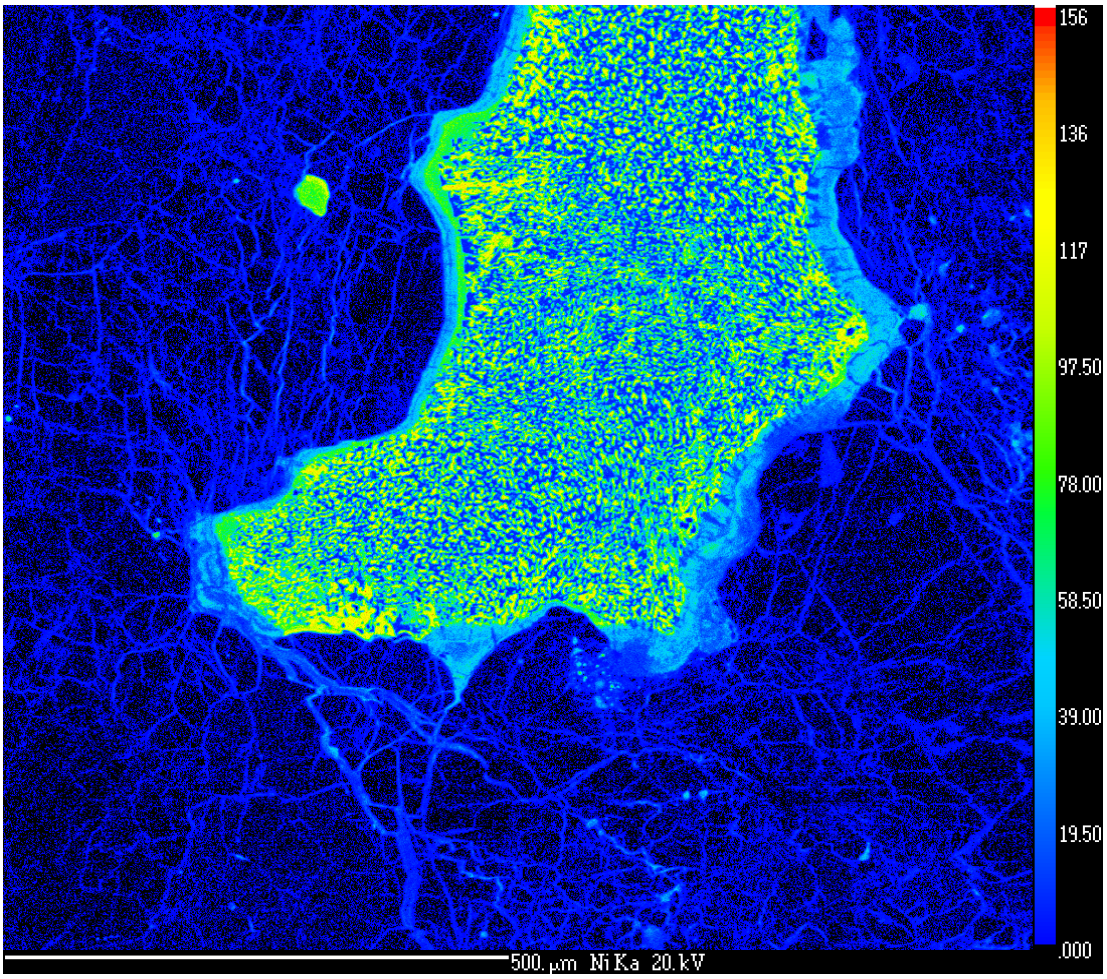

Fig. 3.19. ALH 84058 R. Ni element map of a pearlitic plessite in ALH 84058, showing the fine intergrowth of kamacite and taenite. Also shown is the heterogeneous alteration product forming centripetally around the fine growth with has significant Ni variation throughout. Also visible are surrounding veins that lace through the meteorite.

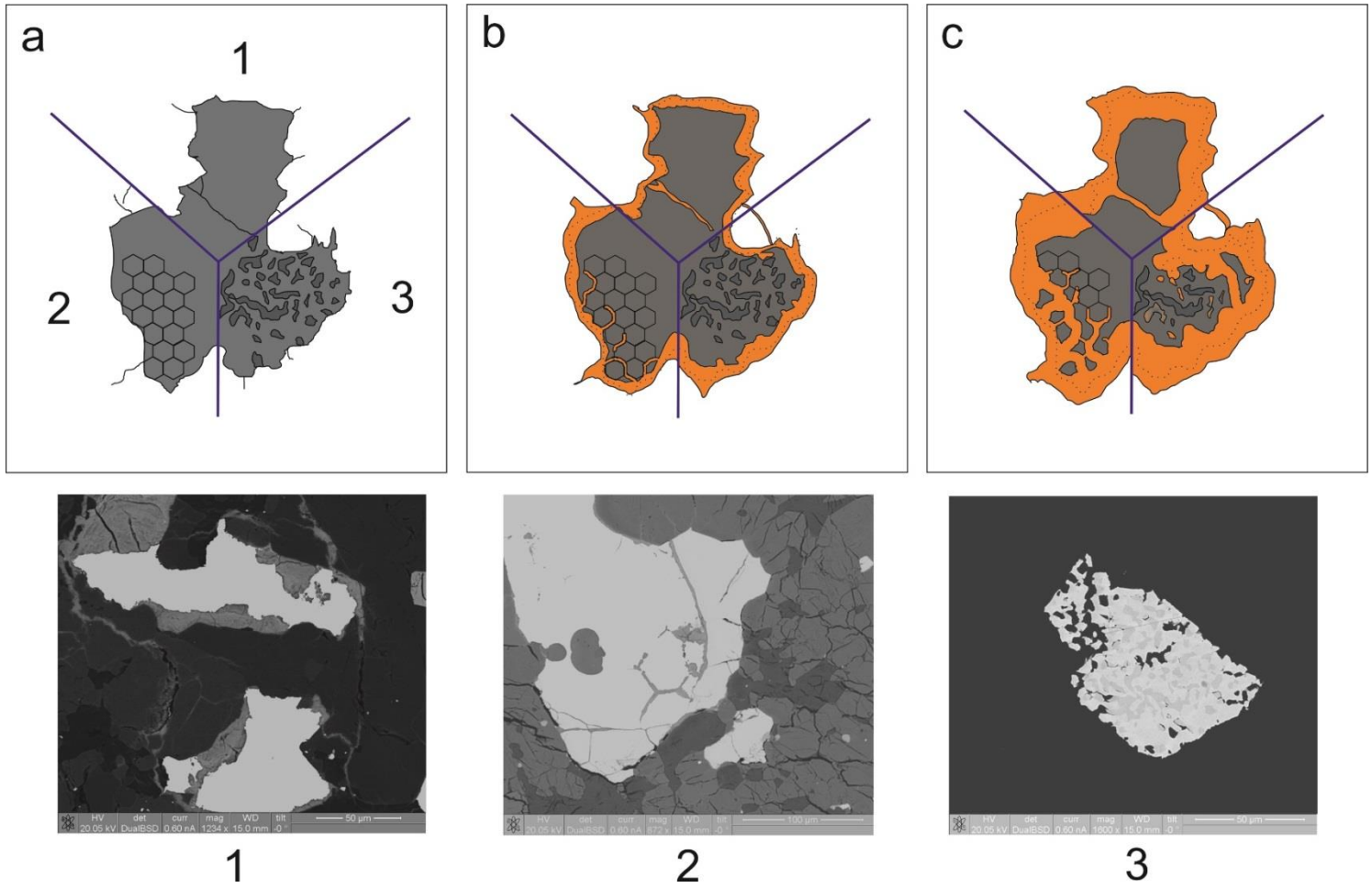

Fig. 3.20. Progression of oxidation in metal grains. The images describes the alteration of a metal grain with three separate textures to a meso-alteromorph. Area 1 is a homogenous kamacite grain with a fracture through, area 2 shows polygonal fracture patterns common in kamacite/taenite intergrowths where the centre of the hexagons are the more Ni rich taenite and more Fe rich areas occur between the joins. Area 3 is a plessite intergrowth of kamacite and taenite where the darker material is the more Fe-rich kamacite and the lighter areas are Ni rich taenite. Underneath the cartoons are a series of images displaying these actual textures in real samples that have undergone various amounts of weathering. All are BSE images: 1 is from QUE 99022, 2 and 3 are from ALH 84056. a) An unaltered metal grain. b) A slightly altered grain. Area 1 is centripetally weathering, producing a layered product radially to the original metal grain. The echino-alteromorph extends into the local fractures and two fractures close together join. The alteromorph morphology still resembles the original grain but is filling a slightly larger area than the original grain and is therefore becoming a meso-alteromorph. Area 2 shows alteration along the edges of the hexagonal taenite grains, altering the Fe rich areas preferentially. Area 3 shows a similar process where some kamacite grains have been completely weathered out and centripetal weathering is still occurring. C) Area 1 weathering has progressed centripetally at a comparatively slower rate to areas 2 and 3. Area 2 shows several dislocated grains of taenite isolated in the alteromorph as the weathering front advances quickly to fresh surfaces opened up by the hexagonal planes of weakness. Area 3 shows severe weathering with much of the original mineral gone. Several grains of kamacite that have been altered have coalesced and broken a piece of taenite off.

Alteration Features:

Kamacite is the most heavily weathered phase in all samples. In QUE 99022 and the interior of ALH 78130 there are many pockets of Fe-oxyhydroxides in the shape of kamacite grains that are assumed to be wholly disaggregated crystals (iso-alteromorph and holo-alteromorphs). The weathering patterns of kamacite types 1- 3 are summarised in Fig. 3.20.

1) **Homogenous grains:** These demonstrate a centripetal progression of weathering, as the halo of alteration product that initially forms, expands inwards until the entire grain is altered. Ragged edges are common where alteration has initiated around the outside of crystals. Almost all crystals are found with halos of alteration product surrounding them, the thickness of which varies dependent on the weathering state of the meteorite. The alteromorphs often have cracks around their margins, which are probably dehydration shrinkage cracks. Veins appear in close proximity to kamacite grains, leading away from altering grains through mostly pre-existing fractures. They increase in size and frequency with proximity to the altering grains. The initial replacement of the primary mineral leads to a holo-alteromorph which progresses centripetally inwards (or along planes of weakness such as internal fractures). When a mineral has been almost or completely replaced, the alteromorph becomes significantly more porous (and so becomes a poro-alteromorph). In some cases, this porosity has combined to make large cavities in the centre of the alteromorph (centro-poro-alteromorph) (Fig. 3.21.). The product of centripetal weathering is colloform and zoned with varying amounts of Fe, and the alteromorph is always a holo-alteromorph in that it always resembles the shape of the parent grain. In completely weathered grains with no

.parent remnants, the product becomes homogenous without zonation. Where kamacite grains are adjacent to taenite, the kamacite is preferentially altered.

2) **Plessite:** These intergrowths alter along the paths of greatest iron concentration, leaving grains with higher Ni contents to weather more slowly, often leaving them as islands in an alteromorph. The pattern of alteration is vermicular rather than centripetal and the plessite intergrowths are noted for faster alteration relative to homogenous grains.
3) **Hexagonal polycrystalline agglomerates:** These alter along paths of Fe/kamacite concentration, leaving hexagonal taenite grains to alter more slowly.
4) **Melt spherules:** These are highly vulnerable to alteration and are the first type of kamacite to transform completely. In the rim sample of QUE 99022 and the interior of ALH 78130, kamacite is absent from the melt veins except in rare spherules, probably because they have altered out. Evidence for this comes from the observation of many spherule shaped pockets of alteromorph in the melt veins.

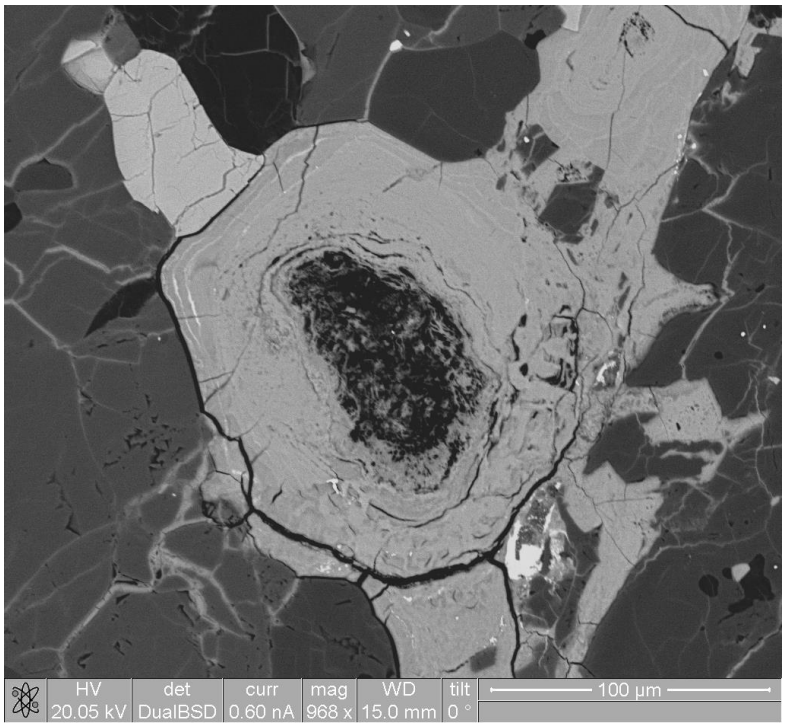

Fig. 3.21. QUE 99022 BSE image. Centro-poro-alteromorph formed from the alteration of kamacite in the rim of QUE 99022. Some small relicts of the parent mineral remains around the outer edge. The product is highly heterogeneous and concentric.

3.2.6. TAENITE: 0.6-2.1% ABUNDANCE

Habit and Occurrence:

In all meteorites taenite is less abundant than kamacite, and it usually occurs in close proximity to kamacite. The maximum crystal size is 700 µm (QUE 99022) and, thus, smaller than kamacite. Intergrowths with kamacite are common and are described in Section **3.2.5.** In the rim of QUE 99022 taenite is largely absent from the melt vein regions, however, in the interior it is present throughout the melt veins as spherules. Very little taenite occurs in the most intense area of weathering (along the weathered melt veins of QUE 99022, interior of ALH 78130).

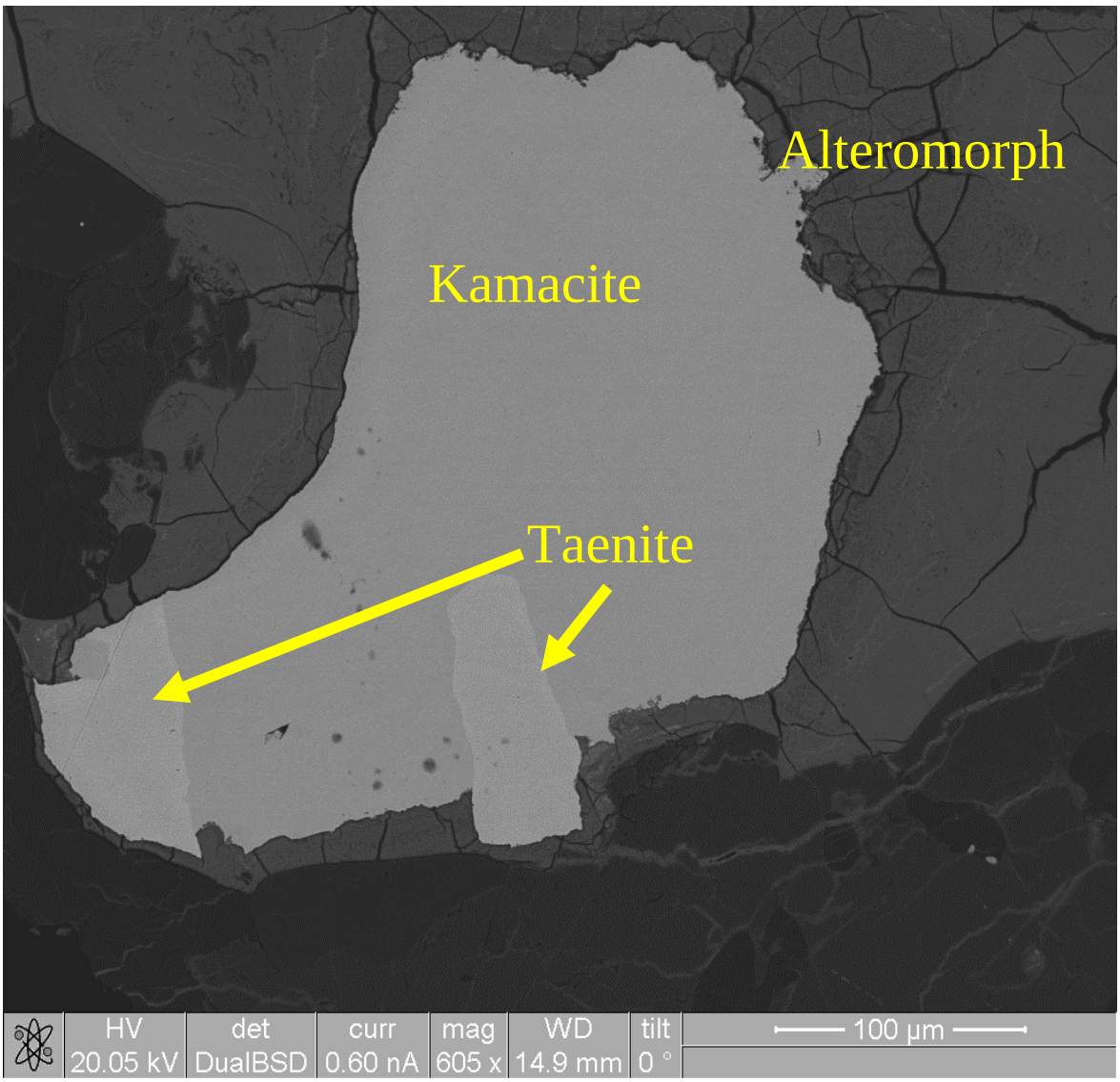

Fig. 3.22. QUE 99022 BSE image. Kamacite and taenite are altering to similar products, but the taenite (brighter) is altering more slowly than the kamacite (darker) which is receding around the intergrown taenite grain.

Large grains of taenite (> 400 μm) in QUE 99022 and in ALH 78130 have retained the primary "M" shaped linear profile of nickel concentrations, with higher Ni rims than core (thus forming an "M" shape in a line graph representation of Ni concentration) that are formed from slow cooling of taenite when initially formed (Wood, 1964). Few pure taenite grains exist in ALH 84056, which is mostly dominated by pearlitic plessite intergrowths.

Alteration features: Taenite alters less readily than kamacite, with adjacent crystals and intergrowths of both, demonstrating preferential kamacite breakdown (Fig 3.20; Fig. 3.22). Taenite weathering follows a similar evolution to kamacite, with a halo of Fe-oxyhydroxides forming around the crystals which progresses centripetally inwards. The more Fe-rich areas in heterogeneous taenite/taenite-kamacite intergrowths alter preferentially, typically leaving behind hexagonal patterns of Ni blebs. The taenite crystals that are enriched in Ni at the outer edges alter more slowly than less Ni-rich grains, because Ni-rich material is more difficult to alter than Ni-poor (Bland and Lee 2006). Ragged edges of grains show the areas altering to Fe-oxyhydroxides, which contain small amounts of Ni. The alteromorph formed from taenite is heterogeneous with variable amounts of Fe, resulting in a similar colloform alteromorph to kamacite.

In QUE 99022 taenite within the initial 300 μm of the fusion crust has been entirely altered to Ni-rich Fe-oxyhydroxides, there is no taenite, or Ni-rich products in the zone of intensive weathering that follows the melt veins.

In the more weathered areas, such as in ALH 78130 interior and QUE 99022 rim, Ni is retained in pockets of iso-alteromorphs and so even where entire grains have been disaggregated, it is possible to discern which alteromorphs originated from taenite. The increased Ni in surrounding alteromorphs rarely extends beyond a few μm from the weathering parent grains. The most weathered taenite crystals are much more enriched in Ni compared to Fe, which appears to migrate into the iso-alteromorph. Silicate alteration (e.g. pitting, etching) is often associated with heavily weathered grains.

3.2.7. CHROMITE 0.4-1.6 % ABUNDANCE

Habit and Occurrence:

Chromite occurs as clusters of small crystals (<40 µm) in plagioclase (Fig. 3.23.) and as large crystals up to 600 µm in length, and they do not appear in chondrule remnants. Most large chromite crystals occur adjacent to kamacite and taenite crystals and the small clusters show a range of sizes and of habit (euhedral to anhedral) and are produced by shock (Rubin 2003). Many of the larger chromite grains in QUE 99022 have melted margins, forming small melt pockets. They often contain many fractures and appear to be relatively brittle in comparison to other minerals.

Alteration Features:

Even in the most altered regions (e.g. the rim of QUE 99022 and ALH 78130 interior), where kamacite and taenite have been completely removed, chromite is not observed to be weathering. However, in element maps of alteration assemblages there are low levels of chromium and it is unlikely to have been derived from another source. Chromite is extremely resilient to weathering and the only occurrence of chromite weathering is in the rim of QUE 94214 (Fig. 3.24.), where a small number of large crystals near the fusion crust are surrounded by alteromorph containing minor amounts of Cr as well as large amounts of Fe, some Si, Cl, Ni and S.

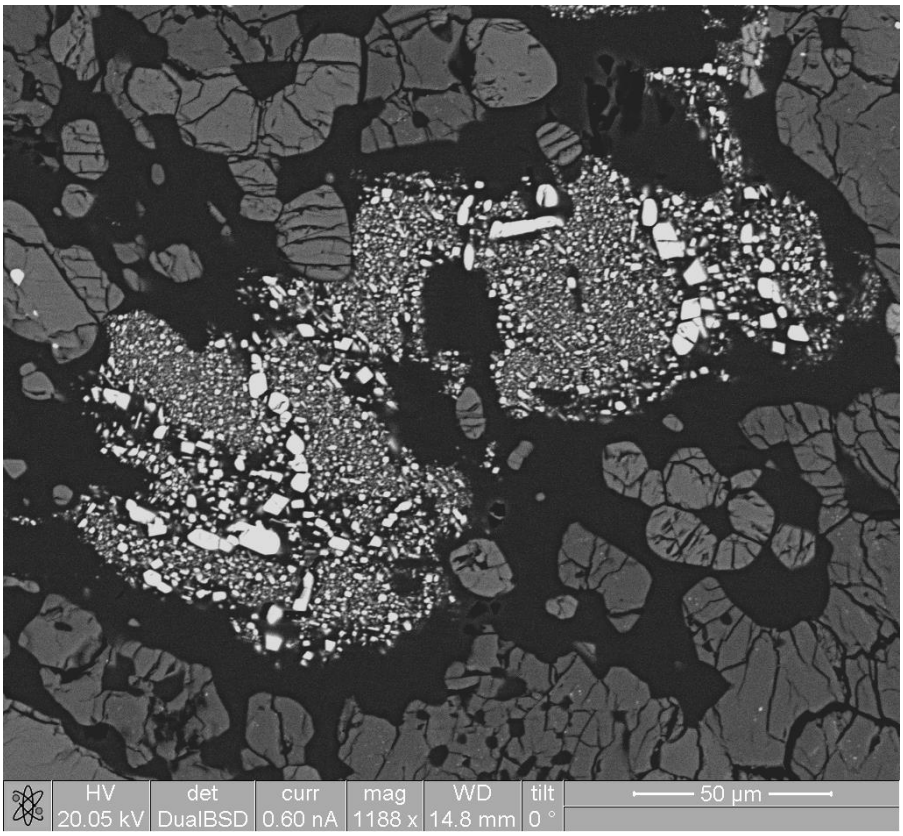

Fig. 3.23. QUE 94214 BSE image. A cluster of chromite crystals in the centre of a maskelynite grain. Many are cubic vary in size. The clusters are common across the meteorite.

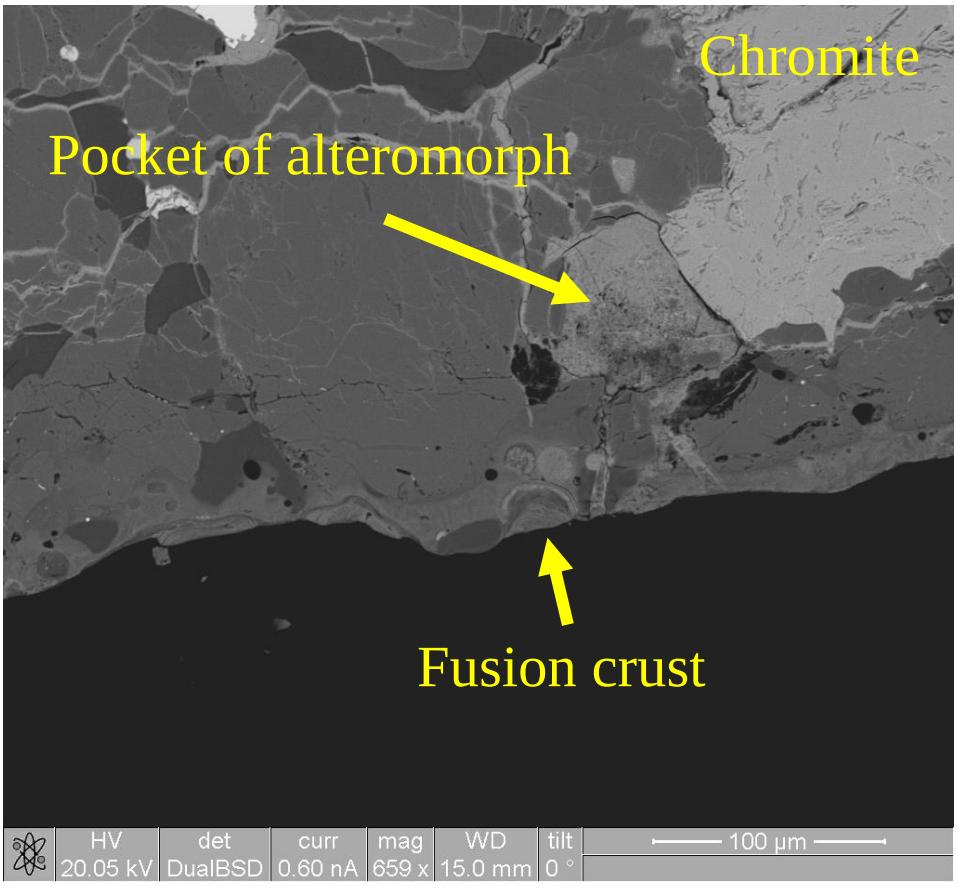

Fig. 3.24. QUE 94214 BSE image. A chromite grain proximal to the fusion crust of the meteorite is supplying elements to the large pocket of alteromorph.

3.2.8. PHOSPHATES 0.2-2.2% ABUNDANCE

Habit and Occurrence:

Phosphates are rare and usually small (< 10 µm), but can occur as crystals up to 500 µm long; in a thin section there are commonly fewer than 10 crystals. They do not occur within chondrule remnants and are all anhedral, regardless of size. Two species of phosphate are identified in element maps: a more Ca rich species and a Cl rich species (apatite and chlorapatite, Fig. 3.25.); both varieties are of equal abundance. Most are cross-cut by transmineral fractures and frequently they contain silicate inclusions, most commonly pyroxene.

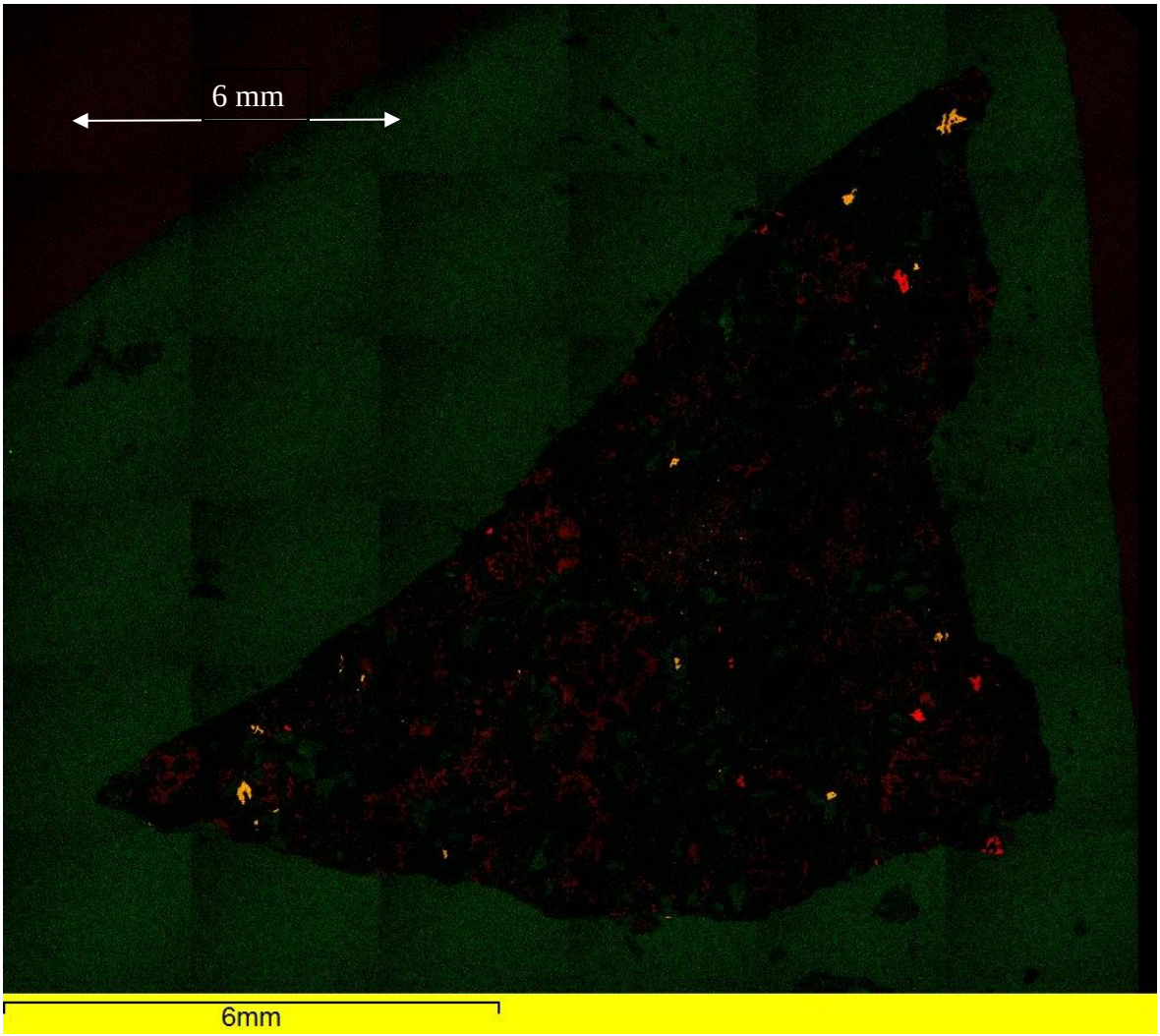

Fig. 3.25. ALH 78130 element map. Ca—red, Cl—green. The two species of phosphate, merrilite and chlorapatite, can be discriminated by the Cl contents. The orange colour crystal denotes chlorapatite, red crystals are whitlockite.

Alteration Features:

There is little evidence of phosphate alteration in any of the samples. Alteration of phosphates is only observed in the rim sample of QUE 94214 (within 300 μm) and the rim sample of ALH 78130. The altered phosphate in QUE 94214 is a chlorapatite (Fig. 3.26.). The chlorapatite is altering to a hydroxyapatite and the secondary products deposit inside and proximal to the altering mineral. The alteration vein is large compared to other veins in the sample (100 μm, whereas most are < 10 μm) and the walls are irregular, indicating dissolution. Several relict crystals of phosphate are suspended in the alteration pocket. EDS spectra show a large amount of Fe and Ni also present in the alteration product and so it is assumed that a mixture of phases occur, most likely a mix of Fe-oxyhydroxides and hydroxyapatite (Boudreau and McCallum, 1990).

Rounded grain contacts with veins occur in several places which is suggestive of dissolution. The thick section of ALH 78130 rim preserves an area of alteration product that has grown from a vein containing significant amounts of P, Ca and Fe. As the only indigenous source for P in the sample is phosphate, it is assumed that this has originated from the minor amounts of phosphate dissolution but no parent mineral can be discerned.

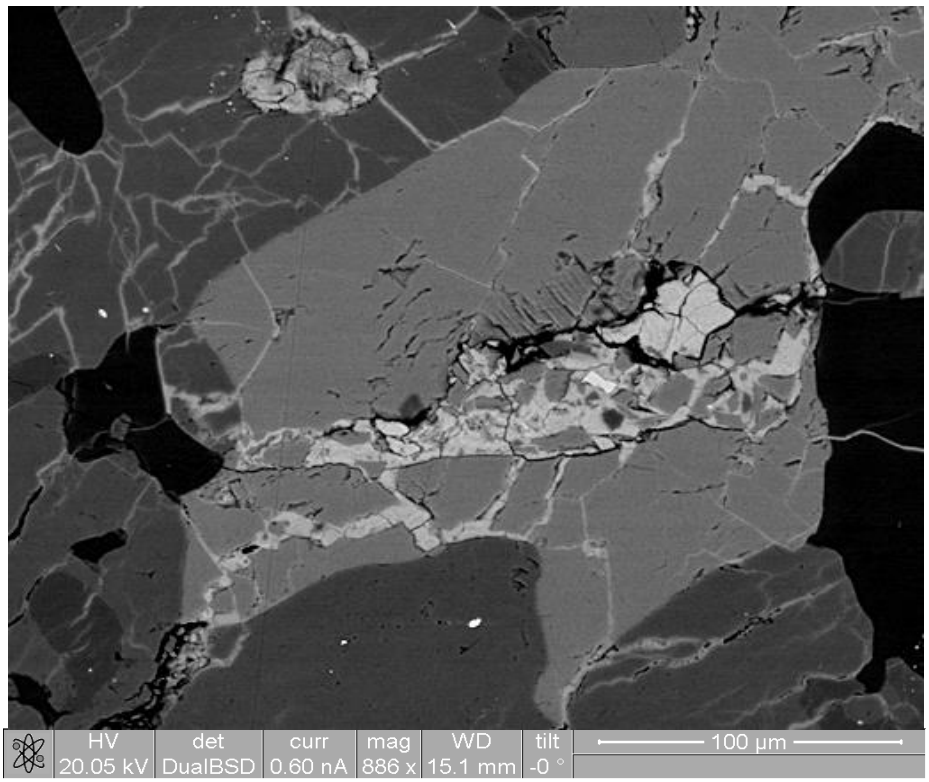

Fig. 3. 26.
QUE 94214 BSE image. The sample shows the only observed case of phosphate alteration in any of the samples. A large vein penetrates and contains hydroxyapatite and Fe-oxyhydroxides.

3.2.9. MELT PRODUCTS/POCKETS

Habit and Occurrence:

Melt veins occur in QUE 99022 in both rim and interior, ALH 78130 in interior and ALH 84056 interior and were observed in chips of QUE 94214. As melt veins were not present in QUE 94214 thin and thick sections, they were not studied in detail. Melt pockets vary in size and are a common feature in all meteorites studied here.

In QUE 99022**,** melt veins cover a large part of the sample (~40%). In the interior section of ALH 78130, two melt veins dominate the sample and cover ~50% of it. ALH 84056 interior has one melt vein cross cutting and covering roughly 10% of the sample. The veins are comprised of melted kamacite, taenite and sulphide spherules (Fig. 3.17 B), with some parts surrounded by melted silicates. They lace through the meteorite, branching and cover large areas. Where the melt veins bisect kamacite, taenite or troilite grains, there is a significantly increased concentration of melt spherules from the adjacent grains.

Many areas have patches of melt droplets in all phases, although many more are concentrated in plagioclase than anywhere else. The larger melt veins have open fractures through them and the largest fractures are in areas of melt veins, and adjacent to them.

Alteration Features:

Where melt veins exist they concentrate iron staining, which radiates from the vein, notably in ALH 84056 interior, which is otherwise pristine (Fig. 3.27.). ALH 84056 contains the best preserved melt veins as they have only experienced minor oxidation/hydration and so most metal/troilite spherules are still present.

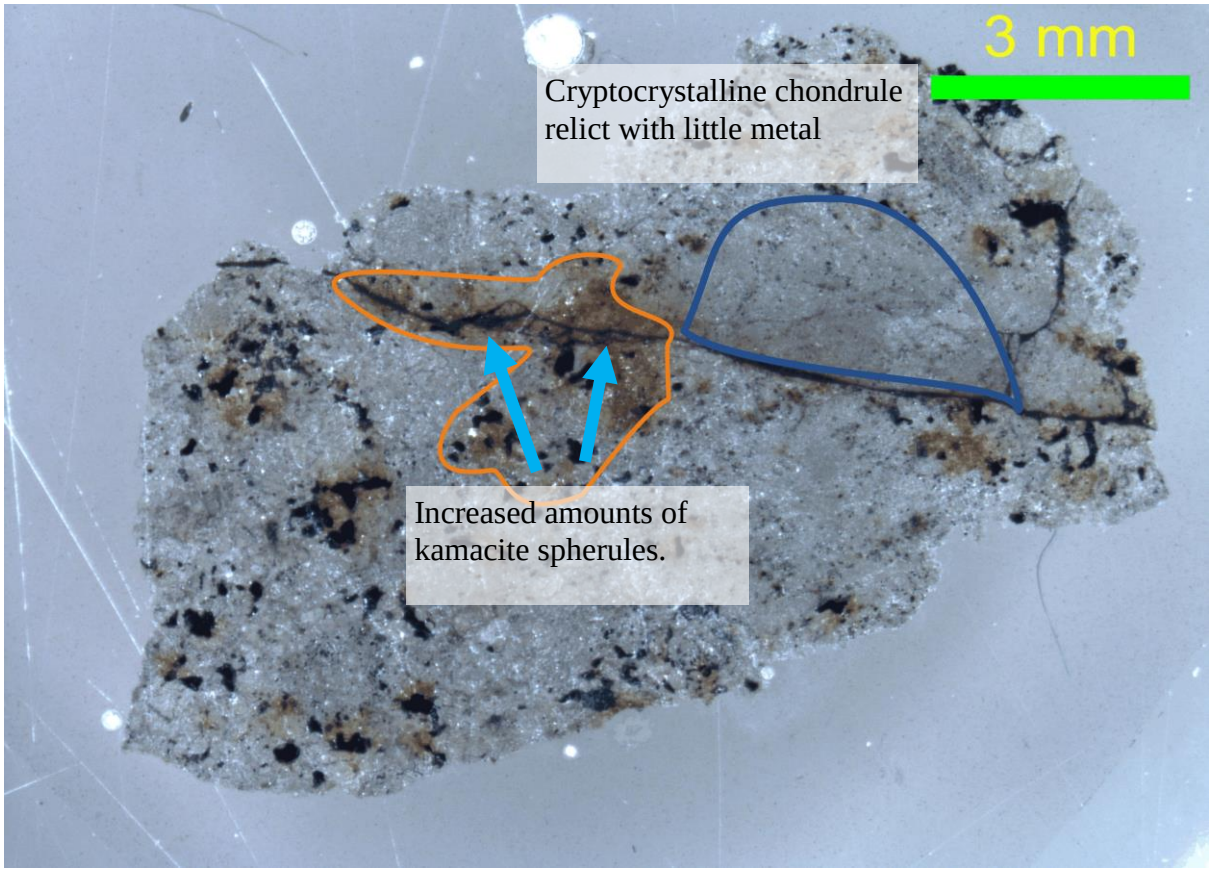

Fig. 3.27. ALH 84056 binocular photo. The blue line outlines a cryptocrystalline chondrule relict and the orange surrounds an area of intense iron staining. A melt vein bisects the sample. Where it crosses the cryptocrystalline chondrule there is little noticeable impact on the alteration pattern, but where the vein crosses metal grains, a significant increase in rust is observed.

In QUE 99022 most of the melt veins do not retain their original mineralogy and have instead been altered to Fe-oxyhydroxides but remnants of the original compositions are observed in places in the interior section. There is a “buffer zone” around the melt veins where there are few or no large kamacite, taenite and sulphide crystals and this is wider in the rim section (around 1 mm either side) than the interior sample (0.5 mm either side).

The most weathered melt veins are in ALH 78130 interior, where in many places the melt veins appear to be metal- and sulphide-free and very porous, suggesting the total removal of the original minerals, which has left behind the porous pathway of silicates and alteromorphs.

3.2.10. LARGE POCKETS OF ALTERATION PRODUCT

There are many occurrences of large pockets of alteration product with no associated parent mineral, some are infilled pre-existing cavities, and some are the end result of complete replacement of original minerals. The pockets of alteromorphs that have totally replaced the parent mineral are often iso-alteromorphs and so a hint to the parent is given by the shape of the pocket. Some of these are centro-poro-alteromorphs with large open pores in the centre, a form that only occurs in pockets larger than 250 µm (Fig. 3.28.) and the alteromorph itself is commonly very porous. These occur in QUE 99022 in the rim and ALH 78130 interior and the pockets are typically Fe-oxhydroxides with minor amounts of Si, but occasionally (such as in ALH 78130) clays are mixed in with some of the larger pockets of Fe-oxyhydroxides, although most are almost entirely Fe-oxyhydroxides.

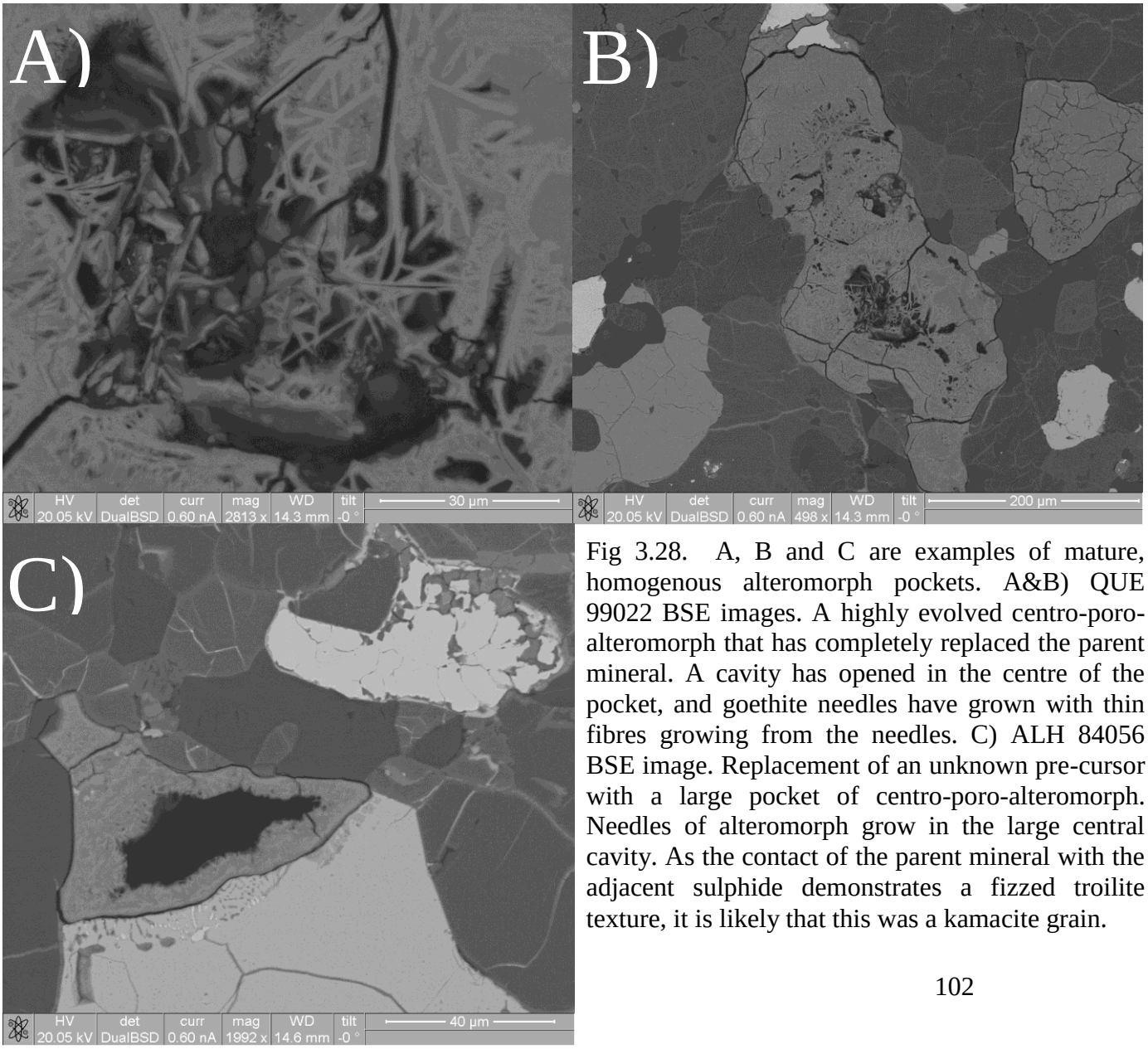

Fig 3.28. A, B and C are examples of mature, homogenous alteromorph pockets. A&B) QUE 99022 BSE images. A highly evolved centro-poro-alteromorph that has completely replaced the parent mineral. A cavity has opened in the centre of the pocket, and goethite needles have grown with thin fibres growing from the needles. C) ALH 84056 BSE image. Replacement of an unknown pre-cursor with a large pocket of centro-poro-alteromorph. Needles of alteromorph grow in the large central cavity. As the contact of the parent mineral with the adjacent sulphide demonstrates a fizzed troilite texture, it is likely that this was a kamacite grain.

Pocket homogeneity varies with size: alteromorphs in larger pockets are more homogenous, whilst smaller pockets preserve the colloform pattern formed from centripetal weathering of metal grains (**Section 3.2.5,** Fig. 3.21**.**). The pockets largely occur adjacent to, or along, large fractures in the samples, with very few observed away from heavily weathered areas. Some large pockets formed through total replacement of primary minerals have formed mesoalteromorphs (Fig. 3.29). These display the original shape of the primary mineral but expand during formation, forming fractures around the product. They have later reduced in volume, presumably from dehydration, leaving behind deep intermineral fractures surrounding them. Some fractures cross cut alteration pockets, suggesting some mechanical stress post-dating alteromorph deposition, however most seem to pre-date the alteromorphs.

In ALH 78130, ALH 84058 and ALH 84056 the largest pocket (500 μm) contains well-formed rosettes of goethite needles. These needles have only formed where there are large centro-poro-alteromorphs in mature pockets with little chemical heterogeneity. In ALH 84056, a clear relationship with fizzed troilite is observed. Contacts with fizzed troilite are common around entire grain replacement.

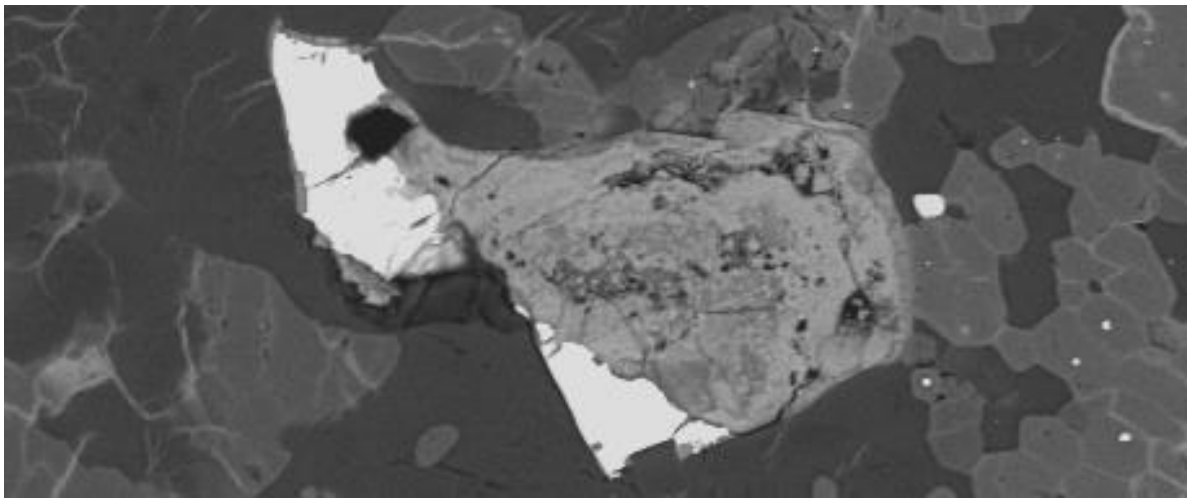

Fig. 3.29. ALH 78130 Interior thin section BSE image. Mesoalteromorph resulting from the breakdown of a kamacite grain.

3.3. OXIDATION PERCENTAGES

For every meteorite in the study, the quantity of oxidised material of the three most weatherable phases (kamacite, taenite and troilite) was measured in 2D space (as described in Section 2.4.3.). With these percentage measurements, it is possible to compare the relative amounts of oxidation in different samples. These are summarised in table 3.2.

The percentages of oxidation of kamacite, taenite and troilite all show a positive correlation indicating that they are all weathering in the same conditions (Fig. 3.30). It is clear that the minerals are weathering at different relative rates, since less troilite (22 %) is altered than taenite (62 %) and kamacite (73 %) in the most weathered meteorites.

Correlation coefficients have been calculated using polynomial linear regressions (Fig. 3.30). The linear regression for sulphide vs taenite and taenite vs kamacite have non-zero intercepts. The taenite-kamacite regression is expected to have this non-zero intercept as kamacite is observed to be more weatherable than taenite, and so it is likely that when no taenite is weathered, some kamacite will be. The sulphide vs taenite intercept is contrary to the petrological study, however, as sulphides have been observed to be more robust than taenite. This suggests that the regression may not be linear, but this requires more data to confirm.

The correlation coefficients of sulphide oxidation to both kamacite and taenite are similar, and are less strong than the coefficient between kamacite and taenite, which is almost a perfect correlation. Two samples are significantly more weathered: ALH 78130 interior and QUE 99022 rim which both have a high level of oxidation with little original kamacite and taenite remaining, and these meteorites represent the upper end of the weathering spectrum. In contrast, the least altered sample is ALH 84056 interior with very little kamacite or taenite alteration. One outlier of significance is QUE 94214 interior which has

a disproportionately raised amount of sulphide alteration compared to kamacite and taenite alteration.

Using Fig 2.9 it is possible to consider what volume of the minerals has altered (with the assumption that the alteration is even all over and spherical). QUE 99022 and ALH 78130 have high levels of kamacite alteration (68.96% and 73.01% respectively), which would result in the volume of altered kamacite to be above 95% in both (96.5% and 97.02%

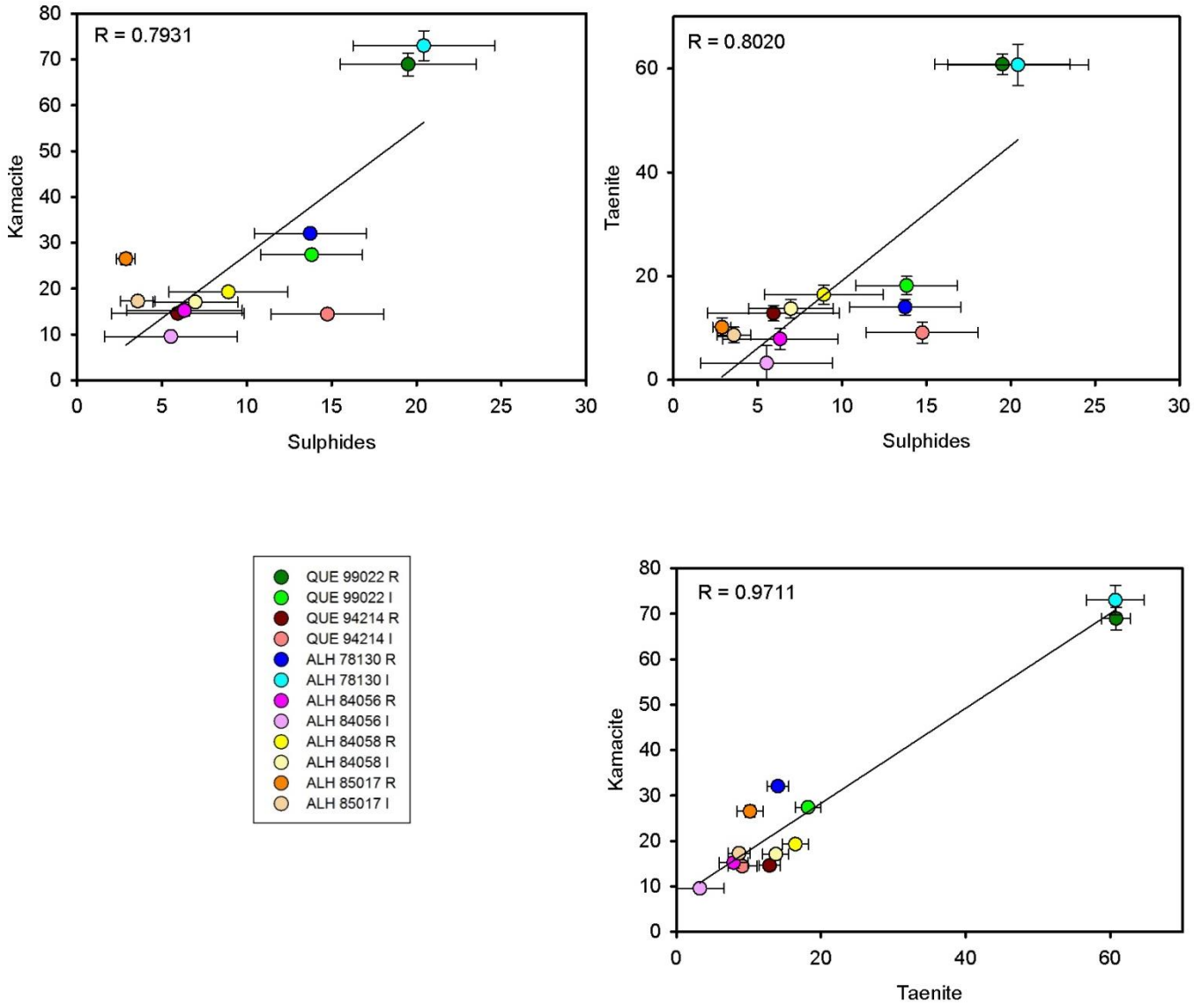

Fig 3.30. Percentages of alteration to Fe-oxyhydroxides in the three most weatherable minerals present in the meteorites. Error bars were generated from repeat measurements (details in Section 2.4.3). Each graph has the correlation coefficient (R – generated from polynomial linear regression) in the top left corner.

respectively) and so have very little volumetric kamacite remaining. Samples with more than 21% of a mineral altered in 2D equate to over 50% mineral volume altered.

Samples such as ALH 84056 with <10% alteration of metals (e.g. interior kamacite alteration) have <27.1% altered volume and so the theoretical altered volume is considerably higher than 2D area measured. For an accurate 3D measurement to be made, CT scanning would be required.

3.4. FRACTURE PATTERNS

There are two types of fractures: intermineral and transmineral (Fig. 3.31.). Their frequency and size is mineral dependent and they are largely caused by mechanical weathering and by pre-terrestrial shock processes and provide a starting point for veins to penetrate the meteorite. Weathering at areas of excessive free energy, i.e. crystal defects, cleavage planes and inclusions is significantly more rapid and so crystals that have excessive microfractures and defects are significantly more susceptible to weathering. Veins mostly exploit pre-existing fractures and so recognising the fracture patterns within a meteorite becomes important for understanding how weathering fronts progress.

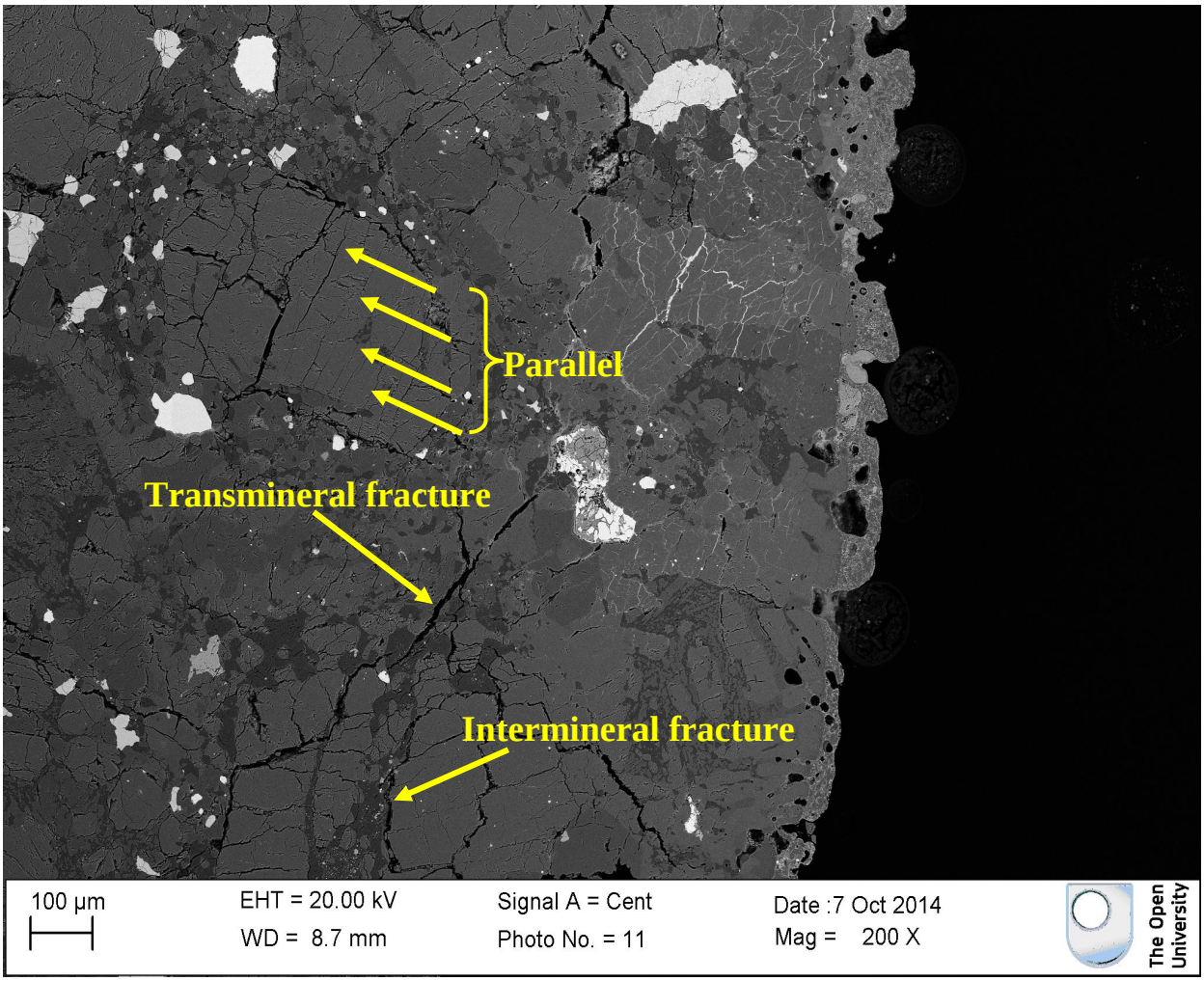

Fig. 3.31. ALH 85017 BSE. This illustrates the different fracture types present in the meteorites studied. Parallel fractures that travel through olivine, transmineral fractures that cross many mineral types with little mineral specific orientation effects and intermineral fractures that travel through the mechanical plane of weakness between mineral boundaries.

Mineral properties control the path of fractures through the meteorites and this is most noticeable in intermineral fractures and in small transmineral fractures. Large fractures (>1.5 mm length) are not mineral specific. Intermineral fractures tend to be less extensive and are most common around olivine crystals. They are assumed to be from mechanical expansion and contraction from the large temperature variations that meteorites experience in Antarctica (André et al. 2004). Intermineral fractures are generally regular and have regular accordant walls, so are more likely to have been formed from mechanical alteration rather than chemical. Olivine concentrates a large number of intermineral fractures which include the prevalent shock-created planar fractures. Of all the mineral species in the meteorites, olivine is consistently the most heavily fractured whilst metal grains are almost never fractured. It is plagioclase and maskelynite that preserve significant difference in fracture patterns whereby maskelynite has few if any transmineral fractures unless they are large (>1.5 mm), whereas untransformed feldspar has a high density of brittle fractures, many of which are infilled with alteromorph (which is meteorite dependent, Fig. 3.16 B; Fig. 3.16 D). However, these fractures are not often linearly extensive and so form fracture networks. The rare transmineral fractures cutting through maskelynite must be terrestrial in timing, and are most likely to be derived from the mechanical freeze thaw processes since fractures are even, and brittle sided fractures rather than chemically expanded and with sawtooth edges.

The progressive evolution of fractures-veins is summarised in Fig. 3.32. All filled fractures demonstrate some level of chemical expansion, and where veins have been chemically expanded the margins are often rounded, or, when penetrating through a cleaved mineral, become stepped along the cleavage planes. Chemical expansion increases the propagation

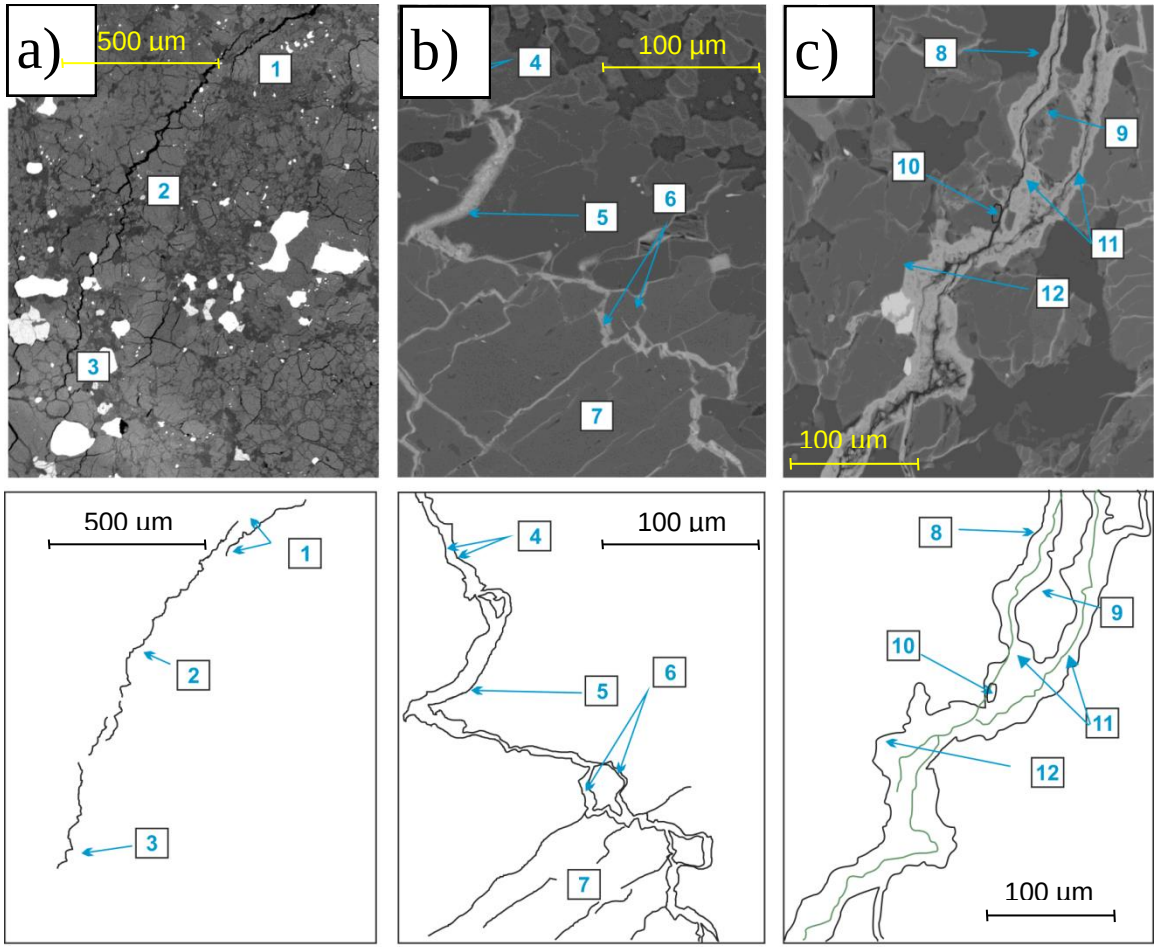

1 - En echelon fractures.
2 - Stepped fracture through olivine cleavages.
3 - Intramineral fracture.
4 - Sides of the fracture still "fit" together, indicating little dissolution.
5 - Loss of definition at edges of fracture and curve developing indicating some dissolution.
6 - Two small fractures have joined, isolating a lithorelict in the centre of the vein.
7 - Small veins follow planer fractures in an olivine crystal.
8 - Large vein cuts through several mineral types with no perturbation due to mechanical weaknesses in the minerals. There are no longer stepped patterns.
9 - Pits in surrounding silicates where they are being dissolved.
10 - Isolated lithorelict being absorbed into the vein.
11 - Fractures through the centre of the vein demonstrate it as a conduit of mechanical weakness. These most likely form from de-hydration of hydrous products.
12 - Sides of the original fracture no longer match up, indicating significant dissolution at the margins.

Fig 3.32. Fracture progression and evolution through a meteorite. a) Transmineral fracture from ALH 84058. This fracture is completely open with no infilling. It diverts around mineral edges where they are proximal to the fracture and across minerals where the boundaries are not proximal. The sharp defined edges of the fracture show no chemical expansion. b) An infilled fracture in QUE 94214. This fracture has undergone small amounts of chemical expansion, evidenced from smoothed margins of the vein. The vein is still relatively immature and so the edges of the vein still mirror each other to some extent. Many smaller veins are joining with the larger central vein. Where veins meet, lithorelict can be isolated and dislocated from the original grain to be an island in the vein. These lithorelicts dissolve quicker as they have an increased surface area. c) A relatively mature vein in QUE 99022. This mature vein has little definition at the vein margins and there is little left of the original fracture margins. In mature veins, differential mineral dissolution becomes evident, with veins thinning through maskelynite and expanding through olivine and pyroxene. Pitting in silicates is commonplace around mature vein margins. A central fracture travels through the interior of the vein, which is common for mature vein systems. These are either formed from dehydration of the alteromorph or are formed by mechanical stresses and thus travel through veins as they are mechanically weak compared to the coherent meteorite. Isolated lithorelicts are still common, and usually rounded.

of veins and fractures and infilling alteromorphs expand and contract with varying hydration levels (Lee and Bland 2004).

In QUE 99022 almost all fractures have been infilled with alteromorph and two large (20 μm) open fractures bisect the rim allowing access to external contaminants. The fractures are lined with thick (variable, but generally <30 μm) deposits of alteration product. Fractures occur around vugs that are probably shrinkage cracks from the dehydration of the secondary minerals.

In QUE 94214 many fractures are open and concentrate most heavily in olivine crystals with some in pyroxene, and very few in maskelynite (which has radial fractures surrounding the grains). Olivine crystals contain extensive planar fractures throughout and pyroxene contains many transmineral fractures. Chondrule fragments seem to contain less fractures, possibly a reflection of their smaller grain size and the fusion crust has very few fractures through it. Most fractures appear mechanical in formation.

ALH 78130 has transmineral fractures throughout the sample whilst intermineral fractures only tend to occur around olivine crystals. Chromite hosts the most small (<10 μm wide) fractures, with olivine hosting the second most fractures. Patches of maskelynite have very few fractures, but where the plagioclase has not been transformed in the interior of the meteorite, there are many small transmineral veins cutting through. These could be chemically propagated, or may be mechanical fractures, that have been subsequently infilled. Large transmineral fractures (>10 μm) are sharp edged and open in the rim sample, and in most cases have very little evidence of alteration along them. Fracture stepping can be seen along mineral cleavage planes and planes of weakness and most of the large transmineral fractures in the interior sample are either filled, or have coating on the sides, which have been chemically widened. It is ubiquitous across all mineral types that the large transmineral fractures are cross-cut. There is no obvious widening effect along the veins in different mineral types, suggesting that dissolution is occurring along the

veins in all minerals at roughly the same rate. Dislocations of olivine are observed where fragments are being plucked from the edges of veins (Fig. 3.33.).

In ALH 84056, fractures occur in all minerals with the exception of maskelynite. In the interior sample, almost all fractures are open and mechanical in formation, evidenced by the fresh edges that match up with very little loss of material. In the rim there are more chemically widened fractures that are proximal to weathered metal grains and to the fusion crust.

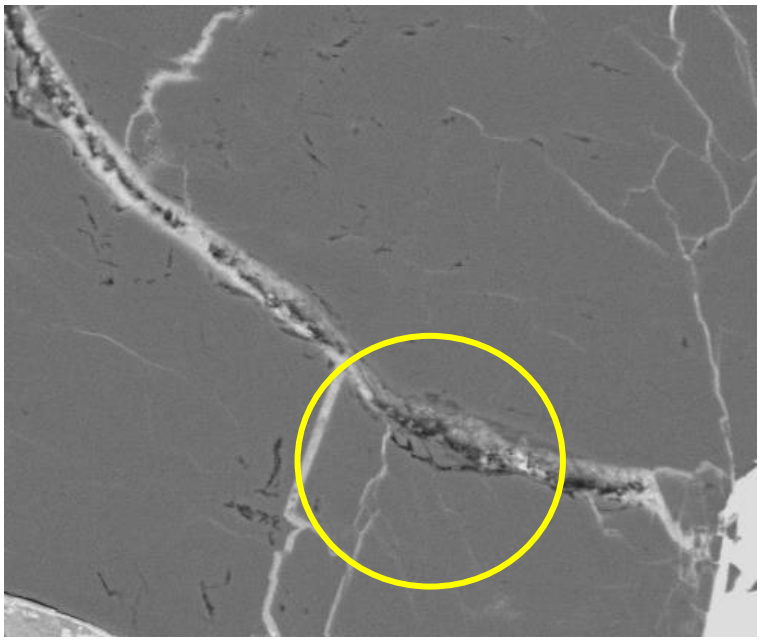

Fig. 3.33. ALH 78130 BSE image. Transmineral fracture cross-cutting olivine. Stepped dislocation of olivine fragments occur along the margin of the vein.

Most of the fractures in ALH 84058 are open, and less than 20 % are infilled with alteration products. Many of the olivine crystals contain many small (< 5 μm) fractures. The feldspar has many fractures and veins throughout. Many large veins are intruding from the fusion crust and these are associated with heavy silicate pitting. Most of the fractures in ALH 85017 are open with no alteration product and are therefore clear-cut, straight edged. Near the fusion crust, many of the fractures are infilled with sulphide melt. Some of these have been altered to Fe-oxyhydroxides, but most are the original melt.

A comparison of fractures infilled with alteration product with open fractures demonstrates the level of weathering in a sample. The percentage surface area of each thin section

covered with infilled fractures was measured for each meteorite and is summarised in Table 3.2 and Fig. 3.34. The percentage vein coverage was then compared to the oxidation percentages of kamacite, taenite and sulphide since these are the source of the majority of the alteration products in the meteorites.

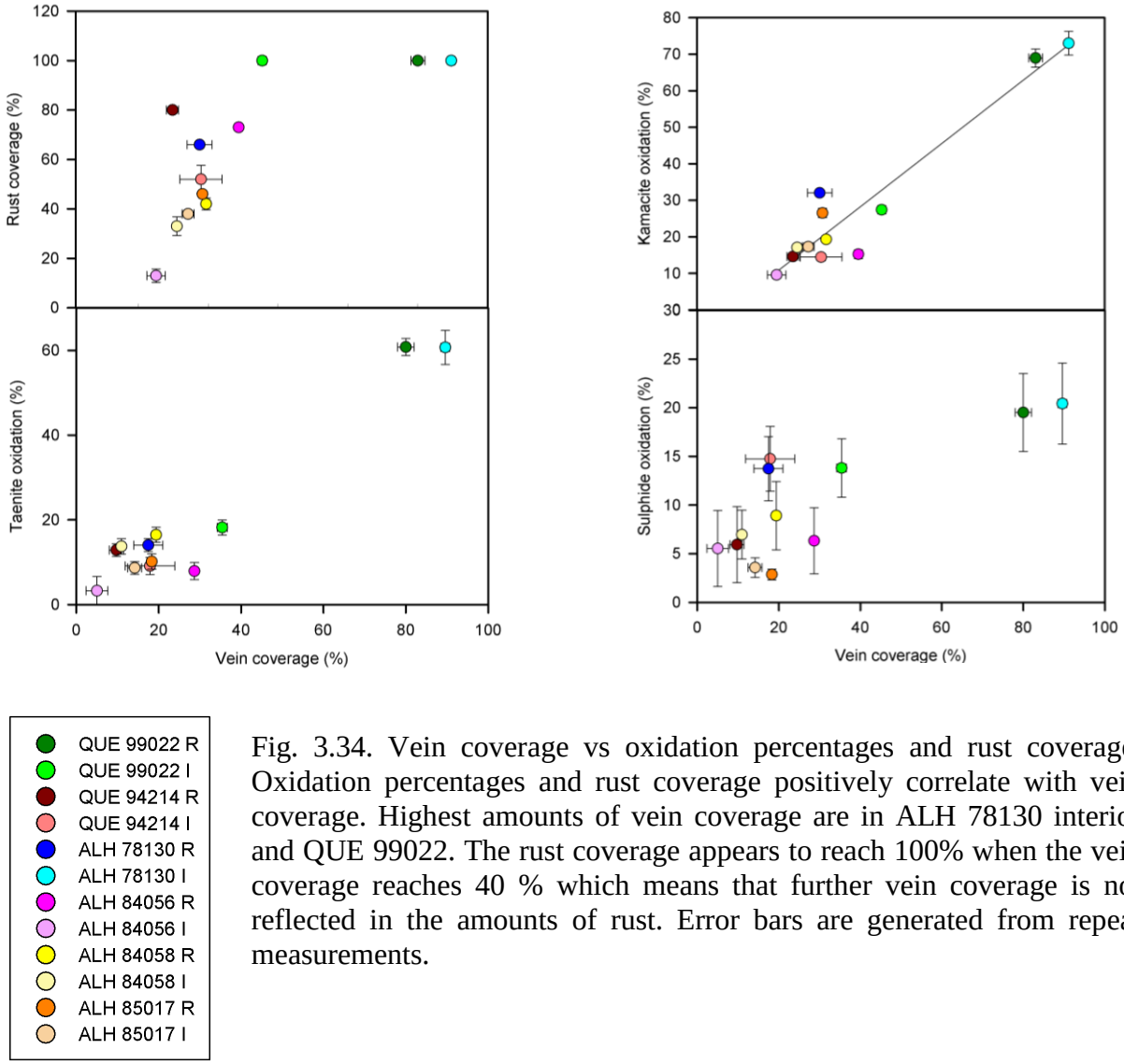

Fig. 3.34. Vein coverage vs oxidation percentages and rust coverage. Oxidation percentages and rust coverage positively correlate with vein coverage. Highest amounts of vein coverage are in ALH 78130 interior and QUE 99022. The rust coverage appears to reach 100% when the vein coverage reaches 40 % which means that further vein coverage is not reflected in the amounts of rust. Error bars are generated from repeat measurements.

The vein coverage is highest in the interior of ALH 78130 and the rim of QUE 99022, and lowest in ALH 84056 interior. A strong positive correlation is observed between kamacite oxidation and vein coverage, which implies that kamacite has driven the majority of the vein production. Taenite and sulphide oxidation also have a positive correlation, but to a lesser extent. The levels of rust coverage across samples are also strongly correlated to the vein coverage, with high rust cover relating to high levels of veining. Rust covers 100 % of the sample once 40 % of fractures have been infilled with veins which means that any further progression of veining is not reflected in the area covered by rust, which is the basis of major scales of weathering used for Antarctic meteorite weathering classifications (Wlotzka 1993).

3.5. Antarctic Varnish

Antarctic varnish occurs on the rims of all meteorites except QUE 99022. Element maps show an enrichment of K in the outer rim in the patches of Antarctic varnish and on some meteorites this is more prominent. The varnish is chemically heterogeneous, but mostly consists of Fe, Si, S, Al and K. In ALH 85017, the material infills cavities near the surface (Fig. 3.35). One feature of the varnish is that there is always a dislocation fracture at the contact with the meteorite. The layers of varnish vary in silica and iron content depending on the proximity to metal grains at the meteorite rim that weather at a fast rate and the contents of the weathered metal are added to the varnish layering. Consequently varnish in these circumstances has significant input from the meteorite rather than being purely a deposit derived from aerosol particles, described by Giorgetti et al. (2007). In this respect, the composition of the varnish varies as it is dependent on the proximity of metal grains in the meteorite.

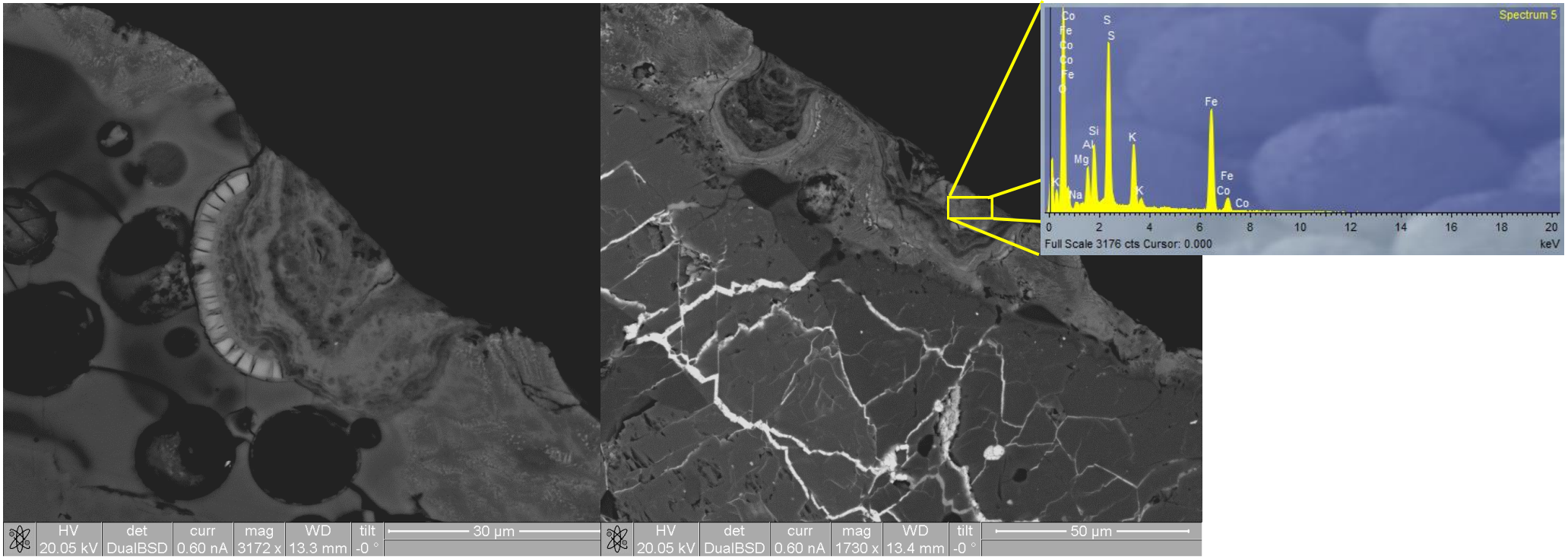

Fig. 3.35. QUE 94214 BSE images. Antarctic varnish drapes the outer edge of the fusion crust, infilling cavities and irregular depressions in the surface. The product is dark and multi-layered. The darker layers are highly siliceous. The lighter layers contain more Fe, S, Al and K. Pitting in olivine occurs underneath the pocket of varnish on the second image. An EDS spectrum is displayed of a typical area of Antarctic varnish. The Co is an incorrect labelling of Fe peaks by the automated recognition software.

3.6. MUSEUM WEATHERING

The term ‘museum weathering’ refers to post-collection weathering and can occur at any stage after collection. It affects all samples but is rarely reported outside the context of curational facilities (e.g. Velbel, 2014). Samples were stored for 3 years at The Open University and displayed evidence of museum weathering. All samples were maintained at ambient temperature with no special humidity measures and because the thin and thick sections were cut in 2012 by the Smithsonian Institution and the sections were examined between 2012 and 2015, we have a discrete time period over which the alteration is known to have occurred. Prior to sectioning, the meteorites were transferred from Antarctica frozen and then thawed in a nitrogen cupboard to remove any water and then stored in a controlled atmosphere.

Museum weathering began with the continuation of metal oxidation following on from alteration in Antarctica and occurs most commonly in thick sections rather than thin sections, which may result from enhanced water retention (see Section 3.8). It is easily recognised in thin and thick sections using secondary electron imaging, as the alteromorphs form topographically positive features because they have a greater volume than the parent minerals. Several examples are illustrated in Fig. 3.36. The growth of Fe-oxides on the surface of polished sections had a variety of morphologies since there was no space restriction for growth. The surfaces of many metal grains have altered in all samples except QUE 94214 and ALH 84056. Surficial growth is observed in ALH 85017, ALH 84058 (Fig. 3.36 A), ALH 78130, QUE 99022.

The rim thick section of ALH 78130 demonstrated a rapid growth of Fe-oxyhydroxides after LA-ICP-MS pits were drilled, where the 60 µm pits were almost entirely filled with alteromorphs within a month of drilling (Fig 3.36 B). This occurred in pits in kamacite and taenite alone and was also observed in the rim sample of QUE 99022. This rapid growth

demonstrates the rate at which fresh surfaces are altered and may be in part due to water being implanted in the surface during ablation.

Spectacular growth was seen on the surface of ALH 85017 R (Fig 3.36 C) where large tubular growths of Fe-oxyhydroxides formed. On the basis of SEM imagery, these are most likely to be goethite. The alteromorphs have formed in a variety of morphologies in the single patch of alteration from the same parent grain. Botryoiodal features, needle structures and amorphous structures are all formed from the same parent mineral. On the same meteorite, rosettes of akaganeite have also formed from a kamacite grain and have spread over adjacent silicate hosted veins (Fig 3.36 D).

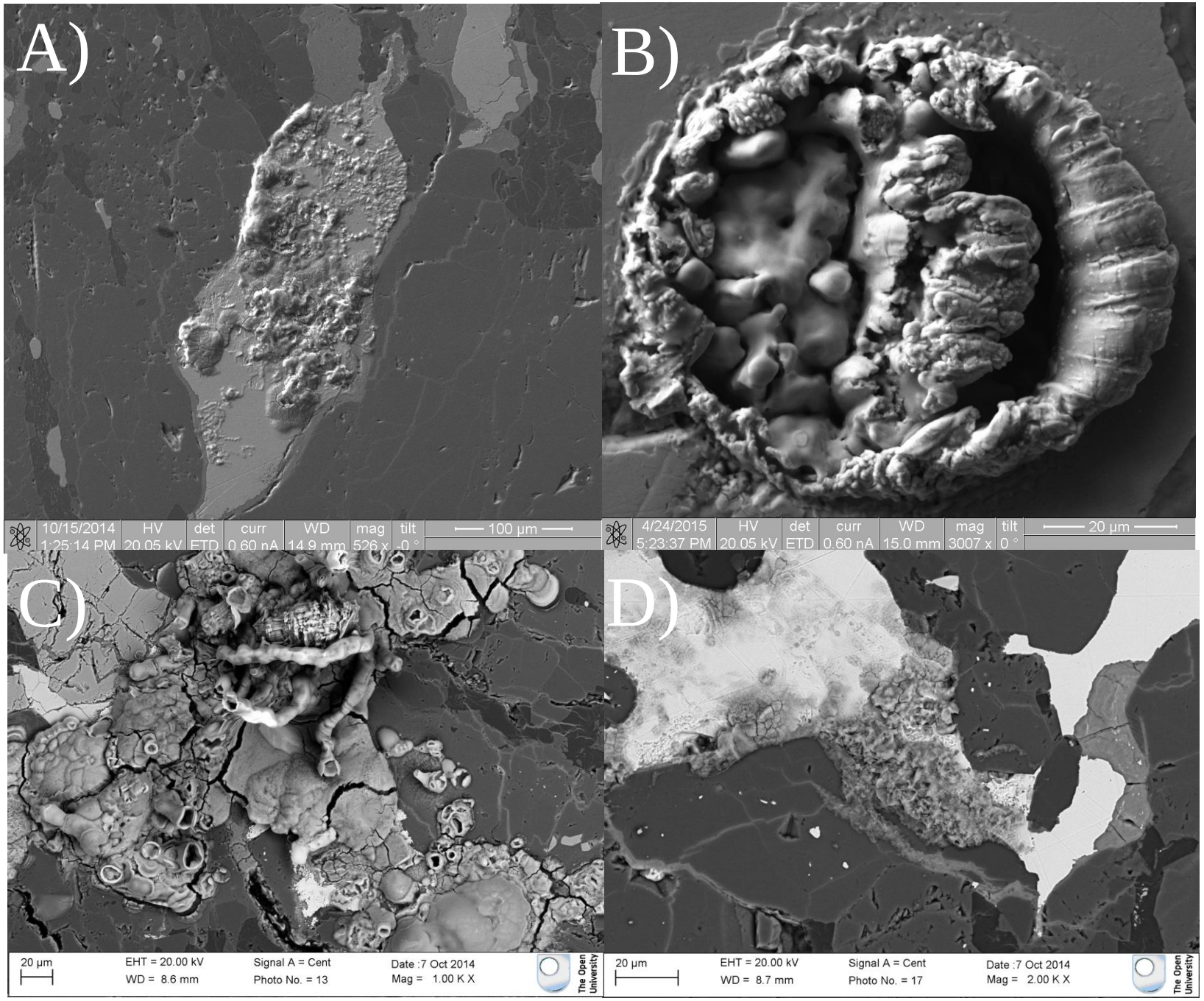

Fig. 3.36. BSE images of museum weathering in thick sections. A) ALH 84058. A kamacite grain has gained a "bubbly" texture as Fe-oxyhydroxides have grown over the surface. This is typical of many sections. B) Laser pit from ICP-MS in ALH 78130. This pit is under 2 weeks old and has infilled with Fe-oxyhydroxides, C) ALH 85017. Several different morphologies of Fe-oxyhydroxides have formed. Tubular growths of what is most likely goethite have grown as well as botroidal needle growths which have grown in a coliform aspect. D) ALH 85017. Rosettes of alteromorph have grown on a kamacite grain. This morphology is typical of akaganeite formation.

3.7. DISCUSSION: THE EFFECT OF SHOCK ON WEATHERING PATTERNS

Shock induced features can have a direct influence on weathering patterns in the meteorites. The shock grades of each meteorite have been determined using the method of (Stöffler et al., 1991), and are listed in Table 3.2 and features in each meteorite in Table 3.3. Most of the features alter the weathering patterns in the surrounding areas. The features that affect weathering patterns are:

- Planar fractures in olivine: The planar fractures in olivine, common to all meteorites studied, create additional access to fresh mineral surfaces for altering fluids. The importance of initial fracture placements, to eventual vein formation and propagation, is discussed above and so the creation of many fractures throughout olivine crystals mean that the olivine hosts a disproportionate number of veins compared to other mineral types, and is the most rusted. Dissolution along these planes of weakness is evident in all the meteorites.
- Transformation of plagioclase to maskelynite. The transformation of plagioclase to maskelynite reduces its weatherability, since no brittle fractures occur throughout the maskelynite. In un-transformed plagioclase, small linearly un-extensive fractures cover the crystals. In plagioclase with infilled fractures, the smaller fractures have expanded and joined up to make larger networks of veins. The pre-existing internal weaknesses in the plagioclase crystals make them more vulnerable to extensive mechanical fracturing (Fig. 3.37).

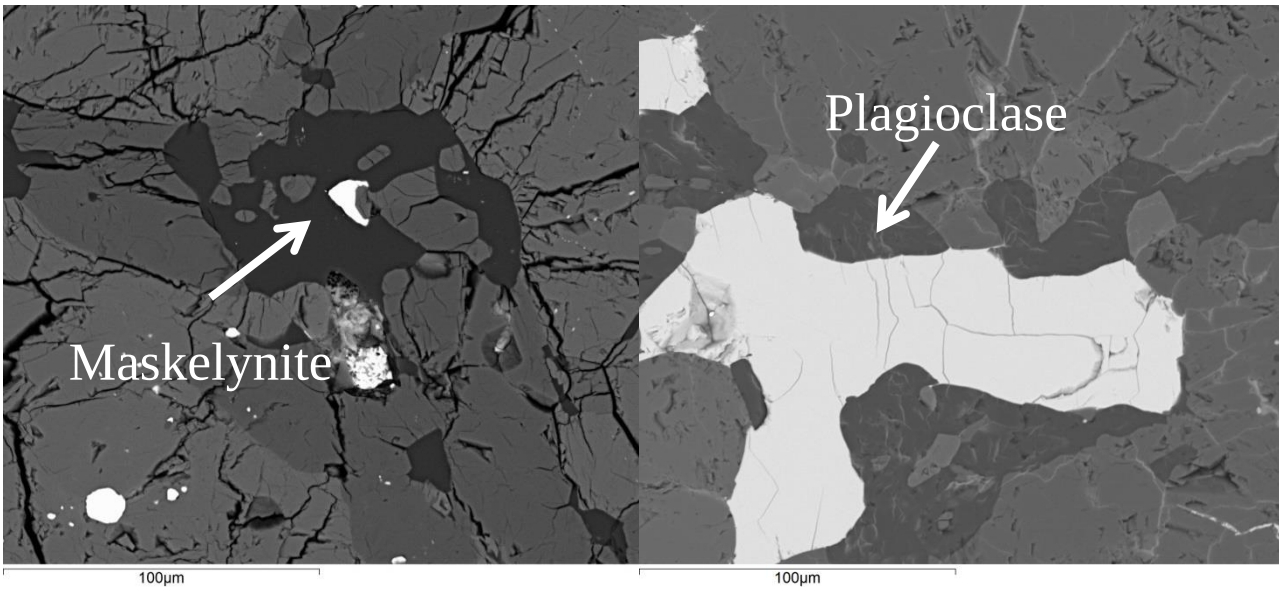

Fig. 3.37. Maskelynite and plagioclase fractures. A) QUE 94214 maskelynite. Smooth with no fractures penetrating. An intermineral vein follows around the grain. B) ALH 78130. Untransformed plagioclase surrounding kamacite is full of fractures, some of which have been infilled with veins. Most of the fractures are not linearly extensive and both begin and end in the crystal, not linking with the intermineral fractures.

- Polymineralic melt veins containing <5 μm spherules of troilite, kamacite and taenite. These melt veins concentrate rust and promote alteration because of the small (<5 μm) spherules of kamacite taenite and troilite contained in the veins, which alter and propagate alteration veins and products. As they are weathered out, they create a porous texture which allows fluid transport through the weathered melt veins. Silicate weathering is prevalent at these locations. The samples that contain melt veins demonstrate a higher porosity and higher amount of weathering surrounding these veins, and the intense weathering of the interior section of ALH 78130 compared to the rim sample, may result from the melt veins that cover the sample which are not present in the rim.
- Fizzed troilite-metal (Scott 1982) occurs in ALH 85017, QUE 99022, ALH 84056 and ALH 78130 (Section 3.2.5) and the fine intergrowth of metals and troilite increases the rate of weathering of both the metal and troilite. These fine grained intergrowths preferentially weather out the Fe-Ni metals in the troilite and replace

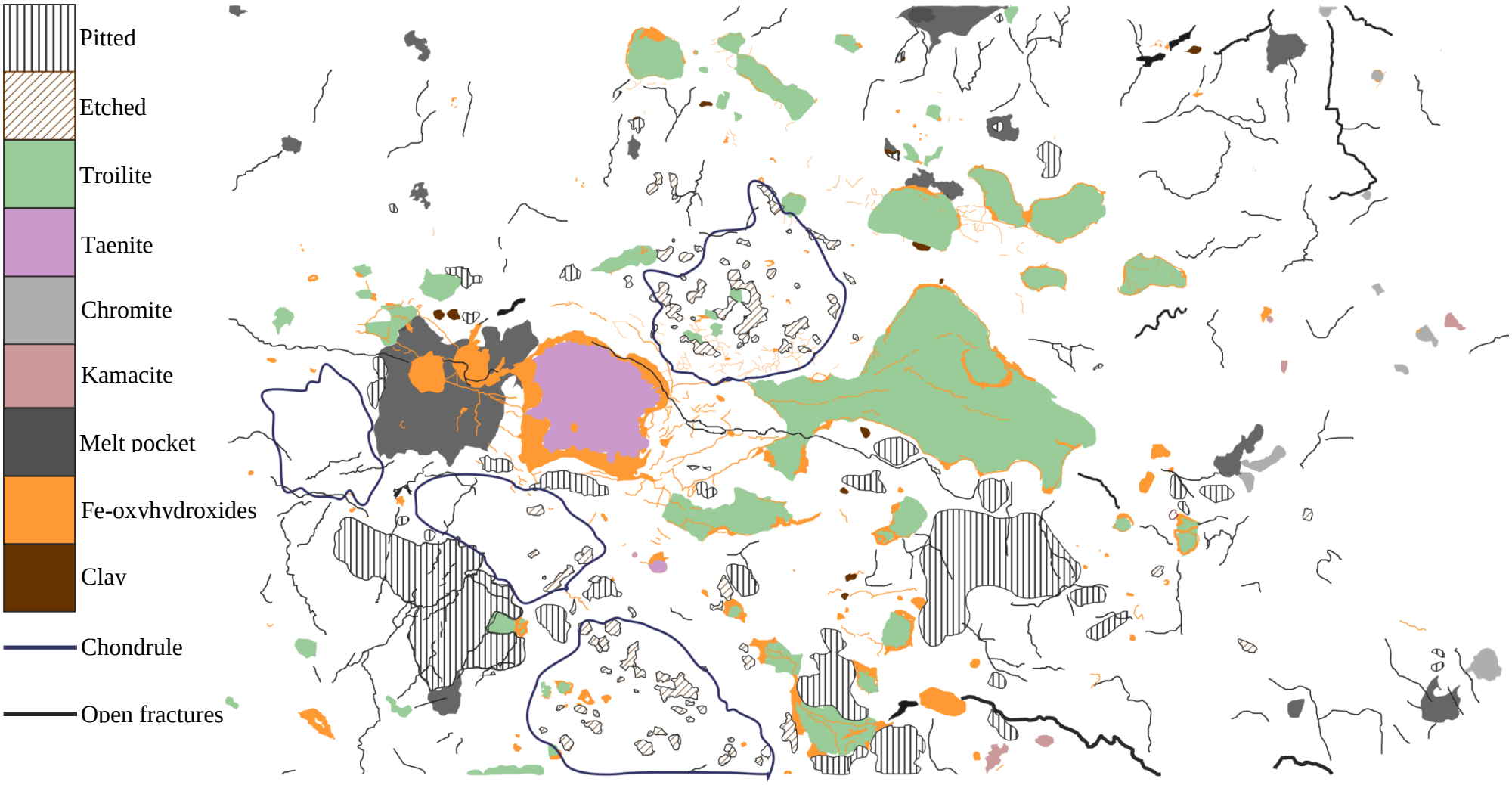

Fig. 3.38. A) Map of area A in QUE 94214. This demonstrates the proximity of the silicate alteration to the sulphide and taenite alteration. The olivine alteration preferentially affects large crystals outside of chondrules, and the pyroxene stripping affects the small crystals in chondrule relicts preferentially.

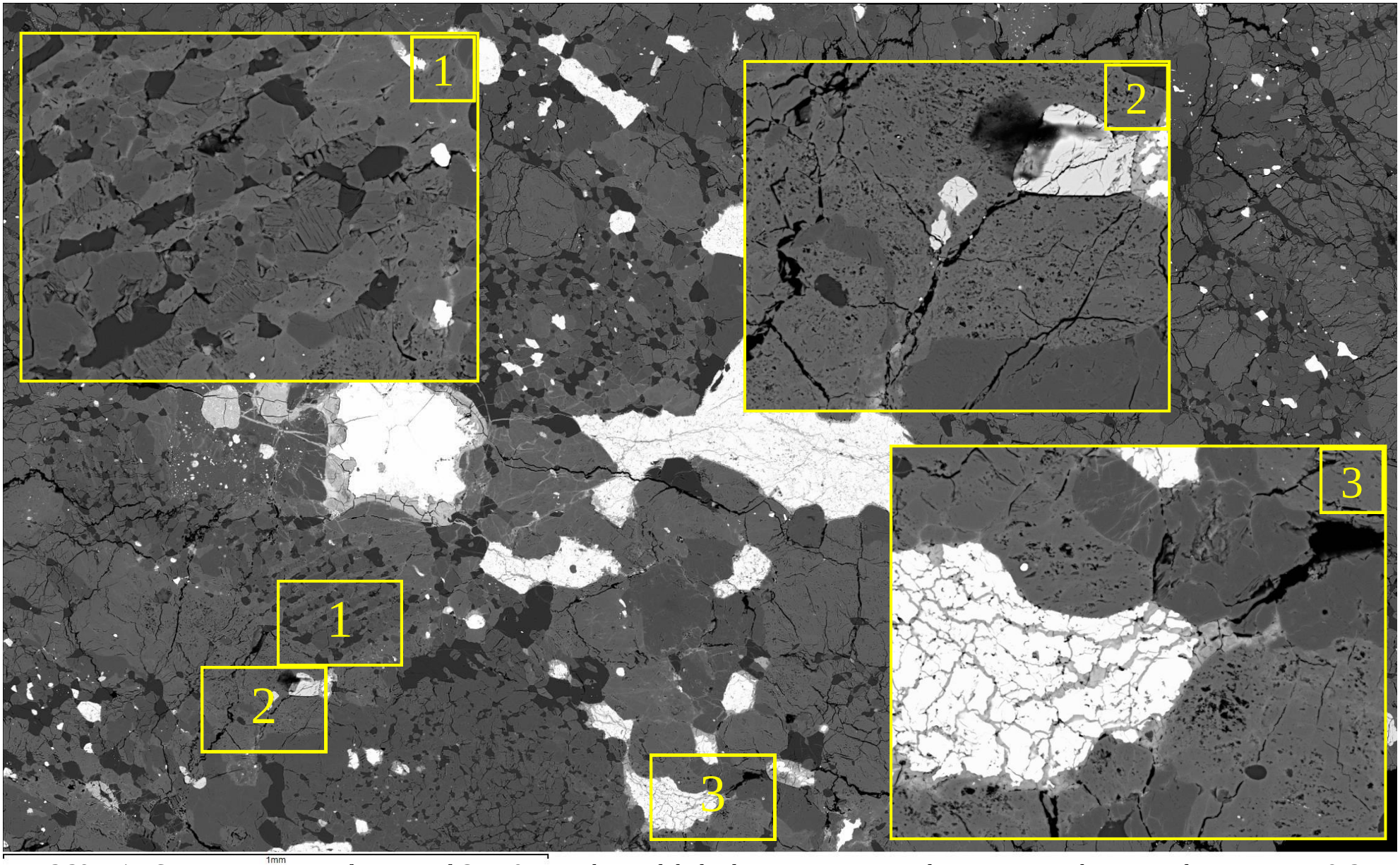

Fig. 3.38. B) BSE image montage of an area of QUE 94214 where sulphide alteration is causing silicate pitting in the surrounding area. 1, 2 & 3 are zoomed images. 1 shows pyroxene stripping along laminations, 2 and 3 show irregular olivine pitting.

Table 3.3. Shock Feature in Studied Meteorites. Grey areas denote the presence of a feature. Shock grades associated with the features are listed alongside. [1]Stöffler et al.,(1991), [2]Rubin (2003), [3]Bennet and McSween (2006).

Shock Features	QUE 99022		QUE 94214		ALH 78130		ALH 84056		ALH 84058		ALH 85017	
	R	I	R	I	R	I	R	I	R	I	R	I
Undulose olivine extinction (S2-3)[1]												
Mosaic olivine (S4-6)[1]												
Planar Fractures (S3-6)[1]												
Maskelynite (S5-6)[1]						40 %		Some				
Clusters of chromite formed in plagioclase/maskelynite (S3-6)[2]												
Polycrystalline kamacite (S3-6)[3]												
Plessite intergrowths (S3-6)[3]												
Melted metal droplets (S4-6)[3]												
Polycrystalline troilite (S4-6)[3]												
Fizzed troilite (S2-6)[3]												
Melted troilite droplets (S4-6)[3]												
Polymineralic melt veins (S4-6)[3]												

them with porous Fe-oxyhydroxides, presenting a larger surface are of troilite for altering fluids to access, and troilite alters from the centre. The fizzes vary in coarseness and size with the more fine grained fizzes weathered more than the coarse and promote weathering in meteorites affected.

- Polycrystalline troilite exerts the second most noticeable effect on the weathering of a meteorite. Pyroxene and olivine break down where they are surrounding alteration of polycrystalline troilite. To understand this relationship more fully a detailed map of an area of polycrystalline troilite decomposing has been made (Fig. 3.38 A.) and the effects are investigated in more detail below.

Effect of shocked troilite

Troilite grains have a high density of veins that follow the planes of weakness created by the polycrystalline microstructures. The main deposits from the alteration product derived from troilite breakdown are restricted to around and within the crystals and do not extend far beyond the original grain (<100 μm). Olivine adjacent to the altering troilite (within 500 μm) alters to an irregular porous texture of etch pits, while the pyroxene alters in a regular pattern along its planes of cleavage, leaving behind fine laminations of parent material (Velbel 2009, Velbel and Barker 2008). Many of the pits formed in the olivine surrounding the troilite are not the v-shaped etch pits commonly found in olivine, but are a more irregular shape, possibly from the convergence of several pits (Velbel 2009). Some of the pits directly adjacent to weathering troilite extend to 5 μm diameter, many of which form in the centre of the olivine crystal rather than the outer edges (Fig. 3.34 B). Outside of the area imaged (width of field ~1.5 mm), the etching and pitting of ferromagnesian minerals does not occur unless in a similar proximity to weathering troilite.

The breakdown of troilite is very destructive to silicates because the hydration of troilite provides sulphuric acid following this reaction:

$$2FeS + 2H_2O + 4½O_2 \leftrightarrow Fe_2O_3 + 4H^+ + 2SO_4^{2-}$$

The hydration of troilite releases H^+ which added to olivine results in its dissolution:

$$Fe^{2+}{}_2SiO_4 + 4H^+ \leftrightarrow H_4SiO_4 + 2Fe^{2+}$$

Since the polycrystalline microstructure renders the troilite much more susceptible to weathering, there is an observable increase in silicate weathering surrounding troilite of this type.

The changes caused by shock processes most affect metal and sulphide grains and almost all make the meteorite more vulnerable to weathering processes. The effects on silicates can both be beneficial to weathering resistance (e.g., the transformation to maskelynite) and harmful (e.g., formation of planar fractures in olivine). Higher shock grades by themselves will therefore not identify whether a sample will weather more strongly, but a cursory study of metal and sulphide forms will inform the likely rate of weathering.

3.8. Discussion: Sample bias between thin and thick sections

The petrological characterisation of most of the samples was performed on thin sections, but thick sections used for LA-ICP-MS needed prior mapping so useful spatially calibrated data could be collected. Thick sections were large (all over 1 cm^3) pieces of meteorite embedded in an epoxy mount, the top surfaces of which were polished to a grade fine enough for analysis. Depth of epoxy plug ranges between 1.5 to 2 cm.

The mapping of these samples led to the observation that there were more alteration products present in the thick sections at the rim, where in the thin section, cavities were present. This was especially true of alteration products that were not pure Fe-

oxyhydroxides which have a more delicate structure (Fig. 3.39). Small pockets of clay were observed in several meteorites in thick section that were not present in thin section. Delicate silicate alteration structures like highly etched areas where thin plates of silicate remain were also not preserved. It is likely that these delicate minerals have been plucked out during thinning of samples and have left cavities behind. In the thick sections, delicate minerals may have been removed from the top few microns of the section face, but remain as they exist in greater depth. It is thus important to assess secondary mineralogy in thick section where possible, otherwise coherent, non-porous alteromorphs will be proportionately over-represented.

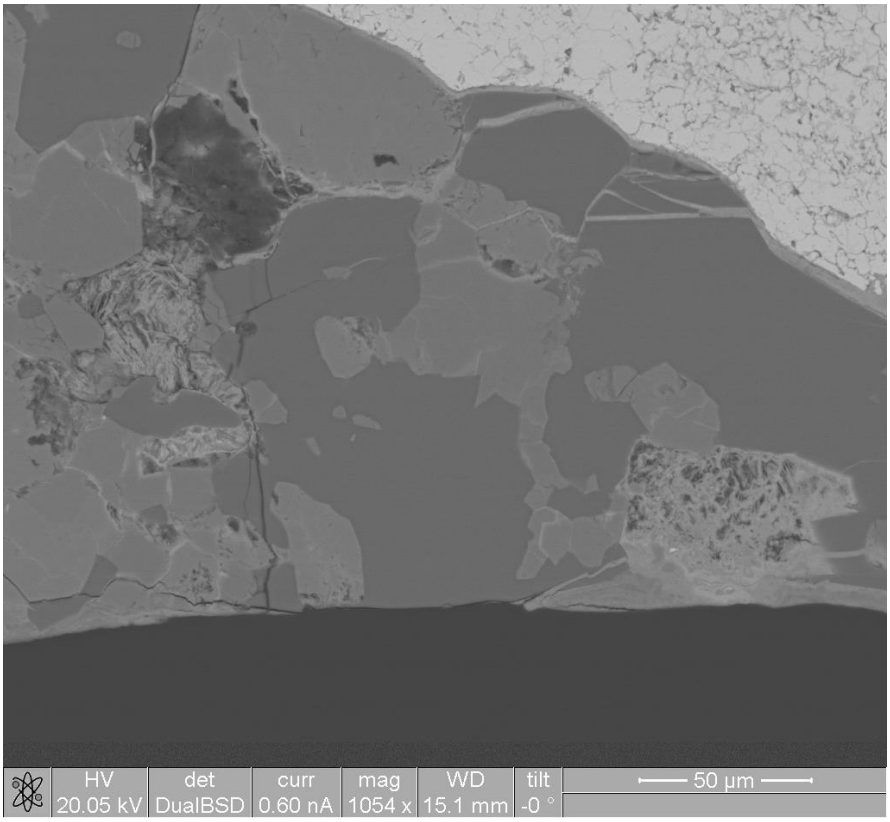

Fig. 3.39. QUE 99022 BSE. Image from a thick section contains pockets of clay minerals and sulphates that are not observed in thin section. The delicate structure of the clays is unlikely to survive the cutting process.

Museum weathering occurs on most thick sections but is rarely seen in thin sections. Since the museum alteration takes the form of hydration of metal grains, this suggests that the thick sections are retaining more water than the thin sections. This is probable, as the increased extent of fracture networks that are present throughout the thick chips will transfer water by capillary action. The water must have been gained from humidity or retained from Antarctica since none of the samples have been exposed to fluids since collection.

CHAPTER 4 – SPATIALLY RESOLVED DATA

This chapter is divided into two main sections; the first describes data from electron microprobe analysis (EMPA), the second presents the results of the Laser Ablation-Inductively Coupled Plasma Mass Spectrometry (LA-ICP-MS) analysis. For both sets of analyses, the results are considered by mineral, rather than by meteorite, to enable a comparison of the effects of weathering between meteorites.

4.1. EMPA DATA

Electron microprobe data were collected in order to measure chemical alteration at a micron scale. All analysis are reported in Appendix I. As the purpose of this study is to examine alteration of minerals, exclusion of non-stoichiometric mineral data would exclude the very minerals that the study is aimed at. In all data that follows, non-stoichiometric data is labelled as such so that due consideration can be taken in discriminating poor analyses from true analyses of altering minerals. Totals between 98.0-102 wt.% were accepted. Errors for EMPA data was calculated from an in-house unknown (garnet) that was measured repeatedly throughout the period of study (full data set in Appendix I). From this data, a standard deviation for major elements, minor elements and trace elements was ascertained.

4.1.1 OLIVINE

The main constituents of olivine measurable by EMPA are: SiO_2, MgO, FeO, MnO, CaO and average compositions in the different meteorites are 73.86-75.05 % Fo (Table 4.1.), and so are within L chondrite classification as set out by Keil and Fredricksson (1964) (Fig 4.1.).

Table 4.1. Average compositions of stoichiometric olivines in study

	SiO_2	TiO_2	Al_2O_3	Cr_2O_3	FeO	MnO	MgO	CaO	Total	%Fo
QUE 99022 R	37.76	0.01	0.11	0.05	22.59	0.42	37.91	0.09	99.45	74.50
QUE 99022 I	37.78	0.01	0.04	0.12	21.97	0.42	38.32	0.04	98.98	75.25
QUE 94214 R	37.87	0.01	0.00	0.03	22.20	0.44	38.38	0.03	99.12	75.10
QUE 94214 I	37.89	0.01	0.02	0.04	22.06	0.43	38.24	0.02	98.86	75.17
ALH 84058 R	37.96	0.00	0.00	0.01	23.55	0.46	38.23	0.02	100.36	73.92
ALH 84058 I	38.45	0.01	0.00	0.01	23.37	0.46	38.35	0.02	100.81	74.12
ALH 85017 R	38.18	0.01	0.00	0.01	21.80	0.44	38.92	0.07	99.71	75.65
ALH 85017 I	38.49	0.01	0.00	0.01	22.45	0.46	39.19	0.02	100.80	75.28
ALH 84056 R	38.59	0.01	0.00	0.03	23.13	0.47	38.56	0.02	100.90	74.43
ALH 84056 I	38.76	0.01	0.00	0.02	22.65	0.46	38.81	0.02	100.80	74.94
ALH 78130 R	38.41	0.01	0.00	0.02	22.63	0.46	38.57	0.02	100.23	74.83
ALH 78130 I	38.26	0.01	0.00	0.02	22.84	0.46	38.57	0.03	100.38	74.66

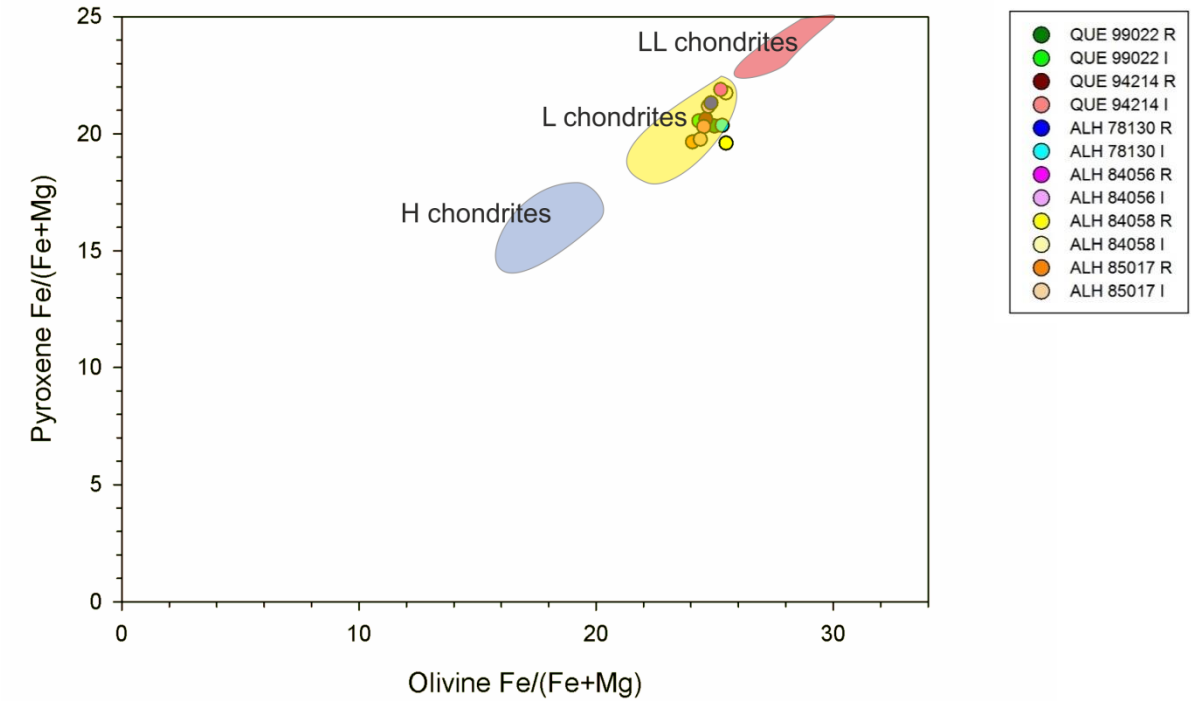

Fig. 4.1. Average olivine and pyroxene compositions measured in each meteorite in the study. All fall in the L chondrite category set out by Keil and Fredriksson (1964).

General Compositions

The olivines in QUE 99022 vary significantly in terms of SiO_2, FeO wt.% and MgO wt.% (Fig 4.2.) with a general spreading of values in the rim compared to the interior. The rim contains many more non-stoichiometric olivines with a greater FeO on average that fall outside of the FeO range that defines L chondrites. These high FeO olivines contain less SiO_2 and MgO, suggesting an enrichment of Fe concurrent with a removal of SiO_2 and MgO.

The non-stoichiometric analyses plot in a well-defined discrete area, evidencing a process in the olivines rather than poor or mixed analyses. The MgO/FeO relationship (Fig. 4.3.) largely follows the substitution line expected in olivine (1:1 negative relationship) in the stoichiometric olivines, but is skewed towards a greater Fe, lesser Mg ratio in the non-stoichiometric olivines.

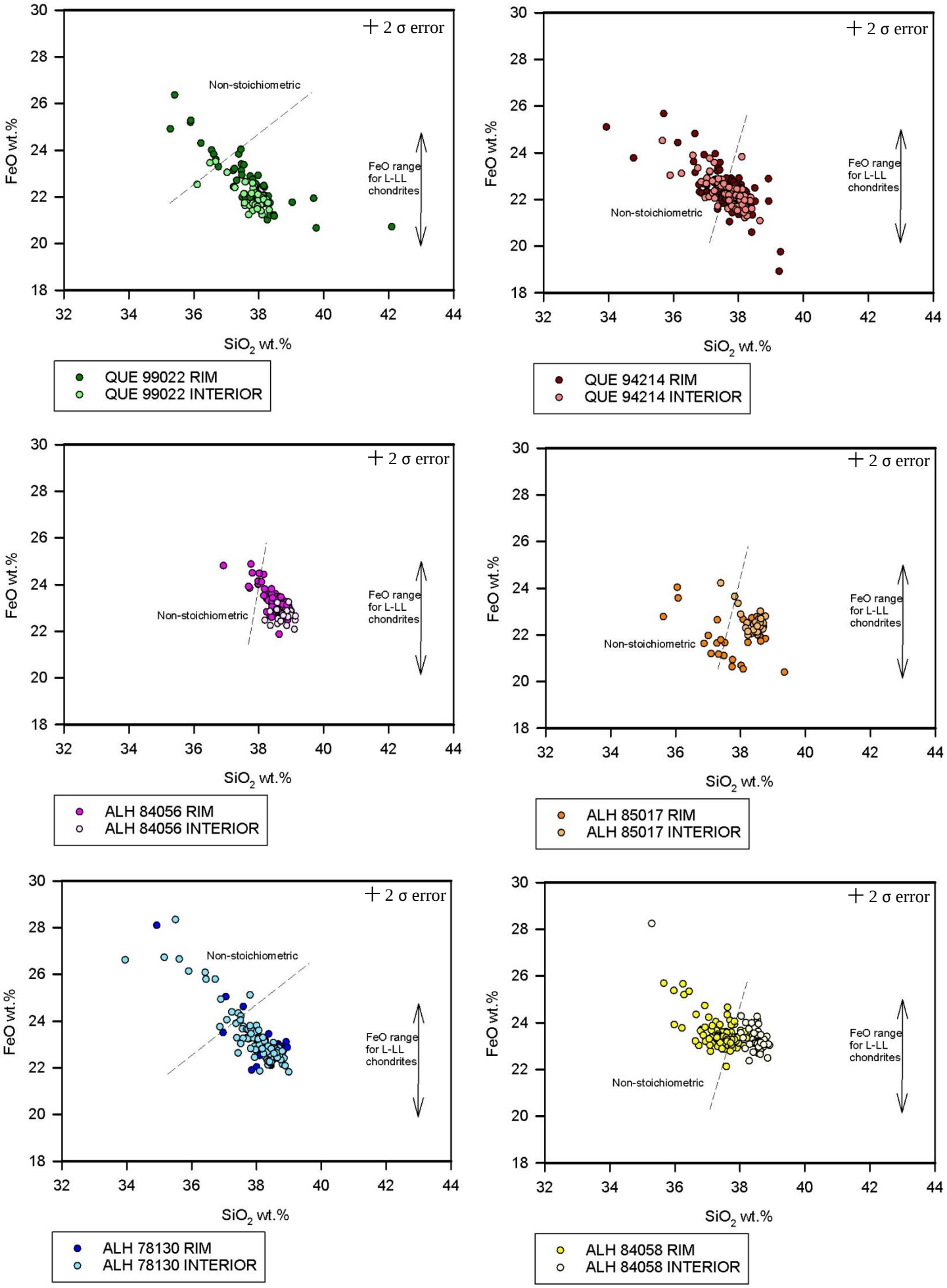

Fig. 4.2. SiO_2 vs FeO of olivines in all meteorites studied. Each graph contains a FeO range as specified by Keil and Fredricksson (1969) as the range of L-LL chondrites olivines. Also included is a dashed line which indicates an extent beyond which over 90% of the analyses are non-stoichiometric olivines.

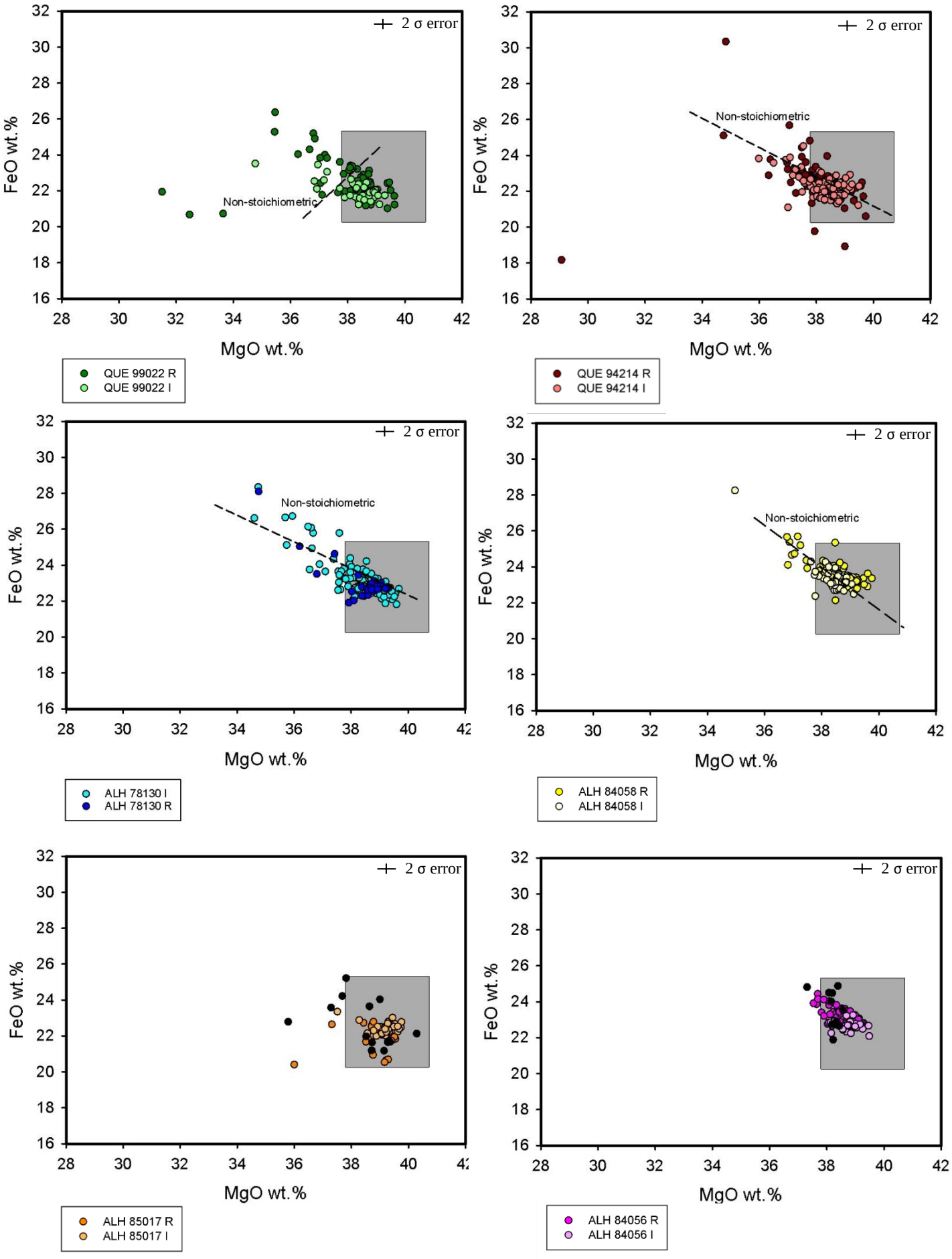

Fig. 4.3. MgO vs FeO of olivines in all meteorites studied. Grey squares denote the area that is defined as L-LL chondrite olivine compositions by Keil and Fredriksson (1964). The top four diagrams have stoichiometry lines, beyond which over 90 % of the analyses are non-stoichiometric. The bottom two diagrams have a third plot (black spots) indicating where non-stoichiometric analyses lie.

In QUE 94214 I there are proportionally more non-stoichiometric olivines than QUE 99022 (31 % in the former vs. 8 % in the latter), which is an indication of more altered olivines in QUE 94214 I, in particular in the interior sample since the rim has a similar number to QUE 99022. The grouping of the non-stoichiometric olivines is also quite different and do not show the high FeO of QUE 99022. Instead it is more similar to ALH 78130 and ALH 84058 which all have a higher MgO:FeO ratio. They similarly have less SiO_2 in the altered (non-stoichiometric) olivines and so appear to be concentrating MgO and FeO rather than removing the MgO and adding FeO as is the case in QUE 99022.

Dissimilar to all other meteorites except ALH 78130, the olivines measured in the interior section contain more non-stoichiometric, apparently altered olivines. Interestingly, most of the olivine analyses still sit in the accepted field for L-LL chondrites (Fig. 4.3.).

ALH 78130 interior contains many non-stoichiometric olivine analyses with high FeO, low SiO_2. No difference in MgO content is observed between the stoichiometric and non-stoichiometric analyses, suggesting that there is an addition of FeO with a reduction in SiO_2 but no loss of MgO. As mentioned previously, a greater number of these non-stoichiometric, low SiO_2, high FeO olivines exist in the interior than the rim and many of these lie well outside of the accepted values for L-LL chondrites (Fig. 4.2., Fig. 4.3.; Keil and Fredriksson, 1964) demonstrating that the interior olivines of ALH 78130 are more altered than the olivines in the rim. The range of MnO wt.% values in both rim and interior is higher than in QUE 94214 olivines, mainly clustering between 0.43-0.49 wt.%.

ALH 84056 and ALH 85017 both show similar trends in that both meteorites have a tight cluster of olivines compositions with little spread. ALH 84056 interior olivines in particular have an extremely small compositional range compared to the olivines in other meteorites. Fig. 4.3 demonstrates that both have almost all their olivine analyses in the L-LL chondrite defined field with little spread beyond. The plots show that the non-stoichiometric olivine analyses are spread evenly across the fields, suggesting that these

are just poor or mixed analyses rather than inherent to an alteration process. ALH 84056 rim compared to the interior shows a spreading of values from the tight grouping of the interior olivines, with a spreading of lower MgO, greater FeO values. ALH 85017 demonstrates a more erratic spreading of values in the rim sample with some low FeO values not seen in the other meteorites.

ALH 84058 olivines cover a moderate spread of MgO, FeO and SiO_2 values compared to the other meteorites in the study, with most of the analyses remaining in the defined field of L-LL chondrites for FeO, but with many points of a lesser MgO than the defined field.

There is a significant rim/interior difference with the rim values containing many more non-stoichiometric values with higher FeO and lower SiO_2. The MgO values between the rim and interior show little difference.

Rusty olivines

To assess whether visible rust makes a measurable difference to olivine compositions, three meteorites with rusted and non-rusted areas, were compared (QUE 94214 R+I, ALH 84058 R+I, ALH 78130 R). The other meteorites were either wholly covered in rust (QUE 99022, ALH 78130 I), or had too few significantly rust covered areas (ALH 84056, ALH 85017).

QUE 94214: There is a general broadening to low SiO_2, low Mg# olivines in rusted areas of QUE 94214 caused by an increase of FeO (Fig. 4.4). The real difference in composition is between the non-stoichiometric olivines that have been altered. Whilst there is a spreading of values between rusted and non-rusted in the stoichiometric olivines, there is a significantly greater range of values in the non-stoichiometric (Fig. 4.4.). The non-stoichiometric olivine in rusted areas shows a significant increase of FeO wt.% with an average FeO wt.% of 23.48 % compared to the stoichiometric rusted olivines (22.17 wt.%)

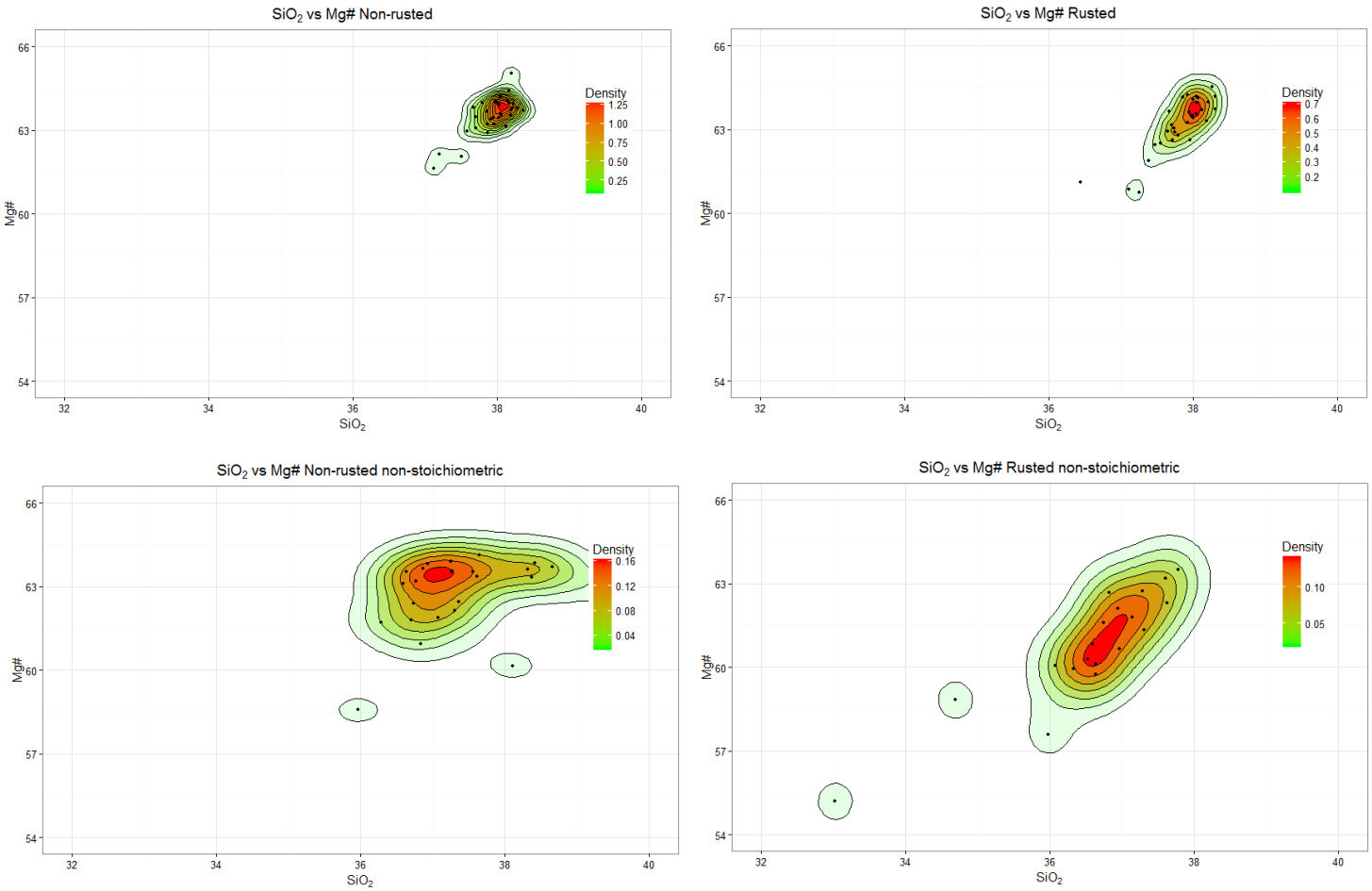

Fig. 4.4. SiO_2 vs Mg# in olivines measured in QUE 94214 I. The colour of the contours reflects the probability of a point occurring in that contour.

and more so compared to the non-rusted stoichiometric olivines (21.98 wt.%). Whilst a few of the non-stoichiometric analyses are potentially poor or mixed analyses, all have good totals (98-102 wt.%) and so most of these analyses are reflecting an addition of Fe-oxide/oxyhydroxides concurrent with a dissolution of the olivine, resulting in a decrease in SiO_2 and MgO. An important difference is recorded in the non-stoichiometric olivines in non-rusted and those in rusted areas. A decrease in SiO_2 is apparent, but a concurrent decrease in Mg# is only slightly in evidence. This demonstrates that the SiO_2 is being removed but there is no addition of FeO. This shows that deposition of Fe-oxides/oxyhydroxides is minimal or absent in the non-rusted areas.

ALH 78130 (Rim): As less than 5 % of the analyses gathered from ALH 78130 were non-stoichiometric, these are likely poor or mixed analyses and are not discussed as part of this data set or included in the analysis. The interior section of ALH 78130 is entirely covered in rust, so rusted and non-rusted areas were only compared in the rim. The rusted olivines in general have more FeO wt.% than the non-rusted (by ~ 0.5-1.0 wt%). The spread of FeO wt.% values is generally lower than in QUE 94214 and there is no appreciable difference in SiO_2, MgO or MnO contents of rusted and non-rusted olivines.

ALH 84058: The rusted and non-rusted olivines in the rim and interior have similar FeO, SiO_2 and MgO contents with no significant differences. Similarly, to ALH 78130, there are <5 % non-stoichiometric analyses which are statistically likely to be poor analyses.

Table 4.2. Average compositions of pyroxenes. Where relevant, an average composition for non-stoichiometric pyroxenes is also given. ALH 85017 R and ALH 84056 I only had single non-stoichiometric analyses, so the average has not been included.

Sample	SiO_2	TiO_2	Al_2O_3	Cr_2O_3	FeO	MnO	MgO	CaO	Na_2O	Total	Wo	En	Fs
QUE 99022 R	55.24	0.19	0.15	0.14	13.70	0.45	29.14	0.70	0.02	99.89	1.36	77.03	21.61
Non stoic	53.20	0.21	0.20	0.60	15.61	0.44	28.03	0.72	0.03	99.60	1.39	75.17	23.45
QUE 99022 I	55.20	0.19	0.14	0.12	13.38	0.45	28.78	0.99	0.02	99.39	1.82	77.12	21.06
Non stoic	53.22	0.16	0.15	0.11	15.65	0.43	27.77	0.77	0.01	98.63	1.50	74.84	23.66
QUE 94214 R	55.02	0.18	0.14	0.15	13.60	0.46	28.69	0.88	0.02	99.33	1.68	77.44	20.88
Non stoic	53.55	0.18	0.15	0.26	14.91	0.45	28.48	0.75	0.01	99.21	1.55	76.32	22.13
QUE 94214 I	55.38	0.16	0.29	0.18	13.16	0.45	28.58	0.90	0.06	99.32	1.78	77.16	21.06
Non stoic	54.43	0.19	0.18	0.17	14.07	0.45	28.55	0.92	0.02	99.19	1.79	76.94	21.27
ALH 84058 R	54.96	0.16	0.13	0.13	14.36	0.48	28.92	0.80	0.02	100.12	1.51	76.67	21.82
Non stoic	53.58	0.18	0.15	0.24	15.23	0.48	28.65	0.77	0.02	99.74	1.47	75.89	22.64
ALH 84058 I	55.81	0.17	0.13	0.13	14.22	0.48	28.67	0.84	0.01	100.58	1.63	76.71	21.66
Non stoic	53.28	0.14	0.11	0.11	17.06	0.46	27.40	0.88	0.04	100.39	1.68	72.86	25.45
ALH 85017 R	55.00	0.17	0.15	0.11	13.30	0.46	29.06	0.80	0.03	99.34	1.54	78.28	20.18
ALH 85017 I	55.91	0.15	0.15	0.10	13.83	0.49	29.24	0.78	0.04	100.81	1.46	77.38	21.16
Non stoic	54.25	0.16	0.13	0.14	15.04	0.48	29.54	0.75	0.02	100.73	1.41	76.72	21.88
ALH 84056 R	56.11	0.17	0.14	0.12	14.03	0.48	28.95	0.84	0.01	100.90	1.58	76.36	22.05
Non stoic	55.02	0.19	0.16	0.24	15.21	0.48	28.34	0.82	0.02	100.62	1.57	75.66	22.77
ALH 84056 I	56.04	0.16	0.17	0.12	13.74	0.49	28.75	0.81	0.04	100.39	1.48	77.66	20.86
ALH 78130 R	55.67	0.16	0.13	0.12	13.88	0.49	28.67	1.02	0.02	100.25	1.89	76.71	21.40
Non stoic	53.81	0.20	0.17	0.24	16.21	0.48	27.86	0.72	0.03	100.09	1.59	76.62	27.44
ALH 78130 I	55.52	0.17	0.13	0.14	14.12	0.48	28.95	0.80	0.02	100.52	1.50	76.59	21.91
Non stoic	53.19	0.17	0.15	0.11	16.62	0.47	28.17	0.72	0.01	100.19	1.36	74.10	24.54

4.1.2. PYROXENE

The representative compositions of pyroxenes in the study are shown in Table 4.2., full results in Appendix I. There are two species of pyroxene in the samples; a low Ca-orthopyroxene and a high Ca-diopside. Because diopside is an accessory mineral rather than a major constituent, analyses are sparse, so unless specified explicitly, the descriptions below concern low Ca-pyroxene. The average compositions of the low Ca pyroxenes in the different meteorites fall within L chondrite classification (average value $Wo_{1.6}En_{77.1}Fo_{21.3}$) as set out by Keil and Fredricksson (1964) (Fig 4.1.).

General compositions

Pyroxenes in QUE 99022 have very similar FeO and SiO_2 contents in both rim and interior sections (Fig. 4.5), with a small number of non-stoichiometric analyses in the interior section that could be regarded as poor analyses, and a large number of non-stoichiometric pyroxenes in the rim which are higher in FeO, lower SiO_2 (average 1.91 wt.% higher FeO, 2.04 less SiO_2). The non-stoichiometric pyroxenes are outside the FeO range typical of L chondrites (Keil and Fredricksson 1964) as the stoichiometric pyroxenes are all within error of this range (with a single exception).

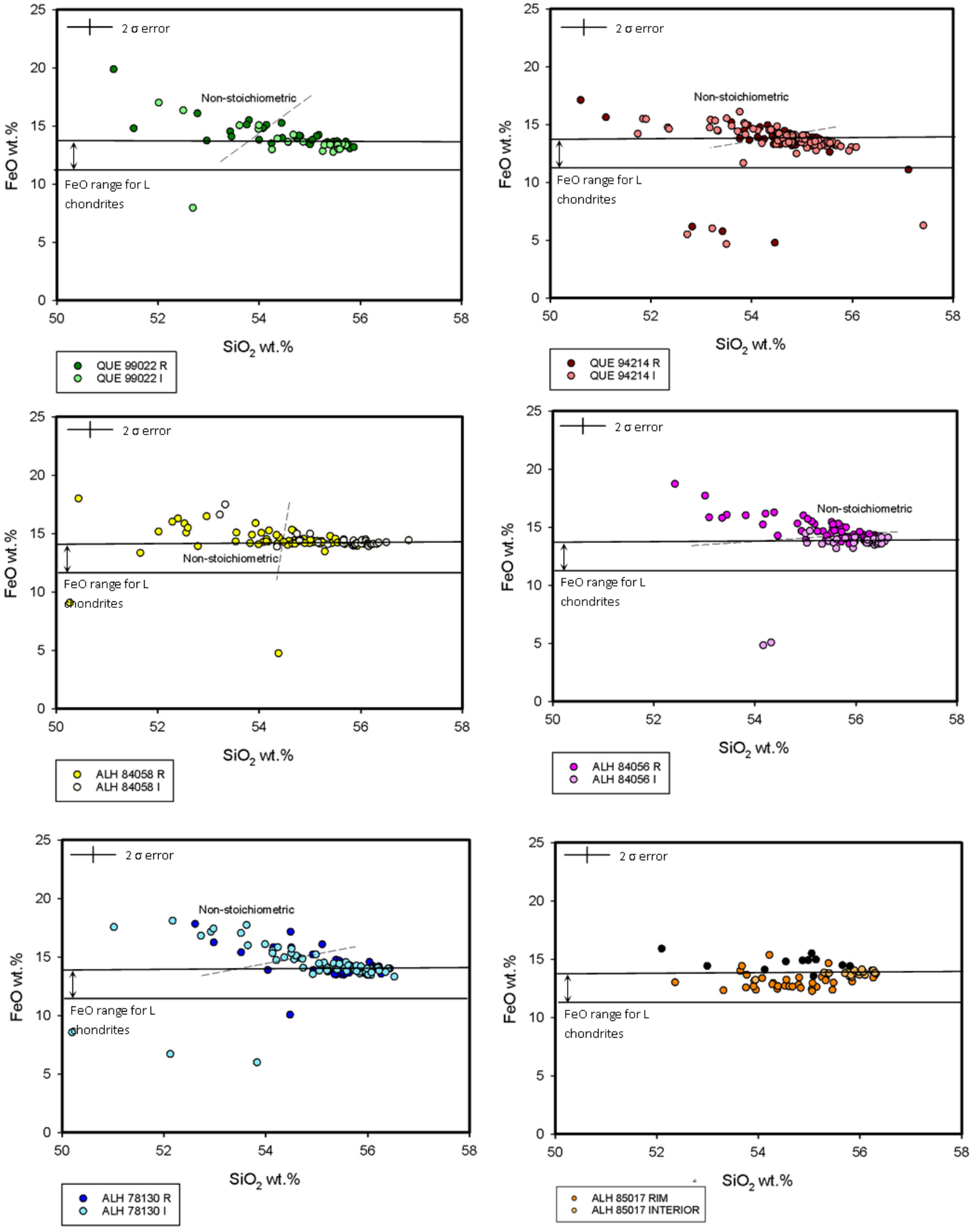

Fig. 4.5. SiO_2 and FeO wt.% content of pyroxenes in the study. Marked on is the range of L chondrite pyroxene compositions set out by Keil and Fredricksson (1964) as well as a dotted line indicating where beyond there are more than 90 % non-stoichiometric analyses. The exception is ALH 85017 which has non-stoichiometric data indicated by black dots.

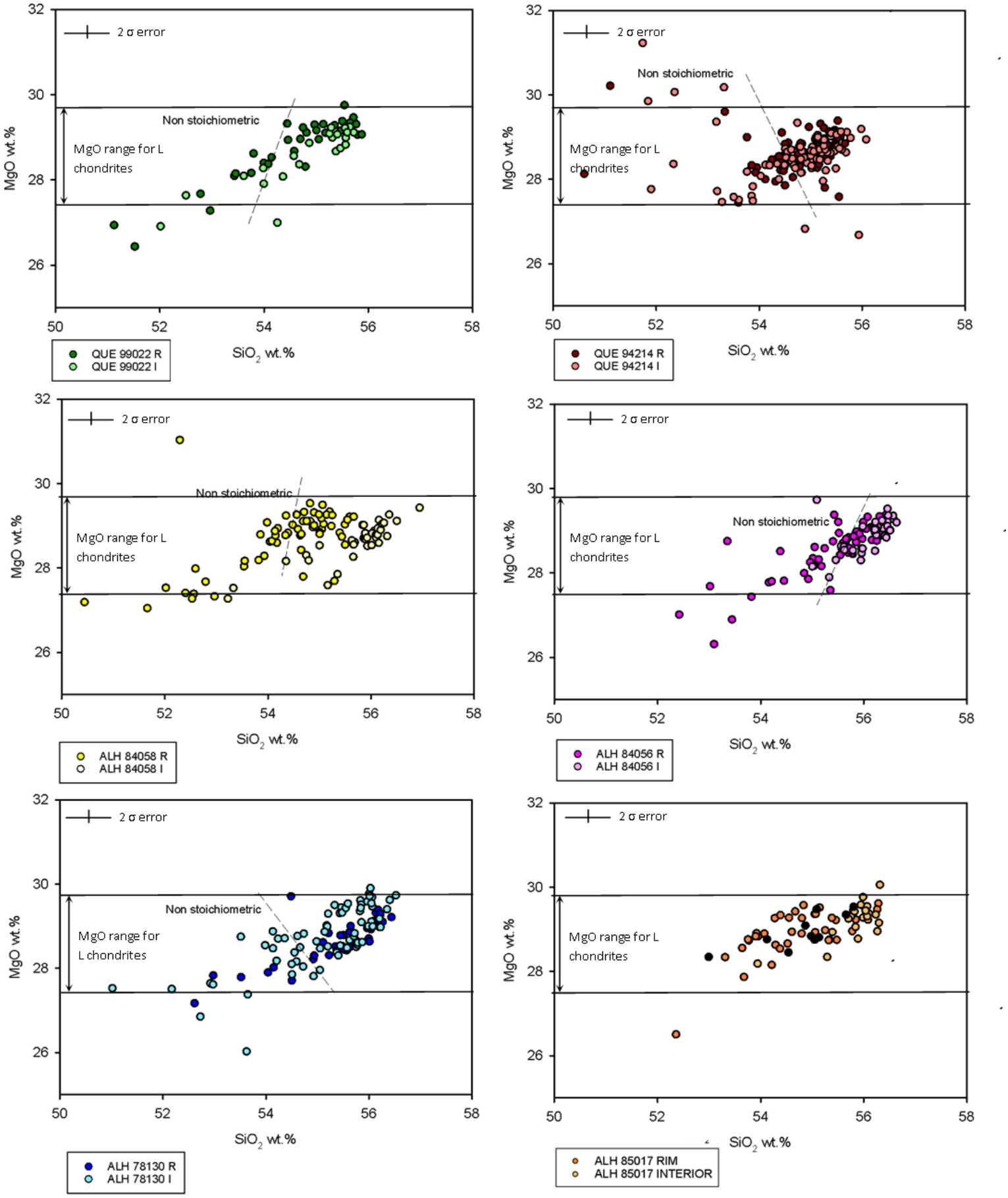

Fig. 4.6. SiO_2 and MgO wt.% content of pyroxenes in the study. Marked on is the range of L chondrite pyroxene compositions set out by Keil and Fredricksson (1964) as well as a dotted line indicating where beyond there are more than 90 % non-stoichiometric analyses. The exception is ALH 85017 which has non-stoichiometric data indicated by black dots.

The MgO shows little difference between the stoichiometric and non-stoichiometric pyroxenes (Fig. 4.6) with almost all of the analyses remaining in the L chondrite range. There is a slight decrease of MgO in the non-stoichiometric analyses with an average decrease of 0.1 wt.% (table 4.2.).

QUE 94214 rim and interior pyroxenes have similar ranges of major elements, but the interior contains many more non-stoichiometric analyses than the rim. The non-stoichiometric pyroxenes cluster similarly to QUE 99022 with lesser SiO_2 and MgO with a corresponding increase of FeO which pushes the compositions out of the field of FeO compositions usual for L chondrites and into the LL field (Fig. 4.5.).

ALH 84058 rim and interior pyroxenes are on the upper limit of the L chondrite field and are borderline LL compositions by the FeO wt.%, however they are safely in the MgO L chondrite field which suggests an addition of Fe in many of the pyroxenes. This is especially apparent in the high FeO pyroxenes. ALH 84058 rim contains many more non-stoichiometric, low SiO_2 pyroxenes than QUE 99022 which is surprising based on the relative amounts of rust in the two samples.

ALH 84056 interior pyroxenes are all within error of the FeO L chondrite field, and as the least weathered meteorite studied, has a tight cluster of major elements with only a single non-stoichiometric analysis, which is therefore likely to be an erroneous analysis. ALH 84056 rim, however, contains many non-stoichiometric pyroxene analyses and is similar to ALH 84058 rim in compositional spread.

ALH 78130 I has the one of the largest compositional spreads of all the meteorites studied, with many non-stoichiometric pyroxene analyses that contain greater FeO and lesser SiO_2, most of which are well outside of the L chondrite field. Even the most extreme FeO wt.% compositions are mostly still in the L chondrite field for MgO. The non-stoichiometric

analyses do largely contain a small drop in MgO with an average drop of 0.81 wt.% (table 4.2.).

ALH 85017 contains very few non-stoichiometric analyses with all being in the interior of the meteorite. These analyses all (except one) have FeO wt.% higher than the range for L chondrites. The MgO wt.% between stoichiometric and non-stoichiometric analyses is the same.

With the sole exception of ALH 84056, there are no significant rim-interior differences in pyroxene composition in any of the meteorites.

Rusted pyroxenes

Pyroxene compositions were also compared in the two meteorites (QUE 94214 and ALH 84058) that had sufficiently discrete areas and analyses.

QUE 94214: Fig. 4.7 A) shows the significant differences between stoichiometric and non-stoichiometric pyroxenes. The non-stoichiometric, non-rusted pyroxenes have a similar compositional spread to the non-stoichiometric rusted pyroxenes with any differences between them being within error. The stoichiometric rusted and non-rusted pyroxenes show a slight spreading of FeO and SiO_2 in the rusted area, but these differences are again, mostly within error. The non-stoichiometric pyroxenes have a significantly lower SiO_2 regardless of whether they are rusted or not and the change in FeO is restricted to a few pyroxenes rather than a general FeO increase in all pyroxenes.

ALH 84058: The rusted stoichiometric pyroxenes show an increase of FeO wt.% in some of the analyses (Fig. 4.7 B) but most are in a similar field to the non-rusted pyroxenes. The non-stoichiometric pyroxenes in the rusted areas, however, show a significant increase in FeO and decrease in SiO_2 in the majority of analyses. The non-stoichiometric non-rusted pyroxenes still contain many lower SiO_2 points but do not necessarily have an increase in FeO that the rusted ones do.

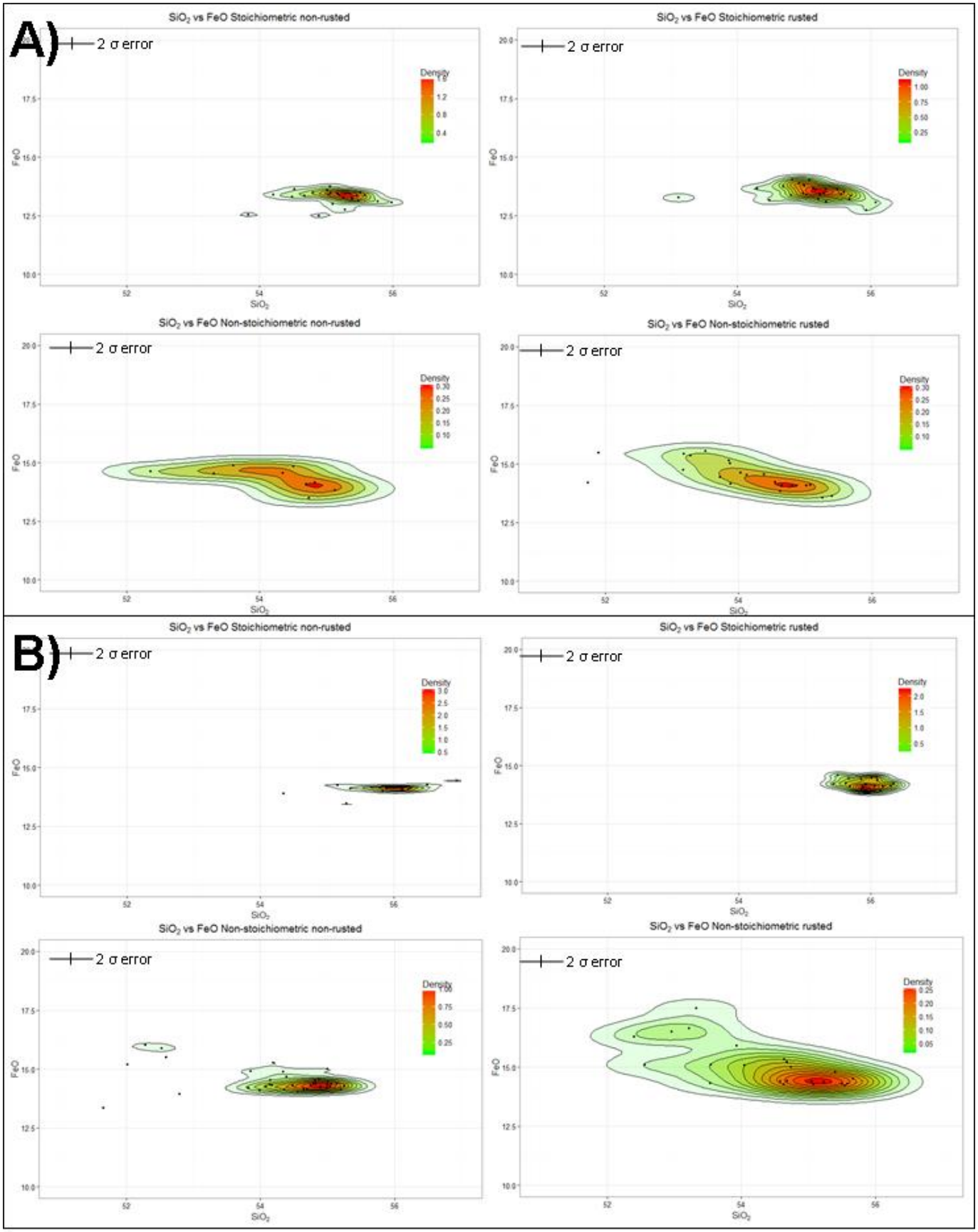

Fig. 4.7. A) QUE 94214 pyroxenes SiO_2 and FeO wt.% compositions sorted by rusted areas, non-rusted areas and stoichiometric and non-stoichiometric pyroxenes. B) ALH 84058 pyroxenes similarly sorted.

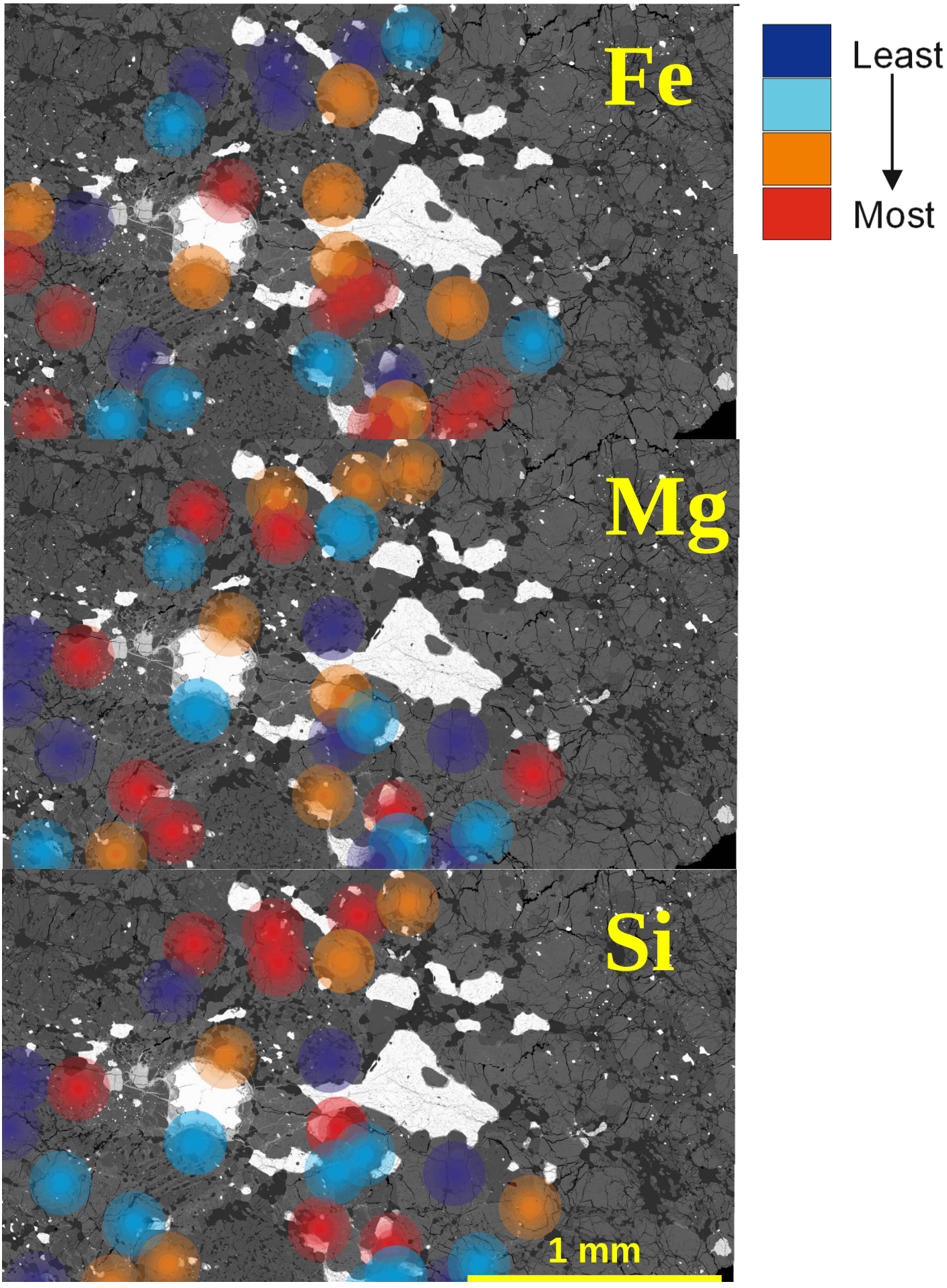

Fig. 4.8. EMPA data overlain on BSE image. Colours of points designate relative compositions of olivine and pyroxene crystals. Analyses were split into four groups based on their relative ranking of elemental compositions (with olivine and pyroxene being separated first) to demonstrate spatial distribution of elemental change.

Measuring the effect of sulphide weathering on olivine and pyroxene crystals

Correlating petrographic and EMPA data provides the means to determine the distances associated with sulphide weathering. An area of QUE 94214, with visible sulphide-related silicate weathering textures, was characterised in Section 3.7; Fig. 3.59 and used to layer the EMPA data.

Many of the points measured by EMPA had low totals and non-stoichiometric compositions. Some of the analyses in table 4.3 have been highlighted in red where the crystal is very altered and has been assigned to the mineral group that was most likely the pre-cursor. These analyses are potentially mixed with an alteration phase also measured. As the crystals were visibly altered (etched) and small pockets of clay and large pockets of Fe-oxyhydroxides are observed in this area, the inclusion of alteration products in these analyses would result in a lower total as all alteration phases observed are hydrated. This made rejecting analyses based on total and stoichiometry counterproductive and so standard analysis between groups of EMPA analyses were carried out throughout.

Olivines and pyroxenes were separated into four groups, based on FeO, MgO and SiO_2 compositions (listed in Table 4.3.). Higher FeO values in olivine and pyroxene are measured in areas proximal to weathered grains (within 300 μm on average; Fig 4.8.). In all etched olivine crystals, with one exception, FeO wt% is higher than average by up to 3 wt.% higher than the average olivine composition of the interior of QUE 94214. MgO content is lower than average by up to 4 wt. % (Table 4.3.), suggesting removal of MgO. SiO_2 also decreases with increasing FeO content. The etched olivine crystals have the lowest SiO_2 content with 3-4 wt.% less than the highest values. The decrease in SiO_2 demonstrates that any clays forming are not in the proximal olivine grains and so the SiO_2 must be mobile.

The small pyroxene crystals in chondrules that were stripped along cleavage planes, and altered more strongly than larger crystals (Fig. 3.15), are diopside, identified from analyses and element maps (Fig 4.9). The diopside grains have low SiO_2 (44 wt.% compared to analyses elsewhere in the interior averaging 52 wt.%) and are visibly etched. They have lower MgO and CaO contents than diopside measured elsewhere in the meteorite, and their compositions are no longer stoichiometric.

A map of Fe content in QUE 94214 highlights enrichment along fractures and imperfections in the crystals (Fig. 4.10). The combination of increased FeO with the decrease in SiO_2 and MgO demonstrates that there is deposition of Fe-rich alteration products along the fractures and imperfections, while the SiO_2 and MgO is removed. This is whole crystal dissolution of olivine, with all constituent elements being put into solution, but the FeO is immediately deposited from solution as Fe-oxyhydroxides along planes of dissolution in the parent olivine where nucleation is easiest. As the whole area has greater FeO, mostly lesser MgO and SiO_2, the effect of the weathering of silicates is seen to pervade the whole 2 mm area and is not limited to the adjacent crystals.

Table 4.3. Pyroxene and olivine analyses from an area of sulphide weathering in QUE 94214. Average interior values are added for comparison.

Pyroxene/	P2O5	SiO2	SO2	TiO2	Al2O3	Cr2O3	MgO	CaO	MnO	FeO	NiO	Na2O	K2O	Cl	Total
precursor	0.24	43.87	0.75	0.06	0.44	0.05	27.70	0.38	0.37	21.56	0.41	0.03	0.00	0.08	95.92
Diopside	0.05	44.53	0.76	0.42	0.80	0.72	13.14	17.12	0.19	15.00	0.24	0.51	0.00	0.24	93.70
	0.15	53.19	0.15	0.21	0.30	0.16	27.44	0.73	0.43	14.43	0.10	0.02	0.00	0.03	97.32
	0.00	53.28	0.14	0.17	0.24	0.10	27.46	0.94	0.43	15.35	0.06	0.02	0.00	0.00	98.18
	0.00	53.85	0.09	0.16	0.22	0.13	27.61	0.99	0.45	15.14	0.06	0.02	0.00	0.01	98.72
	0.00	54.03	0.06	0.23	0.25	0.12	28.08	0.71	0.46	14.63	0.03	0.01	0.00	0.00	98.59
	0.00	54.54	0.14	0.17	0.17	0.13	28.65	0.83	0.44	14.22	0.04	0.00	0.00	0.02	99.35
	0.00	54.83	0.03	0.19	0.18	0.10	28.67	0.90	0.45	14.15	0.02	0.00	0.00	0.00	99.52
	0.00	54.93	0.04	0.17	0.18	0.16	28.39	0.95	0.44	13.87	0.03	0.02	0.00	0.00	99.17
	0.02	54.99	0.03	0.18	0.14	0.29	28.43	0.86	0.46	13.46	0.00	0.02	0.00	0.01	98.89
	0.08	55.00	0.04	0.17	0.15	0.51	28.56	0.60	0.44	13.82	0.05	0.05	0.00	0.01	99.47
	0.01	55.14	0.02	0.23	0.16	0.14	29.00	0.74	0.47	13.66	0.03	0.00	0.00	0.00	99.60
Interior average	*0.02*	*54.48*	*0.04*	*0.18*	*0.35*	*0.18*	*28.39*	*1.06*	*0.45*	*13.85*	*0.12*	*0.09*	*0.01*	*0.01*	*99.23*
Olivine/	**P2O5**	**SiO2**	**SO2**	**TiO2**	**Al2O3**	**Cr2O3**	**MgO**	**CaO**	**MnO**	**FeO**	**NiO**	**Na2O**	**K2O**	**Cl**	**Total**
precursor	0.16	35.97	0.36	0.02	0.42	0.00	34.63	0.06	0.40	24.50	0.45	0.04	0.00	0.02	97.05
	0.00	35.98	0.17	0.02	0.12	0.02	34.49	0.04	0.42	25.39	0.09	0.03	0.00	0.00	96.77
	0.11	36.08	0.17	0.00	0.12	0.00	35.56	0.02	0.38	23.63	0.03	0.00	0.00	0.03	96.13
	0.18	36.44	0.09	0.00	0.08	0.05	36.08	0.04	0.41	22.96	0.08	0.00	0.00	0.05	96.45
	0.17	36.53	0.15	0.00	0.08	0.03	35.95	0.02	0.41	23.69	0.05	0.00	0.00	0.00	97.08
	0.01	36.64	0.17	0.00	0.15	0.00	35.74	0.00	0.41	24.07	0.02	0.00	0.00	0.00	97.20
	0.00	36.64	0.08	0.00	0.08	0.02	36.39	0.01	0.43	24.15	0.08	0.03	0.00	0.00	97.91
	0.06	36.83	0.16	0.04	0.02	0.03	37.55	0.02	0.41	22.35	0.03	0.02	0.00	0.03	97.54
	0.07	36.97	0.15	0.00	0.02	0.01	36.10	0.02	0.42	23.40	0.10	0.00	0.00	0.02	97.27
	0.00	37.12	0.09	0.03	0.00	0.01	36.94	0.01	0.40	23.77	0.17	0.01	0.00	0.00	98.54
	0.11	37.15	0.10	0.00	0.09	0.06	36.60	0.02	0.42	22.62	0.05	0.00	0.00	0.03	97.24
	0.26	37.20	0.09	0.00	0.12	0.00	37.39	0.01	0.41	22.79	0.09	0.00	0.00	0.01	98.38
	0.08	37.26	0.11	0.04	0.07	0.02	36.50	0.02	0.43	23.58	0.11	0.04	0.00	0.02	98.29
	0.00	37.30	0.12	0.03	0.06	0.00	36.68	0.00	0.42	23.11	0.05	0.00	0.00	0.01	97.77
	0.11	37.39	0.12	0.00	0.04	0.01	37.18	0.01	0.42	22.89	0.03	0.01	0.00	0.01	98.20
	0.07	37.71	0.05	0.00	0.02	0.01	37.74	0.02	0.43	22.52	0.02	0.00	0.00	0.01	98.60
	0.06	37.96	0.09	0.00	0.01	0.01	37.59	0.03	0.42	22.45	0.05	0.02	0.00	0.02	98.71
	0.01	38.00	0.05	0.03	0.01	0.01	38.79	0.01	0.43	21.76	0.00	0.00	0.00	0.00	99.10
Interior average	*0.04*	*37.71*	*0.03*	*0.01*	*0.03*	*0.03*	*38.28*	*0.04*	*0.43*	*22.20*	*0.07*	*0.01*	*0.00*	*0.01*	*98.90*

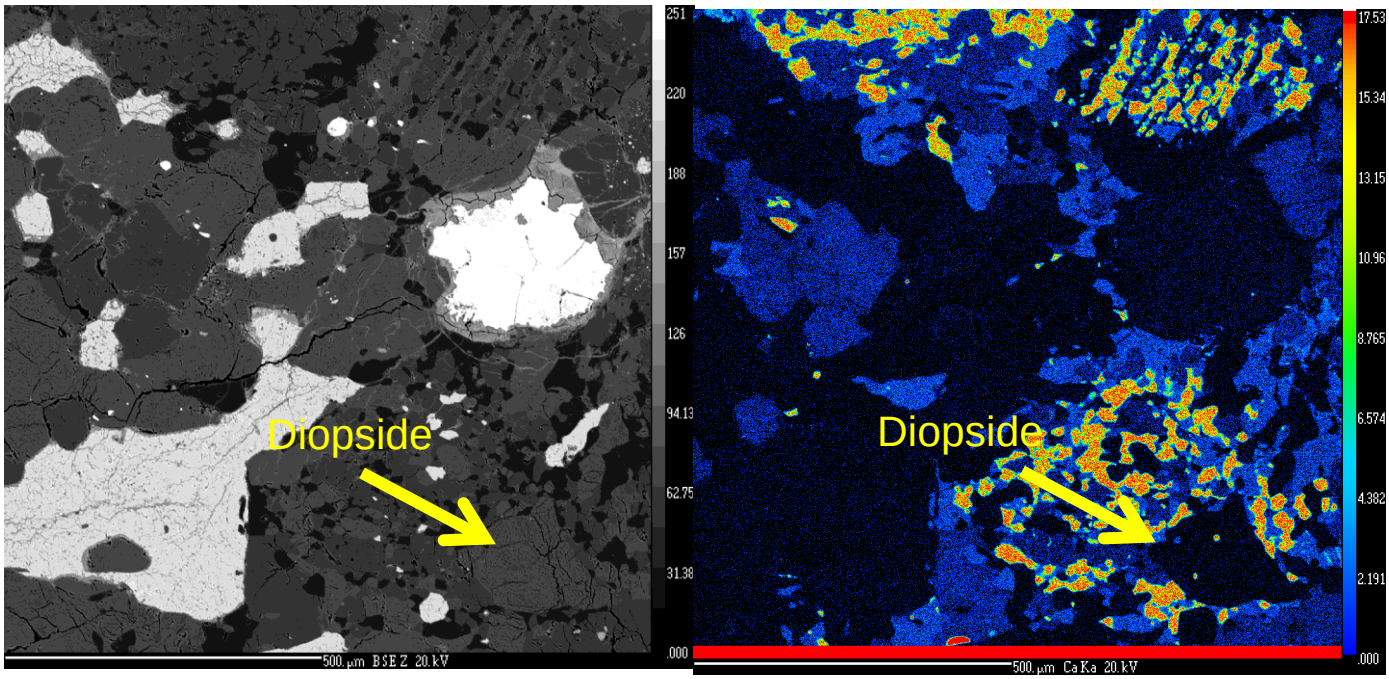

Fig. 4.9. BSE image and corresponding Ca map of sulphide weathering region in QUE 94214. The small crystals in adjacent chondrule relicts that were observed to preferentially weather in section 3.7. are mapped by EMPA and shown to be high Ca diopside crystals.

Fig. 4.10. Composite map of a BSE image of QUE 94214 with the Fe content overlain. Concentrations of Fe are greater at crystal imperfections.

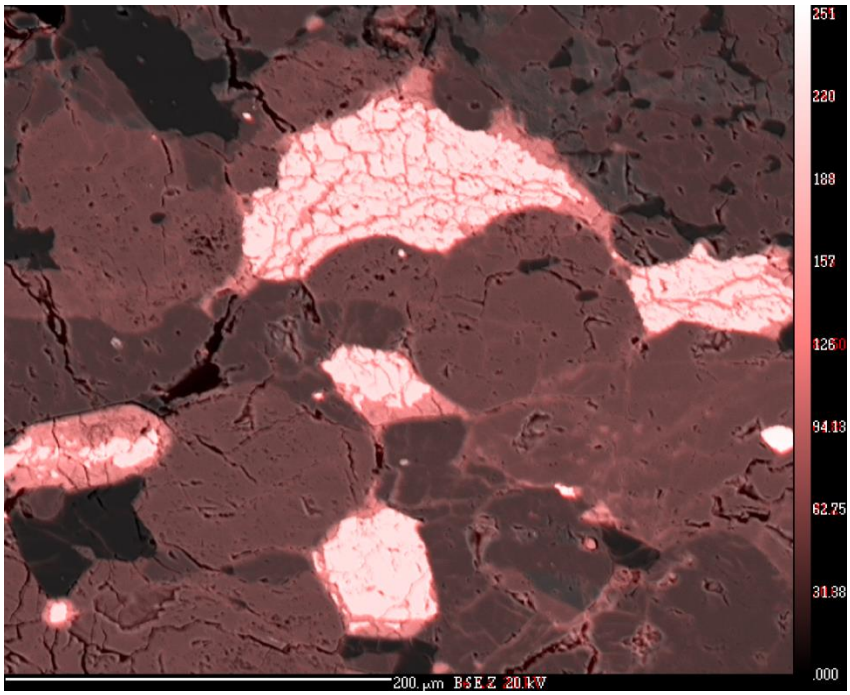

Interpretation of ferromagnesian mineral data

An important point of note in both the olivine and pyroxene analyses is that the progressive weathering pushes the compositions of the ferromagnesian minerals out of the L chondrite composition field and into the LL chondrite field. This is especially apparent in ALH 78130 I which has many analyses with too low MgO and high FeO. The most weathered meteorites (ALH 78130, QUE 99022, QUE 94214) all contain many olivines with non-L chondrite compositions. The least weathered meteorites (ALH 84056 and ALH 85017) have both olivine and pyroxene compositions that tightly cluster in the L chondrite field with little deviation. Many of the analyses in the most weathered meteorites are not true olivines as they are non-stoichiometric, and so the analyses also represent alteration products included in the analyses. The decrease in MgO and SiO_2 that accompanies the increase in FeO most likely demonstrates the dissolution of the olivine and pyroxene and the subsequent immediate deposition of Fe-oxyhydroxides.

This is corroborated by the visibly rusted olivines containing greater FeO. This visible rust is caused by nanophase Fe-oxyhydroxides depositing in the crystals and in fractures throughout the meteorite and is measurable in the olivines. It is not convincingly measured in the pyroxene crystals, however, with the FeO only showing a slight possibility of increase in rusted areas of ALH 84058. The lack of variation in pyroxenes from rusted and non-rusted areas is also possibly due the density of micro fractures in the respective minerals (with pyroxenes containing significantly less microfractures than olivines) and a reflection of the respective weatherabilities. The FeO contents deposited in microfractures and on grain boundaries, rather than incorporated into the crystal structure of a re-crystallized olivine, which corroborates the assertion that olivines have a more pronounced FeO enrichment because of increased microfracture density.

The conditions of the weathering environment can be discerned using the elements that are released in solution from the ferromagnesian minerals. The preferential alteration of

olivine over pyroxene is to be expected from past experimental studies (Luce et al., 1972; Seiver and Woodford, 1978), but is contrary to some findings of Antarctic weathering (Fischer and Burns, 1992; Bland et al., 2006). An explanation for the similarity between weathering rate of Antarctic olivine and pyroxene was only ever tentatively proposed by Bland et al., (2006), whereby topotactic weathering of olivine protected the grain from further weathering. The new data in this study suggests that this is not the case: the release of Mg and Si to solution shows crystal dissolution and the retention of Fe reflects ease of oxidation. The Mg and Si are therefore transported away from the olivine, instead of forming the protective layer suggested by Bland et al. (2006).

pH is known to be a key factor in dissolution rates of ferromagnesian minerals, and there are many documented cases of low pH resulting in more rapid dissolution (Luce et al., 1972; Seiver and Woodford 1978; Bladh 1982). The lower pH of fluids associated with the sulphide weathering in QUE 94214 have led to the greater reduction in MgO and SiO_2 in olivines and pyroxenes. Since this signature does not extend beyond the rusted areas, this low pH fluid must be being neutralised in a short distance (less than the maximum size of the rust patch $\approx$ 1 mm), or, it must be a stagnant fluid with no flow through (closed system). However, this is unlikely since the measured alteration products do not contain significant Mg, and no topotactic protective layer has formed. Since olivine dissolution is the most prevalent of all silicate dissolution then experimental data from Hurowitz et al. (2006) shows that the Mg^{2+}, Fe^{2+} and SiO_2 (aq) concentrations in solution will increase with pH as the H^+ in solution is consumed by neutralisation reactions in the olivine. This is the most likely candidate for acid neutralisation in the meteorites studied, as there is no petrological or chemical evidence of plagioclase weathering. The extent to which the acidic weathering translates into bulk measurements is discussed in Chapter 6.

4.1.3. FELDSPARS

There are fewer feldspar analyses compared to olivine and pyroxene, largely due to the difficulty associated with analysing maskelynite (In ALH 85017, QUE 94214 and ALH 78130) and an issue with one of the spectrometers on the microprobe causing silica excess (elaborated on in chapter 2). Analyses with totals of between 97-103 % were used since maskelynite analyses consistently had higher totals. Average compositions are in Table 4.4., and full analyses in Appendix I. Overall there are little variation in feldspar compositions between samples, between rims and interiors and in rusted areas.

Compositions in all meteorites were an average of $An_9Ab_{84}Or_{7.}$ SiO_2 values did not show any variation between rim and interior in any of the samples, and there is no consistent difference between the most and least weathered meteorites. The same is true for the other main constituents of feldspar ($Al_2O_{3,}$ K_2O, Na_2O).

Rusty feldspars

Since there are few analyses and the little variation between samples, all the rusted and non-rusted feldspars from different meteorites have been collated and plotted together. There are no differences between the areas of rust and those outside of these areas.

4.1.4. ALTERATION PRODUCT

Alteration products from different parts of the meteorites were measured and compared in order to determine their homogeneity within and between meteorites (full results are in Appendix I). Those deposited on, or near (within 100 μm) to the fusion crusts of the meteorites (within 100 μm) were separated in order to compare alteration products in exposed edges with those in the interior. In some meteorites pockets of alteration products were too small to measure by EMPA: ALH 85017, ALH 84056 I and ALH 84058 I. One measurement of Antarctic varnish was made in ALH 84056 where the deposit was thick enough to measure.

Table 4.4. Feldspar compositions measured by EMPA

Sample	SiO_2	TiO_2	Al_2O_3	Cr_2O_3	FeO	MnO	MgO	CaO	Na_2O	K_2O	Total	An	Ab	Or
QUE 99022 R	63.00	0.04	20.37	0.01	2.43	0.01	0.44	2.08	9.30	1.14	99.44	10.26	83.04	6.70
QUE 99022 I	63.09	0.06	20.06	0.20	1.98	0.03	0.72	2.07	9.02	0.98	98.74	10.58	83.45	5.97
QUE 94214 R*	67.25	0.05	22.43	0.04	0.64	0.01	0.15	1.92	9.71	1.09	103.35	9.24	84.52	6.24
QUE 94214 I*	66.12	0.05	21.67	0.16	0.88	0.01	0.29	1.99	9.67	1.07	102.05	9.58	84.28	6.14
ALH 84058 R	62.04	0.05	18.47	0.04	3.44	0.06	3.34	2.15	8.35	1.04	99.38	11.62	81.68	6.69
ALH 84058 I	64.55	0.04	21.21	0.15	1.12	0.00	0.26	2.21	9.57	1.03	100.49	10.65	83.44	5.91
ALH 85017 R	63.50	0.05	20.60	0.30	0.88	0.01	0.32	2.12	9.52	1.15	98.75	10.23	83.16	6.61
ALH 85017 I	64.45	0.08	21.05	0.38	1.31	0.02	0.28	2.44	9.75	1.10	101.06	11.41	82.47	6.12
ALH 84056 R1	66.00	0.06	21.87	0.25	0.75	0.01	0.40	2.18	9.76	0.89	102.23	10.43	84.50	5.07
ALH 84056 I1	65.71	0.04	21.71	0.01	1.01	0.00	0.02	2.17	9.69	1.04	101.55	10.36	83.73	5.91
ALH 78130 R*	65.11	0.05	21.45	0.01	0.58	0.01	0.17	2.37	9.50	0.81	100.22	11.55	83.75	4.70
ALH 78130 I1	64.17	0.04	21.01	0.01	3.04	0.01	0.01	2.24	9.73	0.43	102.08	11.00	86.48	2.51

*Maskelynite analyses

[1]Mixed maskelynite and plagioclase analyses

Major elements - FeO vs NiO (Fig. 4.11)

As Fe and Ni make up a significant portion of the alteration products, they have been separated here into a different section. NiO is highly variable between different meteorites and shows a clear elevation in the most weathered samples, which are ALH 78130 I and QUE 99022. The difference in NiO content between ALH 78130 rim and interior is significant (Fig 4.11.) with the rim alteration products containing < 10 wt.% NiO, but the more weathered interior containing between 2-30 wt.% NiO with the majority between 10-20 wt.%.

There is a negative correlation between FeO and NiO and a similar spread of NiO values in the rim section from QUE 99022 and the interior of ALH 78130. There are many lower FeO points in the rim compared to the interior. Of all the meteorites Ni values are highest in QUE 99022 R.

QUE 94214 alteration products contain significantly less NiO almost all are below 8 wt.% but with some outliers with values >10 wt.% and there are no clear compositional differences between the rim and interior alteration products. In QUE 94214 alteration product pockets that are at the fusion crust have less FeO than those in the interior. In ALH 84058, all pockets near to, or at the fusion crust, have much lower NiO (most have none at all) and FeO. The Antarctic varnish measurement from ALH 84056 has no Ni and contains 50.0 wt.% FeO. The main clustering of ALH 84056 values is between 40-70 wt.% FeO and all have < 10 wt.% NiO.

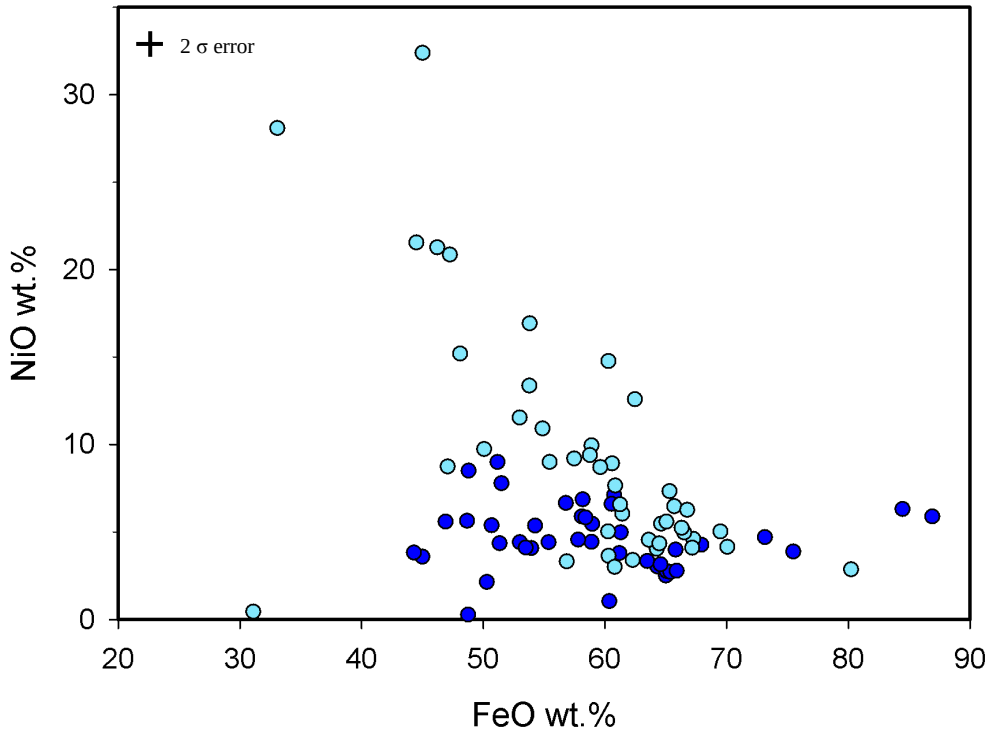

Fig. 4.11. FeO vs NiO wt.% in alteration products of ALH 78130 R (dark blue) and I (light blue).

Minor elements

The SiO_2 content of alteration products in QUE 99022 rim is generally < 3 wt.%, which, whilst low, is still higher than equivalent material in the interior section. QUE 94214 has a higher SiO_2 content in its alteration products than QUE 99022, with up to 10 wt.% SiO_2, and there is generally more SiO_2 in the interior alteration products than in the rim. Alteration products in the interior of ALH 78130 generally contain less SiO_2 than the rim: two of the rim pockets are over 10 wt.% SiO_2 whereas the interior are < 4 wt.% SiO_2.

QUE 99022 has more SO_2 in the rim alteration products than the interior, which contains very little SO_2. The maximum sulphur content appears in pockets in the fusion crust, as is the case in ALH 84058, although in the latter meteorite, most of the S-rich areas also have elevated SiO_2 relative to the main continuum of analyses. In contrast, although ALH 84056

also has pockets with high sulphur contents, they are not in the fusion crust, which are more SiO_2-rich and sulphur-poor.

The rim sample of QUE 94214 has more points with a high MgO (> 2 wt.%) than the interior. ALH 78130 rim resembles the QUE 99022 rim, with relatively high SiO_2 (> 5 wt.%) and MgO (> 2 wt.%) contents, whilst most of the alteration products in the interior of ALH 78130 have very low amounts of SiO_2 (< 3.8 wt.%) and MgO (< 0.91 wt.%).

Many points in the interior of QUE 99022 have high Cl content (over 1.5 wt.%), the highest of all the meteorites studied, but values are significantly lower in the rim (0.2-1.1 wt.%). The interior points are also restricted in FeO with Cl. In contrast, QUE 94214 has more Cl in the rim (0.1-1.8 wt.%) than the interior (0.1-0.9 wt.%) and ALH 78130 interior is lower still (< 0.1 wt.%). The rim, however, has higher values, up to 0.8 wt.%. ALH 84058 has a spread of Cl values (up to 2.0 wt.%), whereas ALH 85017 and ALH 84056 are less variable (0.1-1.8 wt.%). In ALH 84058, many of the high Cl points are the fusion crust pockets at the outer margin of the meteorite, but ALH 84056 does not show this. Cl is about the same in value as the alteration products further towards the interior, which is also true for ALH 78130 and QUE 94214.

Alteration pocket interpretation

The greater amount of SO_2 in the fusion crust pockets suggests external addition to the fusion crust, rather than it being an internally derived weathering product, or, that the difference in redox conditions allowed the SO_2 to deposit. This is as it does not extend to any pockets further into the meteorite than 0.5 mm and are not located exclusively near sulphides or the sulphide melt veins that make up the second zone of the fusion crust (see Section 3.2.4). Elevated SiO_2 wt.% has many more potential sources, since every alteration product pocket has contact with a silicate, and so it is less possible to determine an internal, or externally derived addition. It is likely that this is derived internally rather than from Antarctic ice, as the alteration product pockets in the fusion crusts have been observed to

have stripping of surrounding silicate minerals adjacent to them and so provide clear evidence of an adjacent Si source.

The addition of MgO to the exterior pockets also suggests that there is input from surrounding silicates. The addition of FeO from silicates would be negligible compared to the input from kamacite and taenite and so it is unlikely to show up in the data. The MgO in the meteorite is only located in pyroxene and olivine, and so an increase of MgO is diagnostic of mafic mineral breakdown. The increase in MgO in the fusion crust pockets is reflecting an increase in mafic mineral breakdown in the fusion crust, compared to the interiors of the meteorites. The high Cl contents of QUE 99022 interior are unaccounted for, and are so much greater than any other meteorite, and so contamination of the thin section should be considered. The only indigenous source of Cl in the meteorite is Cl-apatite and so the alternative explanation would require the breakdown of Cl-apatite in only this meteorite. As there is no petrological evidence of this, and QUE 99022 has a very similar alteration patterns to other meteorites in the study, it seems unlikely that apatite breakdown is the source of the observed high Cl-concentrations.

The Fe-oxyhydroxides are highly heterogeneous, in most cases reflecting the directly adjacent crystals. There is an increase of NiO in alteration products in more highly weathered meteorites (QUE 99022 R, ALH 78130 I), reflecting the contribution from increased taenite weathering (Table 3.2.) as the increase is a direct result of the breakdown of taenite, the host of much of the nickel. It is unusual that QUE 94214 has less NiO in its alteration products compared to a relatively unweathered meteorite such as ALH 84056 that is known to have less altered taenite (Table 3.2.). Therefore the mobility of Ni in QUE 94214 is higher and the Ni has been removed from the system. Ni is one of the least readily adsorbed transition metal on Fe-oxyhydroxides and the adsorption decreases with decreasing pH (Rose and Mianchi-Mosquera 1993). Ni mobility and adsorption in Fe-oxyhydroxides is highly similar to Co and so both are discussed in Section 4.2.9.

The usual relative mobilities of Mg and Si is Mg > Si (Venturelli et al., 1997; Auippa et al., 2000), which contrasts with the observations in the alteration pockets of QUE 94214. The low ratio of MgO:SiO_2 in QUE 94214s alteration minerals indicates that the MgO is either less mobile than the SiO_2 or is being removed entirely from the system. As a decrease in MgO has been measured in olivine and pyroxene crystals (and altered grains), the MgO is likely being removed entirely from the system. The decrease of CaO in the alteration products of QUE 94214 compared to other meteorites is unlikely to be because of a source disparity as QUE 94214 has many Ca-rich pyroxenes that are visibly weathered in the interior (as previously detailed in chapter 3) so there should be more Ca in solution than in other meteorites which did not show heavy weathering of high Ca pyroxenes. This means that in QUE 94214 Ca must be more soluble and mobile than in the other meteorites which has led to the CaO being largely removed from the system. The alkali metals are known to be highly mobile in acidic environments, Ca and Mg both have high mobility compared to transition metals (Auippa et al., 2000).

4.1.5. TROILITE

Troilite compositions are important for establishing if any compositional differences resulted in preferential breakdown of sulphides in QUE 94214 (full analyses in Appendix I).

Fe vs Total (Fig. 4.12)

A strong negative correlation exists between Fe wt.% and analysis total, suggesting that lower totals are because of Fe removal. QUE 94214 has many troilite crystals with lower totals, which is most likely to be due to the presence of Fe-oxyhydroxide veins pervading the crystals (see Section 3.7). ALH 78130 also has a wide range of totals as low as 96 %. QUE 99022 has a narrow range of values (97-98 %) with little apparent loss of Fe. ALH

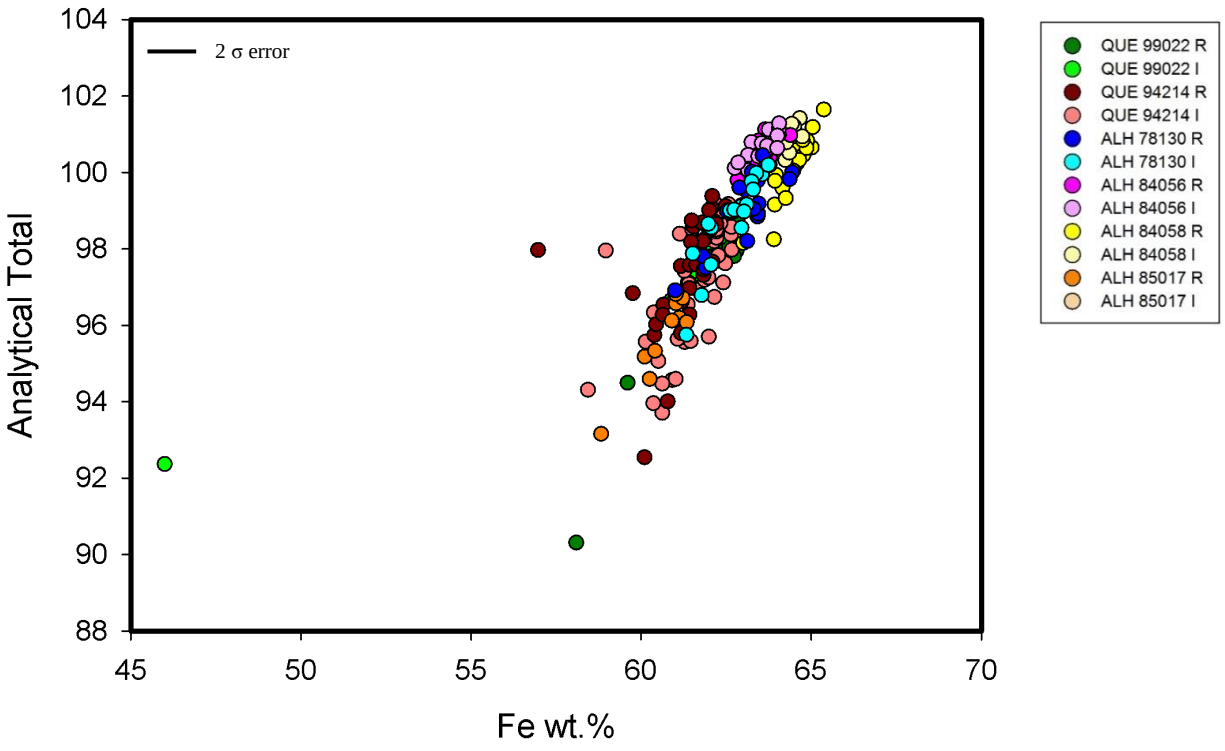

Fig. 4.12. Fe wt.% vs analytical total for all troilite crystals measured.

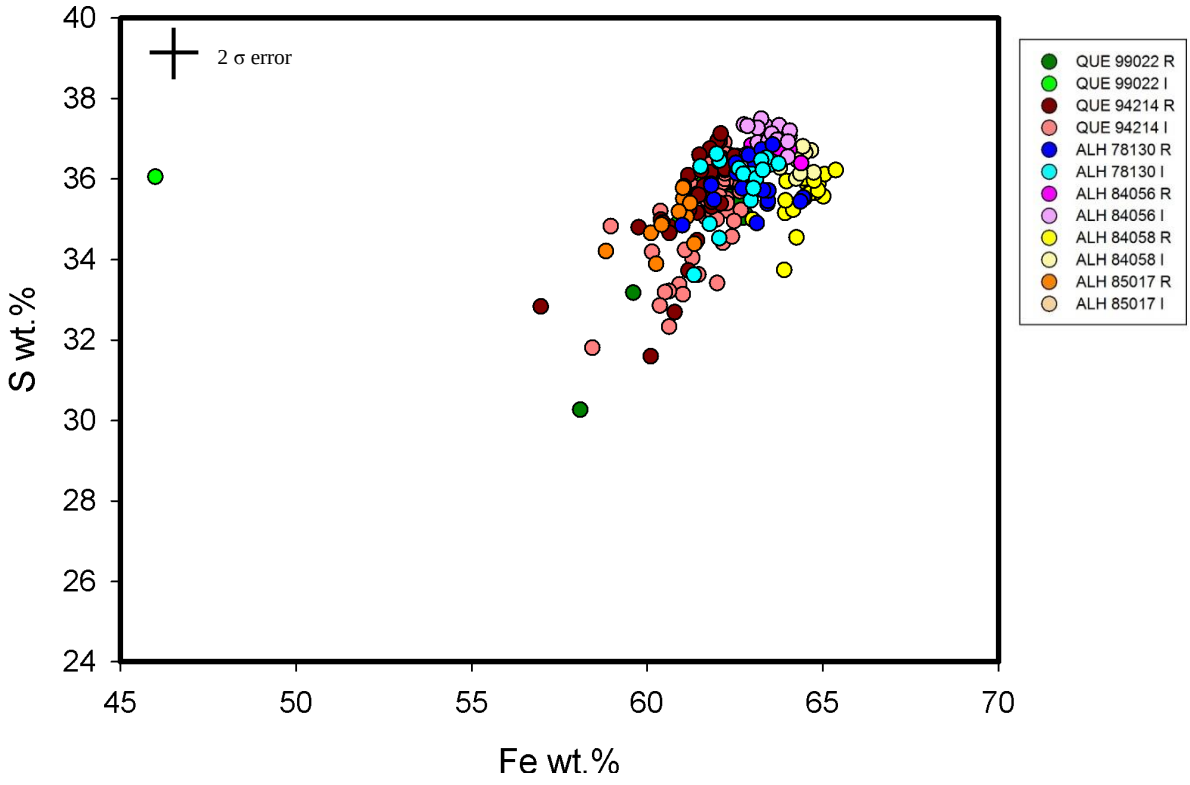

Fig. 4.13. Fe wt.% vs S wt.% in all troilite crystals measured.

84058 also has a very small cluster in both rim and interior and ALH 84056 has the smallest spread of values, with almost all having 100 % totals and between 62-64 wt.% Fe.

Fe vs S (Fig. 4.13)

Rim and interior grains in QUE 99022 have a limited range of S contents (34.8-36.5 wt.%) and QUE 94214 has a wider range, with a greater spread in the interior (32.2-37.0 wt.%) than the rim. (34.7-37.3 wt.%). Clustering of S values reflects the Fe vs Totals clustering, with ALH 84056 having the least spread of values, and ALH 84058, ALH 85017 and ALH 78130 having slightly wider spreads of 34.4-36.5 wt.%.

Ni and Cu

Most of the Cu values in troilite are at, or very close to, the electron microprobe detection limits (below 0.1 wt.%). QUE 99022 has a very tight cluster of values with practically no detectable Ni or Cu in the troilite, with only very few Ni-concentrations > 1 wt.%. ALH 84058 contains a few troilites with high Cu values (over 0.1 wt.%) but with no appreciable Ni. The same is true of ALH 78130. In ALH 84056 and ALH 85017 troilite contains up to 0.4 wt.% Ni and in QUE 94214 has a wider spread of Cu and Ni, with up to 0.35 wt.% Cu in the interior, and rim crystals (with one high outlier) containing up to 2.1 wt.% Ni. This measurement probably reflects the occurrence of small Fe-Ni metal inclusions (described below).

Element maps

Element maps of internal troilite crystals (Fig. 4.14) in QUE 94214 identified many sub µm inclusions of Ni-rich material. It is not possible to say if these are also Fe-rich, as the background from the troilite crystal surrounding the inclusions dominates the Fe signal. However, as the only identified Ni-bearing species in the meteorite is metal, as taenite and kamacite, it is highly likely that the inclusions are metal grains, and good candidate sources for the chemical differences in QUE 94214 troilites.

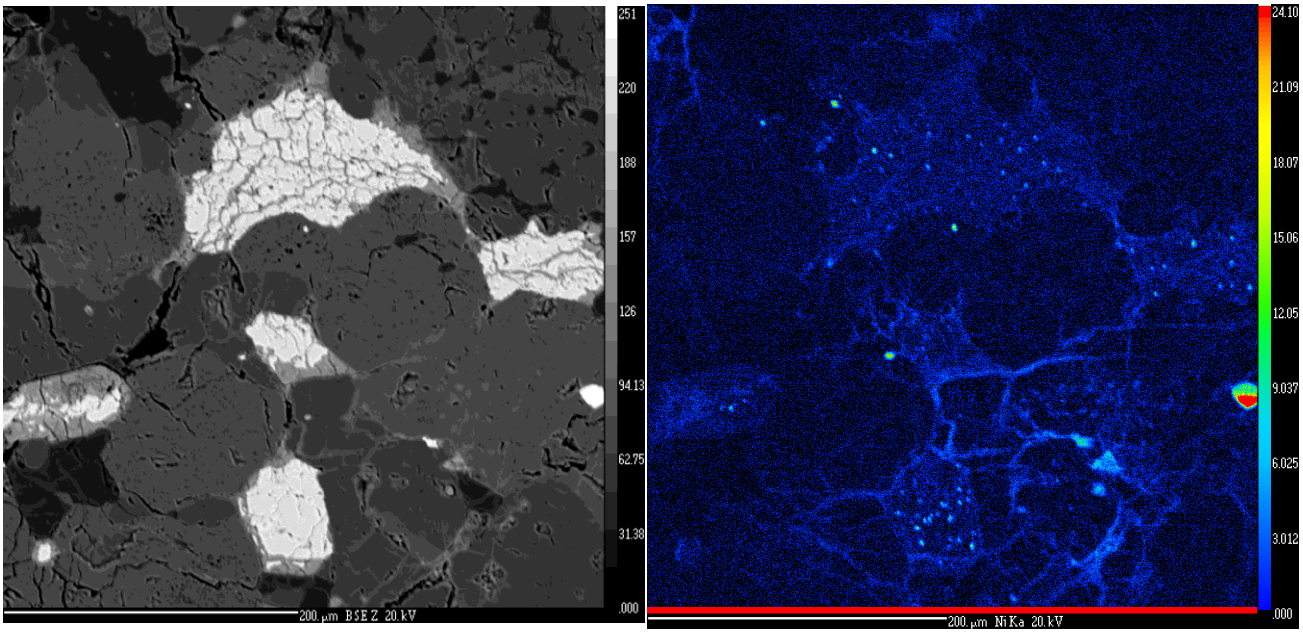

Fig. 4.14. BSE image and corresponding Ni concentration map in QUE 94214. The troilite crystals all have small inclusions of Ni rich material within.

Troilite interpretation

Troilite crystals in QUE 94214 have a significantly different composition from those in other meteorites and with a greater number of low totals and low Fe contents, they are also weathered more strongly than other crystals. Fe-Ni metal inclusions in crystals increase susceptibility to breakdown, since the sub-µm particle size creates an enormous surface area to volume ratio which, combined with the petrological observation of many microfractures throughout the polycrystalline structure, leads to rapid breakdown. The breakdown of these particles also allows greater access for altering fluids by forcing open fractures and creating porous vein structures through the crystals.

4.1.6. KAMACITE AND TAENITE

Fe and Ni were the only elements present above detection limits (>0.1 wt.%) in all kamacite and taenite grains measured. Taenite typically has between 23.2-34.6 wt.% Ni, and 68.1-71.0 wt.% Fe. Kamacite grains have between 3.6-8.4 wt.% Ni and 88.7-95.5 wt.% Fe. In all meteorites, there are rare occurrences of metals in-between these two compositions. Low totals (<98 %) are prevalent in the rim samples and in the interior of the most weathered samples. This is most likely to be an indication of the presence of Fe-oxyhydroxides.

4.1.7. CHROMITE

There were no variations in chromite within of between meteorites and compositions were consistently 53-55 wt.% Cr_2O_3, 29-31 wt.% FeO, 5-5.5 wt.% Al_2O_3, 2.5-3% TiO_2 and 1.8-2.5 wt.% MgO.

4.2. LA-ICP-MS

Spatially resolved trace element data were collected using Laser ablation-inductively coupled plasma-mass spectrometry (LA-ICP-MS) to compare with bulk trace element data. The comparison of spatially resolved and bulk data allows overall bulk trends to be associated with particular mineral types so that mineral dependent processes can be discerned. Meteorites selected for this were: QUE 94214 R+I, QUE 99022 R+I, ALH 85017 R, ALH 78130 R+I. Full tables of analysis are in Appendix II.

4.2.1. OLIVINE

Typical trace element compositions are listed in Table 4.5. Olivine hosts a number of trace elements listed in Table 4.5 and contains negligible REEs. Comparisons are made within and between meteorites in terms of rim-interior differences and visibly rusted areas. ALH 78130 R, QUE 94214 R+I and ALH 85017 R+I had sufficient analyses in rusted and non-rusted areas to allow useful comparison.

Li content is consistent across all meteorites (0.2-10.3 ppm) with little discernible difference between the most and least weathered meteorites. Li concentrations in rusted areas compared to non-rusted areas show no difference in QUE 94214 and ALH 85017, but, there is a decrease of Li in rusted crystals in ALH 78130. Boron is consistent between meteorites (2-8 ppm with a few rare outliers up to 11 ppm) and low concentrations less than 2 ppm only occur in ALH 78130 R.

Al is predominantly <1000 ppm and the many hot spots (up to 9000 ppm) are likely due to small (< 10µm) feldspars inclusions (usually accompanied by raised Ca). There are disproportionately more high-Al points in QUE 94214 interior than its rim. There is a significant spread of values in the QUE 94214 olivines, with a highly restricted group of low Al values in the interior non-rusted areas (below 600 ppm) which is small compared to the rusted interior points and the rim values which are between 600-5000 ppm. The higher

values possibly result from plagioclase or chromite inclusions, however, this is not apparent in the rusted areas of either ALH 78130 or ALH 85017.

Overall Ca is typically less than 800 ppm but in ALH 78130 there are fewer outliers with higher concentrations of Ca in the interior, than in the rim. In QUE 94214 there is little difference between rim and interior – although there are two high outliers in the interior. QUE 99022 and ALH 85017 have very similar values and there is more Ca in rusted areas than in non-rusted. This is most apparent in ALH 85017 and less so in ALH 78130 and QUE 94214.

Table 4.5. Average trace element compositions of olivine measured by LA-ICP-MS (ppm)

	Li	B	Al	K	Ca	Sc	Ti	V	Cr	Mn	Co	Ni	Cu	Zn
QUE 99022 I	3.11	4.85	1348.63	111.72	382.36	2.44	42.20	5.03	162.61	3164.91	70.80	1365.10	14.75	96.38
ALH 85017 R	3.57	4.60	1534.85	100.00	3247.28	4.25	92.82	14.38	364.50	3357.64	72.72	821.88	101.62	80.50
ALH 85017 I	4.74	8.57	1085.35	383.92	514.07	2.95	56.87	6.37	363.78	4221.51	69.11	697.40	9.61	90.22
ALH 78130 R	3.61	2.89	655.45	22.97	1001.94	3.25	45.44	6.55	226.73	3035.49	51.97	927.31	12.78	76.16
ALH 78130 I	3.08	4.22	562.63	17.96	1362.23	3.48	113.11	7.75	209.16	2959.33	143.79	2660.19	13.22	71.42
QUE 94214 R	3.29	6.61	268.04	4.32	1295.77	4.26	69.11	10.25	406.07	2867.10	69.83	902.35	9.46	64.82
QUE 94214 I	2.68	6.51	1018.92	10.09	658.40	3.17	55.50	6.12	191.82	3001.83	76.71	1115.01	42.91	61.00
Typical 1 sigma error*	**0.28**	**0.94**	**3.98**	**1.31**	**12.5**	**0.14**	**3.38**	**0.48**	**27.74**	**159.01**	**7.65**	**173.6**	**2.05**	**9.18**

Table 4.6. Average trace element compositions of pyroxene measured by LA-ICP-MS (ppm)

	B	Al	K	Ca	Sc	Ti	V	Cr	Mn	Co	Ni	Cu	Zn
QUE 99022 R	7.31	2003.56	143.99	5327.13	6.77	973.11	49.60	1914.90	3541.89	132.36	2574.33	23.77	84.26
QUE 99022 I	5.37	2416.52	148.22	7491.60	9.95	1226.90	47.54	1200.71	3707.77	141.98	3270.19	33.14	125.35
ALH 85017 R	6.14	2499.71	104.14	6358.96	8.45	1156.56	53.17	1717.31	3634.39	64.80	1481.68	44.99	94.32
ALH 78130 R	5.22	1614.51	34.51	5552.69	8.55	1042.48	58.08	2689.12	3238.20	94.36	1800.98	16.32	96.31
ALH 78130 I	4.13	1361.15	16.75	5780.04	8.49	1036.46	43.88	1487.27	3286.93	185.00	3083.91	20.69	86.35
QUE 94214 R	6.12	7984.40	79.97	12359.66	11.33	849.28	48.69	1333.86	2945.54	73.91	1012.82	10.84	63.26
QUE 94214 I	4.81	3964.75	101.32	9899.33	11.28	840.25	49.35	1440.89	3150.95	83.34	772.36	18.50	69.65
Typical 1 sigma error*	**0.73**	**31.56**	**1.44**	**188.73**	**0.28**	**71.7**	**3.49**	**272.13**	**140.03**	**4.32**	**103.77**	**0.53**	**7.2**

*Errors are generated throughout every run from the glitter software used, based on the repeated measurement of a certified standard (NIST 612).

Sc does not vary between the different meteorites, with most values between 1-8 ppm, and Sc is positively correlated with Ca. The only sample that shows variability in Sc content in rusted and non-rusted areas is ALH 85017, which has more high Sc, high Ca points in the rusted areas.

Ti is mostly below 150 ppm with some high outliers which are probably inclusions of either chromite or Ti-magnetite. In terms of rusting, there are more high Ti points in the rusted olivines of ALH 85017 which correlate positively with high V and Cr, and so are likely to be due to inclusions of chromite (observed both petrographically and during processing of laser ablation data). High Ti concentrations in ALH 78130 I do not correlate well with Cr and petrographic observations do not show any surficial Ti-magnetite or chromite inclusions. However, inclusions may have been present beneath the ablated surface.

Mn values vary across the meteorites with values of 1500-4050 ppm. The most restricted range is in ALH 85017 R (3000-3700 ppm, n=24). The largest spread of values is in QUE 99022 (2700-3900 ppm). QUE 94214 has lower Mn values than ALH 85017 on average, with the main clusters of rim and interior values being very similar. ALH 78130 has quite restricted values in both the rim and interior, with most of the values between 2500-3200 ppm. In QUE 94214, Mn values are lower on average in the rusted areas than in the non-rusted olivines (Fig. 4.15.). This is also true in ALH 78130 R where the rusted rim olivines have lesser Mn on average than interior olivines which is not noted for ALH 85017.

ALH 85017 R has the lowest Co value on average (<88 ppm) whilst ALH 78130 I has the widest spread of values of any sample, with many high points up to

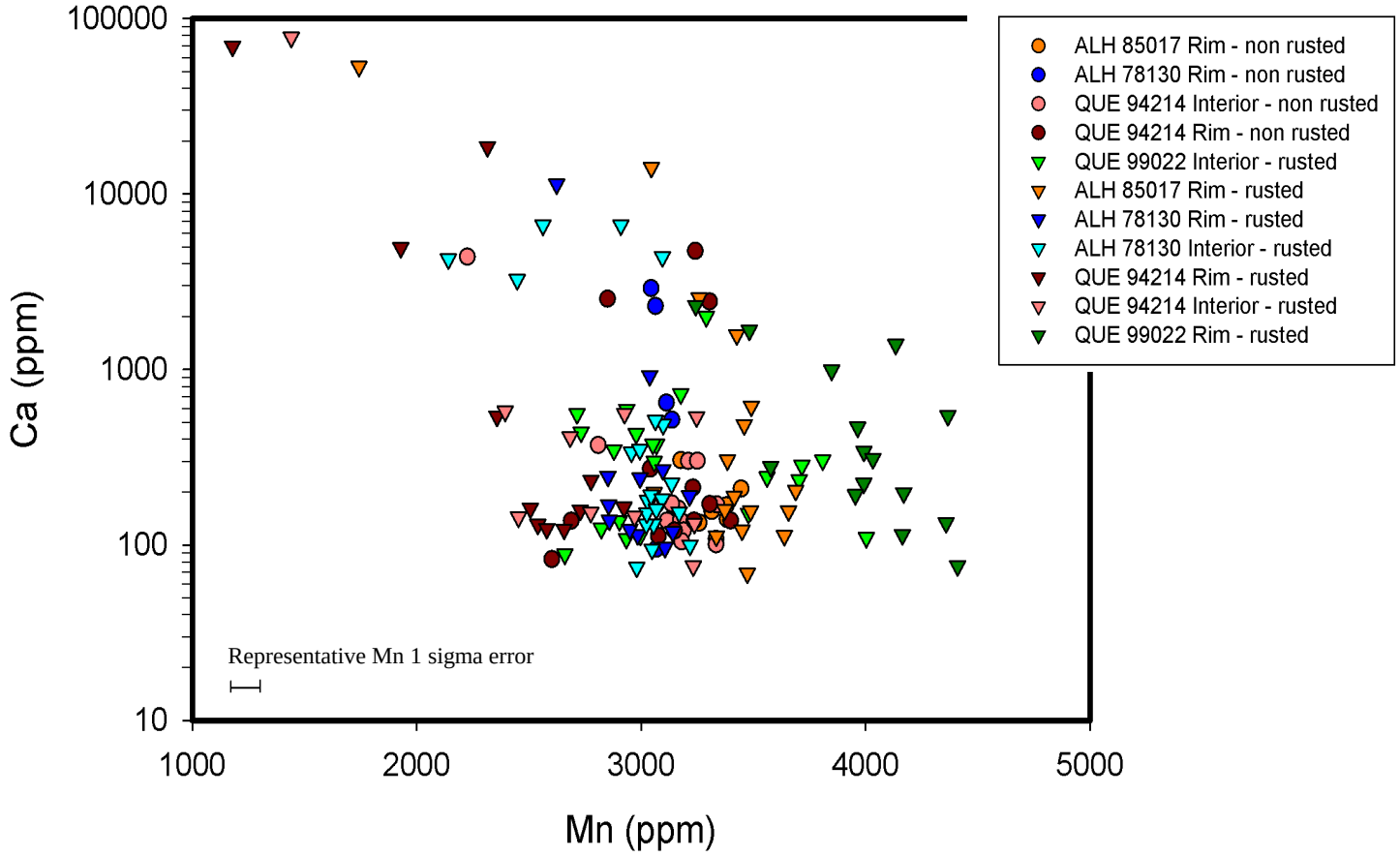

Fig. 4.15. Mn vs Ca in olivines. Rusted olivines are designated by triangles. Standard error for Ca measurements not included due to logarithmic plot, but is 12.5 ppm.

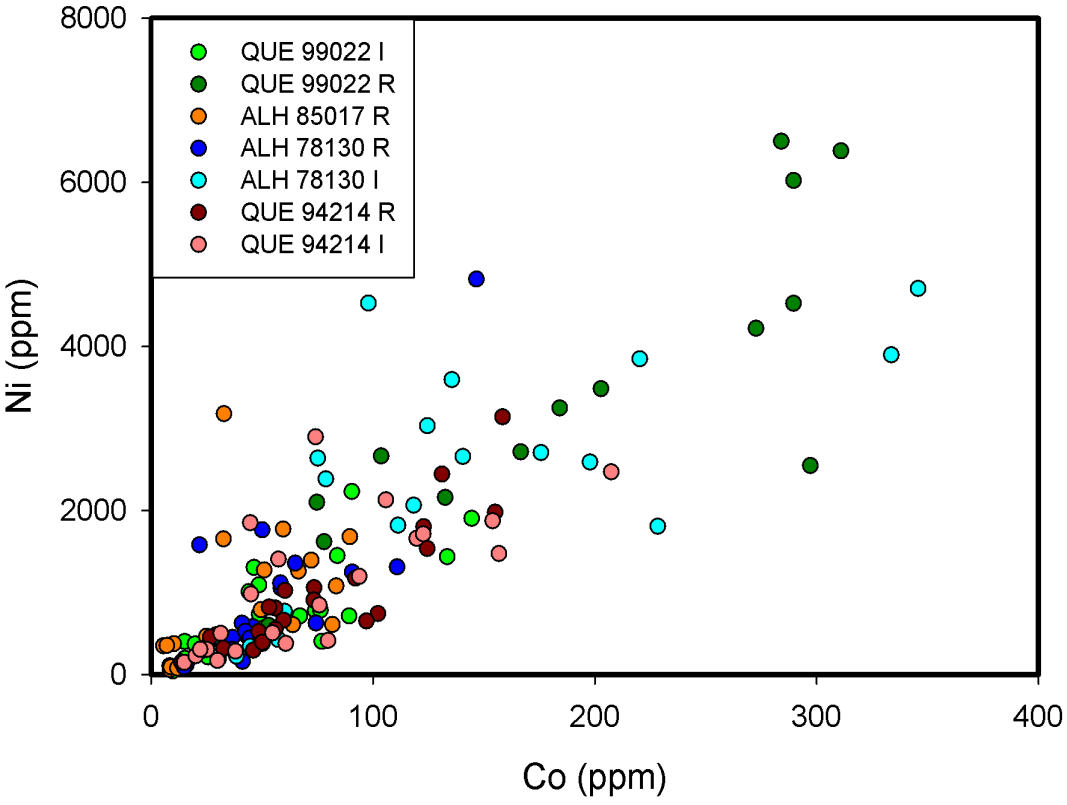

Fig. 4.16. Co vs Ni in olivines measured by LA-ICP-MS. The 1 sigma error is smaller than the symbols (7.65 ppm Co, 173.6 ppm Ni).

370 ppm Co, considerably larger range than the rim values. QUE 94214 has an intermediate spread of values with very little difference between rim and interior values and has a similar spread to QUE 99022 I. Co and Ni are strongly correlated in the olivine data.

Ni is also a potential indicator of deposited alteration product and so has been plotted against Co to show any correlations (Fig. 4.16). Co and Ni predominantly occur in the meteorites as constituents of the most weatherable minerals – kamacite and taenite, and so they have been plotted together in the olivine data as they demonstrate where alteration products derived from the Fe-Ni metals have been deposited. There is a positive correlation between Co and Ni when contents get above a certain level (~30 ppm Co, 600 ppm Ni), which is good evidence for them both being hosted in alteration products rather than being crystallographically hosted. The largest spread of Ni values is in ALH 78130 I. ALH 85017 R has fairly restricted Ni values of up to 2000 ppm. QUE 99022 I has a similar spread with only marginally more Ni on average. ALH 78130 I has significantly more Ni than the rim, with a range of values between 200-4700 ppm compared to 50-1800 ppm in the rim (with one outlier). QUE 94214 has a range of values mostly below 2500 ppm, and so has a lesser Ni content on average than ALH 78130. There is no difference in rim and interior Ni values. No correlation of Co, Ni content with rusting in QUE 94214 is seen. However, in ALH 78130 the rusted olivines have higher Co and Ni. This is especially prevalent in the interior section of the meteorite compared to the rim. This effect is less pronounced, but still present in ALH 85017.

In all samples Cu contents are below 100 ppm. ALH 85017 shows no differences between rusted and non-rusted olivine crystals. In ALH 78130 and QUE 94214, there are more high Cu points in the rusted areas than in the non-rusted. Zn contents are between 50-150 ppm for olivines in most meteorites, but QUE 94214 rim and interior both have many olivines with lower Cu-concentrations (15-50 ppm). Zn contents in QUE 94214 show a large

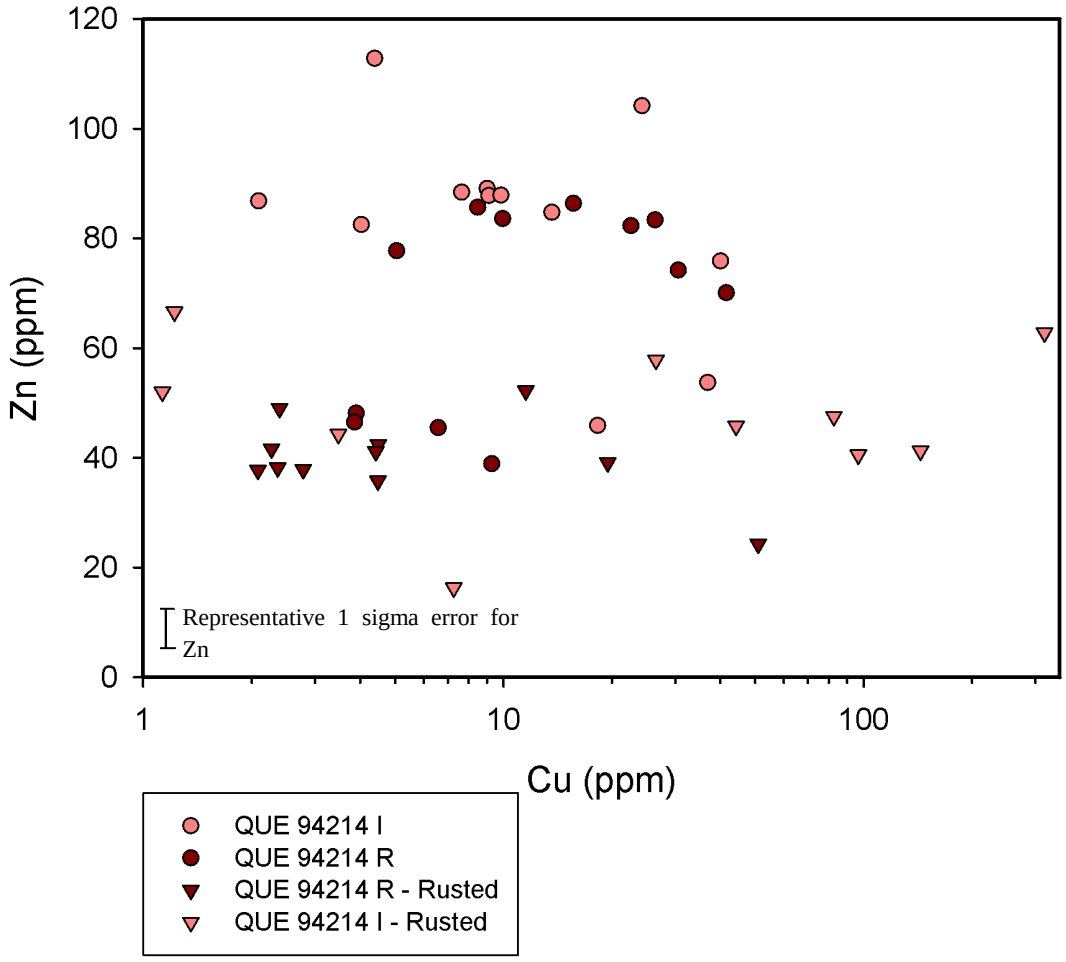

Fig 4.17. Cu vs Zn in olivines of QUE 94214. Rusted olivines have comparatively lesser Zn than non-rusted. Errors for Cu are not shown due to the logarithmic scale, but average at 2.05 ppm. Cu and Zn are plotted together as they have similar concentrations and both share the same crystallographic site in olivine (Wedpohl 1969).

difference between rusted areas and non-rusted areas, with considerably more Zn in the non-rusted areas (Fig. 4.17). ALH 78130 olivines show this to a lesser extent and ALH 85017 olivine results do not show this.

4.2.2. PYROXENES

Average pyroxene compositions of each meteorite are listed in Table 4.6. Rim and interiors of meteorites were compared as well as rusted and non-rusted areas. Rusted areas of QUE 94214 and ALH 78130 were examined and compared to non-rusted areas (ALH 85017 had insufficient pyroxene analyses in rusted areas for meaningful comparison).

The pyroxenes host minor amounts of boron, which are too close to the detection limit to be useful. Ca content is very similar between meteorites, with most pyroxenes containing 4400-9500 ppm. The rusted and non-rusted areas do not show variations of Ca content.

Sc content is < 10 ppm in all pyroxenes, with little variation between rims and interiors and rusted/non-rusted areas. The only meteorite that appears different between rim and interior is QUE 99022, which has 2-5 ppm less Sc content in the rim compared to the interior.

Al content is 1000-4000 ppm in pyroxenes from the different meteorites but is highly variable. ALH 78130 contains less Al than the other meteorites. QUE 99022 contains less Al in the rim than the interior (<1000 ppm in the rim, between 910-4000 ppm in interior). The rim pyroxenes of QUE 94214 generally contain less Al, although compositions overlap between the rim and interior samples. There are marginally more high Al pyroxenes in the rusted than non-rusted areas of QUE 94214.

K content varies between pyroxenes in the different meteorites, with very low abundances in QUE 94214 (< 15 ppm) and up to 200 ppm in QUE 99022, ALH 85017, ALH 78130), although most are below 90 ppm. QUE 99022 has a similar amount of K in the rim compared to interior, as does ALH 78130, which has a positive correlation between Al and K (which may be a result of plagioclase inclusions; seen to contain several thousand ppm K in section 4.2.3.) and there is no separation between QUE 94214 rim and interior, but there is a small separation in rusted and non-rusted areas with the rusted areas being depleted in K by an average 2.0-3.0 ppm (from the average non-rusted content of 6.0 ppm).

Ti content in pyroxenes is mostly between 500-1600 ppm and there is no consistent difference between rusted regions and non-rusted regions or rims and interiors. The only separation within samples is seen in QUE 94214, where a greater Ti content is present in pyroxenes of non-rusted areas of QUE 94214 (600-1100 ppm in rusted, 1000-1300 ppm in non-rusted).

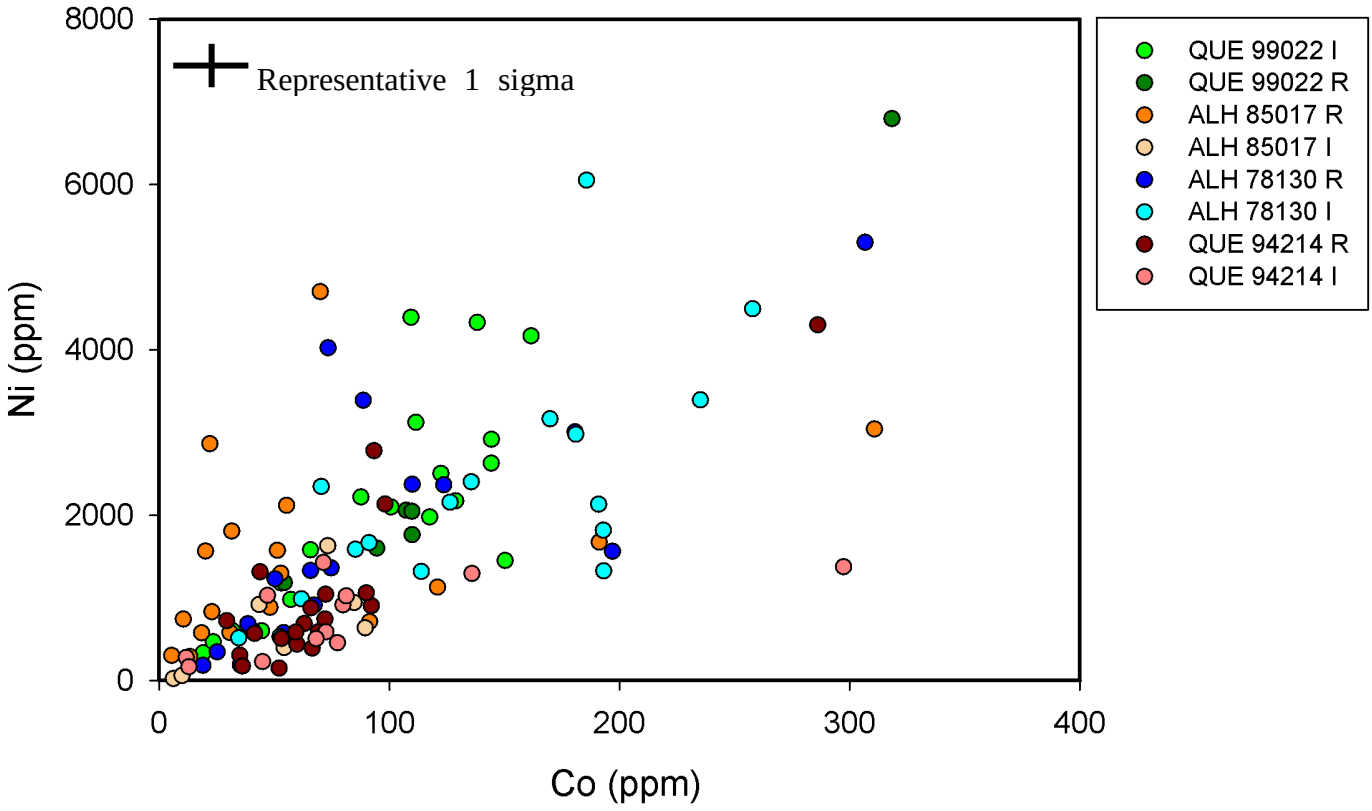

Fig. 4.18. Co vs Ni in all pyroxenes measured.

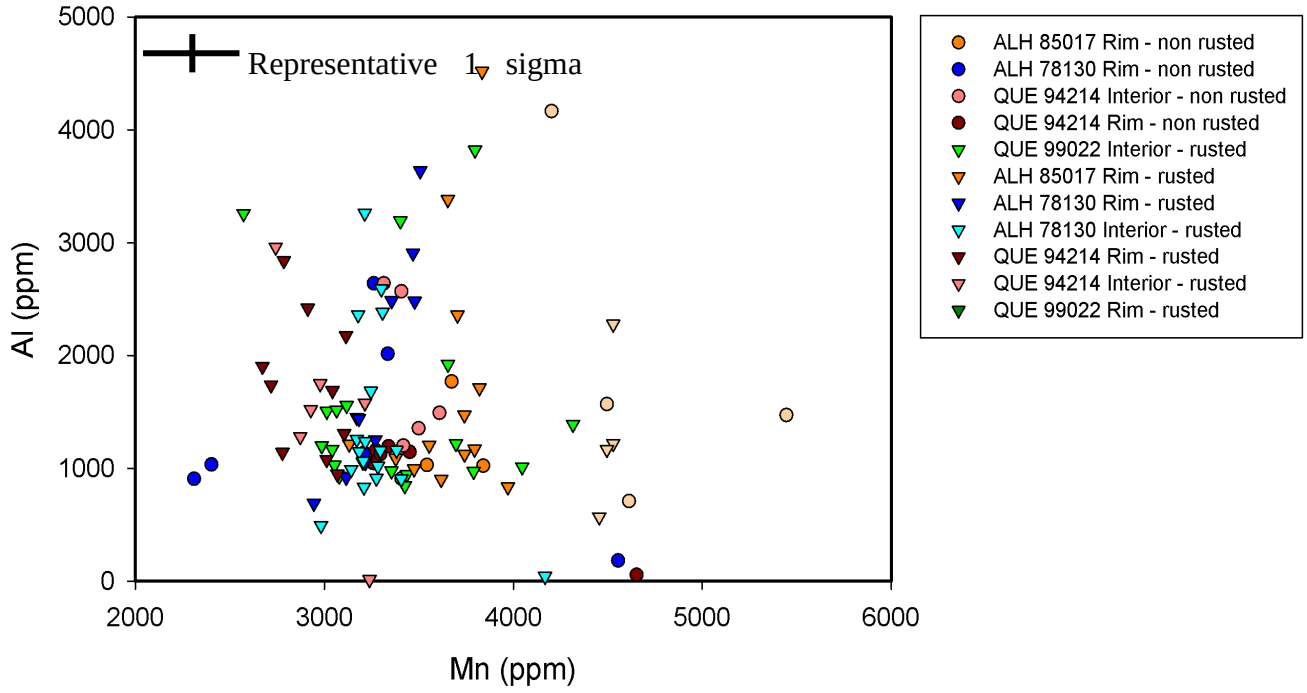

Fig. 4.19. Mn vs Al in all pyroxenes measured by LA-ICP-MS. Mn has been plotted against Al as Al is traditionally a less mobile element (Auippa et al., 2000).

There is a positive correlation between Co and Ni (Fig. 4.18) and the values range from below detection limit to 320 ppm Co, and up to 6700 ppm Ni. The largest range of values is in ALH 78130 (Co 50-3000 ppm, Ni 181-6000 ppm). QUE 99022 has a considerable range (up to 200 ppm Co, 4000 ppm Ni) and shows no rim/interior differences. ALH 85017 has a steeper positive correlation compared to the other meteorites. Almost all pyroxenes measured in ALH 85017 have smaller Co concentrations than QUE 99022. ALH 78130 pyroxenes have the largest range of values in the interior sample, and the rim sample has a smaller range. The rim sample of ALH 78130 contains more Co and Ni in the rusted areas compared to the non-rusted areas. QUE 94214 pyroxenes have a smaller Ni and Co values compared to other meteorites with a more restricted range of Co (mostly below 100 ppm) and Ni (mostly below 1400 ppm). The rusted areas of QUE 94214 are not different to the non-rusted areas.

Mn content varies between the different meteorites with QUE 94214 showing the least Mn in pyroxenes (most values between 2700-3600 ppm) and QUE 99022 having the highest (3000-4050 ppm). There is little rim/interior difference in the pyroxenes of the studied meteorites, however there are notable differences between the rusted and non-rusted areas of QUE 94214, with all rusted pyroxenes measured having consistently smaller Mn values (Fig. 4.19). This is only apparent in QUE 94214.

Cu content is mostly below 40 ppm, with some high outliers in various meteorites. These higher outliers are most common in QUE 99022 I and ALH 85017 R. There are no apparent differences between rims and interiors of meteorites (Cu carriers include troilite and Fe-Ni metal). Rusted areas have no difference in Cu content in all meteorites except QUE 94214, which has less Cu in the rusted areas than non-rusted.

Zn content in pyroxenes ranges between 40-150 ppm on average with similar spreads of values in all meteorites except QUE 94214. The low Zn values in QUE 94214 correspond with low Cu values. No consistent rim/interior differences are measured. QUE 94214 has a

low Zn group of values, which are all in the rusted areas of the meteorite, in both rim and interior sections. These rusted areas have in general 20-30 ppm lesser Zn content.

V and Cr correlate positively in all samples and so are described together (Fig. 4.20). Cr values in pyroxenes mostly range from 0-6000 ppm, V contents are mostly below 100 ppm. There is a very similar spread of values between all meteorites. Only QUE 94214 shows separation with regards to rusted and non-rusted areas, with the non-rusted areas containing less Cr and V compared to rusted areas.

4.2.3. FELDSPARS

Feldspar analyses were sparse as crystals large enough to measure are rare in all the meteorites and analyses were often mixed with surrounding phases and inclusions. Maskelynite proved difficult to ablate and so data from meteorites with maskelynite is almost completely absent. Data were successfully collected from QUE 99022 and ALH 85017. All analyses can be found in Appendix II.

4.2.4. TROILITE

Co and Ni correlate positively in troilite and, therefore, are discussed together. QUE 94214 troilite has greater Co and Ni concentrations in general, compared to other meteorites as all measured sulphides contain over 80 ppm Co and over 2000 ppm Ni. The interior troilite contains more high Ni outliers than any other meteorite. ALH 85017 I contains very little Ni (<500 ppm) compared to the other meteorites (Fig. 4.21).

Cu contents are mostly under 500 ppm with a few higher values. QUE 94214 has the most Cu in general with a range of values between 175-420 ppm, compared to ALH 78130 which is between115-230 ppm and QUE 99022 which is below that. No rim/interior differences were found.

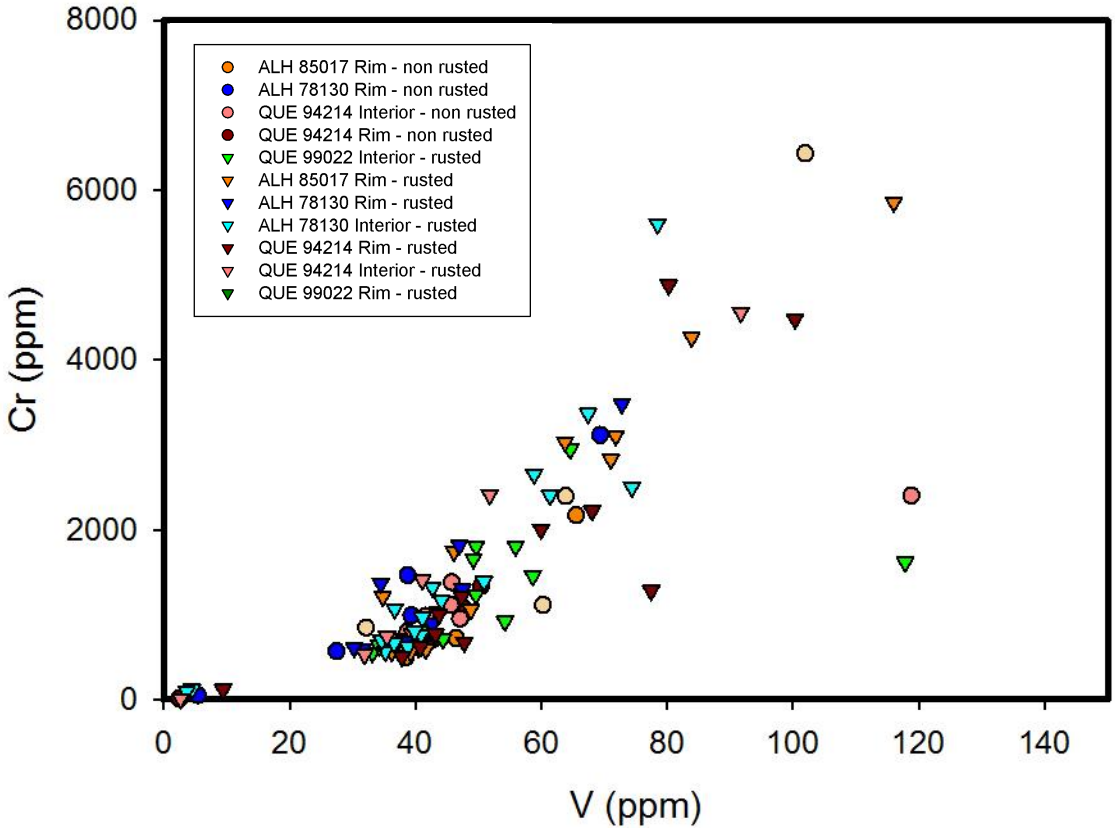

Fig. 4.20. V vs Cr in all measured pyroxenes. The 1 sigma errors are smaller than the symbols. They are plotted together as they both occur in chromites and are useful for determining areas where chromite inclusions have been measured as well as pyroxene.

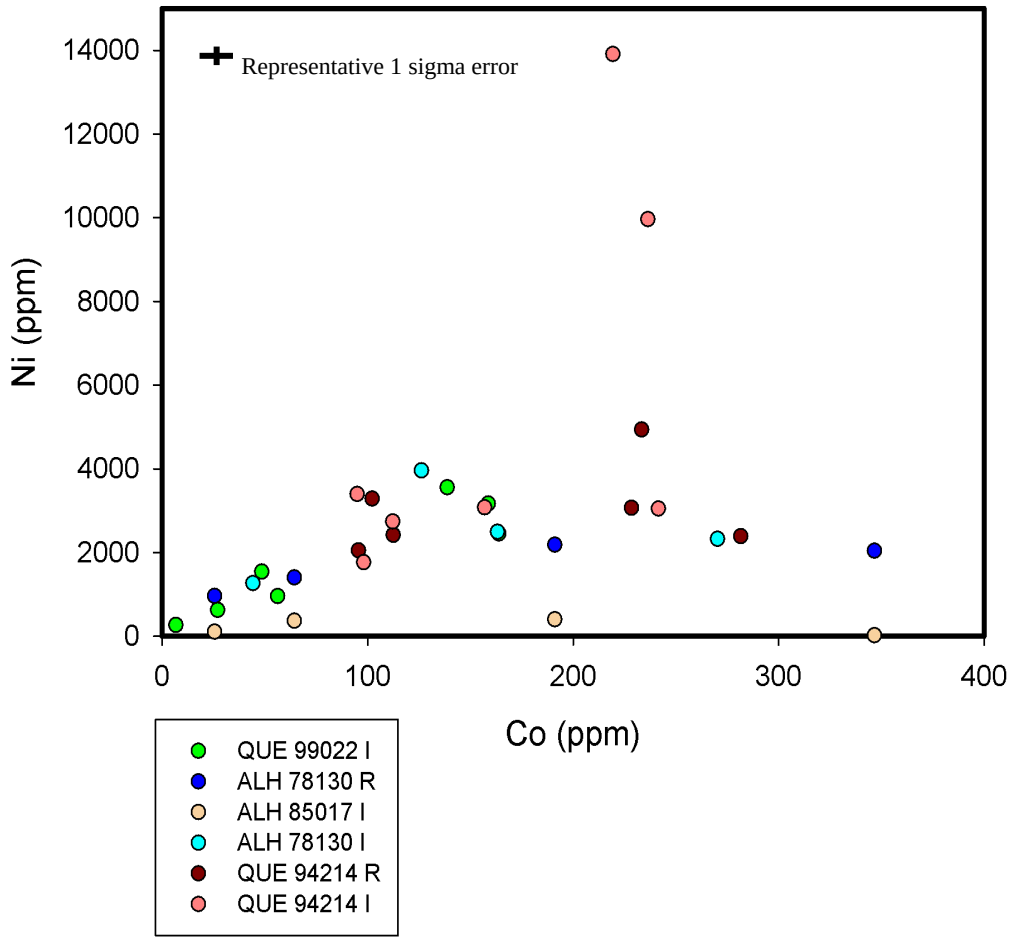

Fig. 4.21. Co vs Ni in all troilite crystals measured.

Mo content of troilite is mostly below 10 ppm and there is very little variation between different meteorites or rims and interiors.

Cr content varies between troilite in different meteorites with many analyses below detection limits, but also some Cr value at the several thousand ppm levels, particularly in QUE 99022. This large difference is potentially due to the presence of small chromite inclusions within the sulphides.

P levels are also variable between samples, with concentrations from below detection limit (e.g. ALH 85017) to 420 ppm. QUE 99022 I troilite has a highly variable P concentration (90-420 ppm), whilst most other meteorites' troilite contain <200 ppm. QUE 94214 has very consistent P concentrations which are similar in all crystals (100-200 ppm).

Mn values are between 40-300 ppm (with a couple of higher points up to 1000 ppm) and are consistent across QUE 94214 troilite, between 120-200 ppm (with two exceptions; 231 and 328 ppm), and are considerably smaller in ALH 78130 with most points below 100 ppm. In QUE 99022 I Mn concentrations in troilite is highly variable since it contains both the lowest and highest values of Mn (20 and 990 ppm). ALH 85017 is also highly variable in Mn content (range 40-670 ppm).

4.2.5. PHOSPHATES

Only a small number of analyses were made on ALH 85017 merrilites since there has been no prior indication that any alteration of phosphates occurs and REE concentrations are displayed in Appendix II.

The phosphates host almost all of the YREEs (Yttrium and rare earth elements) in the meteorites, with a very consistent pattern of concentrations across all phosphates measured (Fig. 4.22). The phosphates have highly variable Si, Al, Cr, Ti, V, Ni, Cu, Zn, Ge (with RSD (relative standard deviation) values of over 50 %). Phosphates host many inclusions (Section 3.2.8) and these elements are almost certainly from small inclusions of feldspars,

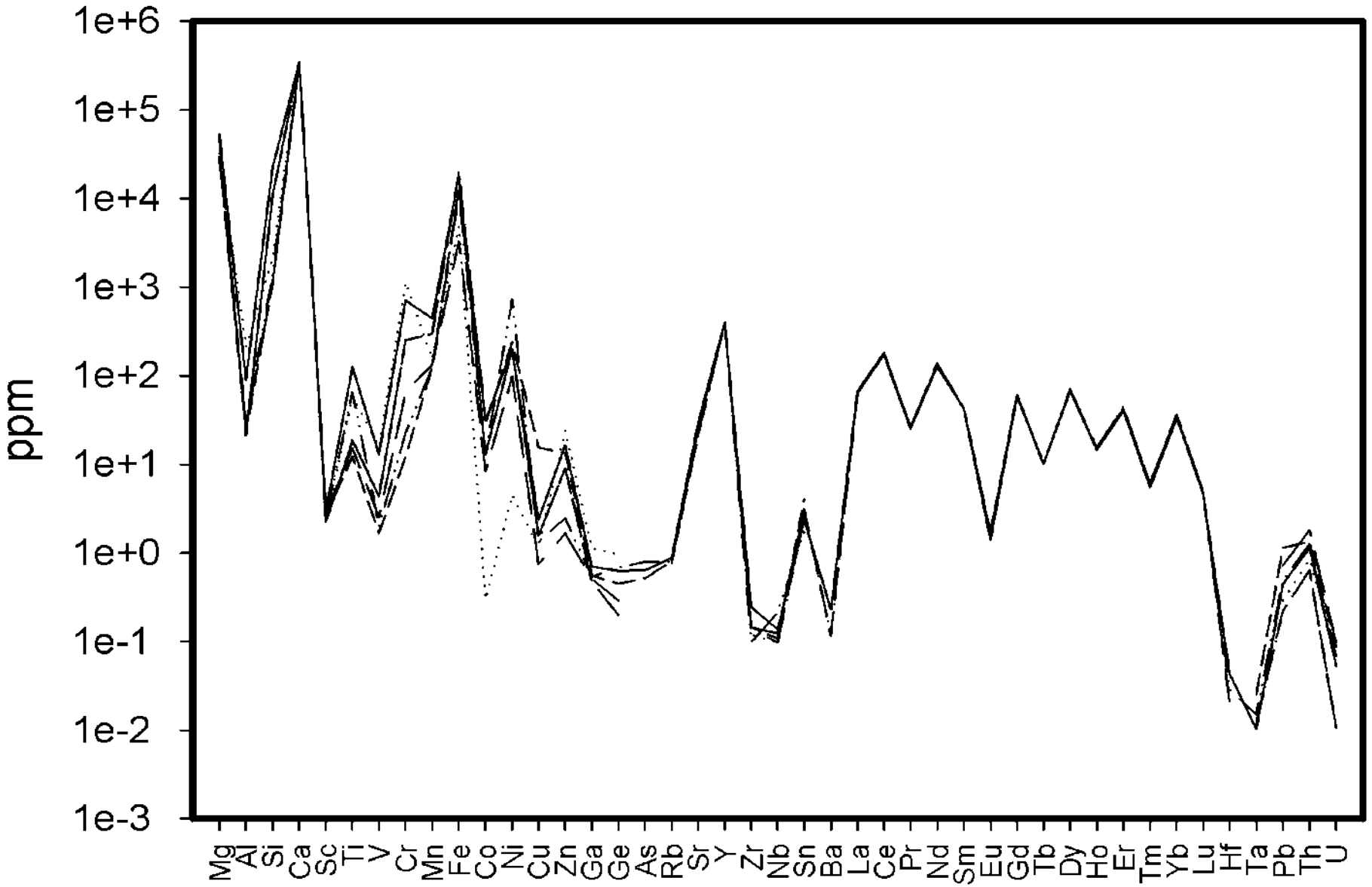

Fig. 4.22. All phosphate analyses from ALH 85017 I.

metals and chromite (which are the most common types of inclusions).

4.2.6. KAMACITE AND TAENITE

Trace elements were measured in kamacite and taenite, but comparisons of rusted and non-rusted areas were not possible. This is because kamacite and taenite grain alteration typically results in rust halos and so all grains are in rusted areas (Section 3.2.5 and 3.2.6).

Co content ranges between 2600-15000 ppm with the most Co in kamacite whilst taenite Co content is < 7500 ppm. The Co content separates the different meteorites with the highest Co content found in kamacite from QUE 94214 I (13000-15000 ppm), and in order of decreasing abundance ALH 78130 (8000-11000 ppm), and in similar position QUE 99022, QUE 94214 R and ALH 85017 between 4000-9000 ppm.

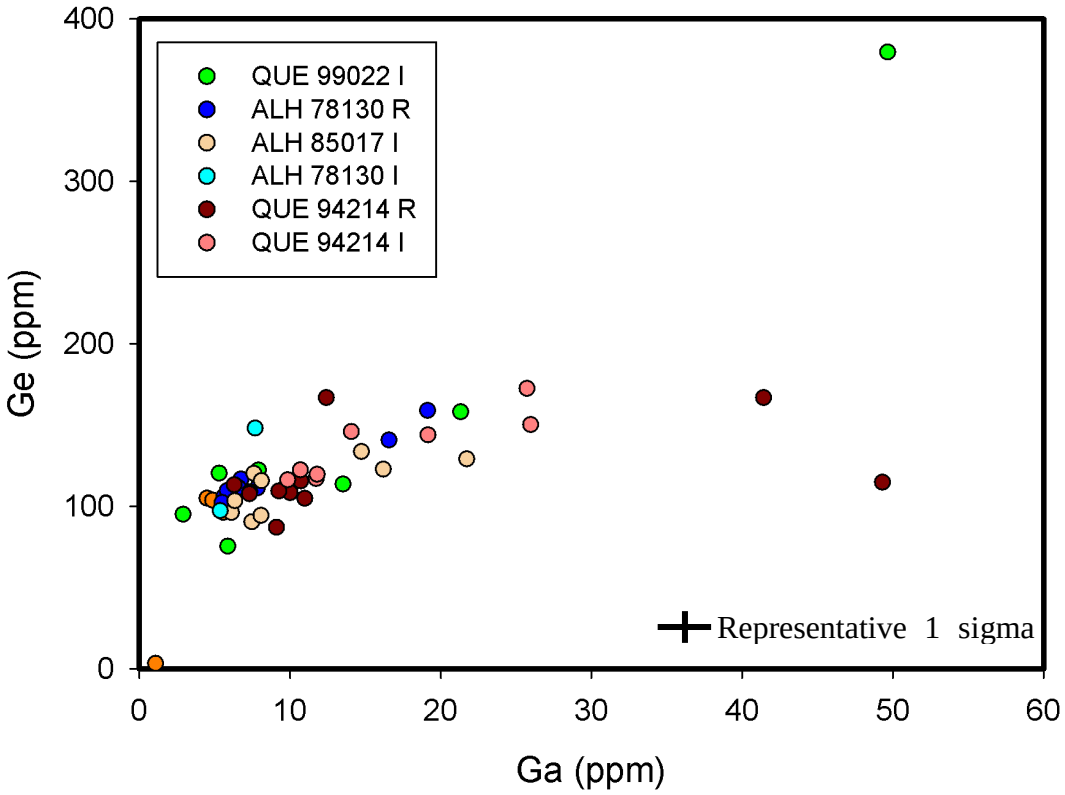

Fig. 4.23. Ga and Ge content of kamacite and taenite measured. They have been plotted together as they exhibit similar geochemical behaviour.

Ga correlates positively with Ge (Fig 4.23) and so they are discussed together. Ga content ranges between 1-50 ppm, and Ge ranges between 70-200 ppm. All meteorites have a similar spread of values, with the most restricted in ALH 78130 (Ga 5-20 ppm, Ge 90-158 ppm). QUE 94214, ALH 85017 and QUE 99022 all cover similar values (Ga 2.91-30 ppm with outliers, Ge 90-180 ppm). No rim-interior differences are measured.

As values are between 10-40 ppm on average with no variation between rims and interiors, and all meteorites have the same (or very similar) ranges. QUE 99022 is the only meteorite that has slightly different values (< 25 ppm).

Mo in metals are almost all < 12 ppm, with little variation between samples. QUE 94214 is the only sample that shows potential rim/interior differences with smaller Mo values in the rim (3-7 ppm compared to 6-12 ppm).

Platinum group elements are mostly <10 ppm in all meteorites with a couple of exceptions: QUE 99022 I has an average value >10 ppm in all platinum group elements (except Rh) due to one particularly high grain measured (containing 30-60 ppm) which appears to be petrographically similar to other grains. QUE 94214 I also has a few anomalously high points which raises the average values significantly. No rim/interior differences are observed.

4.2.7. CHROMITE

As for the phosphates, only a select number of analyses of ALH 85017 were made. Chromite hosts a significant amount of V, Zn, Ga and Mn compared to the other phases in the meteorites.

4.2.8. POCKETS OF ALTERATION PRODUCTS

Trace elements were measured in alteration products in 6 separate pockets QUE 99022 of varying distances from the rim since this was the only sample with pockets large enough

for measurement (results in Table 4.7.). Two pockets in the fusion crust were measured (images are in Fig 4.24; one is connected to the outer edge of the meteorite (A), the other does not appear to be in the two dimensional image (B), one from 1 mm into the sample (C), 2.5 mm into the sample (D), one at 5 mm (E) and one at 5.5 mm (F).

The two pockets in the fusion crust have different compositions to the others: higher Pb (24 ppm and 45 ppm) compared with any other mineral measured or any other oxide pockets (Pb < 0.5 ppm). The increase in Pb is greater in the vein that is connected to the outer edge than it is in the unconnected pocket. However, this analysis had some contamination from a nearby olivine (Fig. 4.24) which would give rise to some differences, but the Pb content in olivines is negligible (Section 4.2.1.). There is enrichment of Sr, Ca, REEs, Al, Cr, and Ba compared to the other measured alteration products.

Table 4.7. All alteration product compositions measured in QUE 99022 R by LA-ICP-MS (ppm)

	A	B	C	D	E	F
Mg	5622.45	6432.34	10300.26	2777.72	2497.82	1500.69
Al	1912.62	1013.37	133.03	1.66	3.06	9.54
Si	951.06	1225.57	1345.84	325.92	354.84	480.19
Ca	50.55	224.60	46.68	20.46	30.27	34.59
Ti	14.20	58.99	24.92	15.93	10.06	3.53
V	7.85	17.77	1.47	0.60	1.10	0.28
Cr	652.39	380.47	28.91	9.98	55.51	16.60
Mn	318.37	287.44	295.98	71.73	51.58	123.56
Co	3665.09	1178.45	2121.34	1023.82	1429.68	1990.24
Ni	96911.87	17731.85	30743.65	28644.96	29330.69	23878.10
Cu	653.92	58.99	74.61	9.10	15.54	41.52
Zn	142.41	23.91	9.70	2.45	3.86	5.38
Ga	91.58	1.47	14.77	19.02	17.23	21.26
Ge	647.16	1.51	204.08	316.93	307.53	280.21
As	78.59	1.76	31.05	56.90	47.80	38.31
Rb	0.58	3.57	0.45	0.08	0.16	0.08
Sr	4.15	73.52	1.14	0.42	0.93	0.52
Y	16.38	2.71	0.78	0.18	0.30	0.46
Sn	11.24	0.77	2.07	2.06	3.05	2.50
Sb	3.00	**BDL**	0.81	0.67	1.53	1.28
W	6.62	0.04	2.28	3.97	3.38	2.48
Pb	23.92	45.34	0.18	0.03	**BDL**	0.01

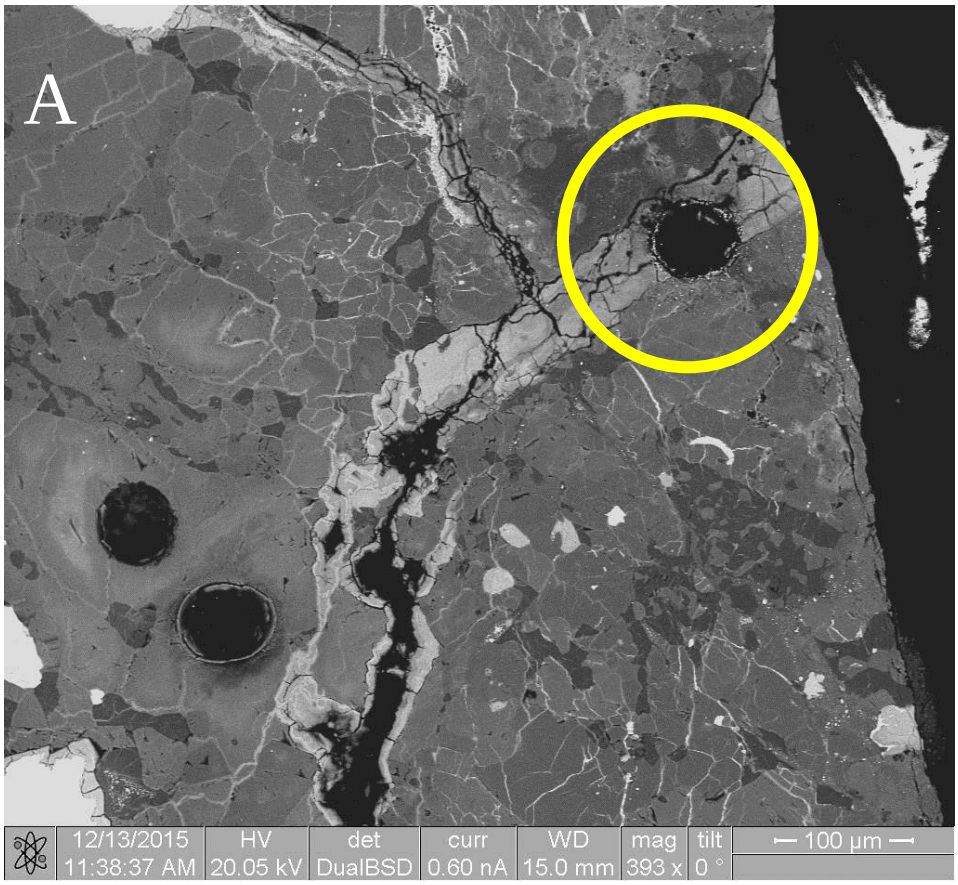

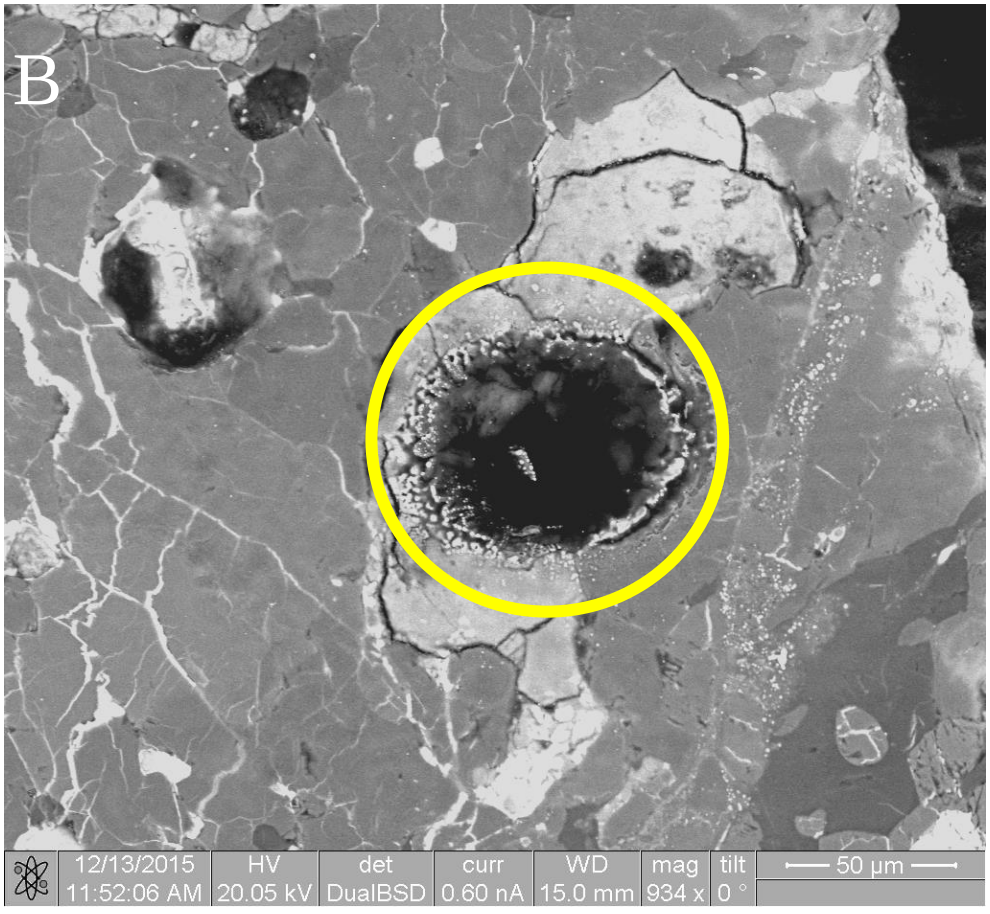

Fig. 4.24. BSE images of laser pits in alteration pockets A and B in QUE 99022 R. {pits are ringed with a yellow circle. A is in a vein connected with the outer edge, whilst B is not as obviously connected.

The REE elements are mostly < 1 ppm, which is almost below detection limit. Pocket B is different from all others; with less Ni, Ga, Ge and more Ca, Sc, Ti, Sr, Ba and Pb. The trace elements of the pockets are compared with the average compositions of other minerals, to asses which minerals are likely to have contributed to formation of the pockets (Figs 4.25 A-F).

The alteration products further into the meteorite (not at the immediate fusion crust) are compositionally similar with variable amounts of the main lithophile elements (Mg, Al, Si, Ca, Mn). A considerable quantity of As is present in the pockets (30-80 ppm), as is Ge and Ga.

Olivine and pyroxene both have very similar patterns of: Mg, Al, Si, Ca, Sc, V, Cr and they are proportionally very similar to the alteration products (Fig 4.25.A&B). Atomically heavier elements than those above have little that matches with the silicates.

Kamacite shows links to Fe, Co and Ni (Fig. 4.25. C) and Ga and Ge in the metals are below the concentrations of most of the alteration products, and so if they are sourced from the metals then preferential retention would be necessary to concentrate them. Sn is potentially from kamacite or troilite (none is measured in taenite; Fig 4.25. D). Chrome is likely to have been sourced from chromite as could V, Mn and Zn (Fig. 4.25. E). The REEs have a startling similar pattern in comparative quantities to the phosphates measured, and so are likely sourced entirely from them with no preferential concentration of one rare earth element over another (Fig. 4.25 F).

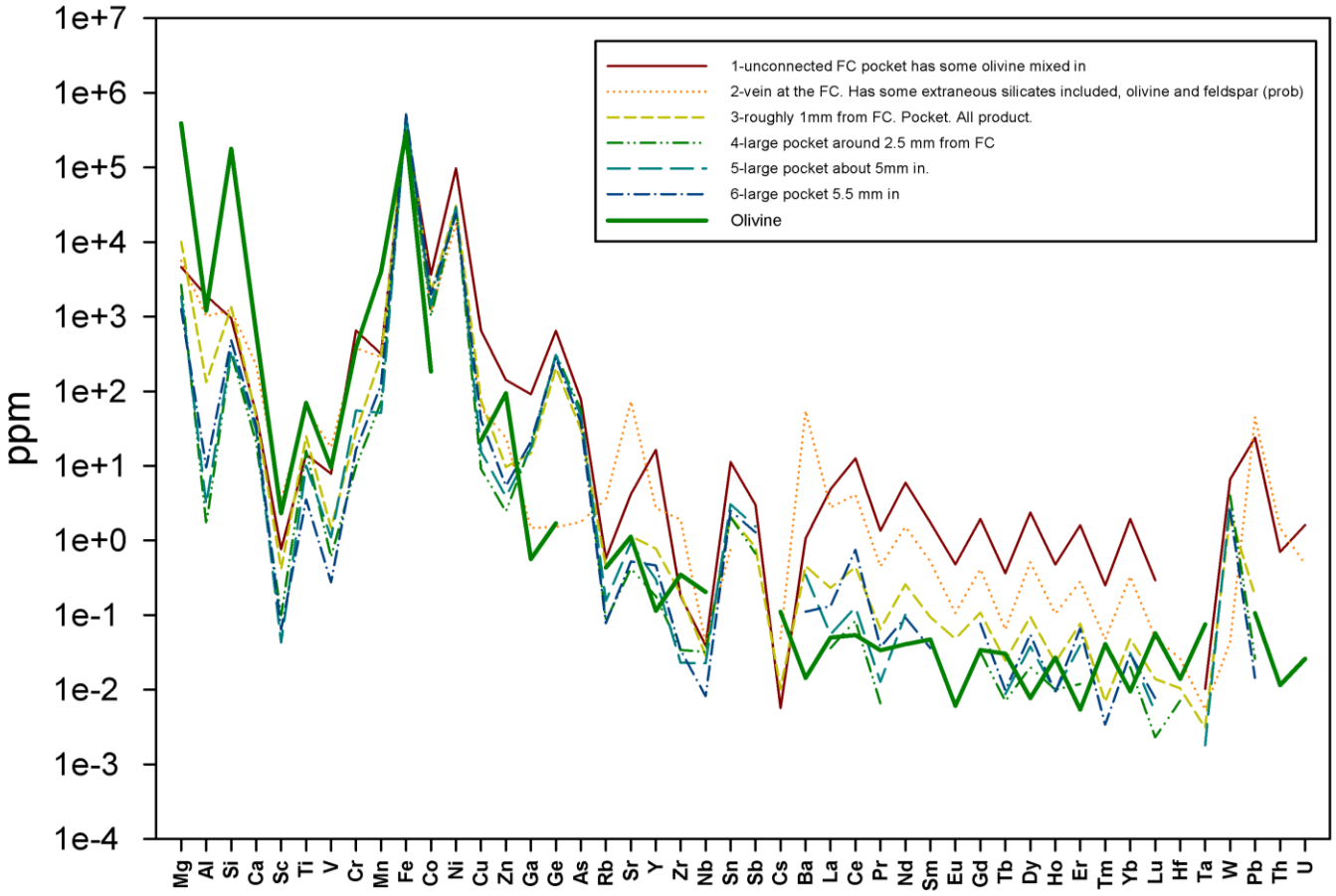

Fig. 4.25. A. Fe-oxide compositions with an average olivine composition plotted for comparison.

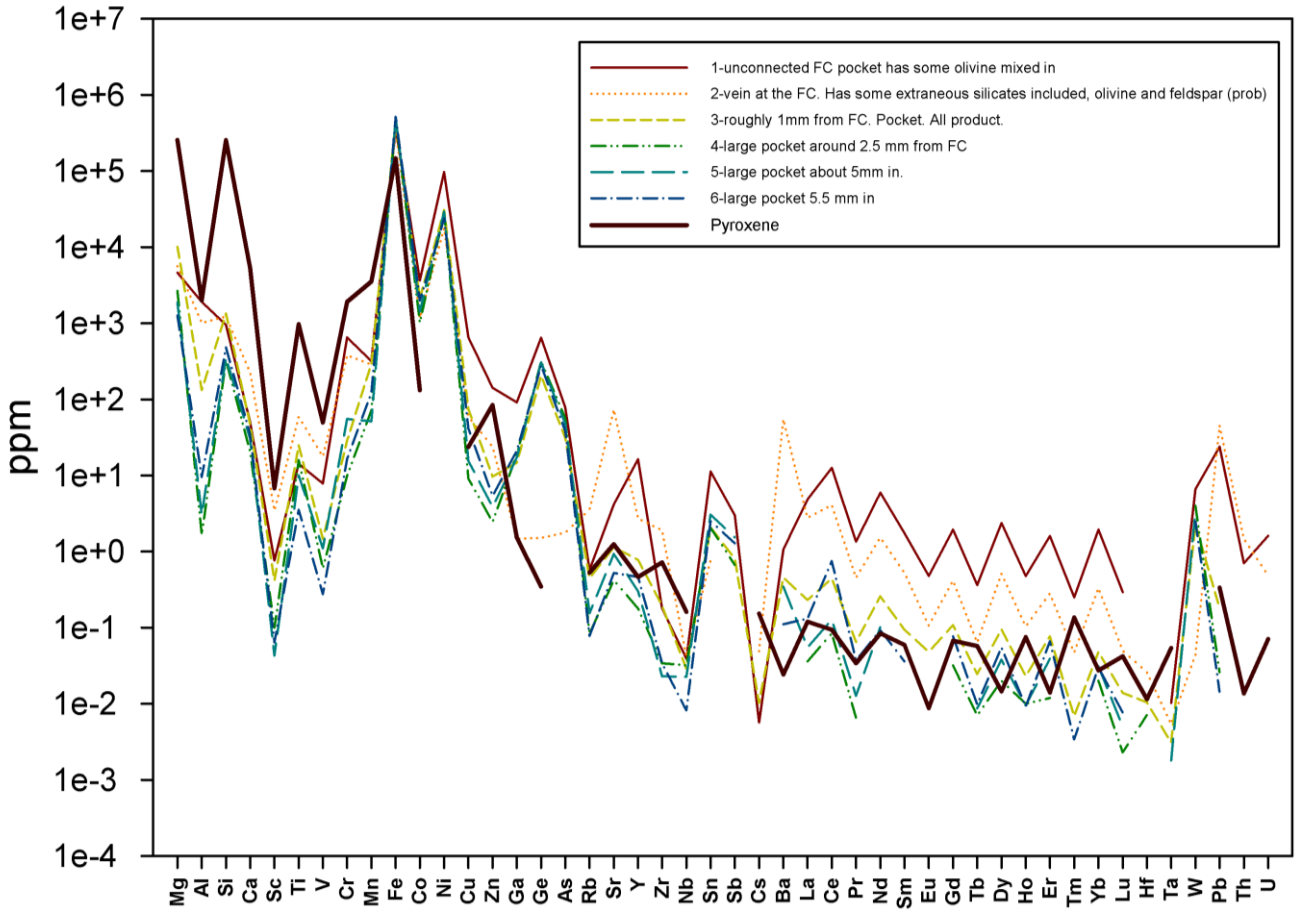

Fig. 4.25. B. Fe-oxide compositions with an average pyroxene composition plotted for comparison.

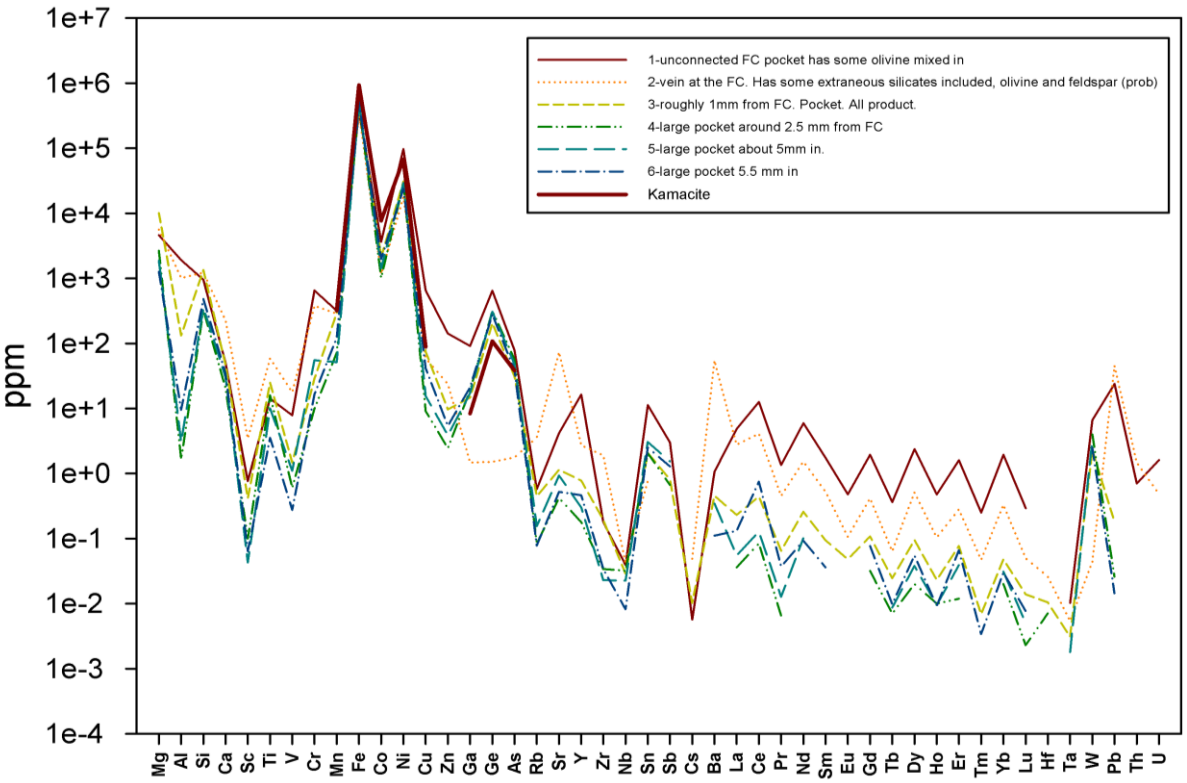

Fig. 4.25. C. Fe-oxide compositions with an average kamacite composition plotted for comparison.

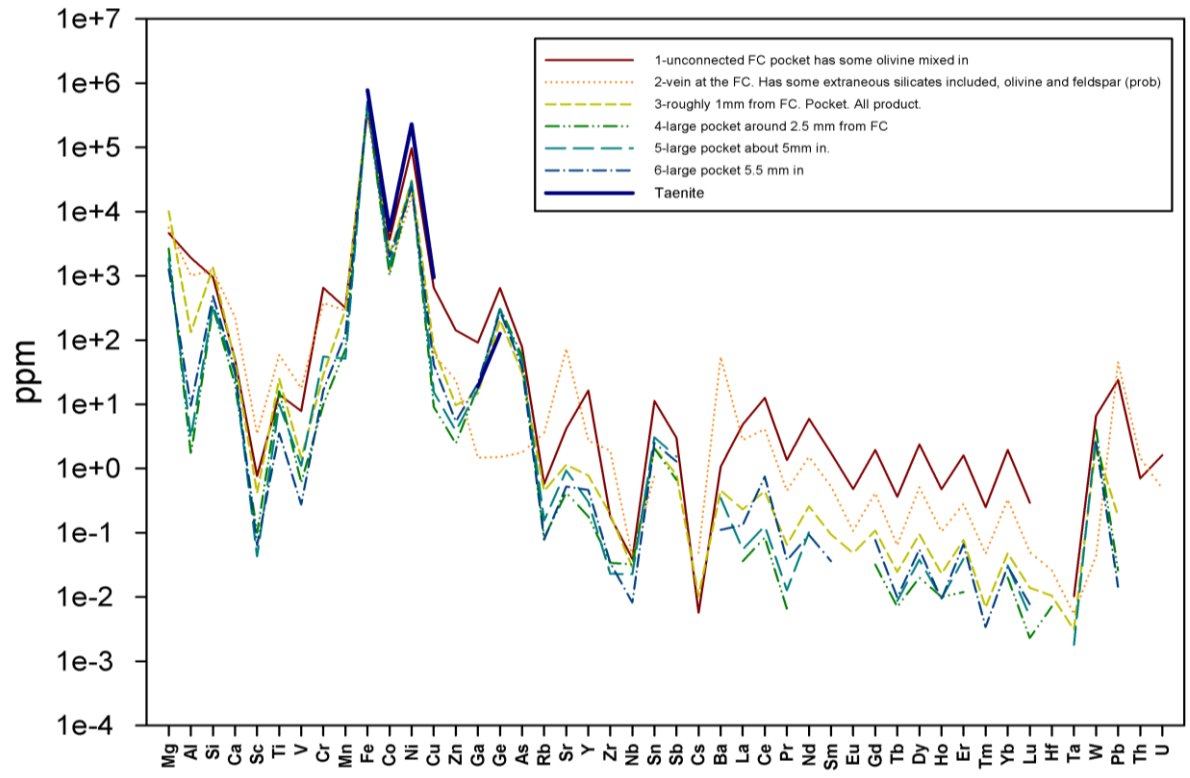

Fig. 4.25. D. Fe-oxide compositions with an average taenite composition plotted for comparison.

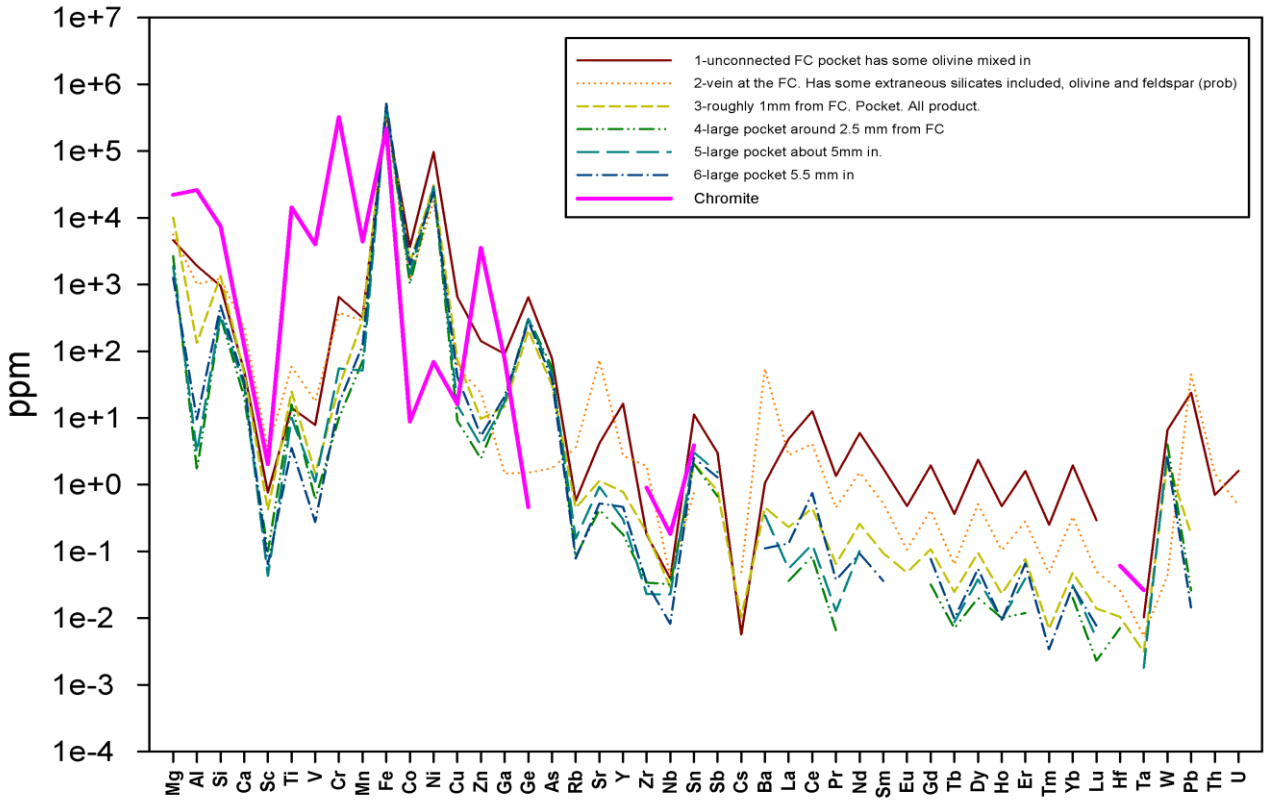

Fig. 4.25. E. Fe-oxide compositions with an average chromite composition plotted for comparison.

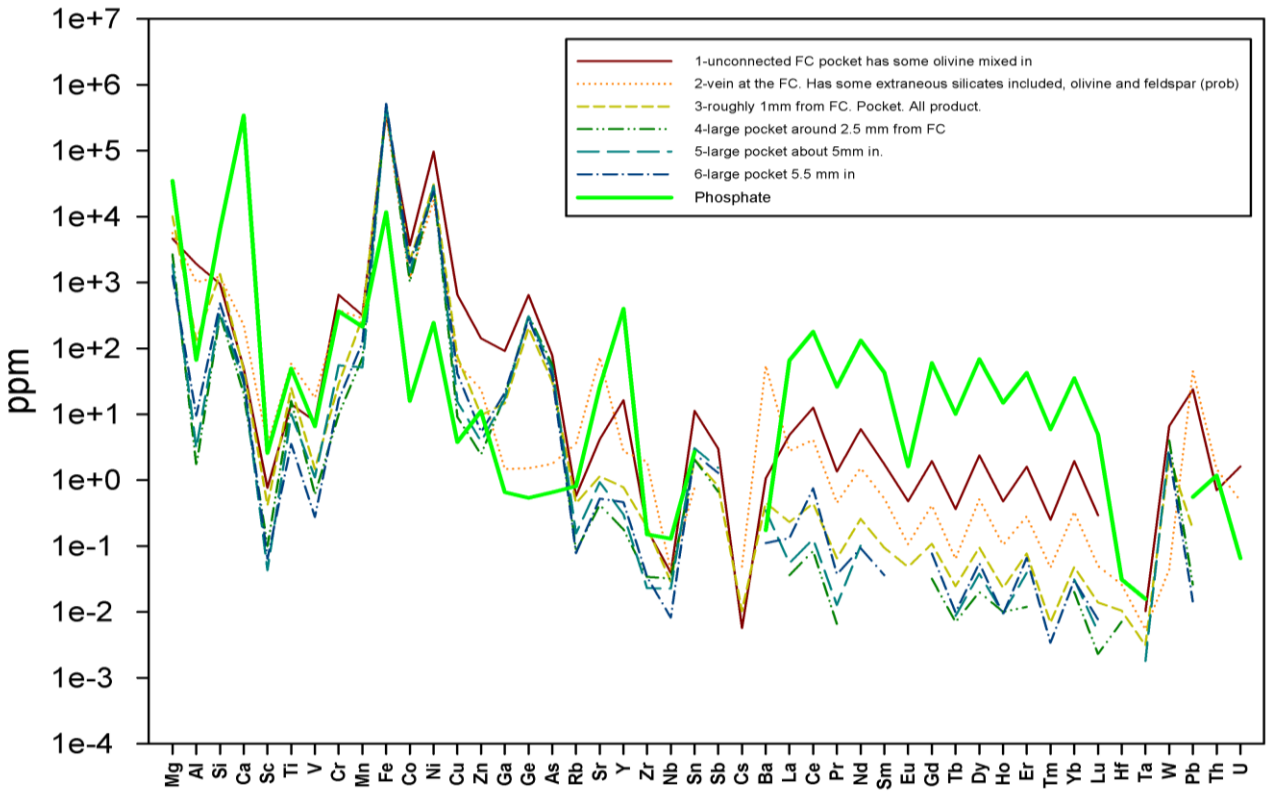

Fig. 4.25. F. Fe-oxide compositions with an average phosphate composition plotted for comparison.

4.2.9 Discussion of LA-ICP-MS data

Two types of weathering are observed in the samples, 'normal' weathering which is present in ALH 78130, ALH 84058, ALH 85017, ALH 84056 and QUE 99022 and 'acidic' weathering as is present in QUE 94214. Changes in olivine compositions are summed up in Fig 4.26 for the two different types of weathering. QUE 94214 is treated separately because it contains many differences in weathering patterns from the other meteorites. Whilst addition of Fe is generally common in all weathered meteorites in the rusted areas, there are different trace element patterns.

The high Al content in olivines from the interior of QUE 94214 may be an indication of a greater number of plagioclase inclusions, or, it may be an indication of Al deposited in alteration products. Petrological observation of the crystals show that the two olivine grains that have the highest Al concentrations contain feldspar inclusions that have been ablated with olivine during LA-ICP-MS analysis. In the other olivines, all but one grain with high Al were positioned directly adjacent to troilite crystals. Al is conserved during dissolution of olivines followed by clay formation, and clay formation has been observed in the interior section of QUE 94214 in areas adjacent to troilite (Section 3.2.1.). As the concentration of Al is higher in the rusted areas, this may be indicating a greater amount of clay formation and deposition in the rusted areas of QUE 94214, but the extra Al needs a source. All of the olivine crystals with high Al are adjacent to feldspars and so may have sourced the Al from these crystals which has gone on to form clays deposited in olivines in fracture planes and in etch pits.

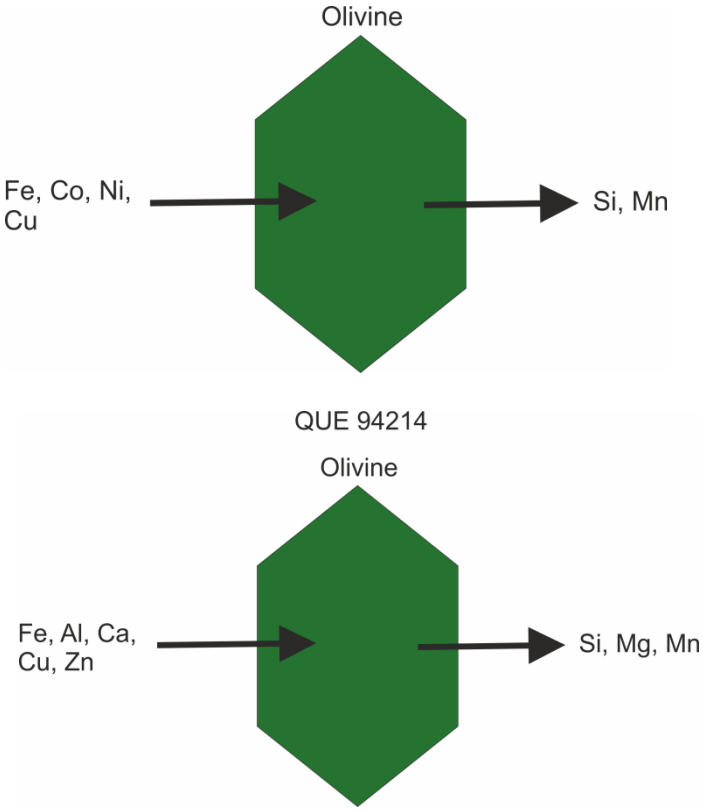

Fig. 4.26. A. Generalised cartoon of olivine additions and subtractions in the two systems. i) ALH 78130 and ALH 84058, ii) QUE 94214 acidic system.

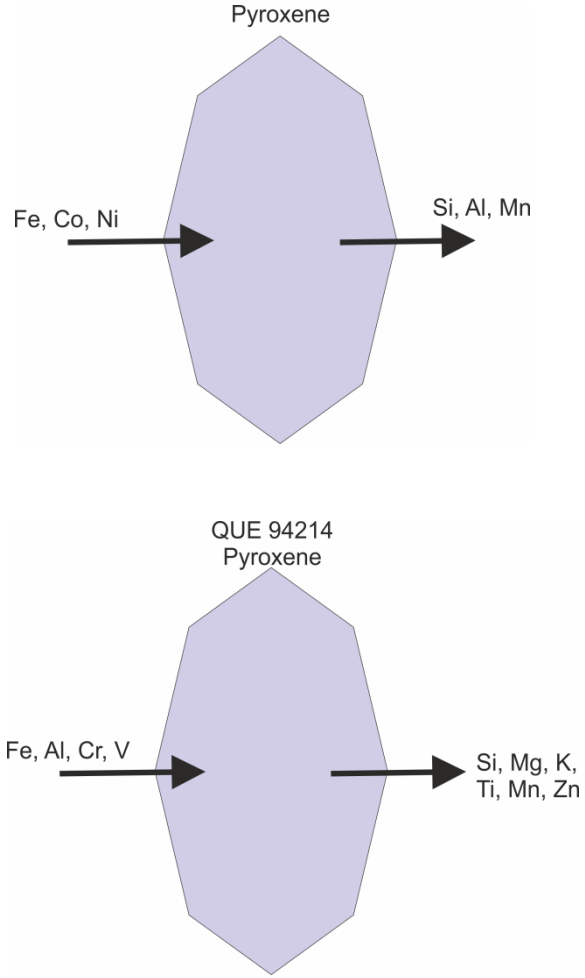

Fig. 4.26. B. Generalised cartoon of pyroxene additions and subtractions in the two systems. i) ALH 78130 and ALH 84058, ii) QUE 94214 acidic system.

There is no petrological evidence of feldspar dissolution, but it is possible the amount of plagioclase required to create these hotspots would be below the level observable. A mass balance calculation is used to test this:

$$Al_R - Al_{NR} = Al_{AD}$$

$$Al_{AD} \times \%Ol_R = Al_{AD\,TOT}$$

$$\%Plag \times Al_{Plag} = Al_{TOT}$$

$$Al_{AD\,TOT} \div (Al_{TOT} \div 100) = \%\, Dissolved\ plag$$

The average value of Al in non-rusted olivines (Al_{NR} ; all values measured in ppm) is subtracted from the average Al content of rusted olivines in QUE 94214 (Al_R), then scaled by the modal percentage of rusted olivine in the samples ($\%Ol_R$) to give the total Al excess in the samples olivines ($Al_{AD\,TOT}$). The average Al content of plagioclase is scaled by the modal percentage to give the total Al content residing in plagioclase (Al_{TOT}). Then the percentage required to make the addition of Al to the olivines is calculated.

The result is that it would take the dissolution of ~ 0.60 % of the plagioclase in the sample to release sufficient Al into solution to deposit and create these hotspots in the olivine (with the assumption of 100 % deposition from solution, which is justified by the low solubility of Al). As this is such a small amount, it is unlikely to be visible in petrographic observations and so plagioclase may well be the source of the Al hotspots.

Al and Fe are regarded as relatively immobile elements because of the strong tendency for them to deposit in alteration products (Auippa et al., 2000; Wedpohl 1969). It is likely that Al in the olivines was scavenged from adjacent plagioclase crystals and had a short transit. This is also corroborated by the petrological observation that all hotspot Al olivines are adjacent to plagioclase (although this is common throughout the meteorite). As the elevated Al values are absent from the rusted areas of ALH 78130 and ALH 85017, it may

be an indication that clay is not forming in the olivines, and that plagioclase is not dissolving in these samples to provide the excess Al.

The restricted range of Mn in olivines in ALH 85017, compared to the other meteorites, is an indication that the larger ranges of Mn in the other meteorites are a weathering effect. The lower values in the more weathered meteorites show the breakdown of the olivine crystals and removal of Mn from the olivines. This is further compounded by the consistently lower Mn values in the rusted areas of meteorites compared to their non-rusted areas. The lack of this pattern in ALH 85017 suggests that the olivines do not break down in the rusted areas as they do in ALH 78130 and QUE 94214.

The difference between rusted and non-rusted areas is significantly more pronounced in QUE 94214 than in ALH 78130. In ALH 78130 either the Mn is more readily oxidised and precipitated as MnO_2 more immediately, or there is less dissolution of olivines and so less Mn is released to solution to be carried away.

The removal of Mn in QUE 94214 rusted areas is likely to be increased by sulphide weathering, which produces a more acidic environment (Sato 1960; Nickel and Thornber, 1977). Mn mobility increases in an acidic environment and deposition of the Fe-oxyhydroxides, that are the most significant sink of Mn, is decreased (Auippa et al., 2000). This increases the transport distance for Mn and so immediate oxidation and deposition within the olivine along cleavage planes is less likely. The nanophase Fe-oxides that make up the visible rust covering the olivine must be less Mn-rich because the Fe cations have a larger radius than Mn, and so are less soluble and deposit preferentially (Auippa et al., 2000).

Fig. 4.27 shows the Eh/pH diagram for Mn and Fe comparative solubilities. The diagram shows the area that must be occupied by QUE 94214 sulphide adjacent areas that allows Fe deposition, but Mn transportation. As QUE 94214 is producing small areas of lower pH

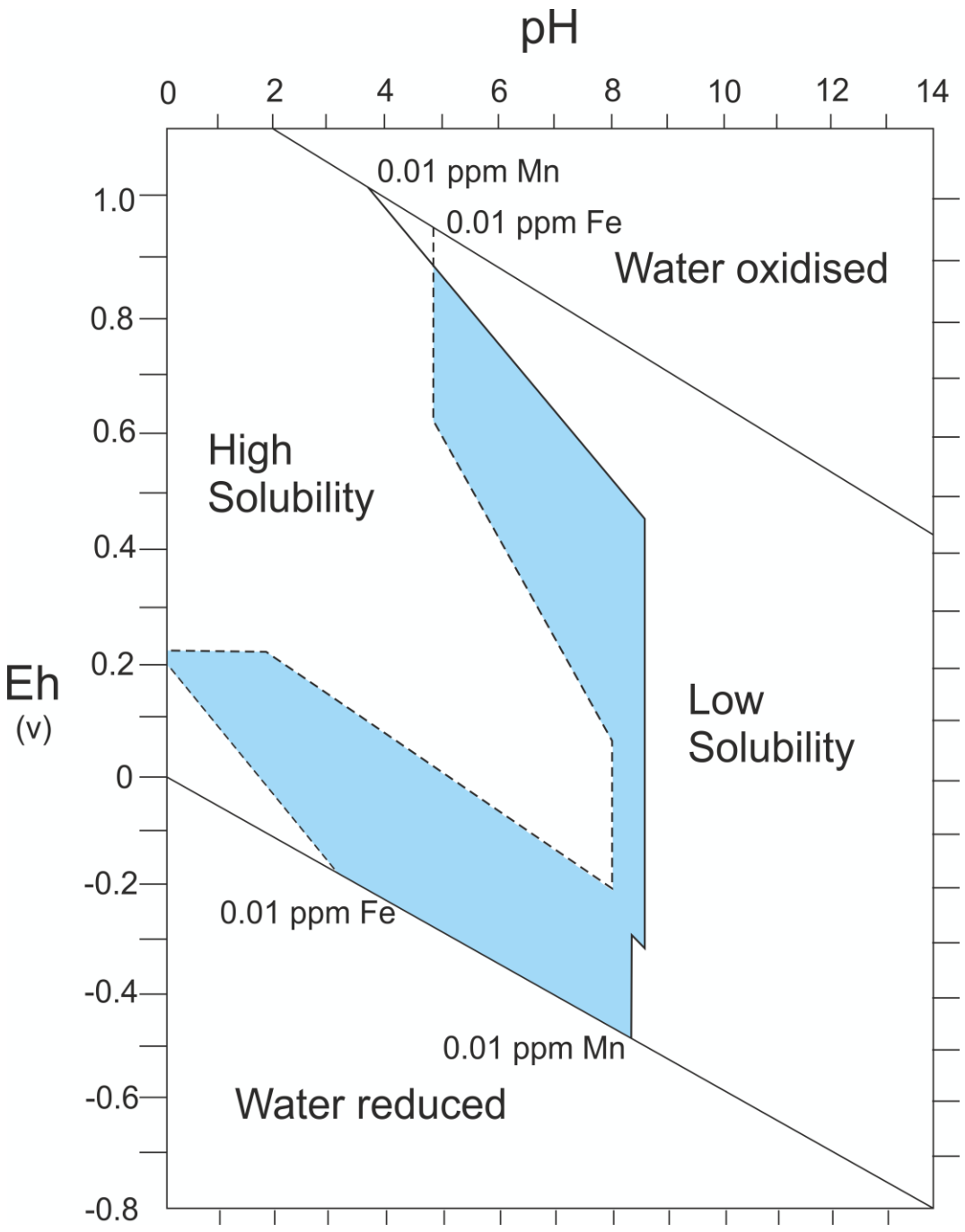

Fig. 4.27. Eh/pH space occupied by all weathering meteorites, dictated by Mn and Fe mobility. The diagram is based on a textbook diagram of Fe and Mn mobility in an Eh/pH space from Wehdpohl (1969). The blue shading indicates the Eh/pH required in fluid for Fe to be deposited and Mn transported. The lines indicate the point at which elements will come out of solution at different conditions.

fluids as a result of sulphide weathering, the solubility of both Fe and Mn is increased compared to the higher pH of ALH 78130 and the other meteorites studied. The extent of changes caused by these low pH areas will be assessed in Chapter 6, where comparisons between bulk measurements and these spatially resolved data are made.

Co and Ni values in both olivines and pyroxenes show the redistribution of elements from Fe-Ni metals across the meteorite. This is clearly seen in ALH 85017 where the values are very low, as is expected in the least weathered meteorite of this study. In contrast, the interior of ALH 78130 is one of the most weathered samples, and also has the largest spread of Co and Ni values. QUE 94214 has a restricted spread of Co and Ni values for the large amounts of weathered kamacite and taenite that was recorded in Section 3.3. QUE 94214 has a similar amount of weathered kamacite and taenite to the rim of ALH 78130 and more than ALH 85017 (Table 3.2.) but does not have the resultant Co and Ni hotspots that the other meteorites do. The lack of correlation of positive Co and Ni concentrations with rusted areas of QUE 94214 is also indicative of the redistribution of Fe-Ni metal hosted elements being different to ALH 78130 and ALH 85017.

This is evidence of different fluid compositions in the rusted areas of QUE 94214 compared to ALH 78130 and ALH 85017. Enhanced mobility of Co and Ni suggest either a lower pH, a less oxidising fluid, or both (Auippa et al., 2000).

The Cu content is enhanced in rusted areas, which is most likely similar to the Co and Ni in that it is adsorbed onto Fe-oxyhydroxides. However, the correlation with rusted areas is apparent in QUE 94214 as well as the other meteorites unlike the Co and Ni. The large Zn difference in QUE 94214 is unique and is potentially showing a redistribution of Zn from olivine and pyroxene concentrating in areas of weathering.

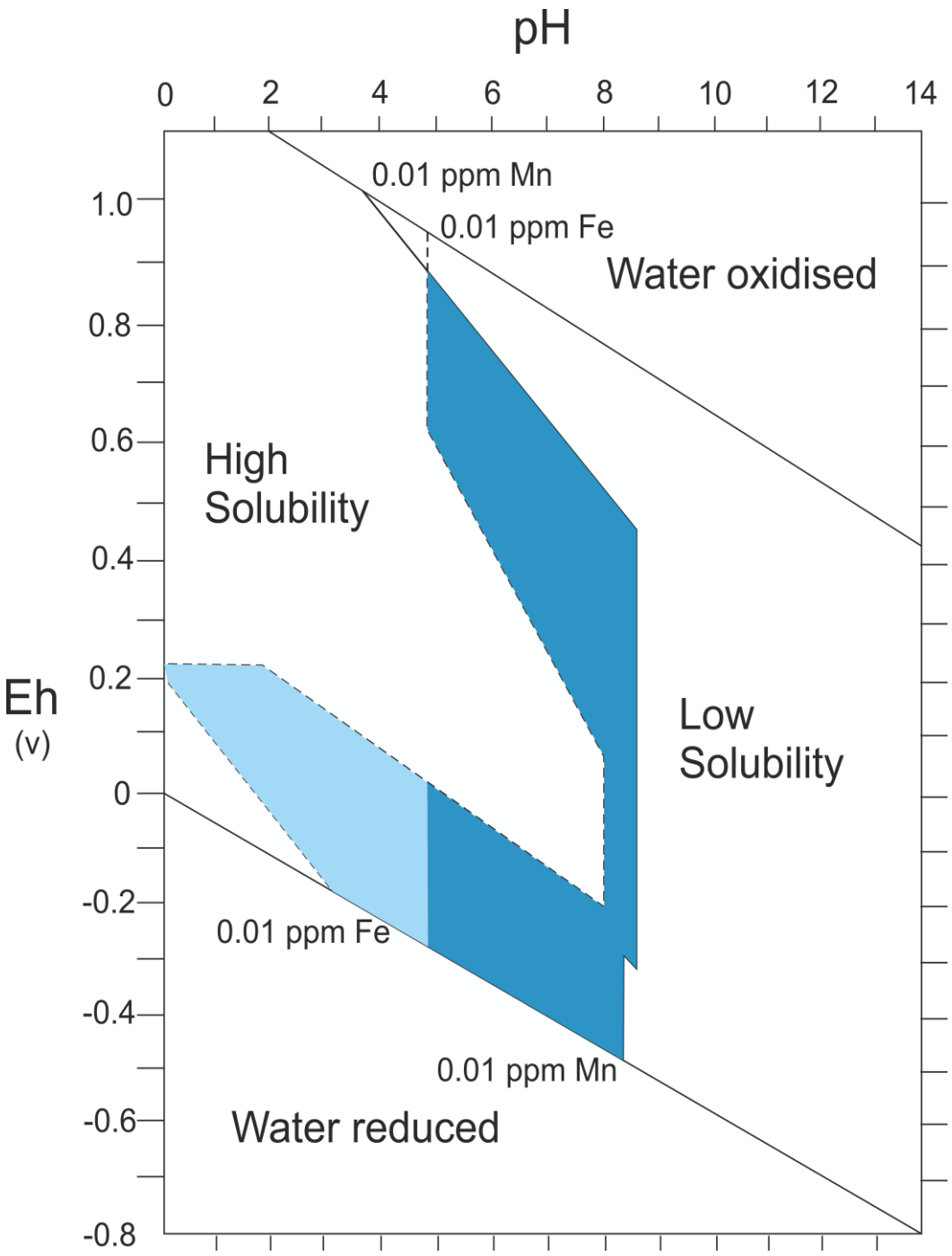

Fig. 4.28. Eh/pH spaces required to be occupied by QUE 94214 (light blue) and ALH 78130 & ALH 84058 (dark blue) fluids to result in the different mobilities of Fe and Mn with the limitation of a <5 pH fluid as is required to produce the mobilities of Cu, Zn, Co and Ni observed..

The differential behaviour of Cu, Zn, Co and Ni in QUE 94214 gives a chance to ascertain probable pH and oxidation state in the sample. Cu is known to be more strongly absorbed by Fe-oxyhydroxides and less soluble in oxidising conditions than Zn, Co and Ni but in an intermediate redox state, this behaviour is reversed (Rose and Bianchi-Mosquera 1993). The retention of Cu in QUE 94214 rusted areas is therefore demonstrating behaviour more likely to occur in the presence of an oxidising fluid. The order of adsorption preference in Fe-oxyhydroxides in oxidising conditions is Cu, Zn, Co, Ni which may explain the lack of Co and Ni hotspots in QUE 94214 silicates. It is known that with a decrease of pH, the adsorption of all of the metals above is decreased also, but as Cu and Zn are more strongly adsorbed by Fe-oxyhydroxides then the pH must be sufficient to allow the adsorption of Cu and Zn, but exclude Co and Ni. Based on experimental studies (specific to goethite adsorption) by Rose and Bianchi-Mosquera 1993, this would require a pH below 5.

Together with the removal of Mn, and using Fig. 4.27 this also narrows the field of Eh values to between -0.25 and +0.22 (Fig. 4.28). The lack of Zn hotspots in ALH 78130 and ALH 85017 rusted areas is probably not a result of adsorption rates into Fe-oxyhydroxides, but of the primary host, olivine, not having weathered sufficiently to release Zn to solution and so is not used in consideration of Eh/pH space. Since Co and Ni are deposited across ALH 78130 rusted areas, the pH must be greater than 5, between 5 and 8.2 (Fig. 4.28) and the potential Eh range as limited by Mn removal and Fe deposition is much larger than QUE 94214; between -0.4 to 0.9.

The order of mobility in both of these systems is therefore Mn > ((Ni ≥ Co) > Zn > Cu) ≥ Fe. Generalised pyroxene additions and subtractions are summarized in Fig. 4.26B. QUE 94214 again shows different trace element patterns and so is separated.

Higher Ti, V and Cr contents of rusted pyroxenes in all the meteorites studied may be related to a higher number of chromite and Ti-magnetite inclusions in the grains, as these elements are all common to chromite and Ti-magnetite (Section 4.2.7.). To assess the

likelihood of these elements being carried within chromite inclusions rather than by deposition from solution, the proportions of Ti and V to Cr in the pyroxenes (as Cr is not known to exist in any significant concentration in other phases) were compared to the proportions measured in pure chromite (Section 4.2.7). The analysis in ALH 78130 rusted areas with the highest Cr content was selected and the average composition of a non-rusted pyroxene was subtracted to give the excess Cr, Ti and V content. The proportions of Cr:V and Cr:Ti were compared to measured chromite compositions and are detailed in Table 4.8 below.

Table 4.8. Proportions of elements in chromite and in rusted pyroxene in ALH 78130

	Pure chromite	ALH 78130 hotspot
Cr: V	83:1	81:1
Cr: Ti	22:1	23:1

From Table 4.8. it is clear that the V and Ti are very likely to be from a chromite inclusion. These elements being enhanced through inclusions is also more likely when considered that these hotspots do not exist in olivine crystals.

The increase of chromite inclusions in rusted pyroxenes may cause or enhance the rust in these particular crystals, as the inclusions are observed largely to be along planes of weakness (cleavage planes, mineralogical weaknesses) and are comparatively small (< 5 µm). The location and the small size increases the weatherability of the inclusions in comparison to large grains of the same minerals as they have greater surface area to volume. The Fe from these vulnerable grains may be weathering, oxidising and creating the rust in these pyroxene grains.

Ca appears completely immobile in the pyroxenes, with no change between rims and interiors or between rusted and non-rusted areas. The Al content in rusted areas does not

appear enhanced as in olivine, with only a mild suggestion of some high Al points. No elevated Al-concentrations caused by feldspar dissolution are observed in the pyroxene, which may be because there are fewer surfaces (fractures) present in pyroxene for alteration products to be deposited.

The Co and Ni contents in pyroxenes are similar in pattern to the olivine contents, in that there is enhancement in the most weathered meteorites (QUE 99022, ALH 78130) and in the rusted areas of ALH 78130, but this enhancement is less obvious than in the olivines and is absent in the rusted areas of QUE 94214. As pyroxenes contain fewer fractures and imperfections than olivine crystals, deposition of alteration products (the probable host of Co and Ni) should be lesser in pyroxenes crystals, explaining the smaller enhancement in Co and Ni and the lack of an Al enrichment in QUE 94214 rusted areas. The lack of difference in rusted areas of QUE 94214 is not explained by a lesser degree of metal alteration, and so the mobility of Co and Ni in QUE 94214 described above is also borne out in the pyroxene compositions. This is backed up by a similar decrease of Zn that is observed only in the rusted pyroxenes of QUE 94214.

The troilite in QUE 94214 is compositionally distinct from the other meteorites, with greater Ni, Co and Cu. This may be contributing to the preferential weathering seen in Section 3.7. The raised values are probably measurements of the small inclusions of Fe-Ni metals observed in Fig. 4.13. Obvious weathering effects in the troilite trace elements appear to be absent.

4.3. SUMMARY

Major and trace elements show that almost all mineral species alter to some extent, the only exception is chromite. Alteration concentrates in small discrete areas, partially marked by rust, and is heterogeneous across all meteorites. In these alteration centres, the features of the minerals present (fractures, cracks, etc.) determine the pattern of

weathering. Weakened structure of sulphides through the increase of fractures and inclusions of easily weatherable Fe-Ni metal results in drastically enhanced weathering of silicates through a drop in pH and Eh, which in turn enhances the mobility of many of the elements liberated from the weathered minerals.

CHAPTER 5 – BULK ROCK ANALYSIS

In many studies only bulk data are used to assess the primary properties of meteorites. Therefore, to test if bulk data can reflect the changes measured using small scale, major and trace element, magnetic and oxygen isotope bulk data was collected and compared to spatially-resolved data presented in chapters 3 and 4.

5.1. ICP-MS ANALYSIS

Table 2.3. Subset samples used in bulk element analysis.

Meteorite	Subsample designation	Meteorite	Subsample designation
QUE 94214	GR – General rim sample with fusion crust removed	**ALH 84058**	GR – General rim sample
	UFC – Directly underneath the fusion crust with the fusion crust removed		GI – General interior sample
	FC – Pure fusion crust		FC – Pure fusion crust
	LA – Least altered area with no visible rust from interior		LA – Least altered sample from the rim
	MA – Most visibly altered material in meteorite from interior		MA – Most altered material in rim
	INTM – Intermediate sample between MA & MC from interior		INTM – Intermediate sample between MA & MC from rim

All rims and interiors of meteorites in the study were analysed using solution ICP-MS to gain both major and trace element compositions. For two samples, QUE 94214 and ALH 84058, six subsamples were taken to investigate any local changes (table 2.3) as an intermediate measurement between the spatially resolved data and the bulk to aid the reconciliation between the two. Rim-interior measurements were compared to see if the more weathered meteorites had distinct patterns from the more pristine samples. The data is summarised in Table 5.1 and described below, with the elements ordered by atomic weight. To compare relationships between elements, correlation coefficients between each

were calculated and are collated in Appendix III, including all errors and detection limits. Errors are calculated from repeat measurements of a standard and are expressed in percent. Elements have classifications next to them indicating group and Goldschmidt geochemical classification to allow group comparisons.

5.1.1. TRACE ELEMENT ANALYSIS

Lithium (Alkali metal, Lithophile)

Li measurements agree with the L chondrite values of Murty et al., (1983), with values between 1.6-2.6 ppm. The ALH 84058 subsets show the least amount of Li in the most altered rim (MA) and the greatest amount in the least altered rim (LA). For QUE 94214 there is no discernible difference between the MA and LA subsets, also true for the rim and interior sections of QUE 99022, ALH 85017 and ALH 78130. However, in ALH 84056 rim and interior samples there is a larger difference with the rim containing 0.6 ppm more than the interior. The highest Li value is in QUE 99022 (2.58 ppm) and the lowest is in ALH 84058 (1.63 ppm). Li is strongly correlated with Rb contents (R = 0.75), reflecting the common major host in plagioclase.

Element specific discussion

Li is not consistently linked with weathering state. There is no correlation between rim and interior samples and enrichment/depletion of Li. The subsets of ALH 84058 show a potential link with Li contents and weathering state, but QUE 94214 subsets show little change between them, with no consistent correlation with weathering. The Li depletion in ALH 84058 may show leaching of plagioclase or a modal abundance difference of plagioclase. As Li is hosted mostly in plagioclase/maskelynite in the samples, the unchanging Li abundances in most samples suggest that dissolution of plagioclase was not an active process.

Table 5.1. All trace elements and major elements measured. Li-U measured in ppm. Al-Fe measured in w.t.%.

	84058 GR	84058 FC	84058 MA	84058 LA	84058 INTM	84058 GI	94214 GR	94214 UFC	94214 FC
Li	2.29	2.08	1.63	2.36	2.06	1.96	2.18	2.13	2.10
B	1.44	1.74	1.02	1.10	2.63	1.66	0.22	0.46	1.12
P	1079.19	790.80	693.36	925.48	1015.17	1080.69	909.41	925.29	938.92
Sc	8.32	7.81	6.70	10.78	8.26	8.11	8.08	8.30	9.89
Ti	768.49	624.36	553.01	2976.22	678.38	646.82	688.10	651.86	786.67
V	68.43	69.69	53.95	76.55	54.75	63.92	74.32	70.22	77.32
Cr	2876.72	3145.38	2246.80	3244.78	2038.27	2682.75	3390.56	3041.08	3376.16
Mn	2603.91	2532.94	2164.23	2821.06	2658.22	2463.69	2625.80	2478.51	2543.96
Co	413.67	802.95	545.25	154.10	357.51	470.65	494.62	879.09	344.61
Ni	9932.00	11570.00	11910.00	6050.00	9725.00	15670.00	8097.00	11670.00	7554.00
Cu	86.25	73.41	90.96	57.56	66.42	130.83	81.26	83.93	85.11
Zn	51.85	51.27	42.14	54.67	46.76	47.47	53.39	49.56	52.07
Ga	5.15	5.36	4.56	4.87	4.67	5.45	5.04	5.38	5.13
As	0.88	1.74	0.02	0.13	1.30	1.20	1.22	1.51	0.01
Rb	2.56	2.47	1.99	2.72	2.53	2.43	2.60	2.43	2.76
Sr	14.49	10.94	9.01	11.42	10.99	10.44	11.57	10.66	13.26
Y	2.65	1.83	1.56	2.40	2.48	2.33	2.06	2.02	2.02
Zr	5.45	4.83	4.19	7.92	5.59	5.06	5.02	5.26	6.37
Nb	0.61	0.33	0.29	3.81	0.59	0.34	0.41	0.36	0.45
Sn	0.28	0.29	0.31	0.18	0.24	0.37	0.20	0.30	0.24
Sb	0.17	0.08	0.09	0.40	0.11	0.10	0.26	0.27	0.27
Cs	0.01	0.01	BDL	BDL	BDL	BDL	0.01	BDL	0.02
Ba	5.06	3.69	3.08	3.89	3.82	3.45	4.59	3.76	7.40
La	0.39	0.27	0.21	0.31	0.35	0.34	0.34	0.28	0.38
Ce	1.17	0.66	0.56	0.82	0.90	0.89	0.87	0.73	0.91
Pr	0.14	0.10	0.09	0.13	0.13	0.13	0.12	0.11	0.12
Nd	0.72	0.49	0.44	0.60	0.66	0.68	0.60	0.53	0.59
Sm	0.23	0.18	0.14	0.23	0.23	0.22	0.22	0.18	0.20
Eu	0.08	0.07	0.06	0.08	0.08	0.07	0.07	0.07	0.08
Gd	0.30	0.21	BDL	2.02	0.30	0.19	0.29	0.27	BDL
Tb	0.06	0.04	BDL	0.40	0.05	0.04	0.05	0.05	BDL
Dy	0.41	0.30	BDL	2.85	0.38	0.26	0.38	0.35	BDL
Ho	0.09	0.06	BDL	0.66	0.09	0.05	0.09	0.08	BDL
Er	0.26	0.19	BDL	1.99	0.25	0.17	0.24	0.22	BDL
Yb	0.26	0.19	BDL	1.98	0.24	0.17	0.24	0.24	BDL
Lu	0.04	0.03	BDL	0.31	0.04	0.03	0.04	0.03	BDL
Hf	0.16	0.14	BDL	1.00	0.14	0.12	0.15	0.15	BDL
Ta	0.31	0.02	0.01	0.63	0.02	0.01	0.01	0.01	0.01
Pb	0.11	0.13	0.07	0.03	0.07	0.12	0.16	0.07	0.56
Th	0.06	0.04	BDL	0.24	0.04	0.03	0.04	0.04	BDL
U	0.04	0.01	BDL	0.06	0.01	0.01	0.01	0.01	BDL
Al	1.15	1.12	1.05	1.18	1.17	1.11	1.17	1.10	1.22
Ca	1.33	1.19	1.20	1.54	1.30	1.31	1.16	1.29	1.42
Mg	14.58	13.98	13.49	15.60	15.20	13.46	13.60	13.24	13.30
Fe	22.20	27.23	25.54	16.62	18.84	23.86	22.18	26.44	19.94

Table 5.1. All trace elements and major elements measured. Li-U measured in ppm. Al-Fe measured in w.t.%.

	94214 LA	94214 MA	94214 INTM	99022 R	99022 I	85017 R	85017 I	78130 R	78130 I
Li	1.99	2.09	1.90	2.55	2.58	2.02	1.97	2.00	1.96
B	**BDL**	0.21	0.01	0.72	1.00	0.26	**BDL**	**BDL**	0.12
P	855.66	942.10	737.31	1158.96	939.01	946.06	818.64	1346.28	748.69
Sc	8.88	7.36	8.17	8.37	8.99	8.39	8.13	7.46	9.04
Ti	728.31	638.20	599.49	593.66	652.30	653.66	580.12	561.74	693.08
V	77.15	74.66	59.24	57.85	67.97	65.95	63.35	51.27	62.19
Cr	3470.14	3521.25	2260.85	2247.37	2795.18	2725.80	2582.80	1937.58	2323.36
Mn	2590.87	2404.27	2328.06	2499.65	2594.31	2601.50	2478.75	2363.43	2511.61
Co	401.49	868.37	810.87	442.45	419.58	643.74	1161.92	539.99	407.38
Ni	8893.0	11020.0	16140.0	10130.0	8644.0	11480.0	12430.0	9442.0	9731.0
Cu	85.79	78.31	103.54	95.51	81.49	87.49	68.87	84.30	97.72
Zn	54.25	51.03	42.62	48.97	52.13	50.11	47.68	44.37	48.10
Ga	5.05	5.50	5.63	5.09	4.90	5.15	5.10	4.70	4.97
As	0.15	1.30	2.24	1.10	0.96	0.35	0.84	0.93	1.77
Rb	2.49	2.46	2.19	2.63	2.86	2.41	2.29	2.49	2.67
Sr	10.67	10.67	9.45	11.06	12.21	10.64	10.01	10.17	11.08
Y	1.95	1.56	1.54	2.62	2.21	2.15	1.95	2.59	2.06
Zr	5.43	4.63	5.25	5.38	5.91	5.22	5.02	4.66	5.72
Nb	0.39	0.32	0.30	0.38	0.43	0.36	0.30	0.42	0.42
Sn	0.23	0.27	0.37	0.30	0.24	0.30	0.30	0.27	0.30
Sb	0.55	0.11	0.17	0.10	0.14	0.16	0.29	0.15	0.38
Cs	BDL	BDL	BDL	0.01	0.01	0.01	BDL	BDL	BDL
Ba	3.62	3.60	3.17	4.02	4.04	3.67	3.33	3.43	3.83
La	0.24	0.21	0.19	0.40	0.33	0.30	0.25	0.37	0.25
Ce	0.64	0.56	0.48	1.06	0.84	0.78	0.67	1.00	0.70
Pr	0.09	0.08	0.08	0.16	0.12	0.11	0.10	0.15	0.10
Nd	0.50	0.43	0.36	0.78	0.62	0.59	0.50	0.73	0.54
Sm	0.19	0.16	0.13	0.27	0.20	0.22	0.19	0.25	0.18
Eu	0.07	0.07	0.06	0.07	0.08	0.07	0.07	0.07	0.08
Gd	2.08	0.30	0.22	0.35	0.24	0.29	0.29	0.28	0.25
Tb	0.40	0.05	0.04	0.06	0.05	0.06	0.06	0.05	0.05
Dy	2.93	0.37	0.31	0.42	0.34	0.41	0.41	0.33	0.33
Ho	0.68	0.09	0.07	0.09	0.08	0.09	0.09	0.07	0.07
Er	2.03	0.26	0.21	0.27	0.24	0.26	0.27	0.21	0.22
Yb	2.01	0.25	0.22	0.27	0.24	0.26	0.24	0.24	0.22
Lu	0.31	0.04	0.03	0.04	0.04	0.04	0.04	0.03	0.03
Hf	1.01	0.14	0.14	0.16	0.17	0.21	0.15	0.15	0.16
Ta	0.62	0.02	0.01	0.02	0.03	0.49	0.23	0.04	0.01
Pb	0.04	0.04	0.03	0.18	0.12	0.07	0.03	0.06	0.04
Th	0.24	0.04	0.04	0.05	0.06	0.06	0.03	0.05	0.04
U	0.06	0.01	0.01	0.02	0.02	0.01	0.01	0.04	0.02
Al	1.15	1.14	1.00	1.08	1.14	1.13	1.05	1.10	1.24
Ca	1.29	1.14	1.23	1.34	1.45	1.28	1.30	1.27	1.28
Mg	13.82	13.13	12.66	14.37	14.68	14.15	13.31	13.40	13.31
Fe	21.17	27.47	29.40	22.01	22.09	23.95	29.35	23.92	21.90

Table 5.1. All trace elements and major elements measured. Li-U measured in ppm. Al-Fe measured in w.t.%.

	84056 R	84056 I	Average	St. Dev	RSD
Li	1.76	2.30	2.10	0.23	11.19
B	1.34	BDL	0.94	0.72	77.00
P	1133.45	1133.64	955.91	164.11	17.17
Sc	7.18	8.93	8.36	0.92	11.02
Ti	539.40	738.96	767.64	524.47	68.32
V	55.53	78.77	66.15	8.73	13.20
Cr	2290.03	3635.98	2791.64	538.44	19.29
Mn	2255.01	2752.05	2513.59	158.54	6.31
Co	951.29	428.17	576.88	253.54	43.95
Ni	26960.00	8813.00	11293.05	4426.29	39.19
Cu	154.77	71.17	88.24	21.98	24.91
Zn	44.45	60.58	49.67	4.48	9.03
Ga	6.64	5.85	5.21	0.47	8.98
As	0.85	0.84	0.97	0.61	63.37
Rb	2.44	2.96	2.52	0.22	8.82
Sr	10.00	11.85	11.03	1.25	11.35
Y	2.33	2.51	2.14	0.35	16.37
Zr	4.30	5.57	5.34	0.80	15.05
Nb	0.30	0.40	0.56	0.77	137.51
Sn	0.63	0.31	0.30	0.09	31.06
Sb	0.22	0.15	0.21	0.12	58.82
Cs	BDL	BDL	0.01	0.01	93.30
Ba	3.43	4.07	3.95	0.93	23.66
La	0.34	0.34	0.30	0.06	21.20
Ce	0.91	0.91	0.80	0.18	22.24
Pr	0.13	0.14	0.12	0.02	19.40
Nd	0.69	0.71	0.59	0.11	19.51
Sm	0.23	0.24	0.20	0.04	18.10
Eu	0.07	0.08	0.07	0.01	8.47
Gd	0.23	0.26	0.42	0.56	135.10
Tb	0.04	0.05	0.08	0.11	137.82
Dy	0.31	0.32	0.57	0.80	140.42
Ho	0.07	0.07	0.13	0.19	144.01
Er	0.20	0.22	0.39	0.56	145.78
Yb	0.22	0.23	0.39	0.56	144.23
Lu	0.03	0.04	0.06	0.09	145.18
Hf	0.16	0.20	0.23	0.27	120.27
Ta	0.01	0.01	0.12	0.21	172.08
Pb	0.08	0.04	0.10	0.12	112.83
Th	0.04	0.10	0.06	0.06	102.69
U	0.01	0.06	0.02	0.02	90.26
Al	1.04	1.31	1.13	0.07	6.48
Ca	1.18	1.31	1.29	0.10	7.57
Mg	12.09	15.01	13.82	0.88	6.36
Fe	31.96	21.92	23.90	3.84	16.07

Boron (Metalloid, lithophile)

B concentrations are all <3 ppm but have large errors (10 % error) due to poor reproducibility. QUE 94214 and ALH 84058 subsets show no relationship between weathering state and B, as the LA and MA samples plot within error of each other. QUE 99022 has less B in the rim than interior (0.72, 1.00 ppm respectively). ALH 84056 interior and ALH 85017 interior have lesser B contents (by 1 ppm in ALH 84056 and 0.3 ppm in ALH 85017) compared to the rims (1.34 and 0.26 ppm). B does not correlate with any other element suggesting an even spread across all phases analysed.

Element specific discussion

B has not moved with weathering, there are no consistent differences between any of the subsets, however it is notable that the two most weathered meteorites (QUE 99022 and ALH 78130) have more B in the interior compared to rim, which may be an alteration feature. B is hosted in clinopyroxene, and so the lack of a change between subsets and between rim and interiors is either reflecting no dissolution/leaching of pyroxenes or it is demonstrating that B is immobile.

Phosphorous (Non-metal, lithophile)

P contents vary over a range of 650 – 1350 ppm between samples and P values from the subsets of ALH 84058 covers almost the entire range of P values in all samples. The highest value is the general rim (GR) and general interior (GI) (1100 ppm) and the MA sample has the lowest value at 690 ppm, with the fusion crust (FC) sample having the second lowest value at 790 ppm. No correlation with state of weathering in QUE 94214 subsets is observed, and many samples show concentrations within error of each other. The two subsets that are not within error of the main cluster are the least altered interior (LA; at a lower 860 ppm) and the intermediate (INTM) sample (which is the lowest value, at 730 ppm). QUE 99022 has a greater concentration of P in the rim compared to the interior (1159 and 939 ppm respectively), as does ALH 85017 (946 and 819 ppm respectively).

ALH 78130 has a very large difference between rim and interior (600 ppm) and ALH 84056 R and I have almost identical values. P strongly correlated to YREEs (Yttrium and rare earth elements) (with the exception of Eu), establishing phosphates as the main host of the YREEs.

Element specific discussion

There is no evidence that P abundance correlates with weathering state, with no consistent rim/interior differences or differences in the subsets, suggesting that the main hosts, phosphates, are not dissolved.

Scandium (Transition metal, lithophile)

Sc ranges between 6.7 – 10.7 ppm and the subsets of QUE 94214 and ALH 84058 cover this whole range. Sc is depleted in the MA subsets, with the MA subsets of ALH 84058 and QUE 94214 containing the least Sc, and the LA with higher concentrations. In QUE 94214, the highest Sc value is in the FC sample. Between the rims and interior of QUE 99022 and ALH 85017, there is very little difference. ALH 78130 shows a significant depletion in the rim sample of 1.5 ppm compared to the interior (at a value of 7.5 ppm) and there is a similar difference in ALH 84056. Sc contents strongly correlate with Mn, Zr, Hf and Ca. This is likely due to them sharing the same host, pyroxene. Sc also has a strongly negative correlation with Fe.

Element specific discussion

Weathering state and Sc depletion are strongly correlated. Since Sc depletion in ALH 84058 and QUE 94214 subsets correlate with the most weathered samples, and Sc is removed from the most weathered areas. The lack of consistent rim/interior differences in the other samples demonstrate that leached Sc is not removed entirely from the samples and instead remains in the localised area, most likely scavenged by Fe-oxyhydroxides. Sc is chiefly hosted in pyroxenes and so the

removal of Sc either demonstrates leaching of pyroxenes, or dissolution. The strong correlation with Ca may suggest that Sc is also occurring in significant amounts in diopside. The high value of Sc in the fusion crust of QUE 94214 may be linked to a surficial deposit.

Titanium (Transition metal, lithophile)

Ti contents range between 540–790 ppm with the exception of one unusually high value of 3000 ppm, which is in the LA subset of ALH 84058. In the other ALH 84058 subsets, the lowest value is in the MA subset (553 ppm) with the FC subset the next lowest (624 ppm). In the QUE 94214 subsets the MA subset has lesser Ti (638 ppm) than the LA sample (728 ppm) by 90 ppm, but the subset with the most Ti is the FC sample (785 ppm) and the subset containing the least is the INTM sample (600 ppm). QUE 99022 has 50 ppm less in the rim (594 ppm), ALH 78130 rim contents are 150 ppm below interior (562 ppm rim, 693 ppm interior), ALH 84056 rim contains 200 ppm less than the interior (539 ppm rim, 739 ppm interior). ALH 85017 has 60 ppm more Ti in the rim than interior (654 ppm rim, 580 ppm interior).

Element specific discussion

Ti correlates with weathering state and there are clear rim/interior differences. All rims are depleted in Ti except ALH 85017. QUE 94214 and ALH 84058 subsets possibly show some depletion with alteration state, but the pattern is not clear. The anomalously high value in ALH 84058s LA subset is possibly due to the inclusion of a rare Ti-magnetite grain, as there is no corresponding Cr excess to indicate a large chromite grain (Fig. 5.1.). The lack of correlation between Cr and Ti shows that the major host of both is not the same mineral (chromite) and so the only other mineral that contains appreciable Ti is Ti-magnetite, which must be the main contributor. The correlation between Ti and weathering is, therefore, most likely reflecting Ti-magnetite breaking down.

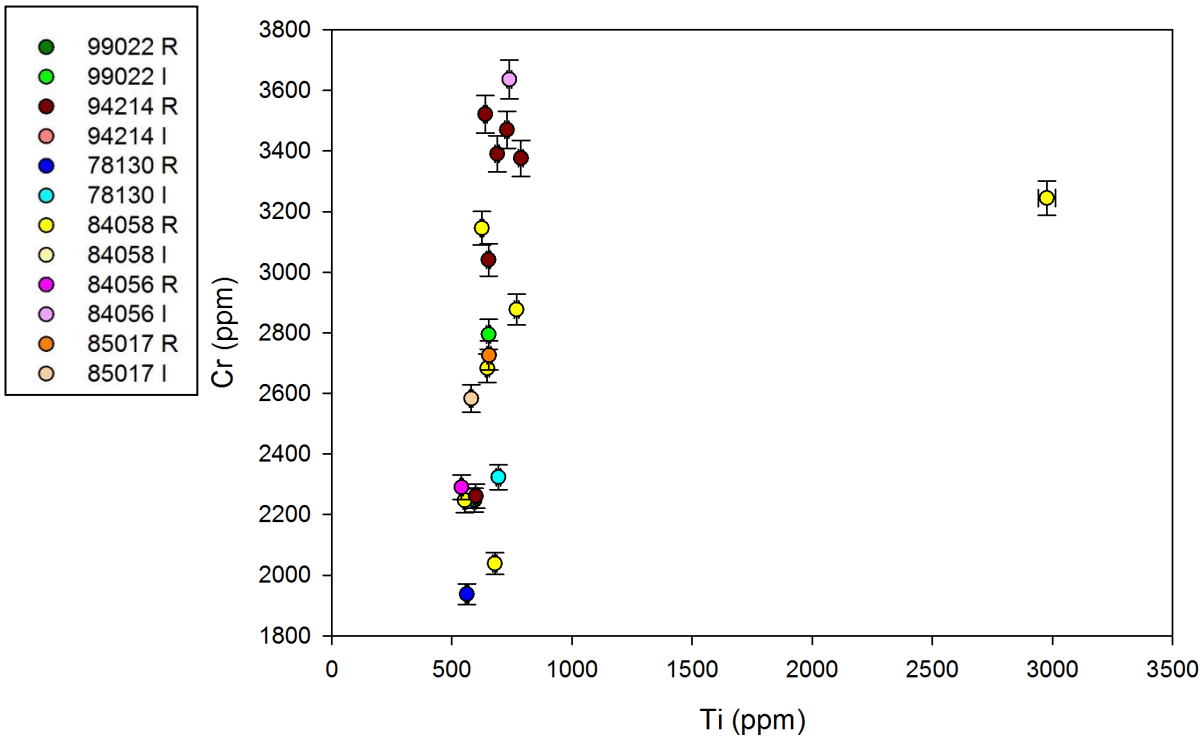

Fig. 5.1. Bulk Ti vs Cr contents. ALH 84058 LA samples has significantly more Ti than the other meteorites, but with no corresponding high Cr, suggesting a rare grain of Ti-magnetite may have been included.

Vanadium (Transition metal, lithophile)

V is between 50–80 ppm and in all samples, with one exception, there is less V in the rim compared to the interior, ~10 ppm, with ALH 84056 showing the largest difference of over 20 ppm. ALH 85017 is the opposite and is 4 ppm higher in the rim. ALH 84058 separates spread between 53–76 ppm with the lowest values in the MA sample and the highest value in the LA. The QUE 94214 separates do not show the same pattern, with the lowest values (60 ppm) being in the INTM subset. The MA and LA subsets plot within 4 ppm of each other, with the MA being the more depleted. A strong correlation exists between chromium and vanadium (with a correlation coefficient (r) of 0.97) and a weaker correlation between V and Sc (r = 0.58) (Fig. 5.2.).

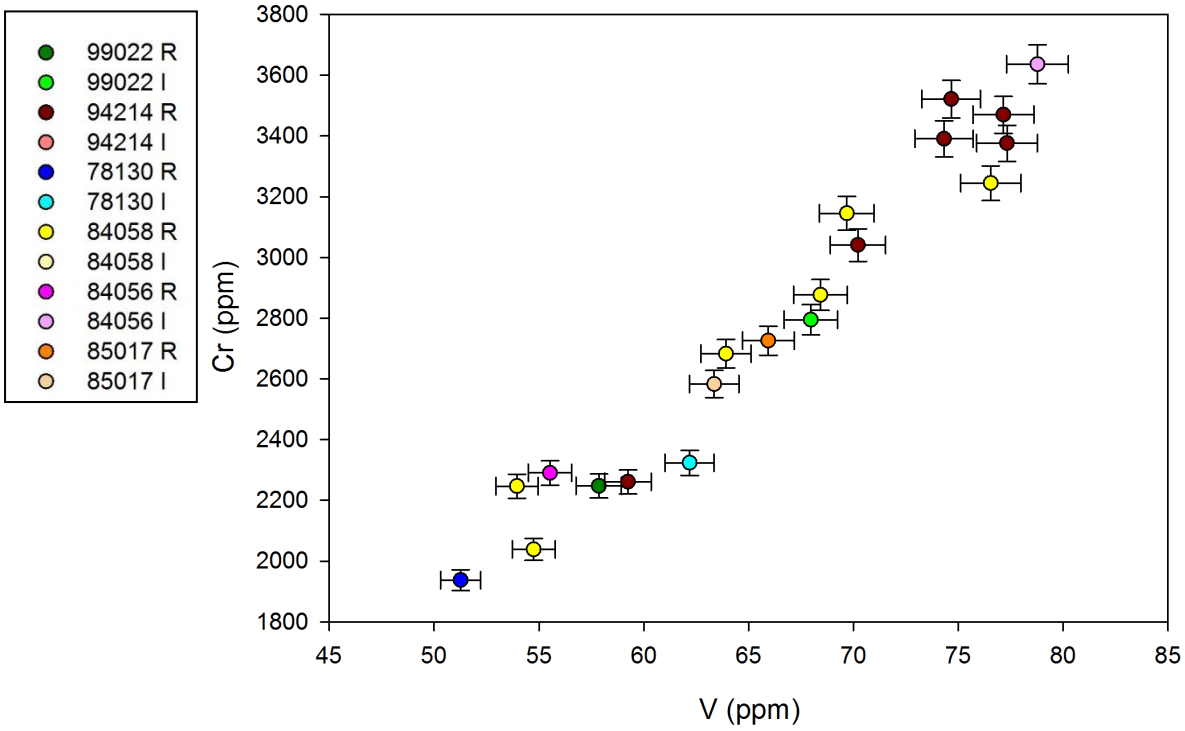

Fig 5.2. Bulk V vs Cr contents for all samples.

Element specific discussion

V is possibly linked to weathering since it is depleted in all rims and was most likely leached from chromites since they are the majority host (Average 4000 ppm; Chapter 4.2.7.). The correlation between Cr and V is either because they have a common host – chromite – or are hosted in the same crystallographic site in pyroxene. V is behaving mobile and appears to have been removed from the system, rather than deposited in the alteration products, as this would lead to no bulk changes. The positive correlation with Sc, which is chiefly hosted in pyroxene and has little to none in chromite (as seen by a lack of correlation between Sc and Cr), indicates that the V content reflects pyroxene as well as chromite compositions.

Chromium (Transition metal, lithophile)

Cr is between 2000–3700 ppm and ALH 84058 has the highest value in its LA subset (3200 ppm) whilst the MA is much lower (2250 ppm). The lowest Cr value is in the INTM sample (2040 ppm) and the QUE 94214 subsets also have the least Cr in the INTM subset, which is separated from the other subset values. The MA subset has the highest Cr of all subsets. There is no consistent rim/interior difference in Cr. There is a greater difference between the R and I samples in ALH 84056, with >1000 ppm more in the interior. There is strong correlation between Cr and V and Zn (Appendix III a).

Element specific discussion

There is no Cr variation with weathering state, or between rims and interiors. This suggests that the chromite, which hosts most of the Cr, is not dissolved and that Cr is not leached. The strong correlation with V and Zn indicates a common host in chromite.

Manganese (Transition metal, siderophile)

Mn values are between 2000–3000 ppm and in all samples (with the exception of ALH 85017), Mn is lower in the rim compared to the interior. The lowest ALH 84058 subset is the MA sample, with 2300 ppm Mn. In the QUE 94214 subsets, the MA sample is the second lowest value at 2400 ppm but with a lesser value in the INTM sample (2330 ppm). There is no variation between the most altered (QUE 99022 and ALH 78130) and least altered meteorites (ALH 84056 and ALH 85017) with QUE 99022 and ALH 85017 both have very similar rim and interior values (2500–2600 ppm). ALH 84056 rim and interior have significantly different values, the rim has 2250 ppm and the interior has 2750 ppm. It is the greatest variation of all the meteorites. Mn strongly correlates with Sc, Zn, Rb and Zr contents (Appendix III a).

Element specific discussion

Mn appears to be highly mobile, with a significant difference between rims and interiors, and it is also depleted in weathered areas. The depletion of Mn in ALH 84058 and QUE 94214 separates indicate that the rim/interior differences reflect a higher degree of bulk weathering in the rims than the interior.

Cobalt (Transition metal, siderophile)

Co values range from 150–1170 ppm. In the ALH 84058 subsets, the least Co is in the LA subsets and the MA subset has the second highest value, after the FC which contains the most Co at 810 ppm. Values contrast in the QUE 94214 subsets, with elevated Co contents (800–900 ppm) in the UFC sample, the MA and the INTM sample. The other three subsets (LA, FC, GR) are much lower (350–500 ppm). QUE 99022 has very similar rim and interior values with less than 25 ppm between them. The sample with the highest Co value is ALH 85017 I with a value of 1140 ppm, which is 400 ppm higher than the rim sample. In contrast, ALH 78130 rim and interior do not display a similarly large difference with the rim being 140 ppm higher than the interior. ALH 84056 has a significant rim-interior difference with the rim plotting 600 ppm above the interior. There is a strong positive correlation between Co and As (r=0.96), and a weaker positive correlation (r=0.61) with Ni (Appendix III a; Fig 5.3.).

Element specific discussion

The correlation between Co and As suggest they are mostly hosted in the same phase, and Co is partially hosted in the same phase as Ni (kamacite/taenite). There is a link between Co contents in the detailed subsets and weathering, but that link does not occur in the bulk samples of the other meteorites. This strongly suggests that the Co movement is localised and is not removed from the system.

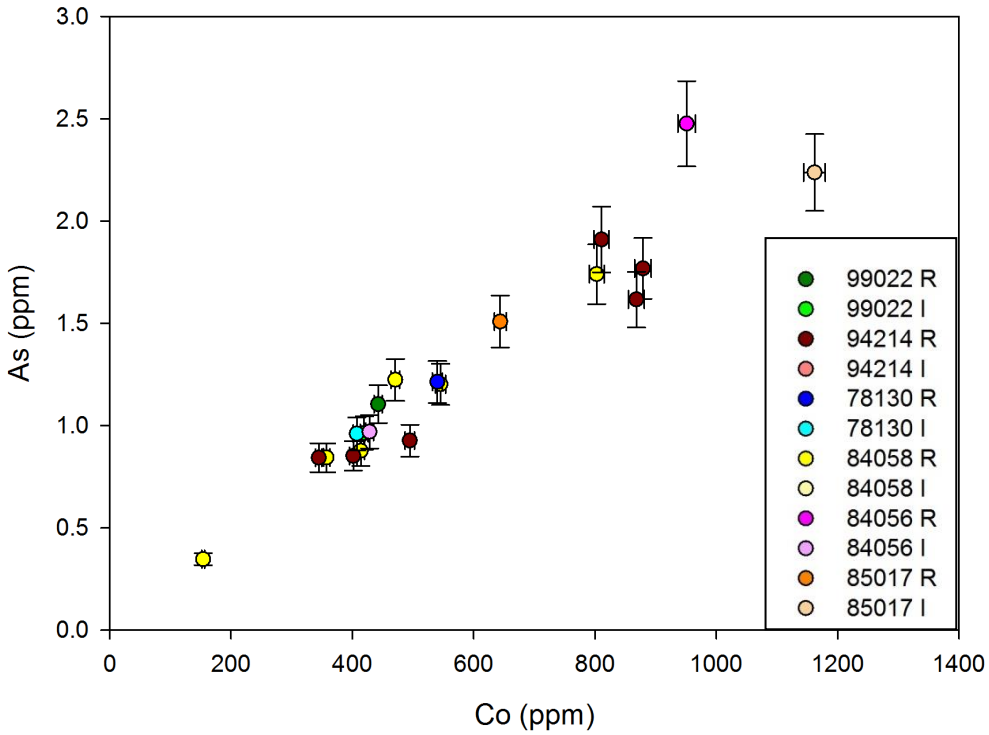

Fig. 5.3. Bulk As v Co contents for all samples

Nickel (Transition metal, siderophile)

Ni is between 7000–12000 ppm with the exception of one anomalously high point in ALH 84056 R, >25000 ppm. There is no consistent difference between rims and interior of samples. The LA sample of ALH 84058 is the lowest Ni value of any of its subsets (at 6000 ppm) and the MA is the second highest value (12000 ppm). The highest value is in the GI sample (15700 ppm). In QUE 94214, there is no real correlation between the various weathered subset samples and the Ni contents; and the most weathered samples do not have elevated Ni contents. The MA and the LA subsets both fall in the middle of the spread of values at 8700 ppm and 11000 ppm with the MA sample plotting higher.

Element specific discussion

Ni is hosted in taenite and kamacite displaying higher concentration in taenite. No consistent links between more weathered samples and greater Ni are observed. In ALH 84058 subsets the LA is depleted in Ni compared to the MA sample, but in

QUE 94214 this is not the case. There is a lesser amount of Ni in the MA sample compared to the LA, and these two values are in the middle of the spectrum of results. The anomalously high point of ALH 84056 R may be because of a disproportionate amount of taenite or kamacite in this sample, or because an alteration process has mobilised it.

Copper (Transition metal, chalcophile)

Cu is between 60–160 ppm with the majority between 65–90 ppm. Cu in ALH 84058 subsets do not vary with weathering state, the interior sample has a higher Cu value than any of the subsets from the rim of the sample. The QUE 94214 subsets show depletion of Cu in the MA subset with a value of 78 ppm compared to the LA sample which has a value of 85 ppm. QUE 99022 rim plots higher than the interior by 10 ppm (96 ppm in rim, 82 ppm in interior), ALH 78130 plots with more Cu in the interior than rim by 15 ppm (84 ppm in rim, 98 ppm in interior), ALH 85017 has more Cu in the rim than interior (87 ppm in rim, 69 ppm in interior). ALH 84056 R Cu content is much higher than the interior by 80 ppm (155 ppm in rim, 71 ppm in interior). Cu and Ni strongly correlate (r=0.84) and Sn (r=0.86).

Element specific discussion

There is no systematic relationship between Cu and weathering state in any of the meteorites. In QUE 94214, the subsets suggest that Cu is removed from the most altered areas, but this is not apparent in ALH 84058 subsets. ALH 84056 R is much higher than the interior (over twice the concentration) and it seems likely that this is a sampling bias of a phase, rather than a weathering effect (discussed further in Section 5.3.1.). The inconsistency of rim/interior differences indicate that there is no common leaching process in all meteorites, and Cu mobility is limited to QUE 94214, ALH 78130 and possibly ALH 84056. Cu is correlated with Ni, but Ni also has strong correlations with other elements (Ga, As) and so the correlation between

the Ni and Cu is likely to reflect the presence of troilite crystals (Table 4.2 whereby troilite contains the most Cu and appreciable Ni).

Zinc (Transition metal, chalcophile)

Zn is between 40–65 ppm and the Zn contents of ALH 84058 subsets show that the MA sample has lower Zn values (45 ppm), and the LA sample has the highest value (55 ppm). In QUE 94214 subsets, the Zn abundances patterns mirror the V in most respects with the INTM sample plotting at the lowest value (42 ppm) and the MA and LA samples plotting within 4 ppm of each other (Fig. 5.4.). In the samples without subsets, the difference between rim and interior is not consistent, because QUE 99022 (49 ppm in rim, 52 ppm in interior) and ALH 84056 (44 ppm rim, 61 ppm interior) have lower rim values than interior, but ALH 78130 and ALH 85017 have very similar rim/interior values (44 and 48 ppm in ALH 78130 and 50 and 48 ppm in ALH 85017). ALH 84056 has a very large difference between rim and interior with the interior having 15 ppm more Zn. There is strong correlation between Zn and V, Cr, Mn, Rb and Ca.

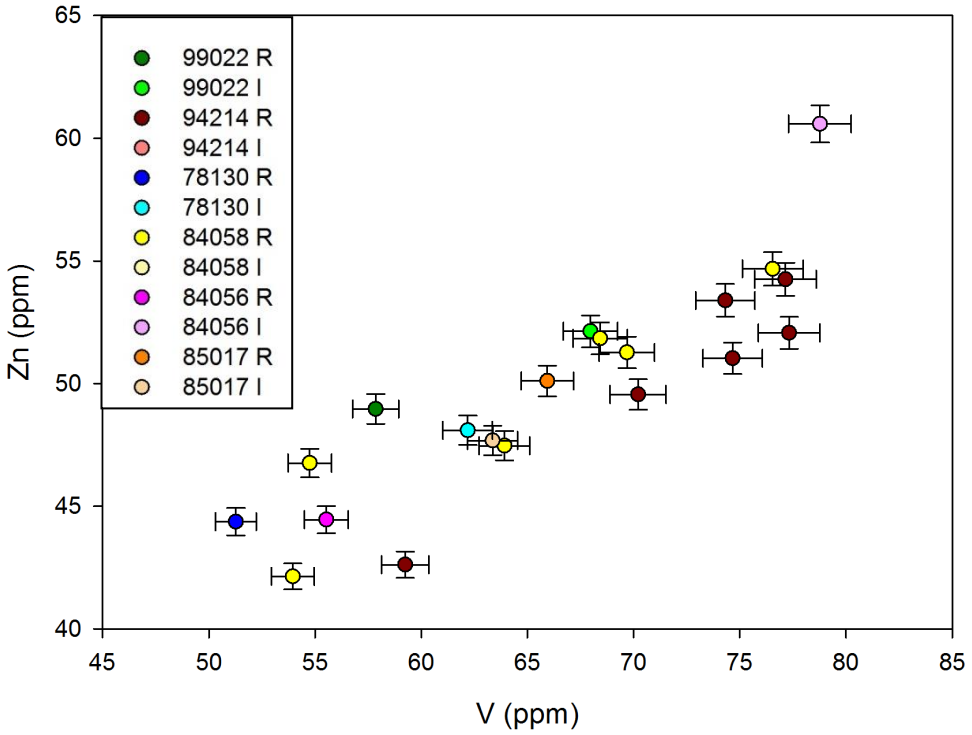

Fig. 5.4. V content vs Zn content. A clear positive correlation exists between the two. ALH 84056 R and I have an especially large separation of values, with the I having an unusually high Zn content.

Element specific discussion

There is a weak correlation between Zn contents and weathering state. Zn is primarily hosted in chromite (3500–4000 ppm average; Appendix II) and secondarily hosted in ferromagnesian silicates (<100 ppm average). Zn contents variations of ALH 84058 subsets indicate the dissolution of chromite. This is not observed in QUE 94214 which suggests that there is chromite dissolution or that there is an immediate deposition of Zn in alteration products. In all but ALH 85017, there is depletion in the rim compared to the interior; however this difference is negligible.

Gallium (Post-transition metal, chalcophile)

Ga values are between 4.6–6.6 ppm and there is no obvious progression of Ga with weathering state. The subsets of QUE 94214 are within 0.5 ppm of each other, with the MA sample having slightly more Ga than the LA sample and in ALH 84058 there is no correlation. Ga is relatively high in QUE 94214 (between 5.0 and 5.5 ppm) and the two most weathered meteorites, QUE 99022 and ALH 78130, both have lower Ga values between 4.6–5.1 ppm. ALH 85017 R and I are both in error of each other at 5.1 ppm. ALH 84056 R and I both have greater Ga content than the other samples (at 6.6 and 5.9 ppm respectively).

Element specific discussion

Ga does not seem to be controlled by weathering, because it is relatively immobile. It can be used as a proxy to test for disproportionate amounts of taenite in different samples as Ga is mostly hosted in taenite. ALH 84056 R and I have increased Ga contents compared to other samples, suggesting that they are likely to contain more taenite modally (which conflicts with thin section studies in Table 3.1).

Arsenic (Metalloid, chalcophile)

As values are evenly spread between 0.3–2.5 ppm. ALH 84058 subsets have the least As in the MA sample (0.02 ppm) and the most in the FC sample (1.74 ppm) which is significantly different from the other samples. In QUE 94214 the least As is in the FC sample (0.01 ppm), although the LA sample also has very little As (0.15 ppm). The highest As concentration is in the INTM sample (2.24 ppm). Three of the other meteorites (QUE 99022, ALH 84056, ALH 78130) all have more As in the rim compared to the interior, however ALH 85017 has 0.70 ppm more As in the interior (0.84 ppm) than the rim (0.34 ppm).

Element specific discussion

There appears to be a link between weathering in the least altered subsets, and low As concentrations, however, this is not observed in all rim/interior pairs. ALH 84058 subsets demonstrate a great enrichment of As (34 % higher than any of the other subsets) in the fusion crust, which might also have caused the enrichments measured in the rims of QUE 99022, ALH 84056 and ALH 78130.

Rubidium (Alkali metal, lithophile)

Rb is between 2.0–3.0 ppm. ALH 84058 subsets fall within 0.7 ppm of each other with little spread. Five of the subset values cluster closely (2.43–2.72 ppm), but the MA subsample of ALH 84058 is depleted in Rb (1.99 ppm). In QUE 94214, the LA subsample and the MA subsample are almost identical (2.49 ppm and 2.46 ppm respectively). The highest value is the FC sample (2.76 ppm). There are no rim/interior variations in Rb in all other meteorites. In both ALH 78130 and ALH 84056 there is a very small enrichment of Rb in the interior compared to the rims (0.5 ppm).

Element specific discussion

Rb is mainly hosted by feldspar (chapter 4) and so the minor differences between rim/interior samples, and within the subsets of QUE 94214, indicates plagioclase

alteration is minor in this meteorite. The more altered ALH 84058 subset may indicate some plagioclase dissolution. The QUE 94214 fusion crust subset is enriched in Rb compared to the other subsets, which may indicate an overabundance of plagioclase, an efflorescence deposit, or an Antarctic varnish deposit (further discussed in Section 5.1.3.).

Strontium (Alkali earth metal, lithophile)

Sr is between 8.6–14.5 ppm. In ALH 84058 subsets, there are four which have very similar values between 10.2–11.0 ppm with two outliers. The low outlier is the MA sample, and the high outlier is the GR sample. The QUE 94214 subsets are more tightly clustered than the ALH 84058 subsets, with three samples within error of each other. These are the LA, the MA and the UFC subsample. The FC sample has the highest value and the lowest is the INTM. QUE 99022 contains more Sr in the interior than the rim by 1.0 ppm (error <0.15 ppm), ALH 85017 contains slightly more in the rim than the interior, ALH 78130 and ALH 84056 both have more in the interior than rim.

Element specific discussion

There appears to be no link between weathering state and Sr content, neither the subsets nor the other meteorites show any consistent trends. Since Sr is mainly hosted in plagioclase, there is clearly no dissolution of plagioclase or leaching or Sr which is consistent with the Rb content.

Yttrium (Transition metal, lithophile)

Y is between 1.5–2.7 ppm. ALH 84058 subsets show a lack of separation between four points with two that separate and plot below by 0.5 ppm which are the MA and the FC sample. The QUE 94214 subsets show four points which plot within error of each other and two that separate by 0.4 ppm which are the MA and the INTM sample. QUE 99022, ALH 78130 and ALH 85017 all contain more Y in the rims than the interiors by 0.2–0.5 ppm. ALH 84056 I plots higher than the R by 0.2 ppm (error <0.03 ppm).

Element specific discussion

Y is enriched in most rim samples, with the exception of ALH 84056. The subsets of QUE 94214 and ALH 84058 both show a depletion in the MA samples, indicating Y leaching. The enhancement of Y in the rim either suggests a leaching of Y from the interior which is being moved to the rim, or is showing a process that only occurs in the interior.

Zirconium (Transition metal, lithophile)

Zr is between 4.1–7.9 ppm. ALH 84058 shows separation of Zr values with weathering state, with the MA sample having the lowest Zr contents (4.1 ppm) and the LA sample having the highest (5.5 ppm). QUE 94214 subsets mirror this with the MA subset having low Zr (4.5 ppm) and the LA sample having the second most Zr (5.5 ppm). The FC sample of QUE 94214 has the highest Zr contents (6.4 ppm). In all other samples except ALH 85017, there is a depletion of Zr in the rim relative to the interior.

Element specific discussion

Zr content is strongly linked to weathering state. With increased weathering, Zr becomes more mobile evidenced by the depletions in the rims of meteorites and in the subsets of ALH 84058 and QUE 94214. Zr is most likely to be hosted by pyroxene crystals, therefore, this is demonstrating either a leaching effect from the pyroxene, or dissolution of the pyroxene.

Niobium (Transition metal, lithophile)

Nb is <0.6 ppm, with the exception of the LA subset of ALH 84058 (3.8 ppm). The MA subset of ALH 84058 has the least Nb (0.28 ppm) whilst the FC and the GI sample subsets have the second least and plot within error of each other (0.3 ppm). QUE 94214s MA and INTM subsets have the lowest values of all the subsets, and are within error of each other (0.32 ppm and 0.30 ppm respectively). The highest concentration in QUE 94214s subsets is in the FC (0.45 ppm), the LA subset has an intermediate value (0.40 ppm). There is no

consistent rim/interior difference in the other subsets. ALH 85017 and ALH 84056 have higher Nb contents in the rims than interiors, and QUE 99022 and ALH 78130 rims and interiors are within error of each other.

Element specific discussion

There is little evidence to suggest that Nb mobilises with weathering apart from some depletion in ALH 84058 subset MA samples, which might indicate some migration. Otherwise there is no consistent rim/interior differences and poor correlation in the QUE 94214 subsets.

Tin (Post-transition metal, chalcophile)

Sn values are all <0.4 ppm with a single exception of 0.6 ppm in the rim of ALH 84056 (the interior is 0.3 ppm lower). ALH 84058 subsets show the least abundance of Sn in the LA sample (0.18 ppm) and the most in the MA (0.31 ppm) and the GI (0.37 ppm). The lowest concentration is QUE 94214 subsets is the GR sample (0.20 ppm) and the highest is the INTM sample (0.37 ppm) with very little spread of values in-between. ALH 78130 and ALH 85017 rims and interiors both plot within error of each other. Sn is higher in the rims of QUE 99022 (0.37 ppm rim, 0.30 ppm interior) and ALH 84056 (0.63 ppm rim, 0.31 ppm interior) compared to their interiors. Sn strongly correlates with Ni contents (r=0.97) as well as Cu, Ga, As and Fe.

Element specific discussion

Sn does not appear to relate to alteration state, as there is no evidence in the subsets and no consistent rim/interior differences between the meteorites. As a chalcophile element, it is probable that some Sn is hosted in troilite, but the main host is kamacite/taenite based on the very strong correlation with Ni.

Antimony (Metalloid, chalcophile)

Most of the samples have <0.3 ppm with a couple of exceptions. ALH 84058 subsets have one high point which is the LA sample. The MA sample and the FC have the least Sb. The lowest QUE 94214 subsets are the MA and FC samples which plot within error of each other. The LA contains the most Sb. In all other samples, the interiors have more Sb than the rims. Sb does not correlate strongly with any other element and has a weak correlation with Sc.

Element specific discussion

Sb appears to be correlated with weathering state, with both of the subsets showing depletion in the most altered samples, and with the rims and interiors of the other meteorites consistently showing depletion in the rim compared to the interior. Due to the complete lack of correlation of Sb with any other element, it must either be highly mobile or spread across many phases. Sb was not measured for most of the LA-ICP-MS studies detailed in Chapter 4, and has only been measured in notable quantity (>1 ppm) in alteration products and so it is unclear which phase is weathering to produce the correlation.

Caesium (Alkali metal, lithophile)

Most of the samples have <0.01 ppm Cs with the exception of one high point, QUE 94214 FC which has a value of 0.025 ppm. The values approach the detection limit of 0.001 ppm and have an error of 18 %; therefore most values are within error of each other and cannot be discriminated or discussed.

Barium (Alkali earth metal, lithophile)

Ba shows no link with weathering, and the single point of note is a high Ba content in QUE 94214 FC (7.4 ppm) which may be linked to an evaporite deposit.

Rare Earth Elements (Lathanides, lithophiles)

Rare earth element concentrations (REEs) in all meteorites are less than 1.2 ppm (Fig 5.5; Table 5.1.). QUE 99022 rim plots consistently higher than the interior for all REEs, but there is proportionately a greater concentration of LREEs compared to HREEs (Fig 5.5). ALH 84056 and ALH 85017 R and I pairs have very similar REE traces with few differences that are not within error of each other. ALH 85017 has a fairly unfractionated trace of REEs with a flat enrichment of all REEs in the rim compared to the interior, with no particular comparative increase of LREEs. QUE 99022 and ALH 78130 show an almost identical Eu content in the rim compared to the interior, unlike the other REEs.

To compare rims and interiors of respective meteorites, the rim abundances were normalised to the interior abundance in Fig 5.6. ALH 78130 R and I have the greatest difference between rim and interior with the rim being significantly more enriched in REEs than the interior, with the exception of Eu. The enrichments and depletions of QUE 99022 are very similar to those of ALH 78130, although there is a significantly higher enrichment of Tb in ALH 78130s rim, compared to interior.

ALH 84058 has four samples with very closely aligned patterns for all elements heavier than Nd. The four that group closely together are the GR, LA, INTM and GI. There is reasonable difference in Ce, with the general rim having the highest amount, with 0.25 ppm more than the second highest subset (0.89 ppm). The MA sample and the FC are both depleted in REEs compared to the other subsamples with roughly 0.2 ppm less than the other subsets. The MA sample is comparatively, the most depleted and the FC is the second most depleted.

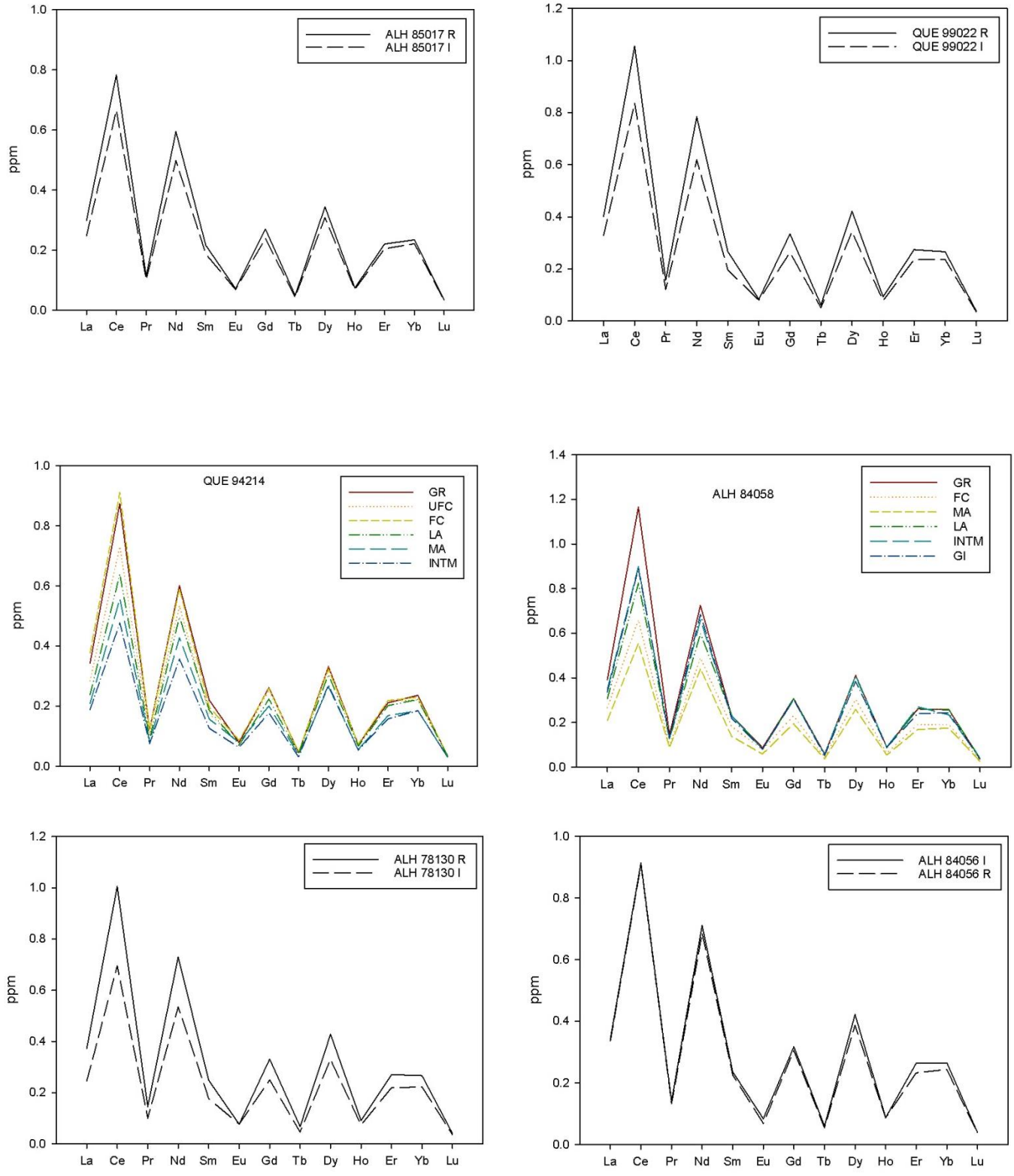

Fig. 5.5. REEs of all meteorites measured.

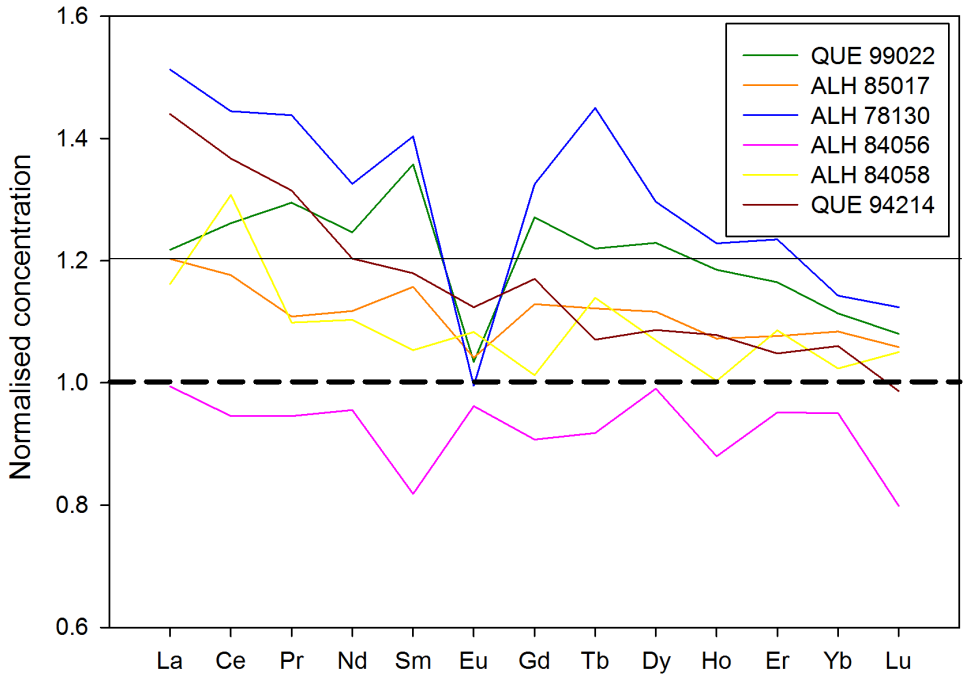

Fig. 5.6. REEs of rims normalised to interior concentrations to discriminate rim/interior differences.

QUE 94214 shows a steadier continuum of values compared to the ALH 84058 subsets, with less grouping and gaps between values. The highest values are consistently the GR and the FC sample for all REEs with the UFC sample just below. The lowest REE abundances are in the INTM and the MA sample.

Element specific discussion

The light rare earth elements (LREEs) in all samples (with the exception of Eu) are hosted in phosphates (Shinotsuka et al., 1995) which apparent in the strong correlation coefficients between the YREEs and P. The general enrichment of LREEs in all ALH 78130 and QUE 99022 may be indicative of greater phosphate concentrations in the rim sample than the interior (sample heterogeneity), or it may be indicative of an alteration process that is enriching the LREEs preferentially over the HREEs. In all samples except ALH 84056, the REEs are enriched in the

rims of the meteorites compared to the interiors. The positive correlation of LREEs with higher levels of P might suggest a modal increase of P in the rims. Since ALH 84056 shows very little rim/interior difference it is unlikely to have experienced leaching of REEs, whilst the other meteorites may have experienced leaching from the interiors, and deposition in the rims.

Eu is primarily hosted in plagioclase (shown by high correlation coefficients with other lithophile elements), and so the lack of variation between rim and interior in QUE 99022, ALH 78130 and ALH 84056 suggests that plagioclase is not dissolved or leached of Eu in these meteorites.

The QUE 94214 and ALH 84058 fusion crusts are significantly different in terms of REEs. QUE 94214 is relatively enriched compared to its subsets, and ALH 84058s fusion crust is significantly depleted compared to its other subsets.

Hafnium (Transition metal, lithophile)

Hf is <0.22 ppm and the associated error is high (5 %), and the detection limit is low (0.002 ppm). ALH 84058 subsets show the lowest concentrations of Hf to be in the MA subset (0.11 ppm) and the highest concentration is in the LA sample (0.21 ppm). The other four subsets plot mostly within error of each other. QUE 94214 subsets also have the least Hf in the MA subset (0.14 ppm). The LA subset is the highest concentration (1.01 ppm). In three of the other meteorites (QUE 99022, ALH 78130 and ALH 84056) there is less Hf in the rim than interior, although the QUE 99022 rim and interior plot within error of each other. ALH 85017 shows the opposite trend.

Element specific discussion

Hf could be linked to alteration since the subsets of ALH 84058 and QUE 94214 have the least Hf in the most altered subsets. This is partially backed up by a

general depletion in the rims of three of the other meteorites which are more depleted than their respective interiors.

Tantalum (Transition metal, lithophile)

Ta is <0.5 ppm, but the reproducibility was good and so the error is small (1.75 % error, 0.004 ppm detection limit). In ALH 84058 subsets there is least concentration in MA (0.01 ppm) and GI subsets (0.01 ppm), the highest concentration is in the LA subset (0.63 ppm). The subsets of ALH 84058 cover the entire range of Ta values across all meteorites (0.01–0.63 ppm). The QUE 94214 subsets cover a similar range of values (0.01–0.62 ppm). The highest value is in the LA subset (0.62 ppm). In three of the other meteorites (ALH 85017, ALH 78130, ALH 84056) there is more Ta in the rim compared to the interiors although most have little difference.

Element specific discussion

There does not appear to be a clear link between alteration state and Ta contents, suggesting that it is highly immobile.

Lead (Post-transition metal, chalcophile)

Pb is <0.58 ppm (8 % error, 0.007 ppm detection limit), but consistently in every sample has enriched rims (Table 5.1.). The FC samples of both ALH 84058 and QUE 94214 separates are the most enriched compared to the other subsets (0.13 ppm and 0.56 ppm respectively). The GR sample of QUE 94214 is the next highest of the QUE 94214 subsets (0.16 ppm) and shows a steady decrease with depth into the meteorite (Fig 5.7). The GI sample of ALH 84058 also has high Pb content.

Element specific discussion

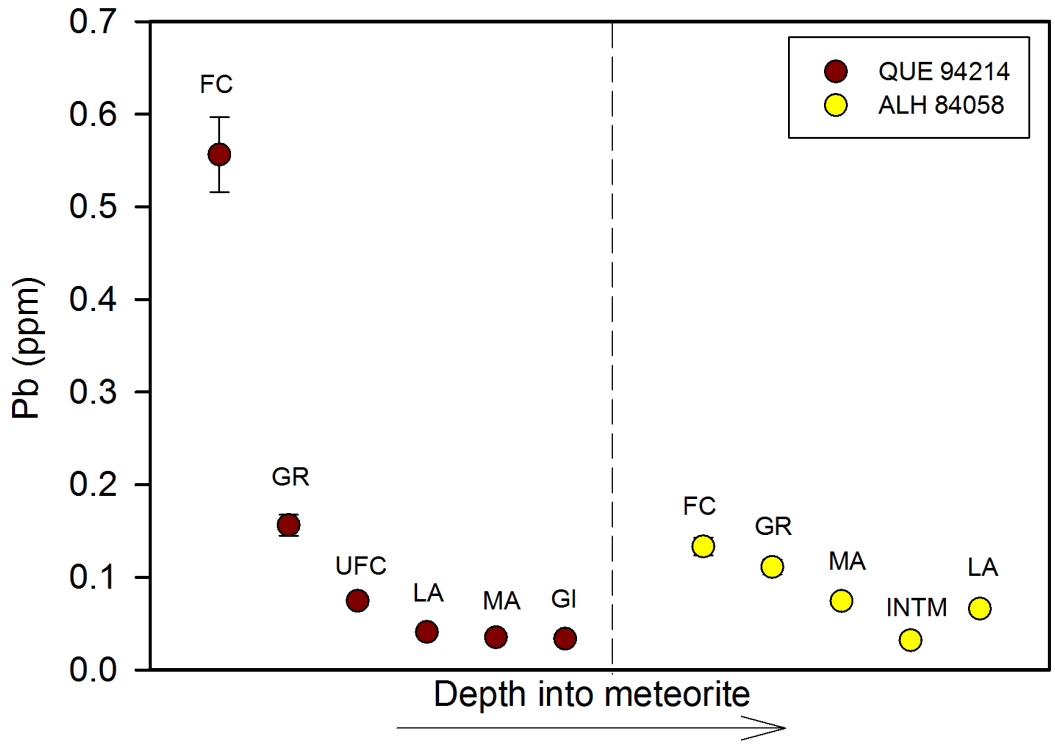

Fig. 5.7. Pb content in the subsets of QUE 94214 and ALH 84058 show constant decrease of Pb with depth into the meteorite.

There does not appear to be a link with weathering in the subsets, however there is a very clear concentration in the fusion crusts which is most likely causing the rim samples to all contain more Pb than the interiors. There is also a clear gradient decreasing with depth in the meteorite in the subsets. This is discussed in greater detail in section 5.1.3.

Thorium (Actinide, lithophile)

Th is <0.1 ppm (2.1 % error, 0.005 ppm detection limit). ALH 84058 subsets show some variation with the MA subset having the lowest concentration of Th (<0.01 ppm) and the LA having the second highest value (0.24 ppm). This is also reflected in the QUE 94214 subsets, with the MA containing 0.04 ppm and the LA containing 0.24 ppm. No consistent rim/interior differences are observed between the other meteorites.

Element specific discussion

Th contents do not strongly link with alteration state, with only ALH 84058 and QUE 94214 subsets showing a potential link.

Uranium (Actinide, lithophile)
U is <0.06 ppm (4.5 % error, 0.001 ppm detection limit) and has no links with weathering. One single high point exists in QUE 94214 fusion crust, which may be related to an evaporite deposit.

5.1.2. Major Element Analysis

Fe, Mg, Ca and Al were measured in the samples by ICP-OES. Si could not be measured as hydrofluoric acid was used in the digestion process which results in the loss of Si.

Aluminium (Post-transition metal, lithophile)
Al is between 1.00–1.31 wt.%, with the highest value in ALH 84056 I and the lowest in the QUE 94214 intermediate subset. The ALH 84058 subsets show the least Al in the MA subset. The other five subsets plot in error of each other with the LA sample having the highest Al. The QUE 94214 subsets have the highest Al value in the FC sample and the least in the INTM sample. The MA and LA samples have almost identical values. QUE 99022 has more Al in the interior (by 0.07 wt.%) than the rim as does ALH 84056 (by 0.25 wt.%) and ALH 78130 (by 0.15 wt.%). ALH 85017 shows the opposite with less Al in the interior compared to the rim of the sample (by 0.03 wt.%). There is a fairly strong negative correlation between Fe and Al ($r = -0.67$).

Element specific discussion

Whilst three meteorites have more Al in the interior than rim, there is no strong link with weathering and Al contents, further supported by the lack of difference in the subsets. Since Al is hosted in plagioclase, this is suggestive that there is no appreciable plagioclase dissolution or immediate deposition in surrounding

alteration products. The increased Al in the FC subsample of QUE 94214 suggests either an overabundance of plagioclase, or a surficial deposit. ALH 84058s depletion of Al in the MA subsample is showing possible dissolution of plagioclase.

Calcium (Alkaline earth metal, lithophile)

Ca is between 1.14–1.54 wt.%. The lowest value of Ca is in the MA subset of QUE 94214 (1.14 wt.%). The highest concentration of Al is in the LA subset of ALH 84058 (1.54 wt.%). The ALH 84058 subsets show the least Ca to be in the MA (1.20 wt.%) and the FC (1.19 wt.%) subsets. Three samples have values within error of each other: these are the GI, the GR and the INTM (1.30–1.33 wt.%). The QUE 94214 subsets also have the least Ca in the MA subset (1.14 wt.%), but the highest value is the FC sample (1.42 wt.%) which is significantly higher than any other of the subsets. The LA subset plots at the same point as the UFC sample (1.29 wt.%). The MA sample plots within error of the GR sample (1.14 wt.% and 1.16 wt.% respectively). QUE 99022 shows significant rim/interior differences with the interior sample having 0.11 wt.% more Ca than the rim (1.45 and 1.34 wt.% respectively). ALH 78130 has the same Ca content in both the rim and interior (1.27 and 1.28 wt.% respectively), as does ALH 85017 (1.28 and 1.30 wt.% respectively). ALH 84056 has significantly less Ca in the rim sample than the interior (1.18 and 1.31 wt.% respectively).

Element specific discussion

There is a potential link between weathering and Ca contents, since the subsets of ALH 84058 and QUE 94214 have the least Ca in their most altered subsets. The rims and interiors of the other meteorites show no consistent variation and the enrichment of Ca in the fusion crust (QUE 94214) may be due to a surficial deposit, since this does not occur in the fusion crust of ALH 84058.

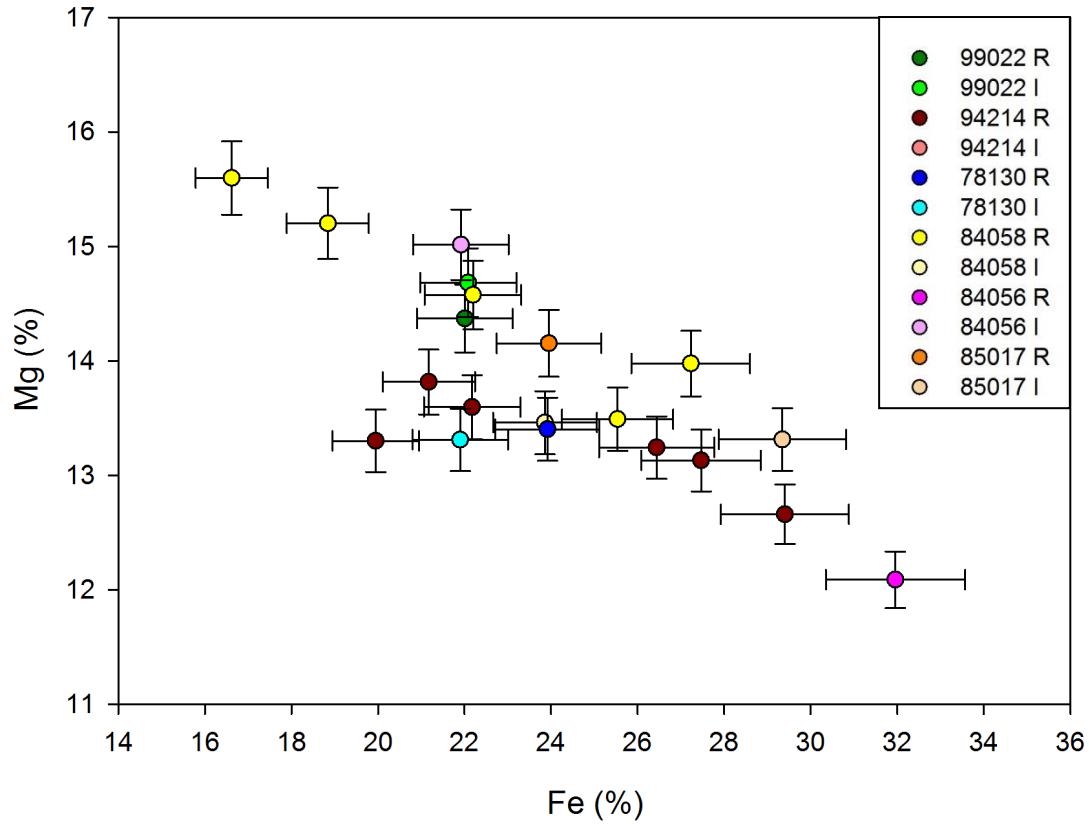

Fig. 5.8. Fe wt.% vs Mg wt.% in all bulk meteorites studied.

Magnesium (Alkaline earth metal, lithophile)

Mg contents vary between 12.0–15.6 wt.% with the highest sample being the LA subset of ALH 84058, and the lowest being in ALH 84056 R. There is a negative correlation between Mg and Fe (r= -0.78; Fig 5.8.) and a weak positive correlation with Ca and Al contents. ALH 84058 subsets spread over a large range of values (13.5–15.6 wt.%) with the least Mg in the GI and the MA samples. The FC subsample is also low in Mg. In the QUE 94214 subsets, the Mg contents of most of the subsets are within error of each other and are between 13.0–13.5 wt.%. The INTM sample has the lowest Mg contents at 12.7 wt.%. QUE 99022 rim and interior both plot within error of each other, as does ALH 78130. ALH 85017 has less Mg in the interior sample and ALH 84056 has significantly more Mg in the interior than the rim.

Element specific discussion

There is no link between weathering and Mg contents in the bulk samples, with the most weathered meteorites having similar Mg contents to the least weathered meteorites. There is also little difference between the rims and interiors of the samples. The subsets of ALH 84058 show some correlation with weathering state however, with lesser Mg in the more altered areas. The QUE 94214 subsets show little separation and do not back up any pattern of Mg removal with weathering.

Iron (Transition metal, siderophile)

Fe is between 16.6–32.0 wt.%. The lowest concentration is in ALH 84058 least altered subset and the highest is in ALH 84056 R. QUE 99022 rim and interior both plot within error (22.1 wt.%). They are at the lower end of Fe abundance compared to the other meteorites. ALH 85017 R plots in a central part of Fe abundance at 24.0 wt.%, the interior plotting much higher at 29.3 wt.%. ALH 84056 has a comparatively lower Fe abundance, with an Fe content of 21.9 wt.%.

QUE 94214 and ALH 84058 subsets cover almost the entire spectrum of results from other samples. In the ALH 84058 subsets, the LA sample has the least Fe at 16.6 wt.%. The sample with the highest Fe contents is the FC sample, followed by the MA sample which is within error. The GR and GI samples are in the centre of the spread of values. In the QUE subsets, the sample with the least iron is the FC subset. This overlaps with the LA sample. The GR sample plots in the middle of the range of values. The MA sample has the second highest Fe contents behind the INTM sample. Three points significantly deviate from the negative correlation of Fe and Mg. These are three subsets of QUE 94214: FC, LA and GR samples. There is a negative correlation between Fe and Mg, and a weaker negative correlation between Fe and Ca and Al (Appendix III a).

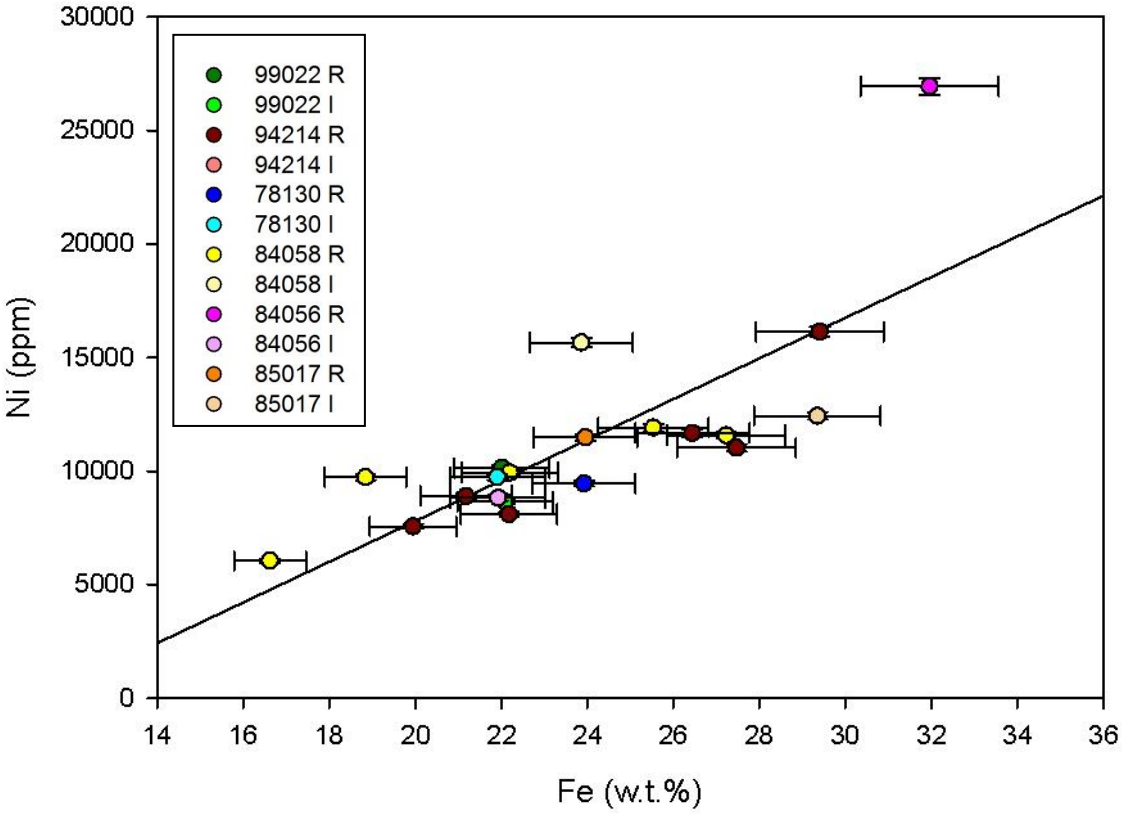

Fig. 5.9. Fe wt.% vs Ni (ppm).

Element specific discussion

In the subsets there is a clear link between weathering state and Fe content, but this is not apparent in the bulk rim and interior samples. Fe vs Ni (Fig. 5.9.) allows discrimination of samples that have a disproportionate amount of metal in them because they have a greater Ni content than the general trend. ALH 84056 R clearly has more Fe-Ni metal because it deviates significantly from the general trend. The general interior subsample of ALH 84058 is also an outlier that could suggest a greater amount of metal is present in this sample.

5.1.3. DISCUSSION OF BULK CHEMICAL DATA

Many elements hosted in part or fully in pyroxene have significant correlation with petrological weathering. Correlations between weathering and Sc, V, Mn, Zr, Hf are suggestive of leaching and partial dissolution of the host. Olivine hosts many of the same traces as pyroxene, but in lesser amounts (Mn, Zr) and so it is not possible to discriminate olivine weathering effects from pyroxene weathering effects using just trace element data. The main host of these elements is assumed to be clinopyroxene based on Wedepohl, et al. (1969) and LA-ICP-MS data from Section 4.2.2.

Sc, mobility appears to be limited from the lack of correlation with rims and interiors. With correlations apparent only in the subsets of QUE 94214 and ALH 84058, the redistribution of Sc appears limited. This is in agreement with weathering profile literature such as (Das et al., 1971) where Sc is conserved in weathering profiles and concentrated in glacial soils. The bulk retention suggests that the Sc is being deposited into alteration products in the meteorites.

V appears to be mobile as the depletions in the rim compared to the interior suggest that the V has been completely removed from the system. The same is true for Mn, Zr and Hf. The depletion of these elements in the rims indicates that they are not deposited in local alteration products, as this would result in little bulk change, and subset change only. The other possibility would be preferential deposition in the interior of the meteorite from the leached rim deposits, although it is difficult to see what mechanism could cause this.

Sb and As are both chalcophile elements and should be present in high concentrations in troilite. The strong correlation between Sb and weathering in rims and interiors, as well as subsets, shows a high mobility, removing the Sb from the system rather than depositing it in alteration products. As only demonstrates weathering trends in the subsets and so must be depositing in local alteration products, otherwise the change would be seen in rim/interior pairs also. Since these are the only two elements contained in troilite that are

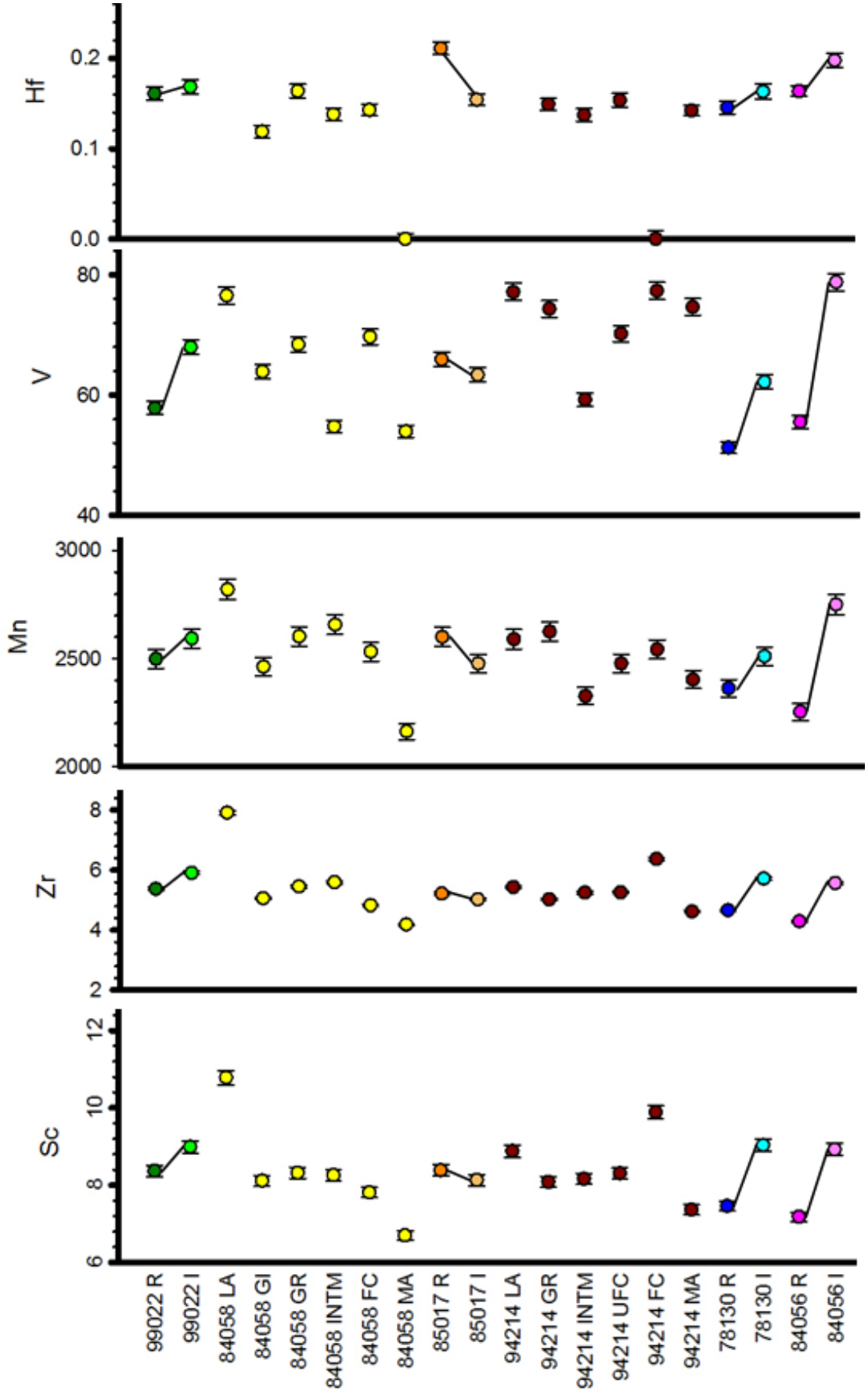

Fig. 5.10. Several trace elements (all in ppm) in all meteorites measured. Tie lines denote rim and interior pairs. ALH 84058 and QUE 94214 LA both plot off the Hf scale at 1.00 and 1.01 ppm respectively.

demonstrably mobilised, there must be leaching of the troilite rather than full dissolution. Alternatively, elements that are neither depleted nor re-distributed could be deposited as iso-alteromorphs (in the same space as the parent grain) with only very little or no movement.

Elements hosted primarily by plagioclase (Li, Rb, Sr, Cs, Ba, Al, Eu and Ca) appear to have very little connection with weathering with the exception is Ca, which is also hosted by diopside and phosphates, and, therefore, may be reflecting weathering of these phases rather than of plagioclase. However, the lack of correlation shows that there is very little to no alteration or leaching of plagioclase.

In ALH 84056 the differences between rim and interior is greater than any other R:I pair. Normalising ALH 84056 R to I (Fig. 5.11) shows that Co, Ni, Cu, Nb, Sn, Sb, Ta and U are higher in the rim compared to the interior. As Co, Ni and Cu were measured in

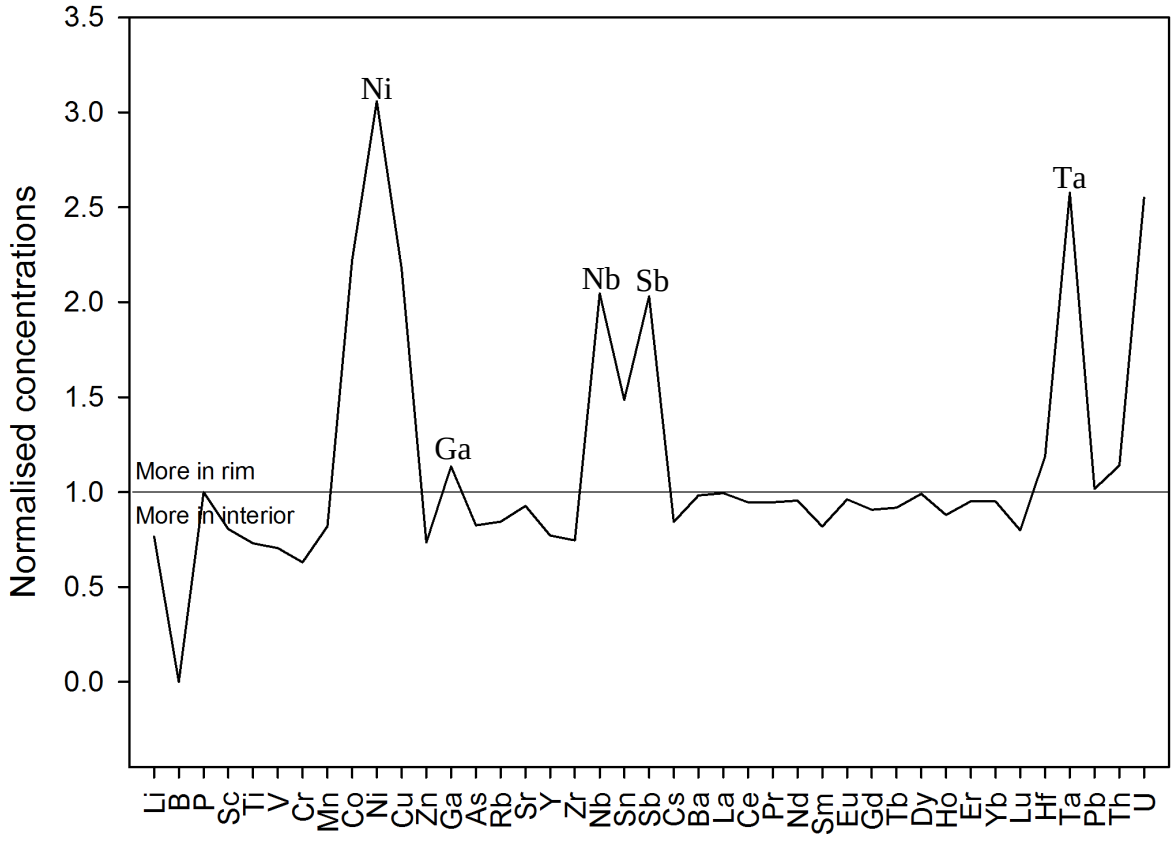

Fig. 5.11. All trace elements measured in ALH 84056 R normalised to the interior to demonstrate the large differences between the two.

abundance in taenite and Sn is strongly correlated with these (Appendix III a), this is likely to represent a large amount of taenite in the rim and, therefore, is not a feature of weathering but is due to sample inhomogeneity. The Sb, Ta and U may be from an external source or from an unknown weathering process.

Fusion crust subsets

The chemistry of the fusion crusts from ALH 84058 and QUE 94214 are different from the other samples and in QUE 94214 there are many element enrichments different to ALH 84058 (Fig 5.12).

QUE 94214 is enriched in Sc, Rb, Sr, Zr, Nb, Sn, Cs, Ba, La, Eu, Hf, Pb, Th, U, Al and Ca in particular. This suggests that there may be a deposit of Antarctic varnish or efflorescence on the surface. Al enrichment also suggests that there could be a comparative overabundance of plagioclase in the fusion crust. Elevated Al/Si ratios have been

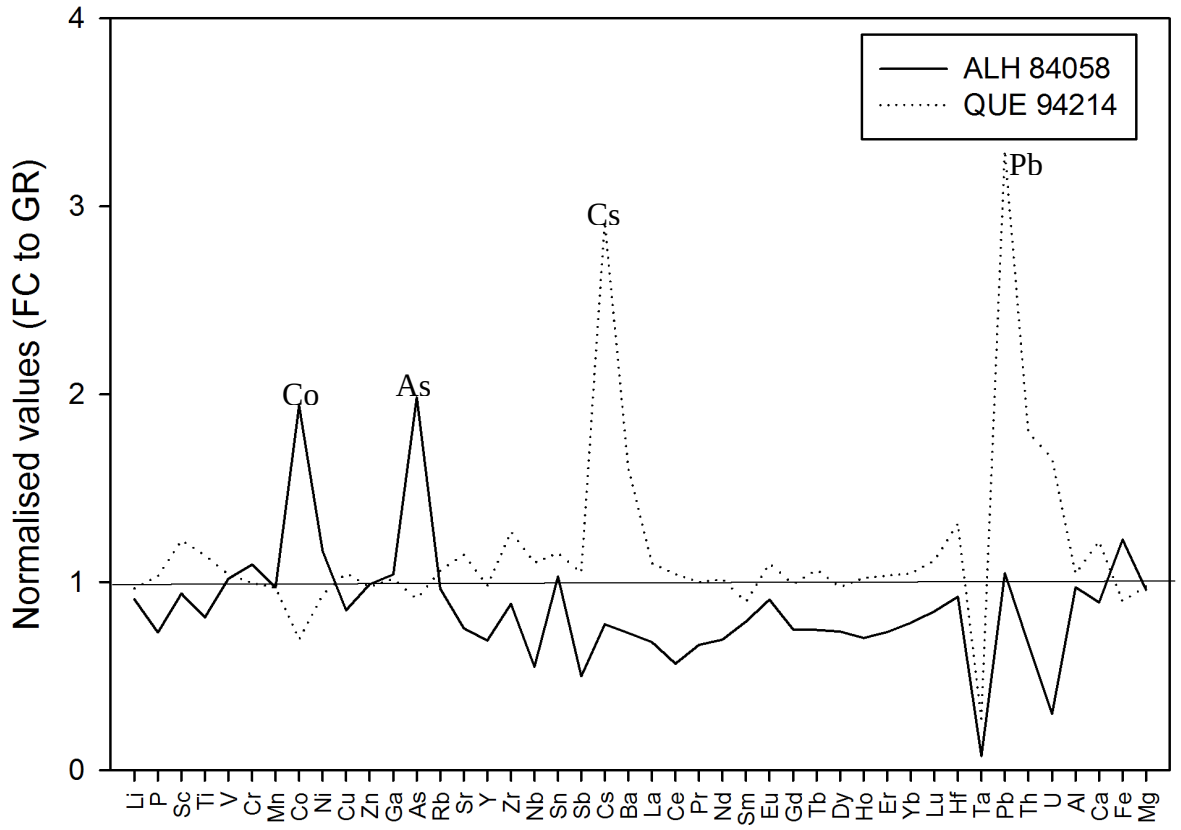

Fig. 5.12. ALH 84058 and QUE 94214s comparative FC compositions. Both have been normalised to the GR samples to discern which elements are concentrated in the FC.

previously noted by Genge and Grady (1999) to occur in many ordinary chondrites when compared to the bulk compositions. This is explained by an increased feldspathoid component in the fusion crust. Many of the trace elements enriched in the fusion crust of QUE 94214 are primarily hosted in feldspar (as detailed in section 4.2).

The area of fusion crust analysed may have been formed from predominantly feldspar if it were the adjacent mineral to this area on atmospheric entry. However, it is also possible that an evaporite deposit exists, as evaporite-bearing meteorites have been previously noted by Velbel et al. (1991) to have Rb, Co and Ca depletion in the interiors of the samples. There is a general Ca gradient in QUE 94214 with Ca contents increasing towards the rim of the sample, with the exception of the general rim sample which is not observed for ALH 84058, and so it is potentially an evaporite deposit. The chemistry of Antarctic varnish is not documented in the published literature, precluding comparison of these new data to published values.

The ALH 84058 fusion crust is depleted in most elements, with the exception of significant enrichment in Co, Ni and As. This is possibly due to the sample heterogeneity and a large amount of metal in this particular fusion crust. Siderophile elements are lost during the formation of fusion crusts through the separation of immiscible Fe-fluids from silicate bulk (Genge and Grady 1999), and so this enrichment is unusual. From a redox perspective, Ni is likely to be preferentially retained over Fe during the formation of a fusion crust as it is less easily oxidised. Since there is not a corresponding increase of Fe in this fusion crust, it is likely that either Fe was lost during atmospheric entry or the increase in Fe that would stoichiometrically follow the increase of Ni (if hosted in kamacite/taenite) is too small (comparatively) to measure.

Lead Contamination

The host of Pb is not known, and it could be distributed amongst several phases. The Pb contents of the subsets show strong correlation with depth, with the fusion crust being

significantly enriched compared to the interior of the meteorites (Fig 5.7). The excess of Pb in fusion crusts has been noted as an atmosphere based terrestrial contaminant before (Arden, 1983). Whilst the timing of the fusion crust formation of the meteorites studied is unknown, their fall is highly unlikely to have post-dated the large recent anthropogenic Pb contamination of the atmosphere if the meteorites have undergone glacial transport (Cassidy et al., 1992). If the meteorites are a result of direct infall to the icefield then the interaction with the atmosphere will be greater and Pb contamination will be correspondingly higher. The clear increase in Pb in the fusion crusts of both meteorites is highly suggestive of atmospheric addition because the maximum contents of Pb in Antarctic ice measured 0.02 mg/kg (Murozumi et al., 1969). This interaction with the atmosphere could be because the meteorites are recent falls, rather than glacial transport, or due to interaction after exhumation with the atmosphere, whilst at the surface of the icefield and during the final stage of Antarctic weathering, or a combination of both of these processes.

Subset Representation

For most elements, the subsamples from QUE 94214 and ALH 84058 spanned the concentration ranges of all the other samples (Table 2.3). This demonstrates the heterogeneity of L chondrites, and the difficulty in testing if an L chondrite is weathered, using just a single set of bulk data. No one element can be used to demonstrate that more highly-weathered meteorites could be distinguished from the less-weathered specimens, and this is likely to be because of the original heterogeneity of the meteorites, as seen in the subsamples. The extent of Mn, V, Hf and Zr loss in the weathered rims is not sufficient to move weathered portions of the meteorites out of the concentration range of unweathered L chondrites. This shows that the discrimination of weathering at the levels seen in these meteorites is only discernible from comparing more and less altered parts of the same meteorite.

5.2. MAGNETICS RESULTS

The main indigenous magnetic carriers in the samples are tetrataenite, taenite, kamacite and to a much lesser extent, troilite (Wasilewski 1988; Gattacceca et al., 2003; Rochette et al., 2012). Tetrataenite has not been identified as a separate mineral from taenite in the petrological descriptions of the sample (Section 3.2.6) as it only exists as thin rims and edges around taenite grains. Tetrataenite is magnetically hard (can be permanently magnetised with a strong magnetic force) and is transformed via atomic ordering below 320 °C (Wasilewski, 1988) from taenite – which is magnetically soft (can only be temporarily magnetised) and as such, has a higher coercivity and remanent magnetic saturation (Wasilewski 1988). Secondary Fe-oxyhydroxides are magnetic and so the process of linking weathering processes to changes in magnetic properties must include the destruction of primary properties and also the introduction of terrestrial properties (Chevrier et al., 2006).

Hysteresis properties

The five key points on a hysteresis curve, used as diagnostic tools, are: Remanant magnetic saturation (M_{rs}), remanant coercivity (B_{cr}), magnetic remanence (M_r), the coercivity (Bc) and the saturation magnetism (M_s) (Fig. 5.13). Remanent magnetic saturation (M_{rs}) is a measurement of magnetisation in a sample that remains once a large magnetic field has been applied and removed. The M_{rs} is sensitive to the presence of tetrataenite and secondary oxidation products. Remanent coercivity (B_{cr}) is the negative magnetisation field required to return M_r to 0 after M_{rs} has been reached.

Hysteresis results

The highest B_{cr} values are in ALH 84058, ALH 85017 and QUE 99022 interior. There is a very large difference between QUE 99022 rim and interior with roughly 150 mT difference. ALH 84056, QUE 94214 and ALH 78130 all plot with low B_{cr} (<50 mT) and cluster tightly. The M_{rs} is highest in ALH 85017, ALH 84058 and QUE 99022 also. There

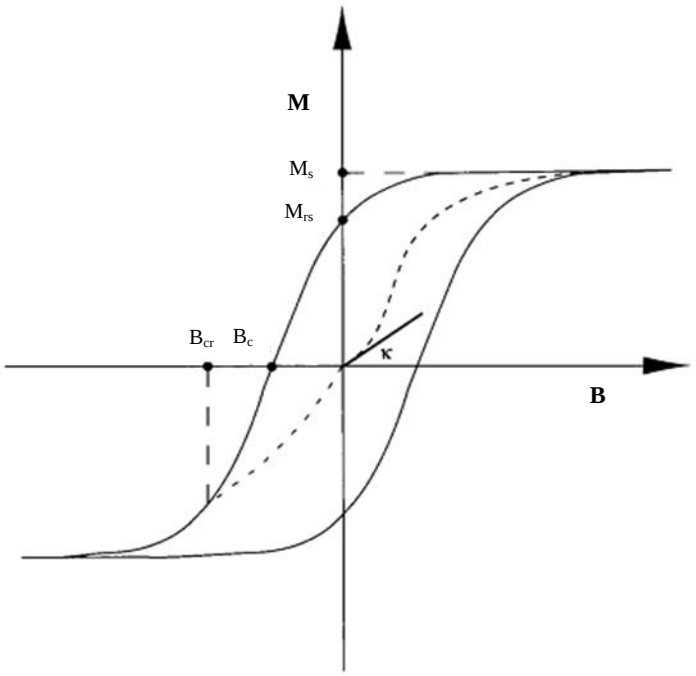

Fig 5.13. A diagram of a hysteresis curve with the most important values labelled (Edwin and Heller, 2003). ƙ is the initial susceptibility, which is ascertained by the initial slope of the B/M curve at low field strength. In this particular case, Mrs and Mr are equivalent as Mr is the magnetic remanence after a field (B) is applied and Mrs is the magnetic remanence after saturation (Ms) has been reached.

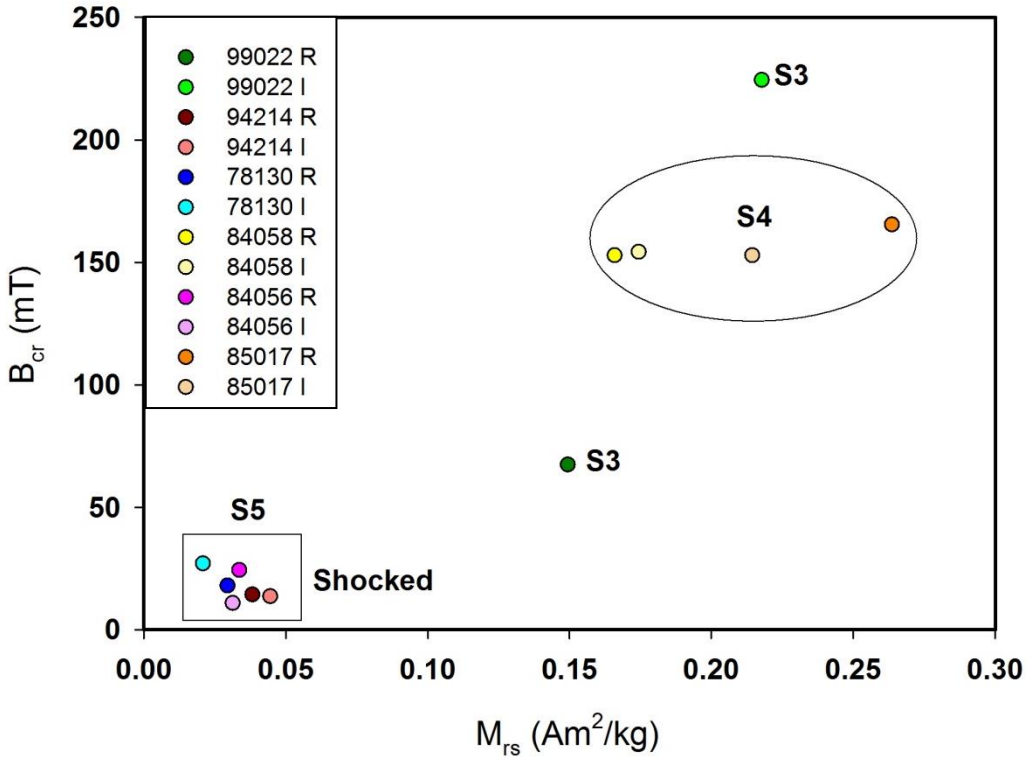

Fig. 5.14 Mrs vs Bcr. The shock grades are as classified in Table 3.2. The meteorites that are S5 all plot with significantly less Mrs and Bcr and do not allow for discrimination based on weathering grades. QUE 99022 has the largest difference from rim to interior, with the rim having a significantly lesser Mrs and Bcr. Errors are smaller than symbols.

is less of a gap separating QUE 99022 rim and interior in M_{rs} compared to B_{cr}. Again, the other three meteorites cluster tightly at low values.

The separation of M_{rs} and B_{cr} values sharply decrease with a shock grade of S5 (Fig. 5.14.). ALH 84056, ALH 78130 and QUE 94214 were diagnosed with a shock stage of S5 (Section 3.7) and all have significantly lower M_{rs} and B_{cr} because of the destruction of the most significant magnetic carrier, tetrataenite. Tetrataenite is known to disorder to taenite when a temperature over 540 °C is reached (Gattaccecca et al., 2003) which is just below the post-shock temperature expected for an S5 meteorite (Stöffler 1993). For the other meteorites, it is possible to use M_{rs} and B_{cr} for weathering comparisons as they have not passed the Curie temperature.

There is no consistent difference between the rim and interior pairs of the lesser shocked meteorites. QUE 99022 shows the greatest difference between rim and interior with the rim having an almost four times smaller B_{cr} and a significant shift in its M_{rs}. The rim of ALH 85017 has significantly higher M_{rs} than the interior and a slightly higher B_{cr}. ALH 84058 shows a smaller shift between rim and interior with very little difference.

Ms does not separate out the shocked meteorites, as it is an induced property and so is more likely to show changes due to weathering. Four of the meteorites (ALH 84056, QUE 94214, ALH 85017, QUE 99022) show a decrease in M_s between rim and interior (Fig 5.15.), however two show the reverse (ALH 78130, ALH 84058). ALH 78130 has a more weathered interior compared to the rim (section 3.1), and so this reversal of pattern is to be expected, if the decrease in M_s is caused by weathering of the magnetic phases and the addition of goethite and other Fe-oxyhydroxides. The largest difference between rim and interior is in ALH 85017, with the rim having a significantly lower M_s than the interior. The most weathered samples, QUE 99022 and ALH 78130 have low M_s values and the most pristine samples have higher M_s (ALH 84056, ALH 85017 I).

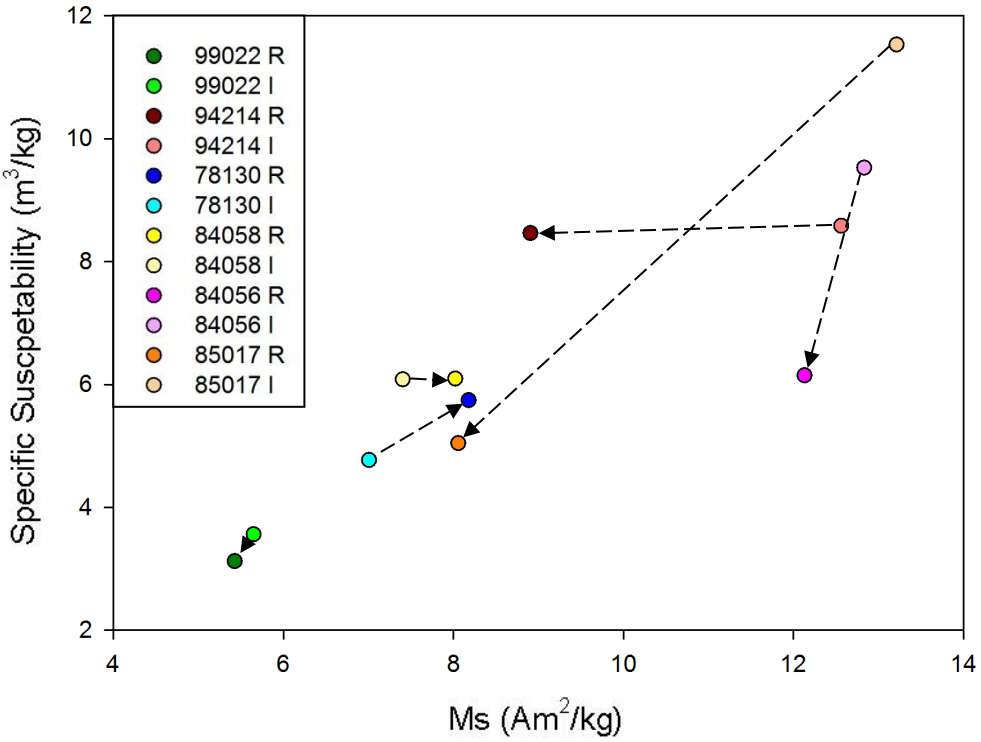

Fig. 5.15. Ms vs susceptibility. Most of the meteorites show a smaller Ms in the rim compared to interior. Errors are smaller than symbols. Tie lines indicate pairs, arrows indicate rims.

B_c appears to correspond to shock stages, with the more shocked meteorites having very low coercivity most likely caused by the ordering of tetrataenite into taenite. No consistent difference between rim and interior of samples can be seen in B_c and the change is (comparatively) small between the rims and interiors.

Susceptibility

The susceptibility was measured and then mass-normalised to give specific susceptibility (χ). It is not affected by the re-ordering of tetrataenite and so can be used to correlate with weathering. It positively correlates with M_s (Fig 5.15). The two least weathered samples have the greatest χ and the more weathered samples have a lesser χ. ALH 84056 R is very different from the interior and also deviates from the M_s:χ correlation. QUE 94214 plots outside the trend as there is no decrease in χ in the rim compared to the interior to accompany the decrease in Ms. There is a general decrease in susceptibility in rims

compared to interiors, but exceptions to this are QUE 94214 and ALH 84058. ALH 78130 interior has a lower susceptibility, but it is more weathered than the rim (Section 3.1).

Links between magnetic properties and petrology

To examine the possible links between the petrology and magnetic properties of the samples, comparison was made to the oxidation percentages obtained in Section 3, Table 3.2. (Fig 5.16). The B_c of the less shocked meteorites (S3-4) shows a weak positive correlation with the percentage of oxidised kamacite and taenite oxidation shows a very weak positive correlation with Ms. QUE 99022 R is a significant outlier in both.

The M_s shows a negative correlation with the extent of kamacite and taenite oxidation with the M_s displaying an exponential decrease with relation to kamacite oxidation, but not taenite (Fig. 5.17.). However, this is largely because of the two outliers of QUE 99022 R and ALH 78130 I, without which there would be a linear negative correlation. M_{rs} and B_{cr} both do not appear to correlate with the oxidation percentages.

The specific susceptibility has a negative correlation with kamacite oxidation and a weaker negative correlation with taenite oxidation. To compare the theoretical path that a weathering meteorite should take, a fresh fall and a theoretical "most weathered" point were added. The most weathered point assumes that no secondary products deposited were magnetic. The line between demonstrates a theoretical regression that many of the meteorites roughly follow and so any deviation from the line should indicate magnetic effects from secondary products or an unusual amount of magnetic minerals in the starting composition.

ALH 85017 has a higher χ in the interior samples than the range defined by Rochette et al. (2003) to be value of fresh L6 falls (Fig. 5.18). As it has been observed to be one of the least petrologically weathered samples, this points to an excess of magnetic metal grains. ALH 85017 I has been previously observed to contain high levels of kamacite and

taenite/tetrataenite in chapter 3, and on inspection of the chips with a binocular microscope – two large metal grains (unknown if kamacite or taenite) are observed.

ALH 78130 I plots higher and some plot with a higher susceptibility than the fall (ALH 85046 I, ALH 85017 I and QUE 94214). These are potentially due to the magnetic effects of the secondary products, as goethite (one of most prevalent hydrated Fe-oxides present in Antarctic meteorites; Gooding 1982) and hematite are known to be weakly magnetic (Uehara et al., 2012). The theoretical regression line of the taenite oxidation (Fig 5.18.) is notable for not being similar to the data with a steeper gradient.

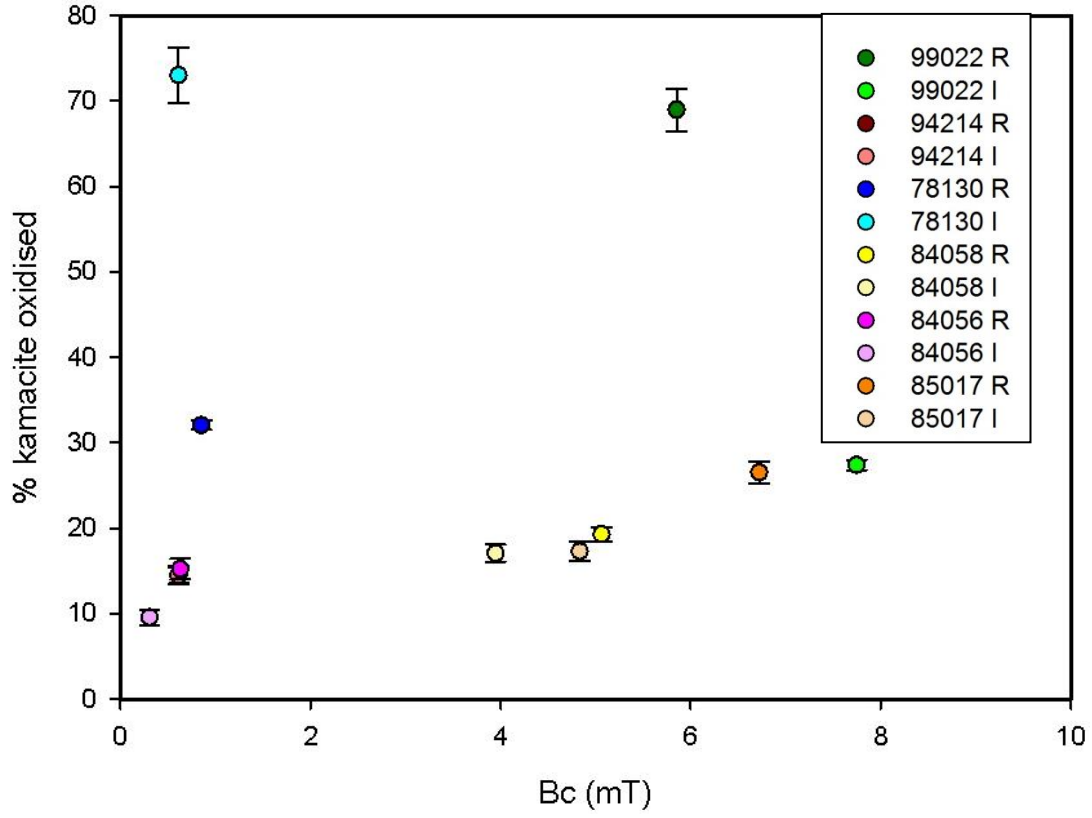

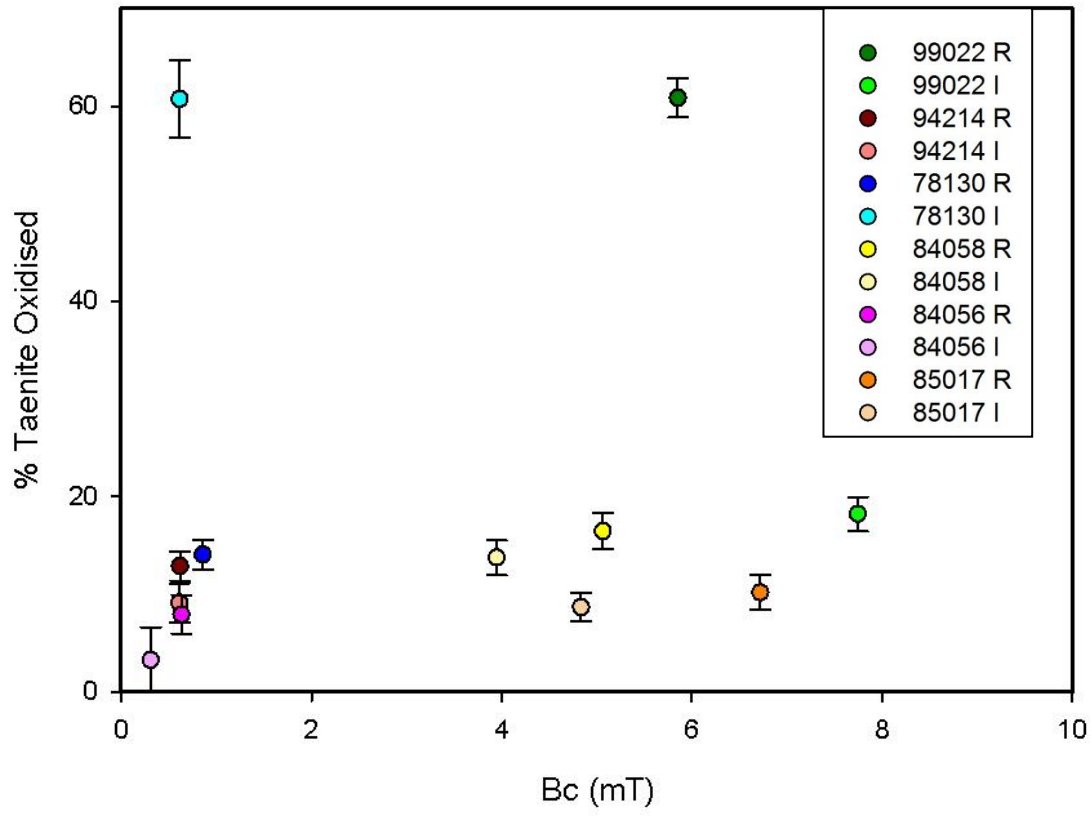

Fig. 5.16. Bc vs % oxidised kamacite and taenite. Bc errors are smaller than the symbols.

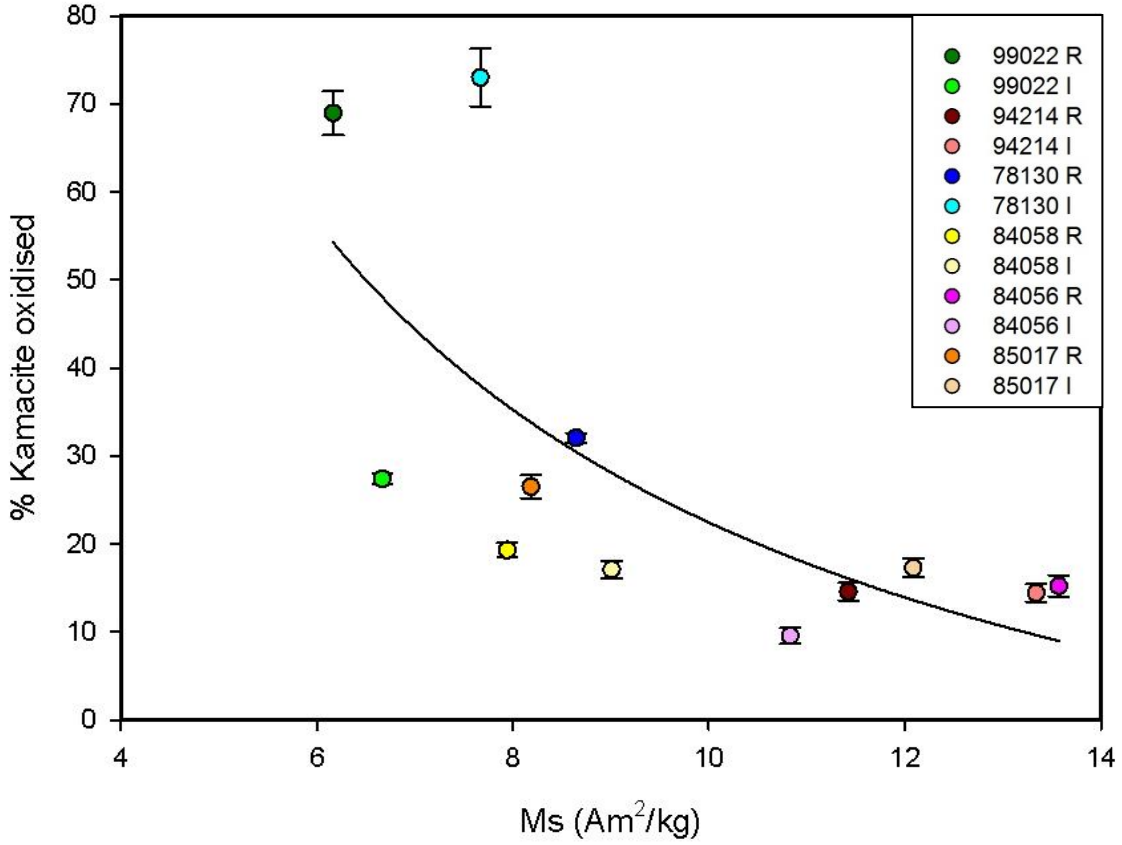

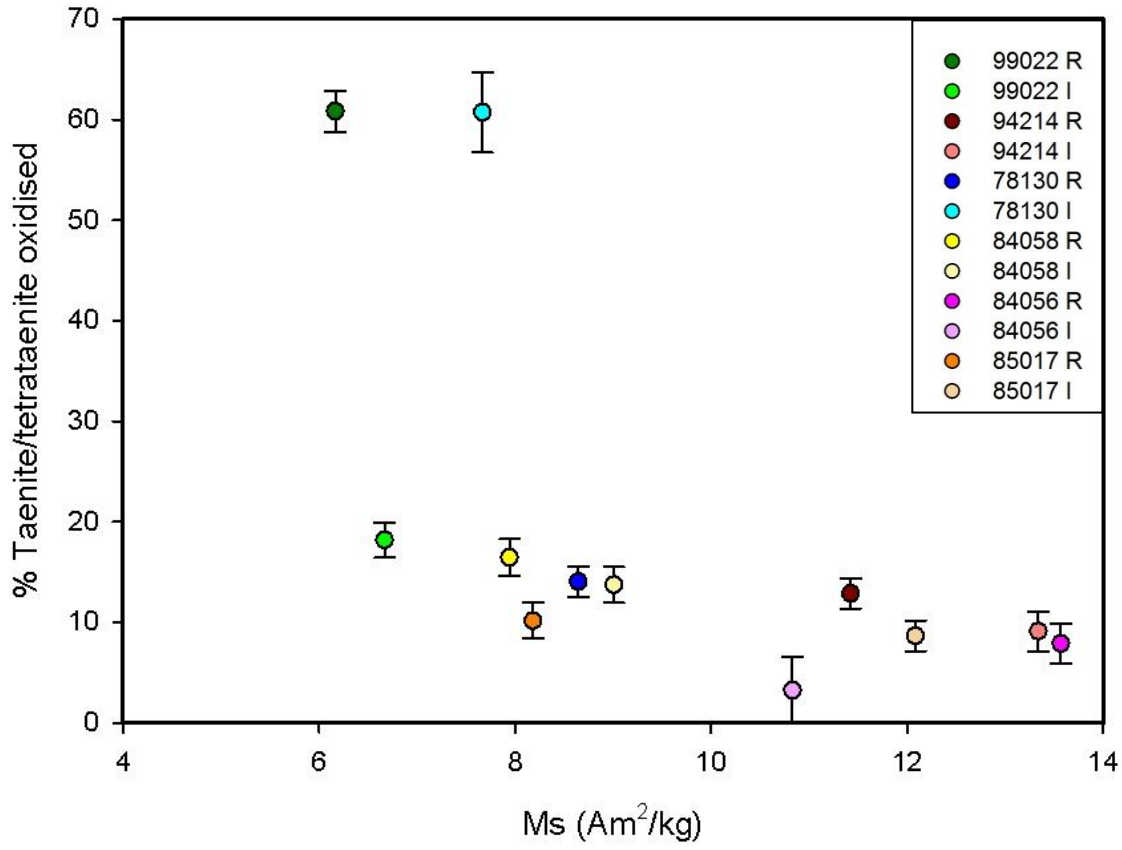

Fig. 5.17. Percentage oxidised kamacite and taenite plotted against Ms. Both show a negative correlation. Ms errors are smaller than the symbols.

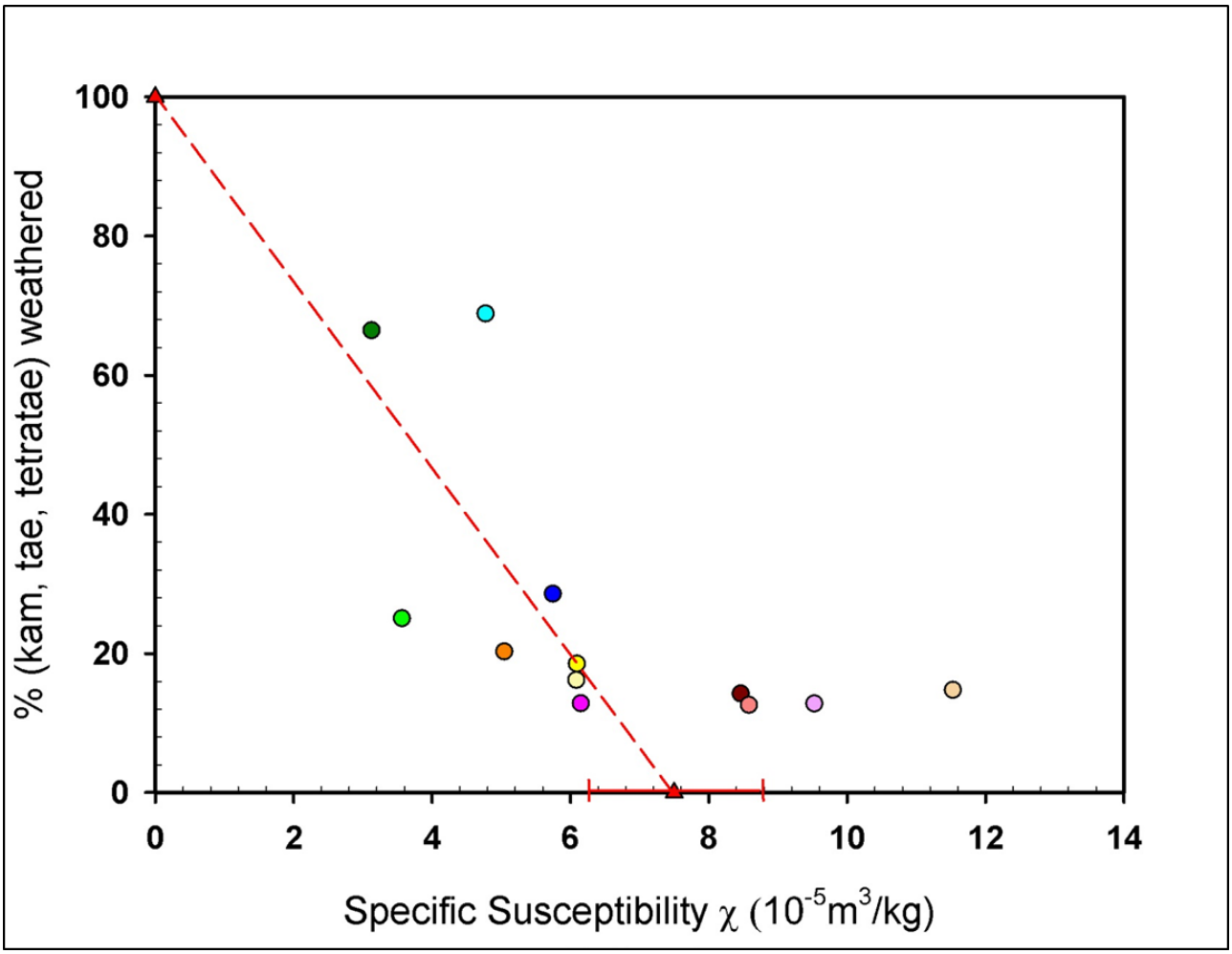

Fig. 5.18. Specific susceptibility and % kamacite, taenite and tetrataenite weathered. These numbers were calculated from combining and scaling the average oxidations of these three minerals for all the meteorites. Red points are the theoretical endpoints of a sample with all magnetic minerals weathered out and replaced with non-magnetic alteration minerals with the average value for a fresh L6 fall (from Rochette et al., 2003) to represent an un-altered sample (error bar shows standard deviation). A negative correlation can be seen between % metal weathered and χ as increasing amounts of metal and sulphide is transformed to Fe-oxyhydroxides. ALH 85017 interior has an anomalously high χ due to two large (1.5–2 mm) metal grains. Specific susceptibility errors are below the size of symbol.

5.3. OXYGEN ISOTOPES

Analysis of oxygen isotopes in the samples was undertaken as the main alteration process in the meteorites involves oxidation. Therefore a shift in isotopes towards terrestrial compositions is possible in altered samples. To explore this link, the oxygen isotopes are compared with the petrology.

Table 5.2. Oxygen isotope results. The deviation (Dev) from the mean of the two measurements is given in the replicate row.

Sample	$\delta^{17}O$ (‰)	$\delta^{18}O$ (‰)	$\Delta^{17}O$ (‰)	$\delta^{17}O$ Dev	$\delta^{18}O$ Dev	$\Delta^{17}O$ Dev	$\delta^{17}O$ 2σ	$\delta^{18}O$ 2σ	$\Delta^{17}O$ 2σ
QUE 99022 R	3.105	3.878	1.088						
Replicate	3.156	3.970	1.092	0.036	0.065	0.003	0.072	0.130	0.006
QUE 99022 I	3.314	4.191	1.135						
Replicate	3.326	4.204	1.140	0.008	0.009	0.004	0.017	0.018	0.007
QUE 94214 R	3.497	4.578	1.117						
Replicate	3.474	4.472	1.148	0.016	0.075	0.022	0.033	0.150	0.044
QUE 94214 I	3.560	4.592	1.173						
Replicate	3.544	4.601	1.152	0.011	0.006	0.015	0.023	0.013	0.030
ALH 78130 R	3.269	4.160	1.106						
Replicate	3.219	4.058	1.109	0.035	0.072	0.002	0.071	0.144	0.004
ALH 78130 I	3.131	3.885	1.111						
Replicate	3.114	3.900	1.087	0.012	0.011	0.017	0.024	0.021	0.034
ALH 84056 R	3.599	4.730	1.139						
Replicate	3.621	4.732	1.160	0.016	0.001	0.015	0.031	0.003	0.030
ALH 84056 I	3.638	4.803	1.140						
Replicate	3.659	4.837	1.144	0.015	0.024	0.003	0.030	0.048	0.006
ALH 84058 R	3.306	4.229	1.107						
Replicate	3.167	3.951	1.113	0.098	0.197	0.004	0.197	0.393	0.008
ALH 84058 I	3.264	4.166	1.098						
Replicate	3.406	4.439	1.098	0.100	0.193	0.000	0.201	0.386	0.000
ALH 85017 R	3.488	4.517	1.139						
Replicate	3.468	4.477	1.140	0.014	0.028	0.001	0.028	0.057	0.001
ALH 85017 I	3.612	4.803	1.115						
Replicate	3.494	4.552	1.127	0.083	0.177	0.008	0.167	0.355	0.017

Oxygen isotopic results are reported in $\delta^{18}O$, $\delta^{17}O$ and $\Delta^{17}O$. $\delta^{18}O$ and $\delta^{17}O$ are calculated as:

$$\delta^{18}O = (({}^{18}O/{}^{16}O_{sample}/{}^{18}O/{}^{16}O_{ref})-1) \times 1000$$

$$\delta^{17}O = (({}^{17}O/{}^{16}O_{sample}/{}^{17}O/{}^{16}O_{ref})-1) \times 1000$$

where ref is the laboratory reference material, obsidian. $\Delta^{17}O$ represents the deviation for the terrestrial fractionation line using a TFL (λ) with a slope of 0.524 (Miller et al., 1999):

$$\Delta^{17}O = \delta^{17}O - (0.52 \times \delta^{18}O)$$

Two groups of samples can be distinguished in $\delta^{18}O$ and $\delta^{17}O$ space, but most of the meteorites are within error of each other (Fig. 5.19.). The group with higher $\delta^{17}O$ and $\delta^{18}O$ overlaps with analysis from Clayton et al. (1991) of L chondrite fall data and contains: ALH 84056 (with the highest values and little rim-interior difference and the least weathered meteorite in this study), ALH 85017 (with a more significant rim-interior difference and another notably less weathered meteorite) and QUE 94214 (a moderately weathered sample). In all three cases, the rim sample has lower $\delta^{17}O$ and $\delta^{18}O$ than the interior. The group with lower $\delta^{17}O$ and $\delta^{18}O$ contains: QUE 99022 (one of the most heavily weathered meteorites), ALH 84058 (a moderately weathered sample) and ALH 78130 (heavily weathered). This group is outside of the field defined by Clayton et al. (1991) as standard for L chondrites.

The $\Delta^{17}O$ (Fig. 5.20) shows that, whilst the meteorites respective rims plot with lower $\Delta^{17}O$ than their rims, they are within the statistics of noise from heterogeneous sampling. However, with the comparison with fall data for the L chondrite group, it is clear that the most weathered meteorites (QUE 99022, ALH 84058 and ALH 78130) have values outside this group. Bland et al. (1991) and Greenwood et al. (2012) demonstrated that with weathering, meteorites are driven towards the TFL. The more weathered meteorites measured here do not show a statistically significant decrease in $\Delta^{17}O$ towards the TFL, but do show the decrease in $\delta^{18}O$ typical of Antarctic meteorites (Greenwood et al., 2012).

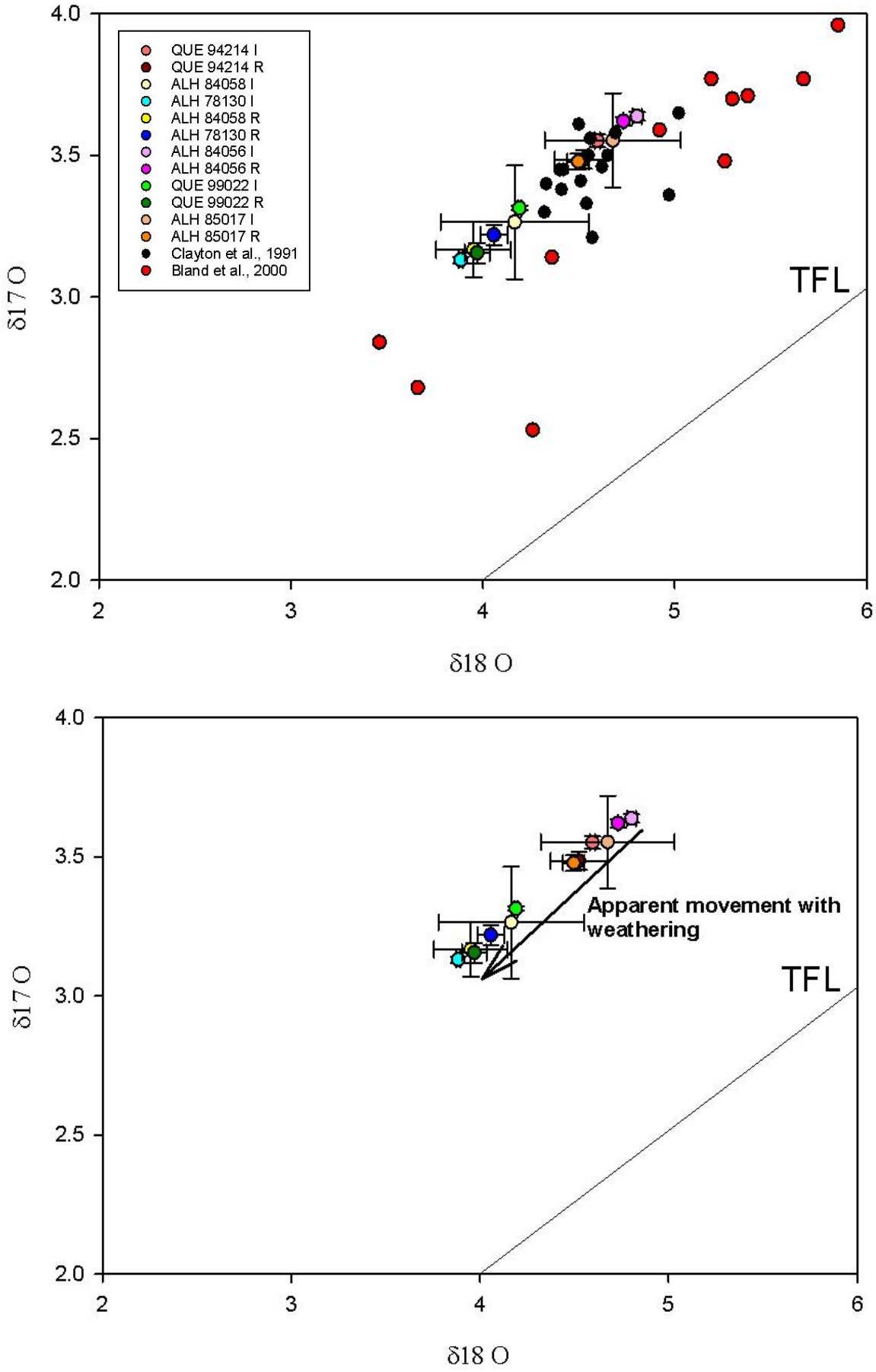

Fig. 5.19. $\delta^{18}O$ vs $\delta^{17}O$ in all samples measured with the terrestrial fractionation line. The top graph includes data from L6 falls taken from Clayton et al., 1991 and data from L6 meteorites over 20 % oxidised from Bland et al. (2000). The lower graph shows the general direction of movement with weathering. The size of error bars may be a reflection of heterogeneously weathered meteorites.

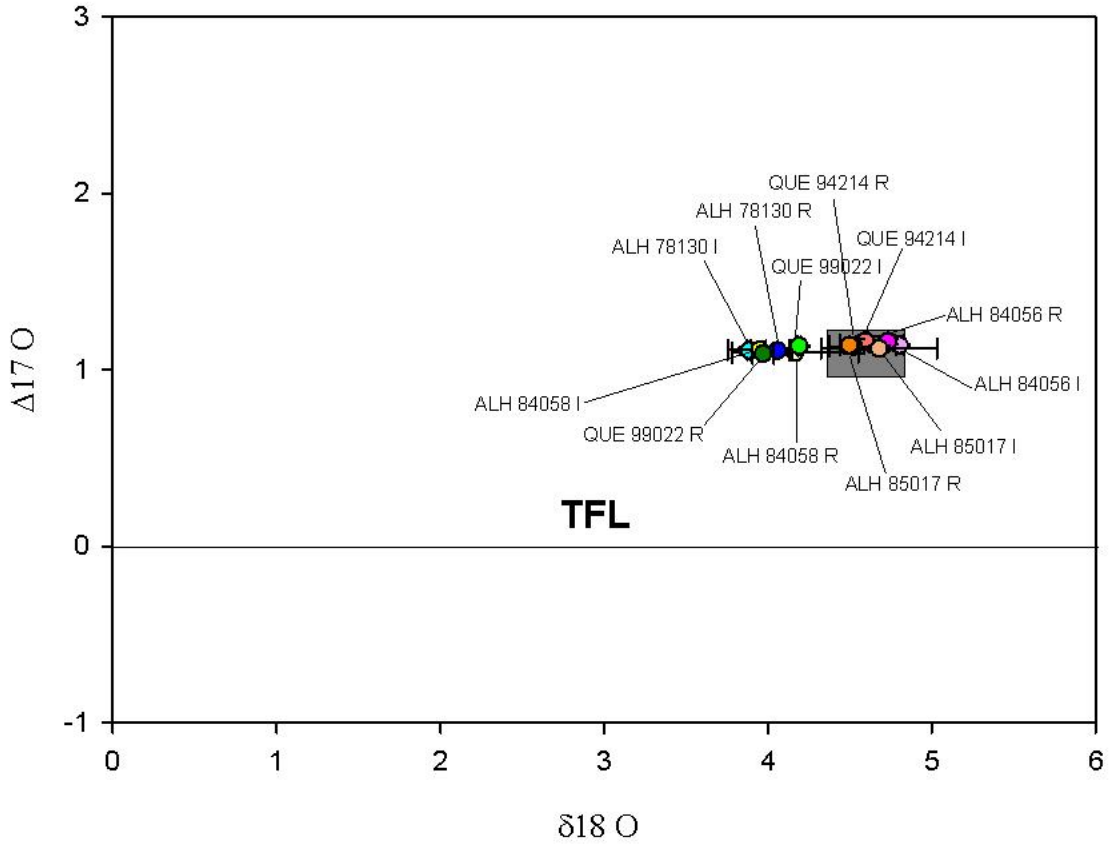

Fig. 5.20. δ^{18} O vs Δ^{17}O in all meteorites studied. A grey box denotes the area of L chondrite falls as defined by Clayton et al. (1990).

All samples, with the exception of ALH 78130, have lower δ^{17}O and δ^{18}O in the rims of the meteorites compared to their respective interiors (Fig. 5.19). With this rim/interior effect, it is possible that this is caused by fusion crust formation which has incorporated terrestrial oxygen, however, ALH 78130 has the reverse pattern and the petrological studies show the interior to be more weathered that the rim and so this is more likely a pattern of weathering.

As the primary form of alteration in the samples is oxidation of metals and sulphides, a significant amount of terrestrial oxygen should be incorporated into the alteration products which will shift the oxygen to a lower δ^{17}O, more terrestrial value (Bland et al., 2000; Greenwood et al., 2012). The shift to lower δ^{17}O and δ^{18} O in the rim compared to the interiors of the meteorites is most likely reflecting the increase of Fe-oxyhydroxides formed. Whilst a reduction in δ^{17}O was reported by Bland et al. (2000), a decrease of δ^{18}O

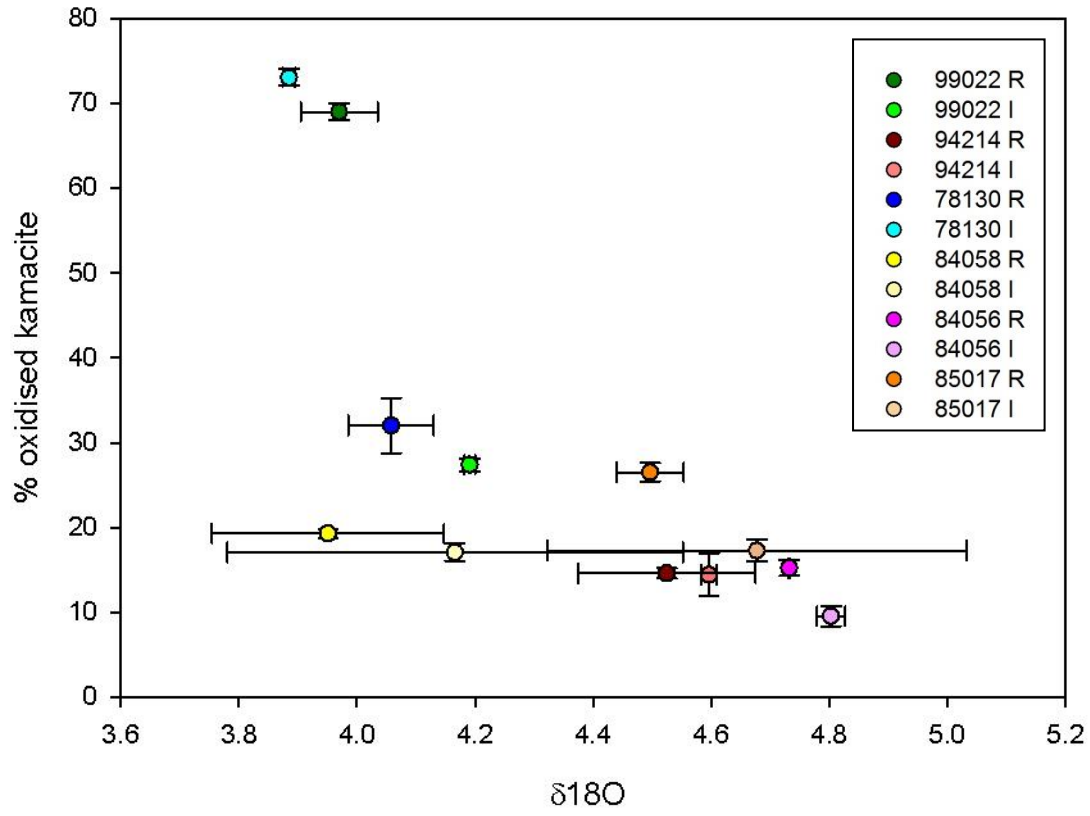

Fig. 5.21. $\delta^{18}O$ vs % kamacite oxidised. A negative correlation is clear between the two, with two high outliers in ALH 78130 I and QUE 99022 R.

was not observed. As this shift is almost slope ½ then it is possible that this is a mass dependent fractionation between the samples.

Links with petrology

To examine the links between alteration related petrological features and oxygen isotopes, $\delta^{17}O$ and $\delta^{18}O$ were plotted against petrological features detailed in Table 3.2. Fig 5.21 shows the oxidation of kamacite compared to the $\delta^{18}O$ of samples. There is a weak negative correlation between kamacite oxidation and $\delta^{17}O$ and $\delta^{18}O$, with more weathered kamacite resulting in lower $\delta^{17}O$ and $\delta^{18}O$. This correlation is stronger in taenite oxidation and slightly weaker with sulphide alteration. With a correlation coefficient of -0.71, the taenite oxidation most strongly correlates with $\delta^{17}O$. $\Delta^{17}O$ does not demonstrate any strong correlation with petrology, with correlation coefficients showing weak correlations at best.

Greenwood et al. (2012) described constant change in oxygen isotopes with terrestrial oxidation of Fe-Ni metal in meteorites, whereas Bland et al. (2000) found a dissimilar pattern with oxygen isotopes only showing change after 25 % of Fe-Ni metals oxidised. Without leaching the meteorite samples, it is impossible to refute either, but in the samples studied, samples with 20 % kamacite oxidation can have significantly lower $\delta^{18}O$ than meteorites with similar levels of oxidation, and above 25 % all (with the exception of QUE 94214 I) have lower $\delta^{18}O$.

CHAPTER 6 – DISCUSSION AND CONCLUSIONS

6.1. LINKING BULK AND SPATIALLY RESOLVED COMPOSITIONS

In Chapter 5, bulk analyses were obtained for trace and major elements of all meteorites and in subsets of two meteorites. These data show that no single element successfully places the meteorites in the same order of 'most to least weathered' established by the petrology. This highlights that the heterogeneity of the weathering environments within single samples, and the limitations in sample availability inherent to meteorite studies are vitally important factors. The data demonstrate the existence of multiple micro-weathering environments on a centimetre scale and comparing spatially resolved and bulk data provides the opportunity to assess how these micro-environments scale to bulk measurements.

In the spatially resolved data, the main features that are noted are: 1) the compositional differences that are derived from the dissolution of ferromagnesian minerals, and 2) the compositional differences derived from Fe-Ni metal redistribution. Spatially resolved data show an increased concentration of Fe, Co, Ni and Cu in ferromagnesian minerals in the meteorites without considerable sulphide weathering (all meteorites except QUE 94214; see Chapter 3). Increases in QUE 94214 also included Fe and Cu, but not Ni and Co.

In the bulk data these increased concentrations of Fe, Co, Ni and Cu are largely not observed when comparing more weathered rims with less weathered interiors of the meteorites. Fe concentrations increase in the smaller subsets of ALH 84058 and QUE 94214, and the two sets of subsamples cover the entire range of Fe values measured in the other meteorites. This indicates that Fe accumulations are only measurable on a scale of less than 2 mm (the largest length of chip for the subsamples), and does not extend to the larger (maximum 8 mm) scale. Ni accumulations only occur in the ALH 84058

subsamples, and are absent in both the QUE 94214 subsamples and the rim/interior bulk measurements of the other meteorites. Since the Ni concentrations are not observed in the spatial ferromagnesian data from QUE 94214, it follows that they are not represented in the subsets either. The lack of correlation in the larger bulk samples of rims and interiors indicates a short transport distance. Higher Co is only measured in QUE 94214 and ALH 84058, thus displaying a similar mobility to Fe. Enhanced Cu is not measured in the most weathered subsets of QUE 94214 or ALH 84058, and there is a potential decrease of Cu in the most weathered subsets of QUE 94214 (for details see Section 5.1.).

The changes in the ferromagnesian minerals that are observed in the spatially resolved data, therefore, does not translate into the bulk measurements of the homogenised large chips (~0.8 g). However, the deposition due to the mobilisation and alteration of metals in the sample is measureable in homogenised chips <0.4 g (average weight of subsample chips). This is a critical concern when performing trace element studies on Antarctic meteorites. If sufficiently large chips cannot be used, care must be taken to select the sample appropriately, and testing for the representativeness of the sample is mandatory. As far as this study can extrapolate, the size of chip needed to homogenise the meteorite must be ≥ 0.8 g. As to how the 0.8 g chips relate to the whole meteorite can only be commented on by comparing the rims and interior chips. Whilst most showed the rim to be more weathered than the interior, this was not true of ALH 78130 and was only marginally true of QUE 94214, but all showed significant difference. None of the meteorites showed no rim-interior difference and so the 0.8 g chips do not well represent the whole meteorite.

There were some unique additions to the ferromagnesian minerals of QUE 94214 measured by LA-ICP-MS. Hotspots of Al, Ca and Zn were measured in olivine and Al, Cr and V were measured in pyroxenes. In bulk samples, Al addition is not observed, with the most and least weathered subsets having almost identical Al values. This could reflect the low solubility, and thus mobility, of Al in circum-neutral environments. Likewise no

additions of Ca, Zn and V were observed, with no alignment between concentration and weathering state. QUE 94214 does, however, have a Cr hotspot in the most weathered subset and so the accumulation of this element in pyroxene crystals may be observed on a larger scale.

The spatial data identifies many elemental depletions: Si and Mn from all olivines (and Mg in QUE 94214), Si and Mn from all pyroxenes, and Al removal in all but QUE 94214 (and Mg, K, Ti, Zn removal from QUE 94214). Mn depletion is observed in both the subsets of ALH 84058 and QUE 94214 and also in all rim/interior pairs with consistent depletions in the rims compared to the interiors. Al removal is measured in the rims of four out of five meteorites, with ALH 84058 subsets having lower concentrations of Al in the most altered subset, and QUE 99022, ALH 78130, ALH 84056 being depleted in Al in the rims compared to their interiors. ALH 85017 is the outlier, but as it is one of the two least weathered meteorites (the other being ALH 84056), it is possible that this is a reflection of less pronounced weathering in this sample.

Mg depletion is not observed in the QUE 94214 subsets, they are within error of each other. K depletion is not measured by the bulk data (see Section 5.1.). Ti depletion from QUE 94214 is maybe present in the weathered subsets, with depletions of Ti in the most weathered subsets compared to the least weathered but other subsets with values covering the ends of the range. Therefore it might be assumed that heterogeneity of Ti is playing a large part in the bulk measurements, because the main hosts are chromite and Ti-magnetite rather than ferromagnesian minerals. Because of the high Ti concentrations in chromite and Ti-magnetite, the measured signal is likely to be dominated by the inclusion of a single chromite crystal in a bulk sample, thus is a feature of the original sample and not a measure for weathering.

The only depletion observed in both spatial and bulk data is the decrease of Mn and Al in the meteorites weathered at more neutral pH (no acidification from sulphides). The Al

removal is only observed in a few of the samples, but Mn removal is observed in all. The leaching and removal of Mn in the meteorites is extensive enough that Mn is completely removed from the rims of the meteorites rather than being deposited in alteration products. This makes it the most consistently mobile element in the meteorites.

An important outcome is that the weathering effect in bulk measurements was only observable by comparison of more weathered parts of the same meteorite with its less weathered counterparts, and very little difference is observed in bulk between the most weathered and least weathered meteorites, making the weathering systems almost entirely closed (with the exception of Mn and Al removal).

6.2. C. W. I. - The Chondrite Weathering Index

In Chapter 1, weathering indices for terrestrial igneous rocks were described. These have been applied to the bulk chondrite data collected in chapter 5 to assess the relevance to chondrites. The two indices considered are the CIA (Chemical Index of Alteration; Nesbitt and Young 1982) and the MIA (Mafic Index of Alteration; Babechuk et al., 2014).

$$\mathrm{CIA} = \left(\frac{\mathrm{Al_2O_3}}{\mathrm{Al_2O_3 + Na_2O + K_2O + CaO}}\right) \mathrm{x100}$$

$$\mathrm{MIA} = \left(\frac{\mathrm{Al_2O_3 + Fe_2O_3}}{\mathrm{Al_2O_3 + Fe_2O_3 + Na_2O + K_2O + CaO + MgO}}\right) \mathrm{x100}$$

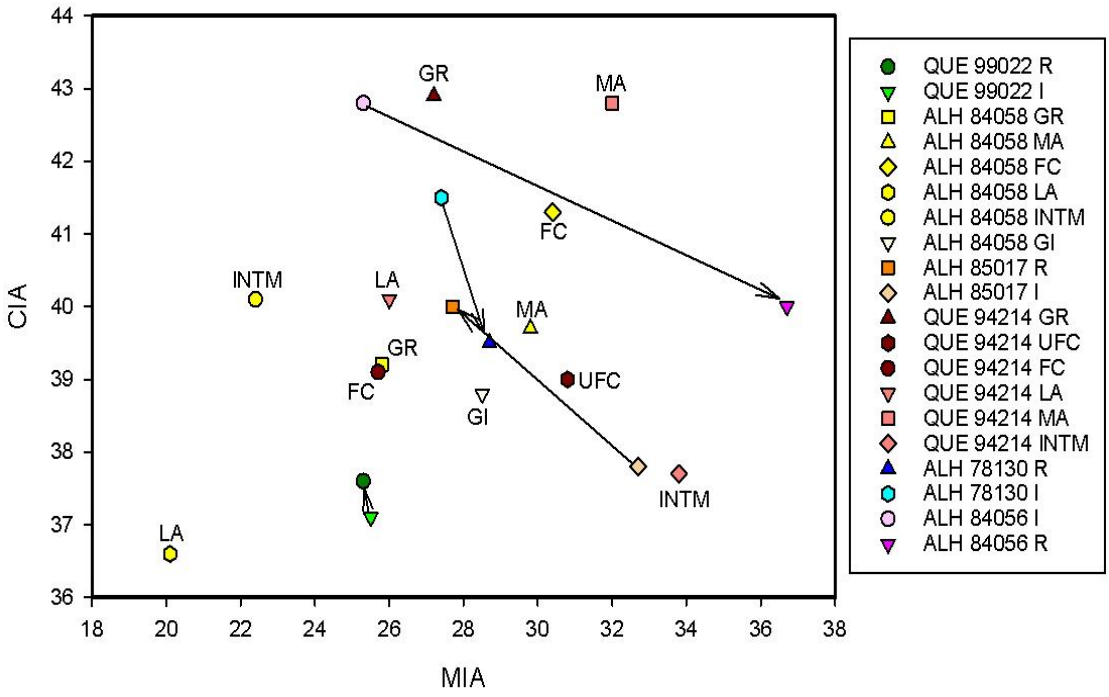

Fig. 6.1. MIA vs CIA calculated using the formulas of Babechuk et al. (2014) and Nebsitt and Young (1982).

Fig. 6.1 shows the resultant values of the indices for the chondrites measured. The two indices prove ineffective at separating more weathered meteorites from less weathered, and have no correlation with the weathering state. There is no clear difference between the rims and interiors and there is no consistent difference in the subsets of ALH 84058 and QUE 94214. As the CIA depends heavily on felsic breakdown, and the feldspars in all chondrites show very little alteration, the CIA is largely redundant. The MIA also fails to align with the chondrite state of alteration as it also depends on felsic breakdown and the Fe in chondrites is mostly in easily oxidised metal instead of the intended minerals, pyroxene and olivine.

The terrestrial weathering indices determine the levels of weathering using a formula that compares mobile and immobile elements (Nesbitt and Young 1982; Babechuk et al., 2014). These formulae have been adapted to represent the changes observed in the bulk subsets of both QUE 94214 and ALH 84058. The index has been made to represent the subsets, as they show consistent differences with weathering, unlike the larger bulk samples. Since the primary heterogeneity of the chondrites masks weathering effects the

larger bulk samples were not taken into consideration. Taking all these into account, the following Chondrite Weathering Index (C.W.I.) formula has been developed:

$$C.W.I. = 100 \times \frac{(Li + \left(\frac{Mg}{10000}\right) + Ba)}{(Li + \left(\frac{Mg}{10000}\right) + Ba + \left(\frac{Fe}{10000}\right) + Sc + V + Mn + Zr)}$$

All values in the formula are in equivalent measurements, in this case ppm and it compares the elements determined as immobile in the weathering chondrites (Li, Mg and Ba) with those determined as mobile (Fe, Sc, V, Mn and Zr). Elements such as Ni that show differences in only one samples subsets have not been included. Fe and Mg have been scaled to a similar magnitude to the trace elements to afford them equal weighting in the formula.

The results of this CWI, applied to meteorites in this study, are plotted in Fig 6.2. The index is able to separate out the most weathered subsets of ALH 84058 and QUE 94214 with the most weathered subsets, and general rim samples plotted considerably higher than the least weathered and interior samples. QUE 94214 fusion crust is a significant positive anomaly, and is reflecting the large amounts of Ba and the large depletion of Fe.

In previous chapters, QUE 94214 has been singled out as undergoing acidic weathering. As the CWI is based on the two samples that had subsets measured (QUE 94214 and ALH 84058) then it has to encompass both acidic and more neutral weathering. The elements used in the CWI are depleted in both subsets and so are common to the two alteration processes. Likewise, the Li, Mg and Ba are immobile in both sets.

This CWI separates out the bulk measurements from QUE 99022, ALH 78130, ALH 84056 and ALH 85017 to some extent, with QUE 99022 having higher values in both rim and interior than the less weathered meteorites (Fig. 6.3.). The CWI expresses that the ALH 85017 and ALH 84056 both have very similar low values. ALH 78130 rim has a

much higher value than the interior, which contradicts the petrography that identifies higher levels of weathering in the interior.

Alkali metals are usually more mobile than the transition metals in terrestrial weathering systems, e.g. Auippa et al., 2000; Wedpohl 1969, but plagioclase stability in solution is known to increase with decreasing temperatures (Gislason and Arnórsson 1993). Plagioclase has shown no signs of dissolution in any of the samples (chapter 3) and so whilst the Li and Ba are treated as immobile in the algorithm, this is a reflection of the plagioclase being resilient to weathering and not releasing these elements to the fluid. The CIW formula primarily reflects the mineralogical stability of the samples in a low temperature, low water environment, and secondarily, reflects the mobility of the elements released to system. Mg is also treated in the algorithm as an immobile element, but

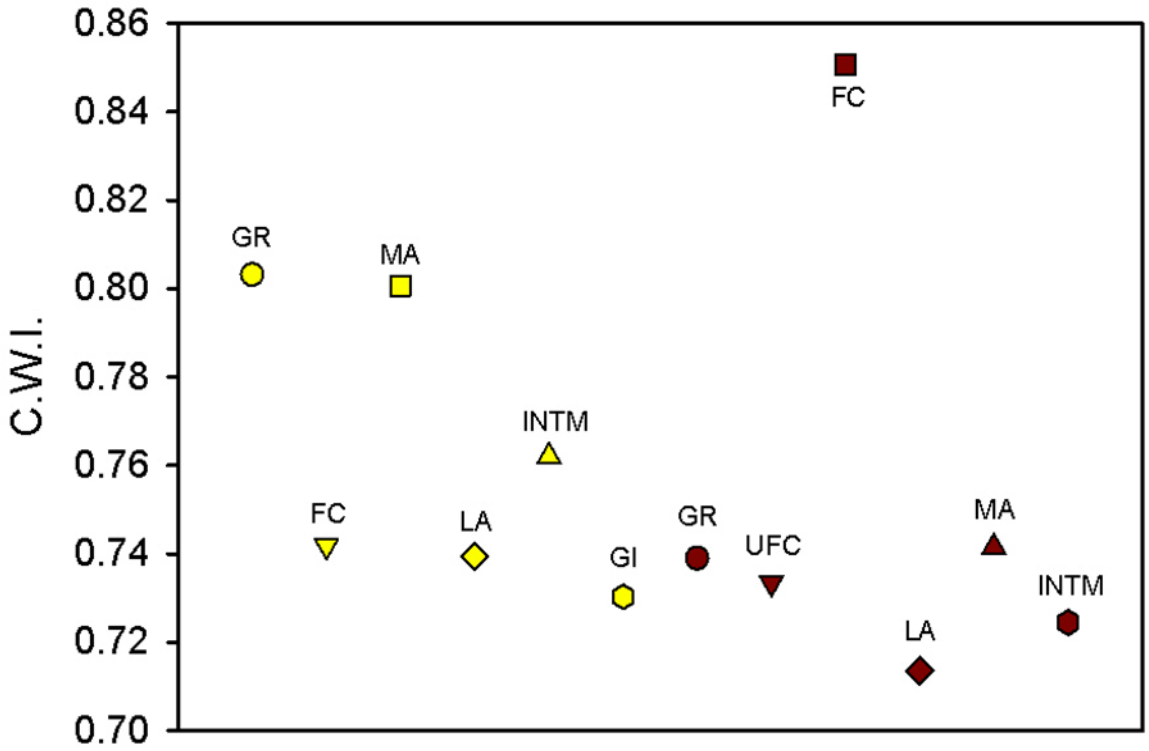

Fig. 6.2. C.W.I. applied to the subsets of ALH 84058 and QUE 94214. The C.W.I. separates out the most weathered subsets and the least altered.

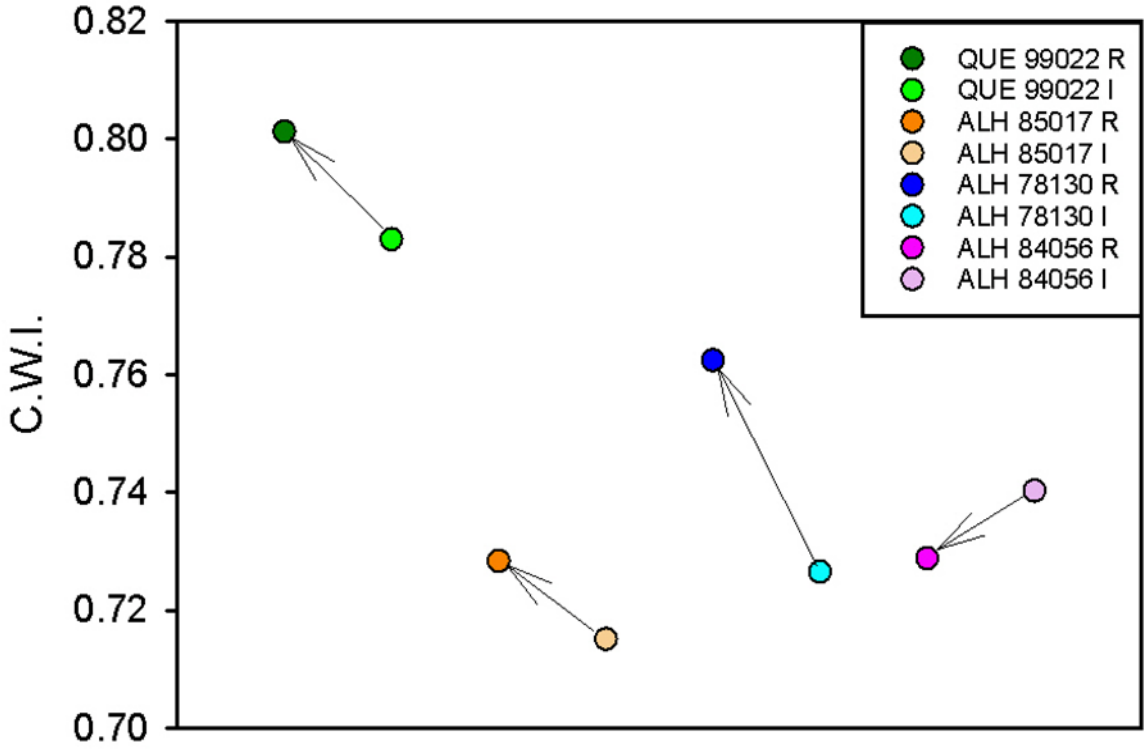

Fig. 6.3. The C.W.I. applied to the rims and interiors of meteorites studied. The two least weathered meteorites, ALH 84056 and ALH 85017 show some separation from the more weathered QUE 99022 and ALH 78130 R, but ALH 78130 I plots in a similar area.

resulting from a different mechanism than that which controls the mobility of Li and Ba. The main hosts of Mg (olivine and pyroxene) have maintained clear evidence for alteration throughout, so Mg immobility is most likely due to incorporation into and adsorption onto alteration products. Mg is a constituent of phyllosilicates (serpentine, smectites) that can form on alteration surfaces (Wilson et al., 2013), and it absorbs strongly onto clay minerals (Wedepohl 1969). However, Mg does not adsorb into Fe-oxides, and so it seems likely that a minor component of clay minerals are sequestering the Mg. These have been observed petrographically in several of the meteorites, and coupled with the observation of preservation bias in thin sections (detailed in Section 3.7.), Mg immobility is corroborating the presence of clay in these meteorites.

Overall, the CWI separates weathered subsets of meteorites from less weathered, and to a lesser degree and with some uncertainty distinguishes between bulk measurements of the most and the least weathered meteorites. Further refinement of the CWI is detailed in Section 6.5.

6.3. Relevance to Mars

The Acid Fog Model

The microenvironment described in QUE 94214 (see chapter 5) with low water/rock ratio, low temperature and low pH is very similar to the conditions assumed to exist on Mars in the acid fog model (Section 1.9.; Banin et al., 1979). The rocks on Mars thereby will undergo a transition from initial acidic conditions towards more alkaline as dissolution of silicates neutralizes the acid (Tosca et al. 2004; Zolotov and Mironenko 2007). This transition from acidic to alkaline assumes a constant supply of liquid water for the dissolution to continue. Whilst the terrestrial residence time and the burial history QUE 94214 is unknown, other meteorites collected at a similar time from Queen Alexandra Mountains have measured terrestrial residence ages of <80 kyr (Benoit and Sears 2000).

Unless the meteorite is collected shortly after its fall it is likely to be able to provide insights into weathering durations much longer than standard experimental studies.

The findings from QUE 94214 sulphide weathering show the vastly increased rate of weathering in low pH environments, with increased silicate weathering and increased mobility of trace elements. It also has caused the weathering of feldspars, which is not observed in any other meteorite. The order of weatherability in the low pH environment appears the same as the more neutral, oxidising environment (kamacite > taenite > troilite > olivine > Ca-diopside > low Ca-pyroxene > plagioclase > phosphate > chromite) but the proportions of weathering in the different minerals are not the same. The ratio of Fe-Ni metal: silicate weathering is significantly lower, with more significant silicate weathering for a similar amount of Fe-Ni oxidation, as is present in other meteorites. The trace element additions and subtractions are significantly different, with enhanced mobility of Co, Ni, Mg and Mn.

The uptake and loss of trace element are clear in the spatially resolved data, but are significantly less clear in bulk data. This is likely due to the small amounts of water involved in the interaction, with little flow through and much stagnation. Water to rock ratios thereby evolve from very high at initial contact to intermediate or lower W/R as more rock dissolves into the fluid. With the fluid being stagnant in the pore and fracture spaces a mechanism for removal lacks and the elements remain in the system. Furthermore, weathering is slowed as the fluid reaches equilibrium with the weathering mineral edges, and seasonal temperature changes or burial may cause freezing. Such a spatially restrictive pattern of trace element movement is averaged by bulk data, which is why many of the spatially resolved observations do not appear in the bulk data.

Petrologically informed locations of increased sulphide breakdown on Mars

Petrology is the key to understanding why low pH weathering is only present in QUE 94214. Whilst a difference in weathering pattern could be driven by changing water/rock ratios, the exact water/rock ratios are not known for these meteorites. The data in Chapters 3 and 4 identified that troilite has preferentially altered because of shock-metamorphism induced microfractures that pervade the crystals, and inclusions of more easily weathered Fe-Ni metals have allowed water to access the inner crystal which has more fresh surfaces. A homogenous crystal can only alter centripetally (Delvigne 2001) and, as is often the case, in low water/rock environments (Lee and Bland 2003) can be coated with a protective layer of Fe-oxyhydroxides that limits further weathering (Lee et al., 2006). The polycrystalline texture of the troilite in QUE 94214 allows preferential weathering that in turn creates the acidic environment as detailed in Chapter 3. The formation of this texture is, therefore, important for the creation of acidic environments.

Sulphides have been identified in a number of places on Mars, both on the present day surface by rovers and in martian meteorites studied on Earth (Burns and Fisher 1990; Greenwood et al., 1997; Rochette et al., 2001) and so the question is whether there are locations on Mars where sufficient shock pressure can be reached to create the shock textures observed in the chondrites studied here.

As detailed in Section 3.7., the polycrystalline texture is a shock produced feature which requires a shock pressure of 35–60 GPa (Barber and Scott 2006). High shock pressures are recorded in the martian meteorites resulting from their ejection from Mars (e.g. Nyquist et al., 2001; Beck et al., 2004; Treiman 2005; Fritz et al., 2005). A launch window of 15-45 GPa exists for the shergottites (Nyquist et al., 2001) and so many of the meteorites have surpassed the requisite pressure to re-order the sulphides to this structure. The prevalent sulphide species found in martian meteorites is pyrrhotite, which is also known to form polycrystalline textures at similar shock pressures to troilite (Rochette et al., 2003;

Louzada et al., 2010) and is hypothesised to exist on large parts of the martian surface (Louzada et al., 2010).

Polycrystalline pyrrhotite is likely to occur in craters, where shock events have had sufficient energy for the texture to form (French 1998) and has been hypothesised to exist in several southern martian craters by Rochette et al. (2003). It has been experimentally theorised to exist in martian meteorites by Rochette et al. (2003) and Louzada et al. (2007), and has been directly observed in ALH 84001 by McKay et al. (1996) and Barber and Scott (2006) and in NWA 7533 by Lorand et al. (2015).

Crater formation on Mars is often linked to hydrothermal activity (Newsom 1980; Rathburn et al., 2002; Abramov and Kring 2005; Changela and Bridges 2010; Schwenzer et al., 2012). Impact-generated hydrothermal and hydrous activity can be long or very short lived, depending on the combination of crater size (as proxy for the deposited heat) and surface temperature (e.g., Abramov and Kring 2005, Schwenzer et al. 2012). Thus, the locations where the polycrystalline texture is expected are also the most likely area of Mars to interact with fluids. Further to this, many craters on Mars have been subsequently infilled by lakes (e.g. Newsom et al. 1996, Goudge et al. 2015). The consequence of this is that the crater floors which have experienced high levels of shock and fluid interaction are also the most vulnerable to alteration through sulphide acidification. Further to this, the crater floors are also highly likely to contain the features described in Section 3.7. (fracturing of silicates, formation of melt veins) which increase weatherability and so enhanced silicate breakdown can be expected in the crater floors.

Meteoritic input in martian soils

Meteorites are also thought to accumulate on Mars in significant quantity, as potential survivability of the meteorites could be billions of years (Bland et al., 2001). The low rate of weathering could create large accumulations of chondritic material on the martian

surface (Boslough, 1988). There have been many estimates of meteoritic content in martian soil, with estimates ranging from 0–40 % (Clark and Baird 1979; Morris et al., 2000). The highest estimate (40% - Clark and Baird 1979) was calculated on the basis of Viking soil analysis. More recent analysis from the Mars Exploration Rovers APXS have resulted in an estimated input of 1–3 % contamination of meteoritic debris in the analysed soil (Yen et al., 2006) and the source of this debris is thought to be micrometeorites, interplanetary dust or remains of impactors (Yen et al., 2006). The flux of meteorites to the surface of Mars brings a large excess of nickel which is the most common element used to constrain meteoritic input (Clark and Baird 1979; Yen and Murray 1998; Yen et al., 2006). Unambiguous evidence of meteoritic input has been found by the MER rovers, both of which have discovered macrometeorites on the surface of Mars, including a large IAB iron meteorite (Fig. 6.4.). Opportunity and Spirit have found and analysed meteorites (Yen et al., 2006), and the Curiosity Rover (Chappelow et al., 2016; Ashley and Golombek 2016), that show clear evidence of weathering and are, amongst other indicators, used to understand the atmospheric history of Mars.

Fig. 6.4. IAB meteorite, "Meridiani Planum" discovered on Mars by the Opportunity rover (Image credit NASA/JPL/Cornell).

How these meteorites interact with the martian soil is largely theoretical. Yen et al. (2006) states a gap of knowledge in the behaviour of nickel solubility under martian conditions, where acid-sulphate weathering dominates the weathering processes. The data from QUE 94214 can contribute to this. Under acidic conditions generated from the weathering of sulphides in the analogue conditions of Antarctica, nickel has an increased mobility to the point of being removed entirely from the meteorite. This means that an addition of nickel to the martian soil, through aqueous interaction with meteoritic debris, is expected in acidic environments. The occurrence of Fe-oxide nodules rich in Ni in Meridiani outcrops (Yen et al., 2006) are consistent with alteration minerals common to the breakdown of chondrites. This is accompanied by the increased mobility of Co. Increased removal of Mn compared to higher pH systems suggests that martian soils with meteoritic input undergoing acidic weathering should also expect higher mobility of Mn.

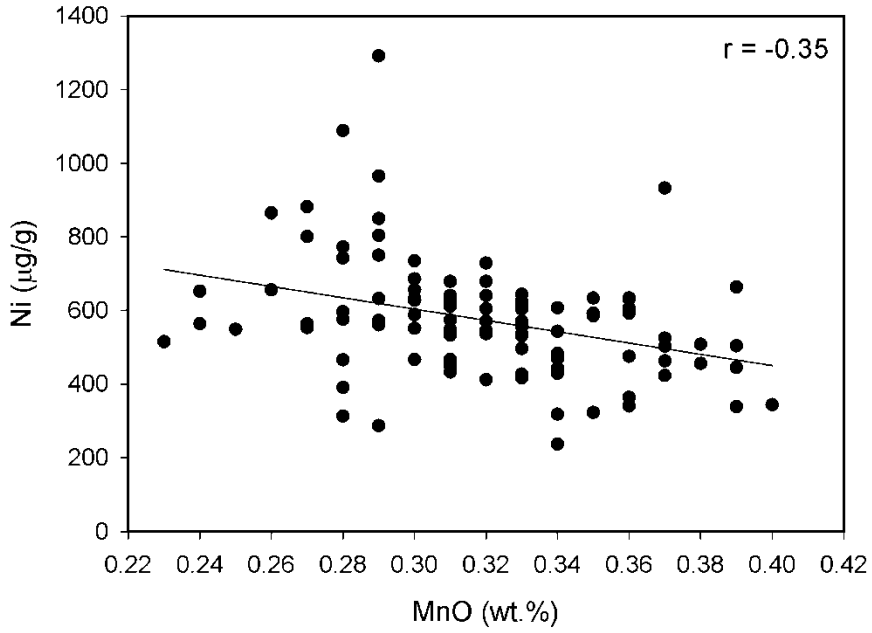

Fig. 6.5. MnO vs Ni of soils measured by APXS on the Mars Exploration Rovers shows a negative correlation (data taken from Yen et al., 2006).

Using data from Yen et al. (2006; and references within), the Mn compositions of martian soils measured in Gusev crater and Meridiani Planum are compared to Ni content in Fig 6.5. High Ni content is frequently attributed to extra-terrestrial input, since a high Ni martian source has not yet been measured that would account for high Ni contents found in soil. In Yen et al. (2006), Ni content of soils is used as a tool to estimate the percentage addition of meteoritic input, with values over 600 ppm considered to indicate significant input. To test the previous statement that acidic weathering of ordinary chondrites should result in higher Mn mobility, the Mn and Ni content are compared in soil measured by APXS. There is a weak negative correlation observed between Mn and Ni, with high Ni content correlating with low Mn values. This may indicate that similar processes occur in the martian soils to those measured as in the L chondrites studied here, and, therefore, should be expected to be more prevalent in older soils since these will have a greater meteoritic contribution.

A simple mass balance calculation has been used to test the theoretical maximum of acid that could be produced through the weathering of a meteoritic component in martian soil. Using the equations of Belzile et al. (2004), troilite dissolution is given as:

$$FeS + 8Fe^{3+} + 4H_2O => 9Fe^{2+} + SO_4^{2-} + 8H^+$$

This assumes some oxidation from water and Fe^{3+}. The calculation uses:

1) the measured average troilite abundance of QUE 94214 (7.25 %; Chapter 3; Table 3.2) with a theoretical sample mass of 1 kg, yielding 72.5 g/kg of troilite. Using the formula above and converting to moles, a total oxidation of the troilite would result in 6.60 moles of H^+.

2) the 2 % meteoritic contribution to the martian soil hypothesised by Yen et al. (2006), 1 kg of martian soil could contain 0.132 moles of H^+ resultant from the oxidation of extra-martian troilite alone.

3) the upper estimate of meteoritic contribution of 40 % to martian soil from Clarke and Baird (1979), 2.64 moles of H^+ per 1 kg of soil could be produced from oxidising troilite.

To see how this H^+ would interact with the martian soil, a simplified composition of martian soil that is 100 % olivine was used to calculate how much could be dissolved from the sulphuric acid produced solely from sulphide dissolution. Olivine is used as it is the mineral that has been observed to have the largest contribution to neutralisation in the samples studied, and is also present in large amounts in the martian soil (22% Fe-forsterite in Rocknest soil (Vaniman et al., 2014)). The equation for the dissolution is as follows:

$$Mg_2SiO_4 + 4H^+ => 2Mg^{2+} + Si(OH)_4$$

Every mole of olivine dissolved requires four moles of H^+. The resulting H^+ created from the above scenarios results in:

1) 23.2 wt.% of total olivine dissolved
2) 0.46 wt.% of total olivine dissolved
3) 9.93 wt.% of total olivine dissolved

Therefore the amount of acid produced in the breakdown of all troilite in QUE 94214 (scenario 1) would result in significant dissolution of the rock, but alone would not be sufficient to dissolve the meteorite. The upper estimate of meteoritic input in martian soil determined from Viking data (scenario 3) shows that the addition of troilite would be sufficient to cause significant dissolution of the olivine at the surface of Mars.

This calculation has been done using data from L chondrites, but meteoritic input would also involve other meteorite groups. As the ordinary chondrites dominate the meteorite population that lands on Earth, it is likely that this is also true of Mars (Yen et al., 2006). As H chondrites are the most common meteorite fall of the ordinary chondrite group, and H chondrites contain on average 7 % troilite (the same as L chondrites: Grady et al., 2014), these two meteorite groups that dominate the influx of meteoritic material are the best meteorites to consider.

As martian meteorites contain <0.6 wt.% sulphide (Mars meteorite compendium), which is less than in case 2) above, the effect of acidic weathering from complete dissolution of these sulphides alone would be small and would likely only affect silicates in direct contact with the sulphides. This acid would, however, be neutralised in the same way as in chondritic material with the dissolution of olivine and pyroxene. To have a significant effect on the surficial weathering of Mars, other sources need to be considered. Indeed, acid weathering from volcanic input is discussed widely for Martian environments.

Acid weathering on Mars – volcanic input

In contrast to the above described local processes, the most important aspect of acid-rock interaction on Mars might stem from a global process of volcanic input into the surface.

There are two pathways: acidic outgassing and deposition of the gases from the atmosphere as acid rain, and boiling of subsurface fluids, which can create acidic vapor-derived pore fluids. For Mars, there is a conundrum in observations: Martian soil and rocks visible from orbit and investigated by rovers contain significant amounts of olivine (e.g., Carr and Head 2010; Ody et al. 2013; Vaniman et al. 2014; Achilles et al. 2016, Ehlmann et al. 2016), which indicates low weathering rates and thus limits the likelihood of extended acid alteration. On the other hand, the detection of jarosite (e.g., Christensen et al. 2004; Rampe et al. 2016) – an indicator mineral for acid alteration, but also dry conditions after its formation (Elwood Madden et al. 2004) – has sparked a long-standing debate about the extent of acid weathering on Mars. Central to the claims of acid-weathered Martian rocks are silica and jarosite findings and their terrestrial analogues (e.g., Fernanez-Remolar et al. 2003; Morris et al. 2005; McAdam et al. 2008; Morris et al. 2016, Kaplan et al. 2016), but studies of acid alteration – modelling and experimental – have demonstrated that basaltic rock compositions are an efficient buffer (e.g., Elwood Madden et al. 2004; Tosca et al. 2004; McAdam et al. 2008, Schwenzer et al. 2016). The results in this study allow further constraints to be put on this issue.

This study demonstrates the buffer capabilities of olivine-pyroxene-feldspar systems under cold, low water to rock ration conditions. For example, the extent of acid alteration in QUE 94214 is seen to be neutralised within 2 mm of the weathering sulphide grain (Fig. 4.8).

The calculations above (p. 263) show that to totally weather a pure olivine target, >7.25 % sulphide is required (the highest calculation run). This upper estimate of sulphide contribution results in 6.62 moles of acid being added to the 1 kg of rock, which is significantly less than the estimate of Craddock and Greeley who estimated an addition of a 120 cm global layer of sulphuric acid by volcanic addition. To directly compare it to the calculations above on page 265, if this interacted with the top 1 kg of martian rock (which equates to 14.92x14.92x14.92 cm cube of olivine, density 3.32 g/cm) then this would be

148 moles of H_2SO_4. The amount of pure olivine needed to neutralise the acid can be calculated. Using the 148 moles of H_2SO_4 above, 74 moles of olivine would be required to neutralise it. This equates to a depth of 44.48 cm.

The upper limit of sulphide weathered (7.25 %) produced 6.62 moles of H_2SO_4 being produced, which in the dimensions of a 1 kg cube of olivine rock would be equivalent to a layer 5.37 cm. As the amount of H_2SO_4 estimated from volcanic exhalation is so much larger than is represented by sulphides, the weathering processes in the martian soil are likely to be far more maturated than in the partially weathered chondrites, but the textures observed in QUE 94214 show that when acid interacts with olivines and pyroxenes on a natural timescale neutralization distances are short and effects can be local. This is in accordance with the localized findings of jarosite, e.g., at Gale Crater (Rampe et al. 2016).

As the amount of sulphuric acid deposited on Mars from volcanic emission has varied throughout time (Fig. 6.6), so too will have the acidic weathering. The 120 cm layer calculated by Craddock and Greeley has formed between the Middle Noachian (4.4. Ga) to the Late Amazonian (0.7 Ga), with the greatest deposition before the Early Amazonian (Fig. 6.6). The 5.37 cm layer of acid that could be produced by a total dissolution of 7.25 % sulphides is equivalent to the period of Mid-Amazonian to Late Amazonian Mars (Fig. 6.6) and so features similar to those formed in QUE 94214 may be found in rocks altered in this time period.

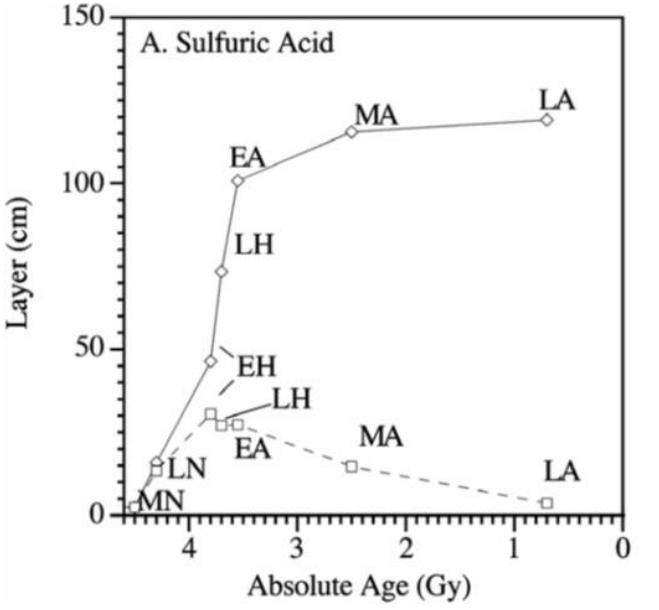

Fig. 6.6. Diagram from Craddock and Greeley (2009) showing a calculated volcanic output of sulphuric acid over time. The solid line indicates cumulative H_2SO_4; the dotted indicates production in each time period.

6.4. CONCLUSIONS

The original aim was to categorise weathering effect in chondrites in order to gain an understanding of alteration progression using bulk chemistry (both major and minor elements), mineralogy, spatially resolved chemical data, magnetic data and oxygen isotopes. A further aim was to combine the different data sets together to find any links, and then characterise the links. These analyses have then been extrapolated to areas of Mars that contain features identified here as important to weathering patterns and to discuss the potential for alteration from acid weathering. Below is a summary of the findings.

ARTEFACTS (CHAPTER 3)

- Thick sections preserve a wider range of alteration products than thin sections, and are more susceptible to museum weathering, with continued oxidation of native metals occurring after curation.
- The delicate minerals such as clays and sulphates are removed during the thin section making process.

MINERALOGICAL CONTROLS ON WEATHERING RATES (CHAPTER 3)

- The order of mineral weatherability (i.e., the ease with which the mineral is altered by weathering) in all meteorites studied is: Kamacite > Taenite > Troilite > Olivine > Pyroxene > Plagioclase > Chromite > Phosphates.
- In all minerals studied, an increase of chemical heterogeneity within the minerals increased their vulnerability to weathering.
- The shock grade of a meteorite directly affects its weatherability. Higher shock grades create more vulnerable meteorites through: 1) Creating melt veins with vulnerable high surface area: volume Fe-Ni melt spherules which, once weathered out, leave behind a porous network for water to penetrate into the meteorite. 2) Re-ordering the Fe-Ni metal grains to more vulnerable textures, i.e., metal fizzes. 3) Planar fractures in olivine crystals create more fresh surfaces to alter as fluids

penetrate preferentially creating a deposit of rust (Fe-oxyhydroxide nano-particles) and a disproportionate amount of vein in olivine crystals. 4) Re-crystallisation of troilite to polycrystalline troilite makes the troilite more susceptible to breakdown by virtue of more fresh surfaces being available to contact with fluid. 5) Fizzed troilite-metal intergrowths have increased weatherability compared to homogenous troilite or metal. 6) General increase of fractures in samples which then are infilled with alteration veins. In all the above cases, increased silicate weathering is associated.

- The transformation of plagioclase to maskelynite renders the feldspar more resistant to weathering through the removal of crystal defects and fractures and homogenises the structure.

CHEMISTRY OF WEATHERING CHONDRITES (CHAPTER 4 + 5)

- Weathering environments in Antarctic chondrites are highly heterogeneous. Many chemical changes operate on a sub mm scale, with the liberation of elements to solution, and subsequent deposition, commonly occurring over less than 1 mm.
- Although many weathering effects are identified using the spatially resolved data, very few of these translate into bulk differences in the meteorites. The combination of primary heterogeneity of the chondrites and the heterogeneity of the weathering environments, results in very little bulk change directly attributable to weathering. The weathering systems of the L chondrites studied are largely closed and with very few bulk changes, even in the most weathered meteorites (restricted to Mn loss) but redistribution of primary elements on a mm scale is prevalent.
- Acidic weathering systems are generated from the breakdown of troilite which acidifies the altering fluid. This causes rapid breakdown of adjacent silicates and ferromagnesiam minerals are most heavily affected. This acidification of fluids enhances the mobility of elements released to solution, and inhibits the deposition

of Fe-oxyhydroxides. There is increased mobility of Mn, Ni, Co, Mg and Si in the meteorite that exhibits significant breakdown of troilite and silicate weathering compared to the other five meteorites which do not have extensive troilite and silicate alteration.

CLASSIFYING WEATHERING IN CHONDRITES

- Estimating the percentage area of the sample which is covered by rust has proven useful as a first assessment of weathering levels. However, if the amount of open fractures infilled with Fe-oxyhydroxides and alteration products exceeds 40 %, there will be 100 % coverage of rust, rendering the intermediate level of weathering as the upper limit for this technique (Chapter 3).
- Comparing the extent of alteration of the three most weatherable minerals (kamacite, taenite and troilite) provides a more accurate petrological quantification of weathering. However this is more time consuming, and might not be practical solely for curational purposes of a large sample set .
- The percentage of vein coverage is directly related to the percentage of kamacite, taenite and sulphide oxidation and so can represent the amount of oxidised areas, and is an effective way of assessing alteration state (Chapter 3).
- Increasing oxidation percentages directly relate to a loss in magnetic susceptibility and smaller $\delta^{17}O$ and $\delta^{18}O$.
- A chemical weathering index has been developed for L-chondrites representing ferromagnesian silicate breakdown:

$$C.W.I. = 100 \times \frac{\left(Li + \left(\frac{Mg}{10000}\right) + Ba\right)}{\left(Li + \left(\frac{Mg}{10000}\right) + Ba + \left(\frac{Fe}{10000}\right) + Sc + V + Mn + Zr\right)}$$

- Areas on Mars such as crater floors that have undergone significant shock pressures will be more susceptible to alteration because of the mineralogical features created by shock, which increase vulnerability to weathering. The creation of polycrystalline pyrrhotite at these locations speeds up the acidification of any altering fluid in the crater, which then enhances the breakup of surrounding silicates. Without the rapid breakdown facilitated by the polycrystalline texture, the fluid has more time to neutralise by altering the local silicates. The acidic fluids resultant from troilite breakdown increases mobility of Mn, Mg, Co and Ni and can remove these entirely from the rocks to be deposited elsewhere. The low water: rock ratios present on modern day Mars make the weathering environments incredibly restricted spatially and so the weathering is highly heterogeneous.
- Studied textures that result from breakdown of sulphides are spatially restricted to a cm scale. The extent of acid weathering does not translate into bulk measurements and petrological evidence of alteration is restricted to a maximum of 1 cm around altering sulphides. This suggests a significant amount of sulphide is needed to acidify a large area, such as a crater lake, more than the 14.5 wt% observed in QUE 94214, which is the meteorite with clearest evidence of acidic weathering.
- Meteoritic components in the martian soil should enrich the soil in Ni, Mn, Co and Mg in acidic conditions. These elements should be highly mobile and, therefore, should create an enriched soil that is more homogenous than a circum-neutral pH alteration environment. A circum-neutral pH and low water: rock ratio should result in heterogeneous weathering patterns because of shortened transport distances of Ni, Mn, Co and Mg and the localisation of weathering centres.
- The upper estimate of meteoritic contribution to martian soil results in a significant addition of troilite which, when weathered, produces enough H^+ to break down significant quantities of olivine during neutralisation.

- The sulphuric acid produced by total dissolution of sulphides in an L chondrite will produce a similar amount of acid as the martian time period between Mid-Amazonian to Late Amazonian.

6.5. FUTURE WORK

The work described above has highlighted the complexity of low water alteration environments and has derived processes from combining data from petrology, spatial and bulk chemical properties and physical properties, but many research areas still require further investigation. Potential future paths of investigation are detailed below.

- Antarctic weathering studies would greatly benefit from compositional measurements of the ice that surrounds weathering meteorites. To understand the extent to which the weathering systems are closed or open, composition of the ice directly surrounding an exhumed meteorite needs to be characterised (using ICP-MS analysis). This would allow an assessment of the exchange of elements between the environment and the meteorite.
- It is important to determine the extent to which halogen and sulphur has been added from volcanism and sea spray by characterising the composition of ice from several fields. If a comprehensive picture were built up of the interactions between volcanic emissions, icefields and then alteration of rock samples were built up, it could allow for identification of ancient volcanic activity in martian history. With the identification of past glacial activity now established in many places on Mars (Head et al., 2006; Head et al., 2010; Hubbard et al., 2011), the interaction between glaciers and volcanically derived volatiles could be a vital part of the redistribution of these volatiles. Understanding how a glacier enriched with volcanically derived materials would interact with underlying basalt could also be vital to geochemical processes active in post volcanic activity. To achieve these aims, samples of ice surrounding meteorites on recovery should be taken. Fields to collect samples from

are preferably: snow/ice from Mt Erebus, Allan Hills, Yamato, Meteorite Hill, Queen Alexandra Range, Pecora Escarpment. As seen in Fig. 1.1., these fields represent an increasing distance from the sea, a major source of halogen input, and would therefore allow discrimination of sea input from volcanic input. Yamato icefield is close to the sea, but with no volcano, and so would allow a baseline of halogen contamination from the sea to be established. Halogen content of collected ice samples can then be compared to the halogen content of adjacent meteorites (preferably with several measurements of different depths into meteorite) and the level of interaction could be assessed.

- Study of the ice compositions in several fields may also help to answer inconsistent evaporite formation across different icefields (see Chapter 1). The composition of the icefields may be the contributing factor to some producing so many more evaporite encrusted meteorites than other adjacent fields. In addition, a useful and potentially vital clue would be the environmental conditions of the icefields, i.e., how much melt and re-freeze occurs on an annual basis. This could be measured by an embedded humidity sensor left for a year.
- The evolution of fluids in altering meteorites is currently poorly constrained and has been extrapolated in this project by using relative mobilities of elements. To further this, long term experimental alteration of meteorites with very small water/rock ratios would allow an accurate picture of how these fluids evolve. It would be beneficial to characterise the ice first, as this would indicate a water/rock ratio and how much water is flowing through the system, and to what extent the water is stagnant within the meteorite. It would also inform the starting composition of the natural fluid in Antarctica. To ascertain fluid content in micro-environments, a flat surface of a meteorite should be treated with pH neutral water and left for at least a year (based on work by Lee and Bland 2006) and preferably in a fluctuating temperature below and above zero degrees. After a year, careful

extraction of small quantities of water from different areas in the meteorite would help determine how linked the pore spaces are and to what extent the micro-environments exist. Based on petrological observations made in this study, it would also be greatly beneficial to do this on a variety of samples with the following features: melt veins, metal deficient (basalt), shocked sulphides, unshocked sulphides, shocked silicates (fractured with no melt).

- The C.W.I needs testing by increasing the sample set to ca. 50 and calculating the index value. This requires ICP-MS analysis of multiple ordinary chondrites to create a robust system. The recommended number of meteorites to make a robust scale would be preferable around 50, with a cursory petrological classification to measure area of meteorite covered by rust and percentage oxidised metals and sulphides.
- More investigation into troilite textures under varying shock pressures would be beneficial, since this area has not been extensively explored. Ideally laboratory simulations would lead to the output of a chart of sulphide textures with increasing shock, which would be of benefit to studies of weathering and of chondrite origins. The interaction of the troilite with metals and silicates under varying shock conditions should also be considered because textures such as the troilite/metal fizzes are very important to weathering patterns.

BIBLIOGRAPHY

Achilles C., Vaniman D., Blake D., Bristow T., Rampe E., Ming D., Chipera S., Morris R., Morrison S., and Downs R. (2016) Mineralogy of Eolian Sands at Gale Crater.

Aiuppa A., Allard P., D'Alessandro W., Michel A., Parello F., Treuil M., and Valenza M. (2000) Mobility and fluxes of major, minor and trace metals during basalt weathering and groundwater transport at Mt. Etna volcano (Sicily). Geochimica et Cosmochimica Acta 64(11), 1827-1841.

Al-Kathiri A., Hofmann B., Jull A., and Gnos E. (2005) Weathering of meteorites from Oman: Correlation of chemical and mineralogical weathering proxies with 14C terrestrial ages and the influence of soil chemistry. Meteoritics & Planetary Science 40(8), 1215-1239.

André M. F., Hall K., and Comte V. (2004) Optical rock properties and weathering processes in polar environments (with special reference to Antarctica). Polar Geography 28(1), 43-62.

Arden J. W. (1983) Distribution of lead and thallium in the matrix of the Allende meteorite and the extent of terrestrial lead contamination in chondrites. Earth and Planetary Science Letters 62(3), 395-406.

Arvidson R., Poulet F., Morris R., Bibring J. P., Bell J., Squyres S., Christensen P., Bellucci G., Gondet B., and Ehlmann B. (2006) Nature and origin of the hematite-bearing plains of Terra Meridiani based on analyses of orbital and Mars Exploration Rover data sets. Journal of Geophysical Research: Planets 111(E12).

Arvidson R., Squyres S., Gellert R., and Mittlefehldt D. (2015) Recent Results from the Opportunity Rover's Exploration of Endeavour Crater, Mars. In Lunar and Planetary Institute Science Conference Abstracts, pp. 1400.

Arvidson R. E., Gooding J. L., and Moore H. J. (1989) The Martian surface as imaged, sampled, and analyzed by the Viking landers. Reviews of Geophysics 27(1), 39-60.

Babechuk M. G., Widdowson M., and Kamber B. S. (2014) Quantifying chemical weathering intensity and trace element release from two contrasting basalt profiles, Deccan Traps, India. Chemical Geology 363, 56-75.

Banin A., Han F. X., Kan I., and Cicelsky A. (1997) Acidic volatiles and the Mars Soil. Journal of Geophysical Research E: Planets 102(E6), 13341-13356.

Barber D. J. and Scott E. R. D. (2006) Shock and thermal history of Martian meteorite Allan Hills 84001 from transmission electron microscopy. Meteoritics & Planetary Science 41(4), 643-662.

Bayly P. and Stillwell F. (1923) The Adelie Land meteorite. Australasian Antarctic Expedition, 1911–14. Scientific Reports.

Beck P., Gillet P., Gautron L., Daniel I., and El Goresy A. (2004) A new natural high-pressure (Na,Ca)-hexaluminosilicate [(CaxNa1−x)Al3+xSi3−xO11] in shocked Martian meteorites. Earth and Planetary Science Letters 219(1–2), 1-12.

Bennett M. E. and McSween H. Y. (1996) Shock features in iron-nickel metal and troilite of L-group ordinary chondrites. Meteoritics & Planetary Science 31(2), 255-264.

Benoit P. H. and Sears D. W. (2000) The Natural Thermoluminescence Survey of Antarctic Meteorites: Ordinary Chondrites at the Grosvenor Mountains, MacAlpine Hills, Pecora Escarpment and Queen Alexandra Range, and New Data New Data for the Elephant Moraine, Ice Fields. LPI Contributions 997, 11.

Benoit P. H. and Sears D. W. G. (1999) Accumulation mechanisms and the weathering of Antarctic equilibrated ordinary chondrites. Journal of Geophysical Research E: Planets 104(E6), 14159-14168.

Bertelsen P., Goetz W., Madsen M., Kinch K., Hviid S., Knudsen J., Gunnlaugsson H. P., Merrison J., Nørnberg P., and Squyres S. (2004) Magnetic properties experiments on the mars exploration rover spirit at Gusev Crater. Science 305(5685), 827-829.

Bintanja R. and Van Den Broeke M. R. (1995) The climate sensitivity of Antarctic blue-ice areas. Annals of Glaciology 21, 157-161.

Bish D. L., Blake D., Vaniman D., Chipera S., Morris R., Ming D., Treiman A., Sarrazin P., Morrison S., and Downs R. (2013) X-ray diffraction results from Mars Science Laboratory: Mineralogy of Rocknest at Gale crater. Science 341(6153), 1238932.

Biswas S., Ngo H. T., and Lipschutz M. E. (1980) Trace element contents of selected Antarctic meteorites. I. Weathering effects and ALH A77005, A77257, A77278 and A77299. Zeitschrift für Naturforschung A 35(2), 191-196.

Bladh K. W. (1982) The formation of goethite, jarosite, and alunite during the weathering of sulfide-bearing felsic rocks. Economic Geology 77(1), 176-184.

Bland P., Berry F., Smith T., Skinner S., and Pillinger C. (1996) The flux of meteorites to the Earth and weathering in hot desert ordinary chondrite finds. Geochimica et Cosmochimica Acta 60(11), 2053-2059.

Bland P., Lee M., Sexton A., Franchi I., Fallick A., Miller M., Cadogan J., Berry F., and Pillinger C. (2000) Aqueous alteration without a pronounced oxygen-isotopic shift: Implications for the asteroidal processing of chondritic materials. Meteoritics & Planetary Science 35(6), 1387-1395.

Bland P., Zolensky M., Benedix G., and Sephton M. (2006) Weathering of chondritic meteorites. Meteorites and the early solar system II, 853-867.

Bland P. A. (2001) Quantification of meteorite infall rates from accumulations in deserts, and meteorite accumulations on Mars. In Accretion of extraterrestrial matter throughout Earth's history, pp. 267-303. Springer.

Bland P. A. (2006) Terrestrial weathering rates defined by extraterrestrial materials. Journal of Geochemical Exploration 88(1–3), 257-261.

Boggild C. E., Winther J. G., Sand K., and Elvehoy H. (1995) Sub-surface melting in blue-ice fields in Dronning Maud Land, Antarctica: observations and modelling. Annals of Glaciology 21, 162-168.

Boslough M. (1988) Evidence for meteoritic enrichment of the Martian regolith. In Lunar and Planetary Science Conference, pp. 120.

Boudreau A. E. and McCallum I. (1990) Low temperature alteration of REE-rich chlorapatite from the Stillwater Complex, Montana. American Mineralogist 75(5-6), 687-693.

Boynton W. V., Ming D. W., Kounaves S. P., Young S. M. M., Arvidson R. E., Hecht M. H., Hoffman J., Niles P. B., Hamara D. K., Quinn R. C., Smith P. H., Sutter B., Catling D. C., and Morris R. V. (2009) Evidence for Calcium Carbonate at the Mars Phoenix Landing Site. Science 325(5936), 61-64.

Bridges J. C., Catling D., Saxton J., Swindle T., Lyon I., and Grady M. (2001) Alteration assemblages in martian meteorites: implications for near-surface processes. In Chronology and evolution of Mars, pp. 365-392. Springer.

Bridges J. C., Schwenzer S. P., Leveille R., Westall F., Wiens R. C., Mangold N., Bristow T., Edwards P., and Berger G. (2015) Diagenesis and clay mineral formation at Gale Crater, Mars. Journal of Geophysical Research: Planets 120(1), 2014JE004757.

Buchwald V. (1990) On the difference between weathering products on Antarctic and non-Antarctic meteorites. In Differences between Antarctic and non-Antarctic meteorites, pp. 24.

Buchwald V. F. and Clarke Jr R. S. (1989) Corrosion of Fe-Ni alloys by Cl-containing akaganéite (beta-FeOOH): The Antarctic meteorite case. American Mineralogist 74, 656-667.

Burns R. G., Burbine T. H., Fisher D. S., and Binzel R. P. (1995) Weathering in Antarctic H and CR chondrites: quantitative analysis through Mossbauer spectroscopy. Meteoritics 30(6), 625-633.

Burns R. G. and Fisher D. S. (1990) Evolution of sulfide mineralization on Mars. Journal of Geophysical Research: Solid Earth 95(B9), 14169-14173.

Cassidy W. (1983) The remarkably low surface density of meteorites at Allan Hills and implications in this for climate change. In Antarctic earth science, p. 623-625, pp. 623-625.

Cassidy W., Harvey R., Schutt J., Delisle G., and Yanai K. (1992) The meteorite collection sites of Antarctica. Meteoritics 27(5), 490-525.

Changela H. and Bridges J. (2010) Alteration assemblages in the nakhlites: Variation with depth on Mars. Meteoritics & Planetary Science 45(12), 1847-1867.

Chen M., Li H., GORESY A. E., Liu J., and Xie X. (2006) Fracture-related intracrystalline transformation of olivine to ringwoodite in the shocked Sixiangkou meteorite. Meteoritics & Planetary Science 41(5), 731-737.

Chevrier V., Mathé P. E., Rochette P., and Gunnlaugsson H. P. (2006) Magnetic study of an Antarctic weathering profile on basalt: Implications for recent weathering on Mars. Earth and Planetary Science Letters 244(3–4), 501-514.

Christensen P., Ruff S., Fergason R., Knudson A., Anwar S., Arvidson R., Bandfield J., Blaney D., Budney C., and Calvin W. (2004a) Initial results from the Mini-TES experiment in Gusev Crater from the Spirit Rover. Science 305(5685), 837-842.

Christensen P., Wyatt M., Glotch T., Rogers A., Anwar S., Arvidson R., Bandfield J., Blaney D., Budney C., and Calvin W. (2004b) Mineralogy at Meridiani Planum from the Mini-TES experiment on the Opportunity Rover. Science 306(5702), 1733-1739.

Clark B. C. and Baird A. (1979) Is the Martian lithosphere sulfur rich? Journal of Geophysical Research: Solid Earth 84(B14), 8395-8403.

Clayton R. N., Mayeda T. K., Goswami J., and Olsen E. J. (1991) Oxygen isotope studies of ordinary chondrites. Geochimica et Cosmochimica Acta 55(8), 2317-2337.

Clayton R. N., Onuma N., and Mayeda T. K. (1976) A classification of meteorites based on oxygen isotopes. Earth and Planetary Science Letters 30(1), 10-18.

Craddock R. A. and Greeley R. (2009) Minimum estimates of the amount and timing of gases released into the martian atmosphere from volcanic eruptions. Icarus 204(2), 512-526.

Cresswell R. G., Miura Y., Beukens R. P., and Rucklidge J. C. (1993) 14C terrestrial ages of nine Antarctic meteorites using CO and CO2 temperature extractions. Antarctic Meteorite Research 6, 381.

Crozaz G., Floss C., and Wadhwa M. (2003) Chemical alteration and REE mobilization in meteorites from hot and cold deserts. Geochimica et Cosmochimica Acta 67(24), 4727-4741.

Cull S. C., Arvidson R. E., Catalano J. G., Ming D. W., Morris R. V., Mellon M. T., and Lemmon M. (2010) Concentrated perchlorate at the Mars Phoenix landing site: Evidence for thin film liquid water on Mars. Geophysical Research Letters 37(22), L22203.

Das H., Zonderhuis J., and Marel H. (1971) Scandium in rocks, minerals and sediments and its relations to iron and aluminium. Contributions to Mineralogy and Petrology 32(3), 231-244.

Delvigne J. E. (2001) Atlas of Micromorphology of Mineral Alteration and Weathering. The Canadian Mineralogist.

Dennison J. E. and Lipschutz M. E. (1987) Chemical studies of H chondrites. II: Weathering effects in the Victoria Land, Antarctic population and comparison of two Antarctic populations with non-Antarctic falls. Geochimica et Cosmochimica Acta 51(3), 741-754.

Dorn R. I. (2009) The Rock Varnish Revolution: New Insights from Microlaminations and the Contributions of Tanzhuo Liu. Geography Compass 3(5), 1804-1823.

Dorn R. I., Krinsley D. H., Langworthy K. A., Ditto J., and Thompson T. J. (2013) The influence of mineral detritus on rock varnish formation. Aeolian Research.

Dreibus G., Wänke H., and Schultz L. (1986) Mysterious iodine-overabundance in Antarctic meteorites. In International Workshop on Antarctic Meteorites, pp. 34-36.

Ebihara M., Shinonaga T., Nakahara H., Kondoh A., Honda M., Miyamoto M., and Kojima H. (1990) Depth-profiles of halogen abundance and integrated intensity of hydration band near 3 mum in ALH

77231, Antarctic L6 chondrites. In Differences between Antarctic and non-Antarctic meteorites, pp. 32-37.

Ehlmann B., Bridges N., Fraeman A., Lapotre M., Edgett K., Johnson J., Cousin A., Yen A., Conrad P., and Thompson L. (2016) Chemistry and Mineralogy In Situ at the Bagnold Sand Dunes: Evidence for Aeolian Sorting and Size-Dependence in Sand Composition. In Lunar and Planetary Science Conference, pp. 1536.

Ehlmann B. L. and Edwards C. S. (2014) Mineralogy of the Martian surface. Annual Review of Earth and Planetary Sciences 42, 291-315.

Evans M. and Heller F. (2003) Environmental magnetism: principles and applications of enviromagnetics. Academic press.

Fernández-Remolar D. C., Rodriguez N., Gómez F., and Amils R. (2003) Geological record of an acidic environment driven by iron hydrochemistry: The Tinto River system. Journal of Geophysical Research: Planets 108(E7).

Fisher D. S. and Burns R. G. (1992) Mossbauer Spectra of H-5 Chondrites from Antarctica. In Lunar and Planetary Science Conference, pp. 367.

Floss C. and Crozaz G. (1991) Ce anomalies in the LEW85300 eucrite: evidence for REE mobilization during Antarctic weathering. Earth and Planetary Science Letters 107(1), 13-24.

Flynn G. J., Moore L. B., and Klöck W. (1999) Density and Porosity of Stone Meteorites: Implications for the Density, Porosity, Cratering, and Collisional Disruption of Asteroids. Icarus 142(1), 97-105.

Ford A. and Tabor R. (1971) The Thiel Mountains pallasite of Antarctica. US Geol Survey Prof Paper 750, 56-60.

Fritz J., Artemieva N., and Greshake A. (2005) Ejection of Martian meteorites. Meteoritics & Planetary Science 40(9-10), 1393-1411.

Gaillard F. and Scaillet B. (2009) The sulfur content of volcanic gases on Mars. Earth and Planetary Science Letters 279(1), 34-43.

Gattacceca J., Rochette P., and Bourot-Denise M. (2003) Magnetic properties of a freshly fallen LL ordinary chondrite: the Bensour meteorite. Physics of the Earth and Planetary Interiors 140(4), 343-358.

Genge M. J. and Grady M. M. (1999) Unequilibrated assemblages of sulphide, metal and oxide in the fusion crusts of the enstatite chondrite meteorites. Mineralogical Magazine 63(4), 473-488.

Gibson E. K., Wentworth S. J., and McKay D. S. (1983) Chemical weathering and diagenesis of a cold desert soil from Wright Valley, Antarctica: An analog of Martian weathering processes. Journal of Geophysical Research: Solid Earth 88(S02).

Giorgetti G. and Baroni C. (2007) High-resolution analysis of silica and sulphate-rich rock varnishes from Victoria Land (Antarctica). European journal of mineralogy 19(3), 381-389.

Golden D. C., Ming D. W., Morris R. V., and Mertzman S. A. (2005) Laboratory-simulated acid-sulfate weathering of basaltic materials: Implications for formation of sulfates at Meridiani Planum and Gusev crater, Mars. Journal of Geophysical Research: Planets 110(E12), n/a-n/a.

Gooding J. L. (1982) Mineralogical aspects of terrestrial weathering effects in chondrites from Allan Hills, Antarctica. Proc. 12th Lunar & Planetary Science Conference Houston, 1981, 12(B2), (Pergamon Press), 1105-1122.

Gooding J. L. (1986) Clay-mineraloid weathering products in Antarctic meteorites. Geochimica et Cosmochimica Acta 50(10), 2215-2223.

Grady M. M. (2000) Catalogue of meteorites. Cambridge University Press.

Greenwood J. P., Riciputi L. R., and McSween H. Y. (1997) Sulfide isotopic compositions in shergottites and ALH84001, and possible implications for life on Mars. Geochimica et Cosmochimica Acta 61(20), 4449-4453.

Greenwood R. and Franchi I. (2004) Alteration and metamorphism of CO3 chondrites: Evidence from oxygen and carbon isotopes. Meteoritics & Planetary Science Archives 39(11), 1823-1838.

Greenwood R. C., Franchi I. A., Gibson J. M., and Benedix G. K. (2012) Oxygen isotope variation in primitive achondrites: The influence of primordial, asteroidal and terrestrial processes. Geochimica et Cosmochimica Acta 94, 146-163.

Grotzinger J. P., Arvidson R., Bell J., Calvin W., Clark B., Fike D., Golombek M., Greeley R., Haldemann A., and Herkenhoff K. (2005) Stratigraphy and sedimentology of a dry to wet eolian depositional system, Burns formation, Meridiani Planum, Mars. Earth and Planetary Science Letters 240(1), 11-72.

Grotzinger J. P., Sumner D., Kah L., Stack K., Gupta S., Edgar L., Rubin D., Lewis K., Schieber J., and Mangold N. (2014) A habitable fluvio-lacustrine environment at Yellowknife Bay, Gale crater, Mars. Science 343(6169), 1242777.

Hagerty J. J. and Newsom H. E. (2003) Hydrothermal alteration at the Lonar Lake impact structure, India: Implications for impact cratering on Mars. Meteoritics & Planetary Science 38(3), 365-381.

Harvey R. (2003) The Origin and Significance of Antarctic Meteorites. Chemie der Erde - Geochemistry 63(2), 93-147.

Harvey R. and Score R. (1991) Direct evidence of in-ice or pre-ice weathering of Antarctic meteorites. Meteoritics 26, 343.

Hausrath E., Treiman A., Vicenzi E., Bish D., Blake D., Sarrazin P., Hoehler T., Midtkandal I., Steele A., and Brantley S. (2008) Short-and long-term olivine weathering in Svalbard: implications for Mars. Astrobiology 8(6), 1079-1092.

Hecht M., Kounaves S., Quinn R., West S., Young S., Ming D., Catling D., Clark B., Boynton W., and Hoffman J. (2009) Detection of perchlorate and the soluble chemistry of martian soil at the Phoenix lander site. Science 325(5936), 64-67.

Heumann K. and Gall M. (1987) Geochemical investigations to explain iodine-overabundances in Antarctic meteorites. Geochimica et Cosmochimica Acta 51(9), 2541-2547.

Heumann K., Neubauer J., and Reifenhäuser W. (1990) Iodine overabundances measured in the surface layers of an Antarctic stony and iron meteorite. Geochimica et Cosmochimica Acta 54(9), 2503-2506.

Hewitt C. N. and Jackson A. V. (2008) Handbook of atmospheric science: Principles and applications. John Wiley & Sons.

Hicks L. J., Bridges J. C., and Gurman S. J. (2014) Ferric saponite and serpentine in the nakhlite martian meteorites. Geochimica et Cosmochimica Acta 136, 194-210.

Hirschmann M. M. and Withers A. C. (2008) Ventilation of CO 2 from a reduced mantle and consequences for the early Martian greenhouse. Earth and Planetary Science Letters 270(1), 147-155.

Hsu W., Guan Y., Wang H., Leshin L. A., Wang R., Zhang W., Chen X., Zhang F., and Lin C. (2004) The lherzolitic shergottite Grove Mountains 99027: Rare earth element geochemistry. Meteoritics & Planetary Science 39(5), 701-709.

Hurowitz J. A., McLennan S. M., Tosca N. J., Arvidson R. E., Michalski J. R., Ming D. W., Schröder C., and Squyres S. W. (2006) In situ and experimental evidence for acidic weathering of rocks and soils on Mars. Journal of Geophysical Research: Planets 111(E2), n/a-n/a.

Hynek B. M., McCollom T. M., Marcucci E. C., Brugman K., and Rogers K. L. (2013) Assessment of environmental controls on acid-sulfate alteration at active volcanoes in Nicaragua: Applications to relic hydrothermal systems on Mars. Journal of Geophysical Research: Planets 118(10), 2083-2104.

Jones C. L. and Brearley A. J. (2006) Experimental aqueous alteration of the Allende meteorite under oxidizing conditions: Constraints on asteroidal alteration. Geochimica et Cosmochimica Acta 70(4), 1040-1058.

Jull A. J. T. (2001) Terrestrial Ages of Meteorites. In Accretion of Extraterrestrial Matter Throughout Earth's History (eds. B. Peucker-Ehrenbrink and B. Schmitz), pp. 241-266. Springer US.

Jull A. J. T., Cheng S., Gooding J. L., and Velbel M. A. (1988) Rapid growth of magnesium carbonate weathering products in a stony meteorite from Antarctica. Science 242, 417-419.

Kagi H. and Takahashi K. (1998) Relationship between positive cerium anomaly and adsorbed water in Antarctic lunar meteorites. Meteoritics & Planetary Science 33(5), 1033-1040.

Kaplan H. H., Milliken R. E., Fernández-Remolar D., Amils R., Robertson K., and Knoll A. H. (2016) Orbital evidence for clay and acidic sulfate assemblages on Mars based on mineralogical analogs from Rio Tinto, Spain. Icarus 275, 45-64.

Keil K. and Fredriksson K. (1964) The iron, magnesium, and calcium distribution in coexisting olivines and rhombic pyroxenes of chondrites. Journal of Geophysical Research 69(16), 3487-3515.

Klingelhöfer G., Morris R. V., Bernhardt B., Schröder C., Rodionov D. S., De Souza Jr P. A., Yen A., Gellert R., Evlanov E. N., Zubkov B., Foh J., Bonnes U., Kankeleit E., Gütlich P., Ming D. W., Renz F., Wdowiak T., Squyres S. W., and Arvidson R. E. (2004a) Jarosite and hematite at Meridiani Planum from opportunity's Mössbauer spectrometer. Science 306(5702), 1740-1745.

Klingelhöfer G., Morris R. V., Bernhardt B., Schröder C., Rodionov D. S., De Souza P., Yen A., Gellert R., Evlanov E., and Zubkov B. (2004b) Jarosite and hematite at Meridiani Planum from Opportunity's Mössbauer spectrometer. Science 306(5702), 1740-1745.

Koeberl C. and Cassidy W. A. (1991) Differences between Antarctic and non-Antarctic meteorites: An assessment. Geochimica et Cosmochimica Acta 55(1), 3-18.

Kråhenbühl U. and Langenauer M. (1994) ALH 82102: An Antarctic meteorite embedded partly in ice. Meteoritics 29(5), 651-653.

Krinsley D., Dorn R., and Tovey N. (1995) Nanometer-scale layering in rock varnish: implications for genesis and paleoenvironmental interpretation. The Journal of Geology, 106-113.

Krinsley D. and Rusk B. (2000) Bacterial Presence in Layered Rock Varnish-Possible Mars Analog? In Second International Conference on Mars Polar Science and Exploration, pp. 98.

Kwong Y.-T. J. (1993) Prediction and prevention of acid rock drainage from a geological and mineralogical perspective. MEND.

Langenauer M. and Krahenbuhl U. (1993) Depth-profiles and surface enrichment of the halogens in four Antarctic H5 chondrites and in two non-Antarctic chondrites. Meteoritics 28(1), 98-104.

Langenauer M. and Krähenbühl U. (1993) Halogen contamination in Antarctic H5 and H6 chondrites and relation to sites of recovery. Earth and Planetary Science Letters 120(3), 431-442.

Lee M. R. and Bland P. A. (2004) Mechanisms of weathering of meteorites recovered from hot and cold deserts and the formation of phyllosilicates. Geochimica et Cosmochimica Acta 68(4), 893-916.

Lee M. R., Smith C. L., Gordon S. H., and Hodson M. E. (2006) Laboratory simulation of terrestrial meteorite weathering using the Bensour (LL6) ordinary chondrite. Meteoritics & Planetary Science 41(8), 1123-1138.

Lee M. R., Tomkinson T., Mark D. F., Stuart F. M., and Smith C. L. (2013) Evidence for silicate dissolution on Mars from the Nakhla meteorite. Meteoritics and Planetary Science 48(2), 224-240.

Lorand J.-P., Hewins R. H., Remusat L., Zanda B., Pont S., Leroux H., Marinova M., Jacob D., Humayun M., Nemchin A., Grange M., Kennedy A., and Göpel C. (2015) Nickeliferous pyrite tracks pervasive hydrothermal alteration in Martian regolith breccia: A study in NWA 7533. Meteoritics & Planetary Science 50(12), 2099-2120.

Losiak A. and Velbel M. A. (2011) Evaporite formation during weathering of Antarctic meteorites—A weathering census analysis based on the ANSMET database. Meteoritics & Planetary Science 46(3), 443-458.

Loughnan F. C. (1969) Chemical weathering of the silicate minerals.

Louzada K. L., Stewart S. T., and Weiss B. P. (2007) Effect of shock on the magnetic properties of pyrrhotite, the Martian crust, and meteorites. Geophysical Research Letters 34(5), n/a-n/a.

Louzada K. L., Stewart S. T., Weiss B. P., Gattacceca J., and Bezaeva N. S. (2010) Shock and static pressure demagnetization of pyrrhotite and implications for the Martian crust. Earth and Planetary Science Letters 290(1), 90-101.

Luce R. W., Bartlett R. W., and Parks G. A. (1972) Dissolution kinetics of magnesium silicates. Geochimica et Cosmochimica Acta 36(1), 35-50.

Lundberg L. L., Crozaz G., and McSween Jr H. Y. (1990) Rare earth elements in minerals of the ALHA77005 shergottite and implications for its parent magma and crystallization history. Geochimica et Cosmochimica Acta 54(9), 2535-2547.

Madden M. E., Bodnar R., and Rimstidt J. (2004) Jarosite as an indicator of water-limited chemical weathering on Mars. Nature 431(7010), 821-823.

Marvin U. (1980) Magnesium carbonate and magnesium sulfate deposits on Antarctic meteorites. Antarctic Journal of the United States 15, 54-55.

Masuda A., Tanaka T., Shimizu H., Wakisaka T., and Nakamura N. (1979) Rare-earth geochemistry of Antarctic diogenites. Memoirs of National Institute of Polar Research. Special issue 15, 177-188.

Mawson D. (1915) The home of the blizzard. JSTOR.

McAdam A. C., Zolotov M. Y., Sharp T. G., and Leshin L. A. (2008) Preferential low-pH dissolution of pyroxene in plagioclase–pyroxene mixtures: Implications for martian surface materials. Icarus 196(1), 90-96.

McKay D. S., Gibson Jr E. K., Thomas-Keprta K. L., and Vali H. (1996) Search for past life on Mars: possible relic biogenic activity in Martian meteorite ALH84001. Science 273(5277), 924.

McLennan S., Bell J., Calvin W., Christensen P., Clark B. d., De Souza P., Farmer J., Farrand W., Fike D., and Gellert R. (2005) Provenance and diagenesis of the evaporite-bearing Burns formation, Meridiani Planum, Mars. Earth and Planetary Science Letters 240(1), 95-121.

McSween H. Y. and Keil K. (2000) Mixing relationships in the Martian regolith and the composition of globally homogeneous dust. Geochimica et Cosmochimica Acta 64(12), 2155-2166.

McSween Jr H. Y., Murchie S. L., Crisp J. A., Bridges N. T., Anderson R. C., Bell Iii J. F., Britt D. T., Brückner J., Dreibus G., Economou T., Ghosh A., Golombek M. P., Greenwood J. P., Johnson J. R., Moore H. J., Morris R. V., Parker T. J., Rieder R., Singer R., and Wänke H. (1999) Chemical, multispectral, and textural constraints on the composition and origin of rocks at the Mars Pathfinder landing site. Journal of Geophysical Research E: Planets 104(E4), 8679-8715.

Michalski J. and Niles P. B. (2012) Atmospheric origin of Martian interior layered deposits: Links to climate change and the global sulfur cycle. Geology 40(5), 419-422.

Miller M., Franchi I., Sexton A., and Pillinger C. (1999) High-precision d17O Isotope Measurements of Oxygen from Silicates and Other Oxides: Method and Applications. Rapid Communications in Mass Spectrometry 13(13), 1211-1217.

Ming D. W., Mittlefehldt D. W., Morris R. V., Golden D. C., Gellert R., Yen A., Clark B. C., Squyres S. W., Farrand W. H., Ruff S. W., Arvidson R. E., Klingelhöfer G., McSween H. Y., Rodionov D. S., Schröder C., de Souza P. A., and Wang A. (2006) Geochemical and mineralogical indicators for aqueous processes in the Columbia Hills of Gusev crater, Mars. Journal of Geophysical Research: Planets 111(E2), E02S12.

Mittlefehldt D. W. and Lindstrom M. M. (1991) Generation of abnormal trace element abundances in Antarctic eucrites by weathering processes. Geochimica et Cosmochimica Acta 55(1), 77-87.

Morris R., Ming D., Graff T., Arvidson R., Bell J., Squyres S., Mertzman S., Gruener J., Golden D., and Le L. (2005) Hematite spherules in basaltic tephra altered under aqueous, acid-sulfate conditions

on Mauna Kea volcano, Hawaii: possible clues for the occurrence of hematite-rich spherules in the Burns formation at Meridiani Planum, Mars. Earth and Planetary Science Letters 240(1), 168-178.

Morris R. V., Golden D., Bell J. F., Shelfer T. D., Scheinost A. C., Hinman N. W., Furniss G., Mertzman S. A., Bishop J. L., and Ming D. W. (2000) Mineralogy, composition, and alteration of Mars Pathfinder rocks and soils: Evidence from multispectral, elemental, and magnetic data on terrestrial analogue, SNC meteorite, and Pathfinder samples. Journal of Geophysical Research: Planets 105(E1), 1757-1817.

Morris R. V., Ruff S. W., Gellert R., Ming D. W., Arvidson R. E., Clark B. C., Golden D., Siebach K., Klingelhöfer G., and Schröder C. (2010) Identification of carbonate-rich outcrops on Mars by the Spirit rover. Science 329(5990), 421-424.

Morris R. V., Vaniman D. T., Blake D. F., Gellert R., Chipera S. J., Rampe E. B., Ming D. W., Morrison S. M., Downs R. T., and Treiman A. H. (2016) Silicic volcanism on Mars evidenced by tridymite in high-SiO2 sedimentary rock at Gale crater. Proceedings of the National Academy of Sciences, 201607098.

Murozumi M., Chow T. J., and Patterson C. (1969) Chemical concentrations of pollutant lead aerosols, terrestrial dusts and sea salts in Greenland and Antarctic snow strata. Geochimica et Cosmochimica Acta 33(10), 1247-1294.

Murty S., Shukla P., and Goel P. (1983) Lithium in stone meteorites and stony irons. Meteoritics 18(2), 123-136.

Nachon M., Clegg S., Mangold N., Schröder S., Kah L., Dromart G., Ollila A., Johnson J., Oehler D., and Bridges J. (2014) Calcium sulfate veins characterized by ChemCam/Curiosity at Gale crater, Mars. Journal of Geophysical Research: Planets 119(9), 1991-2016.

Nesbitt H. and Young G. (1982) Early Proterozoic climates and plate motions inferred from major element chemistry of lutites. Nature 299(5885), 715-717.

Nickel E. H. and Thornber M. R. (1977) Chemical constraints on the weathering of serpentinites containing nickel-iron sulphides. Journal of Geochemical Exploration 8(1–2), 235-245.

Niles P. B. and Michalski J. (2009) Meridiani Planum sediments on Mars formed through weathering in massive ice deposits. Nature Geoscience 2(3), 215-220.

Noll K., Döbeli M., Krähenbühl U., Grambole D., Herrmann F., and Koeberl C. (2003) Detection of terrestrial fluorine by proton induced gamma emission (PIGE): A rapid quantification for Antarctic meteorites. Meteoritics & Planetary Science 38(5), 759-765.

Nyquist L. E., Bogard D. D., Shih C.-Y., Greshake A., Stöffler D., and Eugster O. (2001) Ages and Geologic Histories of Martian Meteorites. In Chronology and Evolution of Mars: Proceedings of an ISSI Workshop, 10–14 April 2000, Bern, Switzerland (eds. R. Kallenbach, J. Geiss, and W. K. Hartmann), pp. 105-164. Springer Netherlands, Dordrecht.

Ody A., Poulet F., Bibring J. P., Loizeau D., Carter J., Gondet B., and Langevin Y. (2013) Global investigation of olivine on Mars: Insights into crust and mantle compositions. Journal of Geophysical Research: Planets 118(2), 234-262.

Palme H., Spettel B., Burghele A., Weckwerth G., Wanke H., Delany J., and Prinz M. (1983) Elephant Moraine polymict eucrites: A eucrite-howardite compositional link. In Lunar and Planetary Science Conference, pp. 590-591.

Pokrovsky O. S. and Schott J. (2000) Kinetics and mechanism of forsterite dissolution at 25 C and pH from 1 to 12. Geochimica et Cosmochimica Acta 64(19), 3313-3325.

Poulet F., Bibring J.-P., Mustard J., Gendrin A., Mangold N., Langevin Y., Arvidson R., Gondet B., Gomez C., and Berthé M. (2005) Phyllosilicates on Mars and implications for early Martian climate. Nature 438(7068), 623-627.

Rathbun J. A. and Squyres S. W. (2002) Hydrothermal systems associated with Martian impact craters. Icarus 157(2), 362-372.

Rochette P., Fillion G., Ballou R., Brunet F., Ouladdiaf B., and Hood L. (2003a) High pressure magnetic transition in pyrrhotite and impact demagnetization on Mars. Geophysical Research Letters 30(13).

Rochette P., Fillion G., Ballou R., Brunet F., Ouladdiaf B., and Hood L. (2003b) High pressure magnetic transition in pyrrhotite and impact demagnetization on Mars. Geophysical Research Letters 30(13), n/a-n/a.

Rochette P., Gattacceca J., and Lewandowski M. (2012) Magnetic classification of meteorites and application to the Sołtmany fall. Meteorites 2(1-2), 67-71.

Rochette P., Lorand J.-P., Fillion G., and Sautter V. (2001) Pyrrhotite and the remanent magnetization of SNC meteorites: a changing perspective on Martian magnetism. Earth and Planetary Science Letters 190(1), 1-12.

Rochette P., Sagnotti L., BOUROT-DENISE M., Consolmagno G., Folco L., Gattacceca J., Osete M. L., and Pesonen L. (2003c) Magnetic classification of stony meteorites: 1. Ordinary chondrites. Meteoritics & Planetary Science 38(2), 251-268.

Rose A. W. and Bianchi-Mosquera G. C. (1993) Adsorption of Cu, Pb, Zn, Co, Ni, and Ag on goethite and hematite; a control on metal mobilization from red beds into stratiform copper deposits. Economic Geology 88(5), 1226-1236.

Ruff S. W., Farmer J. D., Calvin W. M., Herkenhoff K. E., Johnson J. R., Morris R. V., Rice M. S., Arvidson R. E., Bell J. F., and Christensen P. R. (2011) Characteristics, distribution, origin, and significance of opaline silica observed by the Spirit rover in Gusev crater, Mars. Journal of Geophysical Research: Planets 116(E7).

Salvatore M. R., Mustard J. F., Head J. W., Cooper R. F., Marchant D. R., and Wyatt M. B. (2013) Development of alteration rinds by oxidative weathering processes in Beacon Valley, Antarctica, and implications for Mars. Geochimica et Cosmochimica Acta 115, 137-161.

Sato M. (1960) Oxidation of sulfide ore bodies; 1, Geochemical environments in terms of Eh and pH. Economic Geology 55(5), 928-961.

Schott J., Berner R. A., and Sjöberg E. L. (1981) Mechanism of pyroxene and amphibole weathering—I. Experimental studies of iron-free minerals. Geochimica et Cosmochimica Acta 45(11), 2123-2135.

Schramm B. (2004) Color atlas of low-temperature alteration features in basalts from the Southern East Pacific Rise. Geochemistry, Geophysics, Geosystems 5(6).

Schultz L. (1986) Allende in Antarctia: Temperatures in Antarctic Meteorites. Meteoritics 21, 505.

Schwenzer S., Abramov O., Allen C., Bridges J., Clifford S., Filiberto J., Kring D., Lasue J., McGovern P., and Newsom H. (2012) Gale Crater: Formation and post-impact hydrous environments. Planetary and Space Science 70(1), 84-95.

Scott E. R. (1982) Origin of rapidly solidified metal-troilite grains in chondrites and iron meteorites. Geochimica et Cosmochimica Acta 46(5), 813-823.

Sears D. W., Yozzo J., and Ragland C. (2011) The natural thermoluminescence of Antarctic meteorites and their terrestrial ages and orbits: A 2010 update. Meteoritics & Planetary Science 46(1), 79-91.

Settle M. (1979) Formation and deposition of volcanic sulfate aerosols on Mars. Journal of Geophysical Research: Solid Earth 84(B14), 8343-8354.

Shinonaga T., Endo K., Ebihara M., Heumann K. G., and Nakahara H. (1994) Weathering of Antarctic meteorites investigated from contents of Fe3+, chlorine, and iodine. Geochimica et Cosmochimica Acta 58(17), 3735-3740.

Shinotsuka K., Hidaka H., and Ebihara M. (1995) Detailed abundances of rare earth elements, thorium and uranium in chondritic meteorites: An ICP-MS study. Meteoritics 30(6), 694-699.

Siever R. and Woodford N. (1979) Dissolution kinetics and the weathering of mafic minerals. Geochimica et Cosmochimica Acta 43(5), 717-724.

Smith C. L., Milnes R., and Eggleton A. (1987) Weathering of basalt: formation of iddingsite. Clays and Clay Minerals 35(6), 418-428.

Squyres S., Arvidson R. E., Ruff S., Gellert R., Morris R., Ming D., Crumpler L., Farmer J., Des Marais D., and Yen A. (2008) Detection of silica-rich deposits on Mars. Science 320(5879), 1063-1067.

Squyres S., Grotzinger J., Arvidson R., Bell J., Calvin W., Christensen P., Clark B., Crisp J., Farrand W., and Herkenhoff K. E. (2004) In situ evidence for an ancient aqueous environment at Meridiani Planum, Mars. Science 306(5702), 1709-1714.

Squyres S. W., Arvidson R. E., Bell Iii J. F., Calef Iii F., Clark B. C., Cohen B. A., Crumpler L. A., De Souza Jr P. A., Farrand W. H., Gellert R., Grant J., Herkenhoff K. E., Hurowitz J. A., Johnson J. R., Jolliff B. L., Knoll A. H., Li R., McLennan S. M., Ming D. W., Mittlefehldt D. W., Parker T. J., Paulsen G., Rice M. S., Ruff S. W., Schröder C., Yen A. S., and Zacny K. (2012) Ancient impact and aqueous processes at endeavour crater, Mars. Science 336(6081), 570-576.

Squyres S. W. and Knoll A. H. (2005) Sedimentary rocks at Meridiani Planum: Origin, diagenesis, and implications for life on Mars. Earth and Planetary Science Letters 240(1), 1-10.

Stöffler D., Keil K., and Edward R.D S. (1991) Shock metamorphism of ordinary chondrites. Geochimica et Cosmochimica Acta 55(12), 3845-3867.

Tosca N. J., McLennan S. M., Lindsley D. H., and Schoonen M. A. (2004) Acid-sulfate weathering of synthetic Martian basalt: The acid fog model revisited. Journal of Geophysical Research: Planets (1991–2012) 109(E5).

Treiman A. H. (1995) A petrographic history of martian meteorite ALH84001: Two shocks and an ancient age. Meteoritics 30(3), 294-302.

Tyra M., Farquhar J., Wing B., Benedix G., Jull A., Jackson T., and Thiemens M. (2007) Terrestrial alteration of carbonate in a suite of Antarctic CM chondrites: Evidence from oxygen and carbon isotopes. Geochimica et Cosmochimica Acta 71(3), 782-795.

Uehara M., Gattacceca J., Rochette P., Demory F., and Valenzuela E. M. (2012) Magnetic study of meteorites recovered in the Atacama desert (Chile): Implications for meteorite paleomagnetism and the stability of hot desert surfaces. Physics of the Earth and Planetary Interiors 200, 113-123.

Vaniman D., Bish D., Ming D., Bristow T., Morris R., Blake D., Chipera S., Morrison S., Treiman A., and Rampe E. (2014) Mineralogy of a mudstone at Yellowknife Bay, Gale crater, Mars. Science 343(6169), 1243480.

Velbel M. A. (2009) Dissolution of olivine during natural weathering. Geochimica et Cosmochimica Acta 73(20), 6098-6113.

Velbel M. A. (2014) Terrestrial weathering of ordinary chondrites in nature and continuing during laboratory storage and processing: Review and implications for Hayabusa sample integrity. Meteoritics & Planetary Science 49(2), 154-171.

Velbel M. A. and Barker W. W. (2008) Pyroxene weathering to smectite: Conventional and cryo-field emission scanning electron microscopy, Koua Bocca ultramafic complex, Ivory Coast. Clays and Clay Minerals 56(1), 112-127.

Velbel M. A., Long D. T., and Gooding J. L. (1991) Terrestrial weathering of Antarctic stone meteorites: Formation of Mg-carbonates on ordinary chondrites. Geochimica et Cosmochimica Acta 55(1), 67-76.

Velbel M. A. and Losiak A. I. (2010) Denticles on chain silicate grain surfaces and their utility as indicators of weathering conditions on Earth and Mars. Journal of Sedimentary Research 80(9), 771-780.

Venturelli G., Contini S., and Bonazzi A. (1997) Weathering of ultramafic rocks and element mobility at Mt. Prinzera, Northern Apennines, Italy. Mineralogical Magazine 61(6), 765-778.

Wasilewski P. (1988) Magnetic characterization of the new magnetic mineral tetrataenite and its contrast with isochemical taenite. Physics of the Earth and Planetary Interiors 52(1–2), 150-158.

Wedepohl K. H. and Correns C. W. (1969) Handbook of geochemistry.

Weiss B. P., Gattacceca J., Stanley S., Rochette P., and Christensen U. R. (2010) Paleomagnetic records of meteorites and early planetesimal differentiation. Space Science Reviews 152(1-4), 341-390.

Welten K. C., Folco L., Nishiizumi K., Caffee M. W., Grimberg A., Meier M. M. M., and Kober F. (2008) Meteoritic and bedrock constraints on the glacial history of Frontier Mountain in northern Victoria Land, Antarctica. Earth and Planetary Science Letters 270(3-4), 308-315.

Wentworth S. J., Gibson E. K., Velbel M. A., and McKay D. S. (2005) Antarctic Dry Valleys and indigenous weathering in Mars meteorites: Implications for water and life on Mars. Icarus 174(2 SPEC. ISS.), 383-395.

White J., EP H., and Mason B. (1967) Secondary Minerals Produced by Weathering of Wolf Creek Meteorite. American Mineralogist 52(7-8), 1190-&.

Wlotzka F. (1993) A weathering scale for the ordinary chondrites. Meteoritics 28, 460-460.

Wolters S. D., Hagene J. K., Sund A. T., Bohman A., Guthery W., Sund B. T., Hagermann A., Tomkinson T., Romstedt J., Morgan G. H., and Grady M. M. (2013) WatSen: Design and testing of a prototype mid-IR spectrometer and microscope package for Mars exploration. Experimental Astronomy 36(1-2), 175-193.

Wood J. A. (1964) The cooling rates and parent planets of several iron meteorites. Icarus 3(5), 429-459.

Yabuki H., Okada A., and Shima M. (1976) Nesquehonite found on the Yamato 74371 meteorite. Sci. Pap. Inst. Phys. Chem. Res., Vol. 70, No. 1, p. 22-29 70, 22-29.

Yen A. and Murray B. (1998) The color of Mars: Oxidation of exogenic metallic iron. In Bulletin of the American Astronomical Society, pp. 1053.

Yen A. S., Mittlefehldt D. W., McLennan S. M., Gellert R., Bell J., McSween H. Y., Ming D. W., McCoy T. J., Morris R. V., and Golombek M. (2006) Nickel on Mars: Constraints on meteoritic material at the surface. Journal of Geophysical Research: Planets 111(E12).

Yoshida M., Ando H., Omoto K., Naruse R., and Ageta Y. (1971) Discovery of meteorites near Yamato Mountains, East Antarctica. Japanese Antarctic Record 39, 62-65.